Testing General Relativity with Gravitational Waves

Dissertation

zur

Erlangung der naturwissenschaftlichen Doktorwürde

(Dr. sc. nat.)

vorgelegt der

Mathematisch-naturwissenschaftlichen Fakultät

der

Universität Zürich

von

Cédric Huwyler

von

Beinwil (Freiamt) AG

Promotionskomitee

Prof. Dr. Philippe Jetzer (Vorsitz und Leitung)
PD Dr. Edward Porter
Prof. Dr. Daniel Wyler

Zürich, 2014

Summary

Although General Relativity (GR) is very successful in the explanation of the gravitational dynamics of massive bodies and the large scale structure of the universe, it cannot be brought into accordance with quantum theories that account for quantum effects on microscopic scales. In addition, certain extensions of GR seem to provide an alternative explanation for dark matter or cosmological inflation. To this end and for the pure sake of testing the pillars of GR, various alternative theories have been proposed. Gravitational Waves (GWs) are a unique tool to verify whether GR is the true underlying theory of gravitation or whether an alternative model has to be preferred. Among the strongest sources of GWs are coalescing supermassive black hole (SMBH) binaries with masses of about $10^4 - 10^{10} M_\odot$. GWs from SMBH binaries are in the frequency band of the planned space-based GW detector eLISA, that aims to be launched in 2034 and could provide excellent tests of GR. From a data analysis perspective, when working in the post-Newtonian (PN) approximation of Einstein's field equations, GR waveforms from SMBHs are entirely characterised by their set of PN coefficients. An accurate measurement of these coefficients will allow us to put strong constraints on the free parameters of alternative theories in the relativistic, strong-field regime. Such tests are highly necessary, as the presence of an alternative theory could corrupt parameter estimation or even prevent detection when using GR templates.

In the first part of this work, we investigate how the introduction of higher harmonics to the gravitational waveform of SMBHs with arbitrary spin-precession changes parameter estimation in the context of a Classic LISA detector. Higher harmonics enrich the gravitational waveform with extra information about the orbital dynamics of the observed binary system and hence allow us to break degeneracies among the binary and the theory parameters to some extent. Working in the stationary phase approximation (SPA) and restricting us to quasi-circular SMBH inspirals only, we introduce six theory parameters that account for modified gravity and truncate the waveform at second PN order. In order to find the error distributions for the theory parameters, we use the Fisher matrix formalism and carry out Monte Carlo simulations for 17 different mass configurations. We find that the use of higher harmonics is mandatory for total redshifted masses $\gtrsim 10^7 M_\odot$ while for lower masses the errors with and without the use of higher harmonics are comparable. We compute the correlations among the theory and the binary parameters and explore up to what maximum redshifts deviations of 1-10% in the theory parameters are still detectable. As a practical application, we compute an optimal lower bound on the Compton wavelength of the graviton. In addition, we investigate the breakdown of the different approximations used when approaching the last stable orbit in the presence of spin-precession.

In the second part, we propose the use of time domain waveforms for tests of GR instead of relying on frequency domain waveforms, since numerical Fourier transforms have become considerably faster since the conception of the SPA. To this end, we introduce modifications to a 2PN time domain waveform and relate it at leading order to a modified waveform in the SPA. We use then a Markov Chain Monte Carlo algorithm to test up to what modifications the eLISA detector is still able to detect non-GR waveforms with GR templates. Moreover, we determine at what point the deviations are so strong that a fundamental bias is introduced into parameter estimation and non-GR templates have to be used, even though GR templates could still be sufficient for detection. We demonstrate that for corrections coming in beyond 1PN order in phase and frequency, GR waveforms are sufficient for both detecting and estimating the parameters of alternative theory signals. However, for theories introducing corrections at 0PN and 0.5PN order, GR waveforms are not capable of covering the entire parameter space, requiring the use of non-GR waveforms for parameter estimation.

Zusammenfassung

Obwohl die Allgemeine Relativitätstheorie (ART) die Dynamik von schweren Körpern und die grobe Struktur des Universums sehr erfolgreich erklärt, sind bisher alle Versuche sie mit Quantentheorien zu vereinen, die sich mit Quanteneffekten auf der mikroskopischen Skala beschäftigen, gescheitert. Ausserdem scheinen gewisse Erweiterungen der ART eine alternative Erklärung für dunkle Materie oder kosmologische Inflation zu liefern. Zu diesem Zweck, und um die Fundamente der ART genauer zu überprüfen, sind diverse alternative Gravitationstheorien vorgeschlagen worden. Gravitationswellen sind ein einzigartiges Werkzeug um zu testen, ob die ART die grundlegende Theorie der Gravitation ist oder ob ein alternatives Modell zu bevorzugen ist. Unter den stärksten Quellen von Gravitationswellen findet man miteinander verschmelzende, superschwere schwarze Löcher (SMBHs) mit Massen von etwa $10^4-10^{10}M_\odot$. Die von solchen Systemen ausgehenden Gravitationswellen fallen in den Frequenzbereich des geplanten satellitenbasierten Gravitationswellen-Detektors eLISA, dessen Start für 2034 geplant ist und der exzellente Tests der ART liefern könnte. Da wir in der post-Newton'schen (PN) Approximation der Einstein'schen Feldgleichungen arbeiten, sind die von SMBHs ausgehenden Wellenformen in der ART aus einer Datenanalyse-Perspektive mit ihrem Satz von PN-Koeffizienten komplett charakterisiert. Eine genaue Messung dieser Koeffizienten wird es uns erlauben, die freien Parameter von alternativen Theorien im relativistischen Bereich mit starken Gravitationsfeldern bedeutend einzuschränken. Solche Tests sind äusserst notwendig, da die Anwesenheit einer alternativen Theorie zu einer fehlerhaften Parameterschätzung führen oder die Detektion mittels ART-Templates sogar ganz verhindern könnte.

Im ersten Teil dieser Arbeit untersuchen wir, wie die Schätzung von Parametern von SMBHs mit präzedierenden Spins im Kontext eines klassischen LISA-Detektors verändert wird, wenn zusätzlich Oberschwingungen der Gravitationswelle eingeführt werden. Oberschwingen bereichern die Gravitationswelle mit zusätzlicher Information über die Dynamik des beobachteten Zweikörpersystems und erlauben uns so, verschiedene Entartungen der System- und Theorieparameter zu einem gewissen Ausmass zu brechen. Wir arbeiten in der Stationary Phase Approximation (SPA) und beschränken uns auf SMBHs, die auf quasikreisförmigen Bahnen ineinanderfallen. Dazu führen wir sechs zusätzliche Theorieparameter ein, die eine modifizierte Gravitationstheorie berücksichtigen, und brechen bei quadratischer PN-Ordnung ab. Wir wenden den Fisher-Matrix-Formalismus an um die Fehlerverteilung der Theorieparameter zu finden und führen dazu Monte-Carlo-Simulationen für 17 verschiedene Massenkonfigurationen durch. Das führt uns zur Tatsache, dass für totale Massen $\gtrsim 10^7 M_\odot$ Oberschwingungen zwingend berücksichtigt werden müssen, während für leichtere Massen die Fehler mit und ohne Oberschwingungen etwa gleichwertig sind. Wir errechnen die Korrelationen zwischen den Theorie- und den Systemparametern und geben maximale Rotlichtverschiebungen an, bei denen Abweichungen von 1-10% immer noch detektierbar sind. Als ein praktisches Beispiel berechnen wir eine optimale untere Schranke für die Compton-Wellenlänge des Gravitons. Ausserdem untersuchen wir das Versagen der verschiedenen benutzten Approximationen, wenn sich die schwarzen Löcher ihrer letzten stabilen Umlaufbahn nähern und berücksichtigen dabei die Anwesenheit präzedierender Spins.

Im zweiten Teil dieser Arbeit schlagen wir vor, statt wie bisher mit Wellen im Frequenzraum zu arbeiten, für Tests der ART Wellen im Zeitraum zu benutzen, da numerische Fouriertransformationen seit der Konzeption der SPA wesentlich schneller geworden sind. Dazu modifizieren wir eine 2PN Wellenform im Zeitraum und setzen sie in führender Ordnung in eine Beziehung zu einer modifizierten SPA-Wellenform im Frequenzraum. Anschliessend benutzen wir einen Markov-Chain-Monte-Carlo-Algorithmus um zu testen, zu welchem Ausmass der eLISA-Detektor nicht-ART-Wellenformen mit ART-Templates noch finden kann. Weiterhin bestimmen wir, wann die Abweichung der geschätzten Parameter so stark wird, dass ein fundamentaler systematischer Fehler vorliegt und nicht-ART Templates benutzt werden müssen, obwohl die

ART möglicherweise noch immer zu einer Detektion führt. Wir zeigen, dass ART-Templates für Korrekturen höher als die 1PN-Ordnung in Phase und Frequenz ausreichend für die Detektion und Parameterschätzung des Signals der alternativen Theorie sind. Für Theorien, die Korrekturen in der 0PN- oder 0.5PN-Ordnung einführen, sind die ART-Templates jedoch nicht in der Lage, den gesamten Parameterraum abzudecken; hier werden nicht-ART-Templates für die Parameterschätzung benötigt.

Acknowledgements

My PhD thesis stands on the shoulders of a multitude of people who gave me technical, organisational and also emotional support during the last four years, for which I am very thankful. In the following, I will address the people that have supported and influenced me most, as it is impossible to list everybody. I apologise in advance to anybody that I have omitted (but not forgotten!).

First and foremost, I would like to express my profoundest gratitude to my principal supervisor *Prof. Dr. Philippe Jetzer*. He provided me with the opportunity to do my doctorate at the University of Zurich. Besides introducing me to the field of gravitational wave astronomy, he also provided for funding that covered for my salary and my many travel expenses for conferences, schools and research stays. I consider myself particularly lucky that I was given the possibility of visiting so many different locations where I got to know many influential people in the field. Whenever I encountered a problem, he was ready to give helpful advice and to provide a practical solution. I also appreciate greatly our many stimulating discussions that often extended beyond physics.

Supervising my Master thesis, *Dr. Antoine Klein* guided my first steps into the field of gravitational wave research and later became an excellent collaborator during the first year of my PhD, before he left for a postdoctoral position in the USA. Whenever I had questions and concerns, he was ready and would patiently point me in the right direction. It was always a pleasure when we met at a conference or when he visited us in Zurich.

Dr. Edward Porter and I started to work together after I submitted my first publication. I experienced our collaboration as very fruitful and enjoyed our stimulating discussions on both subject-specific and other topics. I sincerely appreciate all his contributions of time and ideas, especially his hard work on the code. I admire his deep knowledge in the field of gravitational wave astronomy, especially his expertise in Markov Chain Monte Carlo algorithms. My stays at the François Arago Center in Paris were always intensive and at the same time delightful; I particularly enjoyed the dinners with Ed and his wive Heather. Moreover, I appreciate highly that he agreed to be present as an external expert at my thesis defense.

I also want to express my special gratitude to *Prof. Dr. Monica Colpi* who readily agreed to act as an external expert to assess my thesis.

I particularly appreciate the great atmosphere I experienced with my office colleagues *Simone Balmelli*, *Mario Lubini*, *Lionel Philippoz*, *Crescenzo Tortora* and *Lorenzo de Vittori* that also extended to topics and activities outside of research and formed bonds that will reach beyond academia. In addition, I'm also very thankful to all the other members of my group and of the physics institute for the warm atmosphere.

Moreover, I would like to thank *Esther Meier* and *Regina Schmid* of the Sekretariat for all their work. They readily provided solutions to all my administrational problems, giving me the opportunity to concentrate fully on my work.

My appreciation goes also to some particular fellow PhD students that I know since we were undergraduates. With *Christian Elsasser*, *Roman Gredig*, *Matthieu Jaquier*, *Rafael Küng*, *Gabriel Landolt*, *Tina Wentz*, *Flavio Wicki* and *Oriana Schällibaum* I enjoyed many nice moments, especially over lunch. I am particularly thankful to *Flavio Lanfranconi* for his support and for our many stimulating discussions.

I'm especially grateful to my parents *Ruth* and *Joe*, my sister *Dominique* and my brother *Andres* for their love, encouragement and support throughout the long way that has led to this day. Finally, I would like to thank my beloved girlfriend *Viviane*, who let herself in with a theoretical physicist, for her essential moral support and for enduring with great patience my frequent concerns that I suppose are unavoidable in the life of a PhD student.

I am most grateful to all my friends who make my life as pleasurable as it is.

Thank You.

Cédric Huwyler Zürich, 22 October 2013

Table of Contents

Chapter 1

Introduction

In 1916, almost one hundred years ago, Albert Einstein showed that his earlier devised theory of general relativity (GR) admits wave-like solutions on the spacetime manifold, so-called *gravitational waves* (GWs). GWs propagate with the speed of light and locally 'stretch and squeeze' spacetime. After Einstein had published his results, a long argument started among the community whether GWs really carry energy or whether they are just an artifact of gauge freedom. It was in the 1960s when Joseph Weber started to build so-called resonant-mass detectors, that were made of a piezo-electric material and were expected to respond to a possible GW strain with an electric signal. Already in 1967, he published a paper where he claimed to have detected a GW signal. However, his results where (most certainly rightfully) discredited by the community, since nobody expected GW amplitudes to be as strong as Weber claimed to have detected. In fact, GWs are extremely weak since the coupling constant of GR, that is of the order of $G/c^4 \sim 10^{-45}$, makes the response of spacetime to time-varying matter sources extraordinarily stiff. As a consequence, length scales suffer only a relative change of the order of $\Delta L/L \sim 10^{-20} - 10^{-22}$ under the action of a GW from a source at cosmological distance. In 1974, however, Robert Hulse and Russel Taylor provided evidence for an indirect detection of GWs. They noticed that the observed orbital period of the binary pulsar PSR B1913+16 is decreasing with time and could successfully explain this decay with energy loss through gravitational radiation as predicted by GR. Hulse and Taylor were awarded with the Nobel prize in 1993 for this discovery that ended all discussions whether or not gravitational waves are real, physical effects. In 1992, Kip Thorne, Ronald Drever and Rainer Weiss founded the Laser Interferometer Gravitational-wave Observatory (LIGO) that aims for a detection of GWs through the observation of phase interference in a Michelson-type laser interferometer. LIGO consists of two sites, one in Hanford, Washington and one in Livingston, Louisiana, that use laser interferometers with arm lengths of 4 km each. Along the way, other laser interferometers have been constructed around the world, such as Virgo in Italy and GEO600 in Germany. Currently, LIGO and Virgo are being upgraded and should hopefully provide a first direct GW detection within the next decade. On about the same time scale, pulsar timing arrays that observe the arrival time differences of pulses coming from different pulsars are expected to be ready for a detection of GWs in the nHz regime. In Japan, the KAGRA detector that is placed in an underground tunnel and uses cryogenic mirrors is currently under construction.

Ground-based laser interferometers are limited by noise of mainly seismic and thermal nature and are confined to frequencies in the Hz-kHz regime. To this end a space-based detector, the Laser Interferometer Space Antenna (LISA), has been proposed, that orbits around the Sun behind the Earth and forms a giant triangle of laser arms with lengths of a few million kilometers. Starting as a joint mission between NASA and ESA, LISA has now been established as an ESA-only mission (eLISA) and aims to be launched in 2034. Already in mid-2015, an exploratory mission probing the technologies required for a LISA-like detector, LISA-Pathfinder, will be sent into space. eLISA will open the window of millihertz GW astronomy and

will allow us to observe the strongest sources of GWs that are currently known: supermassive black hole (SMBH) binaries. Black holes are possible endpoints of collapsed stars and possess an event horizon beyond which no escape from them is possible. Consequently, we are ignorant of the inner structure of black holes and are only left with the models provided by GR.

Gravitational waves will not only improve our understanding of astrophysical objects and the structure of the universe, but they will also allow us to perform tests of GR to an unpreceded accuracy. Alongside the development of GR, also theories that describe the microscopic universe to very high precision were devised and could be unified to quantum field theories that are able to describe electromagnetic, strong and weak forces in the same theoretical formalism. However, all attempts to unify such theories with GR have hitherto failed. Consequently, both theories are considered to be limiting cases of a possible grand unified theory and a failure of GR at some point is expected. To this end and in order to explore other features that are currently not explained by GR, many alternative models have been developed over the years. Through solar system observations, various theories could be constrained or even ruled out. However, a multitude of alternative theories is still on the table and incorporates free parameters that need far stronger constraints. This task could be accomplished in an excellent way through space-based GW observations, as they allow us to map the orbital evolution of SMBH binaries in the relativistic, strong-field regime to high accuracy. Since the presence of an alternative theory of gravity can potentially change the orbital dynamics of compact binaries, it can leave an imprint on the emitted gravitational radiation. Data from GW detectors can thus, once available, be used to provide constraints on alternative theories and verify whether GR is the true underlying theory or not.

In this thesis, we address the question to what extent a LISA-like detector will be able to constrain alternative theories and how large the errors on the parameter estimation are, if we use our GR waveforms to detect signals that are generated by a non-GR theory. In particular, we work with gravitational waveforms in the post-Newtonian (PN) approximation and introduce small perturbations to the PN coefficients. If such a modified waveform template achieves a better fit with a signal present in the detector data, we can take this as a clue that an alternative theory explains gravitation better.

Outline

The core of this thesis consists of the publications [1] and [2] that are included in Chapters 7 and 8, respectively. An introduction to the field is provided by the Chapters 2-6.

In Chapter 2, the basic principles of GR and gravitational waves are introduced. To this end, we discuss the linearised Einstein equations and use a multipole expansion to leading quadrupole order to investigate GW generation. Finally, we give a brief introduction to the principles of post-Newtonian theory. In Chapter 3, we unveil the strongest sources of GWs: supermassive black holes. We discuss their orbital configuration and give their gravitational waveform in the PN approximation. Moreover, we address the impact of precessing spins. Chapter 4 motivates why one should test GR and discusses possible imprints that alternative theories of gravity could leave on GWs. We discuss some examples of possible extensions to GR and move then to more generic features that are not present in GR that one could test for. Finally, we establish how GR can be verified through tests of its PN coefficients. In Chapter 5, we give an overview of the instrumental setup and the orbital configuration of a LISA-like detector and introduce how one deals with noise. Chapter 6 reviews the essential methods for extracting information about the source from a signal in the GW detector. To this end, matched filtering and the basic tools for frequentist and Bayesian statistics are introduced: the Fisher matrix and the Markov Chain Monte Carlo algorithm. In Chapter 7, we investigate how SMBH binaries on a quasi-circular orbit with precessing spins can be used to constrain alternative theories. In particular, we introduce higher harmonics to a gravitational waveform with modified PN phase coefficients in the stationary phase approximation to break degeneracies among binary and theory parameters. To this end we use the Fisher matrix formalism and run Monte Carlo simulations for 17 different mass

combinations. In addition, we investigate the breakdown of different commonly used approximations near the last stable circular orbit in the presence of spin-precession. In Chapter 8, we propose the use of time domain waveforms for tests of GR in the context of a LISA-like detector. We use a Markov Chain Monte Carlo algorithm to explore the impact of relying on a GR template to find a non-GR signal. In particular, we assess up to what deviations from the PN coefficients of GR the eLISA detector will still be able to detect non-GR signals with sufficient signal-to-noise ratio, albeit using the wrong waveform model. Moreover, we identify where the estimated parameters using the 'wrong' (GR) model start to deviate significantly from the true source parameters and, consequently, non-GR templates have to be used.

Chapter 2

General Relativity and Gravitational Waves

2.1 General Relativity in a nutshell

The laws of General Relativity (GR) are described by *Einstein's field equations* at any point x on a four-dimensional manifold (which we shall call *spacetime*) with $x = (x^0 = ct, x^1, x^2, x^3)$:

$$R_{\mu\nu} - \frac{1}{2} g_{\mu\nu} R = \frac{8\pi G}{c^4} T_{\mu\nu}, \tag{2.1}$$

or equally (taking the trace and replacing R with T),

$$R_{\mu\nu} = \frac{8\pi G}{c^4} \left(T_{\mu\nu} - \frac{1}{2} g_{\mu\nu} T \right). \tag{2.2}$$

Here, c is the speed of light, G is Newton's gravitational constant and t denotes the time coordinate. To our present understanding, all physical processes in the macroscopic universe are governed by these equations. The left-hand side renders information about the local curvature of spacetime while the right-hand side incorporates the local energy-momentum density. It is thus that non-zero energy creates non-zero spacetime curvature which governs the motion of test-masses. In the words of John A. Wheeler: *"Matter tells spacetime how to curve, and curved spacetime tells matter how to move."*

The energy-momentum density on the right-hand side is represented by the *energy-momentum tensor* $T_{\mu\nu}$ which contains all curvature-generating energy fields. The curvature on the left-hand side is expressed via the *Riemann tensor* $R^{\rho}{}_{\sigma\mu\nu}$ that can be seen as a measure of how parallel-transported vectors change when transported along two different paths. The *Ricci tensor* $R_{\mu\nu} = R^{\alpha}{}_{\mu\alpha\nu}$ and the *scalar curvature* $R = R^{\mu}{}_{\mu}$ are contractions of the Riemann tensor (repeated indices are always summed over). Because Einstein's field equations are formulated only in terms of tensors, they are form-covariant, i.e. they are invariant under the choice of coordinates. The tensor $g_{\mu\nu}$ represents the metric on the curved manifold and allows to express a length element as $\mathrm{d}s^2 = g_{\mu\nu} dx^\mu dx^\nu$, where the dx^μ are coordinate differentials. The metric tensor is used in tensor algebra to raise and lower indices.

In order to establish a connection between the Riemann and the metric tensor, one needs to impose an *affine connection* that defines the parallel transport of vectors. Conveniently, this is done through the definition of a covariant derivative $\nabla_{\partial_\mu} \partial_\nu = \Gamma^{\rho}_{\mu\nu} \partial_\rho$ which defines how one tangent space basis vector $\partial_\mu \equiv \frac{\partial}{\partial x^\mu}$ is derivated along another basis vector ∂_ν at a certain point on the manifold. The symbols $\Gamma^{\rho}_{\mu\nu}$ are called *Christoffel symbols*, a convenient choice (to enforce $\nabla g = 0$) in terms of the metric is

$$\Gamma^{\rho}_{\mu\nu} = \frac{1}{2} g^{\rho\sigma} \left(g_{\mu\sigma,\nu} + g_{\nu\sigma,\mu} - g_{\mu\nu,\sigma} \right), \tag{2.3}$$

where ',' denotes partial derivation. Similarly, the Riemann tensor can be expressed through Christoffel symbols and their derivatives:

$$R^{\rho}{}_{\sigma\mu\nu} = \partial_\mu \Gamma^{\rho}_{\sigma\nu} - \partial_\nu \Gamma^{\rho}_{\sigma\mu} + \Gamma^{\rho}_{\alpha\mu} \Gamma^{\alpha}_{\sigma\nu} - \Gamma^{\rho}_{\alpha\nu} \Gamma^{\alpha}_{\sigma\mu}. \tag{2.4}$$

Test particles on a curved spacetime move on *geodesics*. A geodesic represents the worldline minimizing the distance between two points and is described through the *geodesic equation*

$$\frac{\mathrm{d}^2 x^\rho}{\mathrm{d}\tau^2} + \Gamma^{\rho}_{\mu\nu} \frac{\mathrm{d}x^\mu}{\mathrm{d}\tau} \frac{\mathrm{d}x^\nu}{\mathrm{d}\tau} = 0, \tag{2.5}$$

which can be found by variation of the action $\int \mathrm{d}s^2 = \int \mathrm{d}\tau \sqrt{g_{\mu\nu} \frac{\mathrm{d}x^\mu}{\mathrm{d}\tau} \frac{\mathrm{d}x^\nu}{\mathrm{d}\tau}}$. In flat space, the metric tensor reduces to the Minkowski tensor

$$\eta_{\mu\nu} = \begin{pmatrix} -1 & 0 & 0 & 0 \\ 0 & 1 & 0 & 0 \\ 0 & 0 & 1 & 0 \\ 0 & 0 & 0 & 1 \end{pmatrix}. \tag{2.6}$$

It is straightforward that the Christoffel symbols as well as the Riemann tensor vanish in flat space.

This is indeed a very brief review of the concepts behind GR and serves mainly to establish the notions used throughout this work. More sophisticated reviews can be found e.g. in [3–5].

Conventions

In the following, repeated indices always imply summation, Greek indices stand for four-dimensional vector indices such as x^μ with $\mu = 0, 1, 2, 3$ and Latin indices refer to three-dimensional spatial vector components such as x^i with $i = 1, 2, 3$. Time derivatives are usually abbreviated with a dot, as for example $\dot{\Phi} = \frac{\mathrm{d}\Phi}{\mathrm{d}t}$. Throughout this work, we use the metric signature $(-, +, +, +)$ of (2.6), such that (by general covariance) $\mathrm{d}s^2 = g_{\mu\nu} \mathrm{d}x^\mu \mathrm{d}x^\nu = -c^2 \mathrm{d}\tau$. Boldface symbols stand for three-dimensional vectors such as $\boldsymbol{r}$ with an absolute value of r. Unit vectors are denoted by a hat, such as $\hat{\boldsymbol{n}}$.

2.2 Principles of gravitational wave theory

Gravitational waves are ripples propagating and acting on the spacetime manifold itself. In order to gain an understanding of how fast they travel and what they exactly do to spacetime, one can introduce a perturbation to the underlying metric, similar to pulling a string on a guitar. In the following, we build up basic structures that serve to explore how gravitational waves are generated and how they propagate.

2.2.1 Linearisation of Einstein's field equations

Suppose that we find ourselves in a vacuum far away from gravitational sources, where the flat space Minkowski metric applies. Adding a perturbation $h_{\mu\nu}$ with $|h_{\mu\nu}| \ll 1$ to it results in the perturbed metric tensor

$$g_{\mu\nu} = \eta_{\mu\nu} + h_{\mu\nu}. \tag{2.7}$$

To compute the *linearised* Einstein equations, we follow the ladder from the Christoffel symbols $\Gamma^{\rho}_{\mu\nu}$ up to the Ricci tensor $R_{\mu\nu}$. The linear approximation consists of neglecting terms of the order $\mathcal{O}(h^2)$. To this end, we raise and lower indices with the ordinary flat space metric η. The Christoffel symbols are then

$$\Gamma^{\rho}_{\mu\nu} = \frac{1}{2}\eta^{\rho\sigma}(\partial_\nu h_{\mu\sigma} + \partial_\mu h_{\nu\sigma} - \partial_\sigma h_{\mu\nu}) + \mathcal{O}(h^2)\,. \tag{2.8}$$

We can thus write the Riemann tensor as

$$R^{\mu}{}_{\nu\rho\sigma} = \frac{1}{2}\left(\partial_\nu\partial_\rho h^{\mu}_{\ \sigma} + \partial^\mu\partial_\sigma h_{\nu\rho} - \partial^\mu\partial_\rho h_{\nu\sigma} - \partial_\nu\partial_\sigma h^{\mu}_{\ \rho}\right) + \mathcal{O}(h^2), \tag{2.9}$$

and the Ricci tensor becomes

$$R_{\mu\nu} = R^{\alpha}{}_{\mu\alpha\nu} = \frac{1}{2}\left(\partial^\alpha\partial_\mu h_{\alpha\nu} + \partial^\alpha\partial_\nu h_{\alpha\mu} - \Box h_{\mu\nu} - \partial_\mu\partial_\nu h\right) + \mathcal{O}(h^2), \tag{2.10}$$

where $\Box = \partial_\mu\partial^\mu$ is the d'Alembert operator and $h \equiv \eta^{\mu\nu}h_{\mu\nu}$ is the trace of $h_{\mu\nu}$. The corresponding scalar curvature is

$$R = R^{\mu}_{\ \mu} = \partial^\alpha\partial^\mu h_{\alpha\mu} - \Box h + \mathcal{O}(h^2). \tag{2.11}$$

This takes us at linear order in h to

$$\frac{1}{2}\partial^\alpha\partial_\mu h_{\alpha\nu} + \frac{1}{2}\partial^\alpha\partial_\nu h_{\alpha\mu} - \frac{1}{2}\Box h_{\mu\nu} - \frac{1}{2}\partial_\mu\partial_\nu h - \frac{1}{2}\eta_{\mu\nu}\partial^\alpha\partial^\rho h_{\alpha\rho} + \frac{1}{2}\eta_{\mu\nu}\Box h = \frac{8\pi G}{c^4}T_{\mu\nu}. \tag{2.12}$$

The above equations can be simplified by expressing them in terms of the trace-reversed metric $\bar{h}_{\mu\nu} = h_{\mu\nu} - \frac{1}{2}\eta_{\mu\nu}$. Then (2.12) simplifies to

$$\Box\bar{h}_{\mu\nu} + \eta_{\mu\nu}\partial^\rho\partial^\sigma\bar{h}_{\rho\sigma} - \partial^\rho\partial_\nu\bar{h}_{\mu\rho} - \partial^\rho\partial_\mu\bar{h}_{\nu\rho} = -\frac{16\pi G}{c^4}T_{\mu\nu}. \tag{2.13}$$

We can simplify the resulting field equations further by taking advantage of gauge freedom, in analogy to electrodynamics. An infinitesimal coordinate transformation

$$x^\mu \to x'^\mu = x^\mu + \xi^\mu(x), \qquad |\partial_\mu\xi_\nu| = \mathcal{O}(h) \tag{2.14}$$

transforms the metric perturbation (at linear order in h) to

$$h_{\mu\nu}(x) \to h'_{\mu\nu}(x') = h_{\mu\nu}(x) - \left(\partial_\mu\xi_\nu + \partial_\nu\xi_\mu\right), \tag{2.15}$$

because $g'_{\mu\nu} = g_{\alpha\beta}\frac{\partial x^\alpha}{\partial x'^\mu}\frac{\partial x^\beta}{\partial x'^\nu}$ under coordinate transformations. In terms of the trace-reversed metric, one finds

$$\bar{h}_{\mu\nu}(x) \to \bar{h}'_{\mu\nu}(x') = \bar{h}_{\mu\nu}(x) - \left(\partial_\mu \xi_\nu + \partial_\nu \xi_\mu - \eta_{\mu\nu}\partial_\rho \xi^\rho\right) . \tag{2.16}$$

The gauge transformation (2.14) can be interpreted in a very natural way: we are free to choose our frame of reference and thus our coordinate system. Although an event is described differently in different reference frames, it still describes the same physical process. In the context of GR, fixing the gauge means going to a fixed frame; this is what we are going to do now.

One way to fix the gauge freedom (2.14) is the so-called *De Donder gauge* (in analogy to the Lorenz gauge in electrodynamics)

$$\partial^\nu \bar{h}_{\mu\nu} = 0. \tag{2.17}$$

The transformation behaviour of $\partial^\nu \bar{h}_{\mu\nu}$ is $\partial^\nu \bar{h}_{\mu\nu} \to \left(\partial^\nu \bar{h}_{\mu\nu}\right)' = \partial^\nu \bar{h}_{\mu\nu} - \Box\xi_\mu$, what enables us to achieve $(\partial^\nu \bar{h}_{\mu\nu})' = 0$ by fixing $\Box\xi_\mu = \partial^\nu \bar{h}_{\mu\nu}$. Thus we find the linearised field equations

$$\Box \bar{h}_{\mu\nu} = -\frac{16\pi G}{c^4} T_{\mu\nu}. \tag{2.18}$$

By differentiating (2.18) and applying the De Donder gauge, one immediately arrives at the flat space energy-momentum conservation law

$$\partial^\nu T_{\mu\nu} = 0. \tag{2.19}$$

Thus, at linear order in h, gravitational waves do not enter the energy-momentum tensor and higher order will have to be taken into account in order to compute the energy of a GW [6].

To study the propagation of GWs and their interaction with test masses, it is interesting to look at vacuum solutions of (2.18) where $T_{\mu\nu} = 0$. There the linearised field equations reduce to

$$\Box \bar{h}_{\mu\nu} = 0. \tag{2.20}$$

As $\Box = \boldsymbol{\nabla}^2 - \frac{1}{c^2}\partial_t^2$, this implies that gravitational waves travel at the speed of light. Since the De Donder gauge allows a further coordinate transformation of the form of (2.14) as long as it satisfies $\Box\xi_\mu = 0$, we have four additional degrees of freedom ξ_μ left to simplify our equations. ξ_0 can be chosen such that the trace $\bar{h}$ vanishes (then $h_{\mu\nu} = \bar{h}_{\mu\nu}$). The three spatial components ξ_i can then be fixed in such a way that $h_{0i} = 0$. Then, by applying (2.17), we also find that $\partial^0 h_{00} = 0$, i.e. h_{00} is constant in time and thus we can fix $h_{00} = 0$ for all time. The so-called *transverse-traceless (TT) gauge* is thus defined by

$$h_{0\mu} = 0, \qquad h^i{}_i = 0, \qquad \partial^j h_{ij} = 0. \tag{2.21}$$

A metric perturbation in the TT gauge will from now on be denoted as h_{ij}^{TT}. One can easily verify that the plane wave $h_{ij}^{TT}(x) = e_{ij}(\boldsymbol{k})e^{ikx}$ with $k^\mu = (\omega/c, \boldsymbol{k})$ and $\omega/c = |\boldsymbol{k}|$ solves (2.20) and that $\partial^j h_{ij} = 0$ can be interpreted in this case as $k^j h_{ij} = 0$. Here, e_{ij} represents the 4×4 polarisation tensor. Without loss of generality, we pick $\boldsymbol{k} = (0, 0, 1)$ for a plane wave propagating in the z-direction. Then, one finds as a solution in the TT gauge

$$h_{ab}^{TT}(t, z) = \begin{pmatrix} h_+ & h_\times \\ h_\times & -h_+ \end{pmatrix} \cos\left[\omega\left(t - \frac{z}{c}\right)\right], \tag{2.22}$$

for a plane wave moving along the z-axis and acting on the (x, y) plane with $a, b = 1, 2$ (all other components of e_{ij} are zero). Considering an infinitesimal rigid rod lying in the (x, y) plane, its length element oscillates as

$$ds^2 = (h_+ dx^2 - h_+ dy^2 + 2h_\times dx dy)\cos\left[\omega\left(t - \frac{z}{c}\right)\right]. \tag{2.23}$$

Note the mixing of dx and dy in the last term. If one looks at multiple freely-floating point-masses distributed on a circle, one finds two polarisation modes, a '+' (plus) and a '×' (cross) polarisation, as depicted in Fig. 2.1. The indices in the decomposition of $h^{TT}_{ab}(t, z)$ into h_+ and $h_\times$ in (2.22) were chosen accordingly.

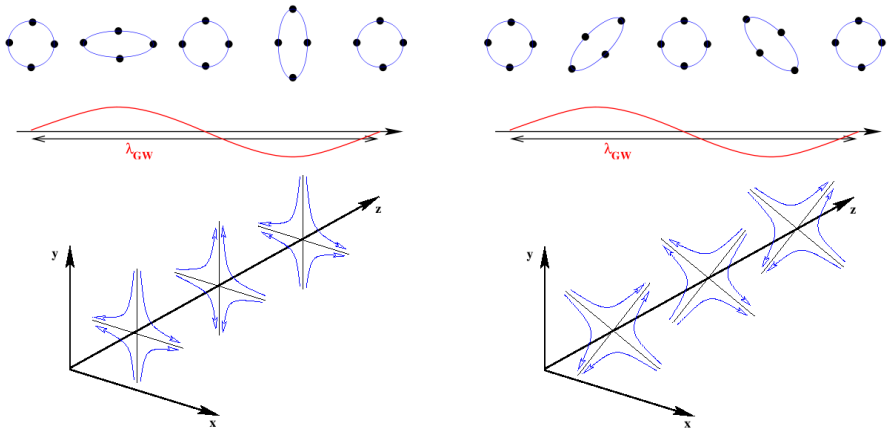

Figure 2.1: *Gravitational waves allow for two different polarisation modes: plus (left) and cross (right) polarisation. Here, a GW that travels along the z-axis and acts on the (x, y) plane is depicted.*[1]

It is possible to define a projector which is able to project every metric perturbation onto its transverse-traceless part. Consider the projection

$$P_{ij}(\hat{\boldsymbol{n}}) = \delta_{ij} - n_i n_j, \tag{2.24}$$

which is transverse along the direction $\hat{\boldsymbol{n}}$ ($n^i P_{ij} = 0$) and has the trace $P_{ii} = 2$. This allows us to construct the Lambda tensor which renders every rank 2 tensor transverse and traceless along $\hat{\boldsymbol{n}}$:

$$\Lambda_{ij,kl}(\hat{\boldsymbol{n}}) = P_{ik}P_{jl} - \frac{1}{2}P_{ij}P_{kl}. \tag{2.25}$$

If we deal with a plane wave $h_{\mu\nu}$ in the De Donder gauge, we are able to project it to the TT gauge through

$$h^{TT}_{ij} = \Lambda_{ij,kl}h_{kl}, \tag{2.26}$$

where summation is implied for repeated indices. We have destroyed the general covariance of GR by linearizing it, jumping to a preferred reference frame. It can be shown from geodesic deviation (see e.g. [6]) that the TT frame is the one where the coordinate difference of two test masses is constant when a gravitational wave passes by.

So far we have investigated the propagation of perturbations on the spacetime manifold. To gain a deeper understanding of gravitational waves, we will need to look at the sources that generate them; this will be covered in the next subsection.

[1] Picture credit: A. Buonanno [7]

2.2.2 Weak-field sources in the low-velocity expansion

In the following, let us introduce the idea of a multipole expansion of the linearised field equations, inspired by [6]. In the previous subsection, we have found using the De Donder gauge (2.20),

$$\Box\bar{h}_{\mu\nu} = -\frac{16\pi G}{c^4} T_{\mu\nu}. \tag{2.27}$$

It is well-known from electrodynamics that such a differential equation can be solved via a Green's function G that satisfies $\Box_{\boldsymbol{x}} G(\boldsymbol{x}-\boldsymbol{x}') = \delta^4\left(\boldsymbol{x}-\boldsymbol{x}'\right)$. The Green's function that fulfills this requirement is commonly known as the *retarded Green's function* and is given by

$$G(\boldsymbol{x}-\boldsymbol{x}') = -\frac{1}{4\pi|\boldsymbol{x}-\boldsymbol{x}'|}\delta(t-\frac{|\boldsymbol{x}-\boldsymbol{x}'|}{c}-t'). \tag{2.28}$$

One can then find the solution of (2.27) by integrating over the one-point solutions $G(\boldsymbol{x}-\boldsymbol{x}')$:

$$\bar{h}_{\mu\nu}(x) = -\frac{16\pi G}{c^4}\int \mathrm{d}^4x'\, G(\boldsymbol{x}-\boldsymbol{x}')\, T_{\mu\nu}(x'). \tag{2.29}$$

Plugging in (2.28) and projecting onto the TT gauge, we arrive at

$$h_{ij}^{TT}(t,\boldsymbol{x}) = \Lambda_{ij,kl}(\hat{\boldsymbol{n}})\frac{4G}{c^4}\int \mathrm{d}^3x' \frac{1}{|\boldsymbol{x}-\boldsymbol{x}'|} T_{kl}\left(t-\frac{|\boldsymbol{x}-\boldsymbol{x}'|}{c};\boldsymbol{x}'\right), \tag{2.30}$$

where $\hat{\boldsymbol{n}}$ is the unit vector pointing along the propagation direction of the gravitational wave. Now suppose the energy-momentum density of the source is restricted to a compact zone and the observer is far away from that source. Without loss of generality, let the coordinate origin be within the source's center of mass. Then $\boldsymbol{x'}$ lives only within the source while $\boldsymbol{x}$ is a constant vector pointing from the center of mass of the source to the observer. This yields $|\boldsymbol{x}'| \ll |\boldsymbol{x}| \equiv r$ and allows us to approximate to first order that $\hat{\boldsymbol{n}} = \frac{\boldsymbol{x}}{|\boldsymbol{x}|}$ and

$$|\boldsymbol{x}-\boldsymbol{x}'| = r + \bigtriangledown_{\boldsymbol{x}'}|\boldsymbol{x}-\boldsymbol{x}'|\Big|_{\boldsymbol{x}'=0}\cdot\boldsymbol{x}' + \mathcal{O}\left(\frac{|\boldsymbol{x}'|^2}{|\boldsymbol{x}|}\right) = r - \hat{\boldsymbol{n}}\cdot\boldsymbol{x}' + \mathcal{O}\left(\frac{|\boldsymbol{x}'|^2}{|\boldsymbol{x}|}\right). \tag{2.31}$$

Then one finds (to leading order)

$$\bar{h}_{ij}^{TT}(x) \simeq \frac{1}{r}\frac{4G}{c^4}\Lambda_{ij,kl}(\hat{\boldsymbol{n}})\int_{\text{source}} \mathrm{d}^3x'\, T_{kl}\left(t_{\text{ret}}+\frac{\boldsymbol{x}'\cdot\hat{\boldsymbol{n}}}{c};\boldsymbol{x}'\right), \tag{2.32}$$

where $t_{\text{ret}} \equiv t - \frac{r}{c}$ is the retarded time. This expression is valid for arbitrary velocities. In the following we aim to perform a low-velocity expansion of (2.32), assuming that $v/c \ll 1$, where v is a typical velocity within the source. This is equivalent to $\frac{\omega|\boldsymbol{x}'|}{c} \sim \omega\frac{\boldsymbol{x}'\cdot\hat{n}}{c} \ll 1$, where ω is a typical angular frequency within the source. By writing the energy-momentum tensor in (2.32) as a Fourier integral, we can expand it around t_{ret} as

$$\begin{aligned}
T_{kl}\left(t_{\text{ret}}+\frac{\boldsymbol{x}'\cdot\hat{\boldsymbol{n}}}{c};\boldsymbol{x}'\right) &= \int \frac{\mathrm{d}^4k}{(2\pi)^4}\,\tilde{T}_{kl}(\omega,\boldsymbol{k})e^{-i\omega\left(t_{\text{ret}}-i\boldsymbol{k}\cdot\boldsymbol{x}'\right)}e^{-i\omega\frac{\boldsymbol{x}'\cdot\hat{\boldsymbol{n}}}{c}} \\
&= \int \frac{\mathrm{d}^4k}{(2\pi)^4}\,\tilde{T}_{kl}(\omega,\boldsymbol{k})e^{-i\omega t_{\text{ret}}+i\boldsymbol{k}\cdot\boldsymbol{x}'}\left[1+(-i\omega)\frac{\boldsymbol{x}'\cdot\hat{\boldsymbol{n}}}{c}+\frac{(-\omega^2)}{2}\left(\frac{\boldsymbol{x}'\cdot\hat{\boldsymbol{n}}}{c}\right)^2+\ldots\right] \\
&= T_{kl}(t_{\text{ret}};\boldsymbol{x}') + \frac{1}{c}x^i n_i\,\partial_{t_{\text{ret}}}T_{kl}(t_{\text{ret}};\boldsymbol{x}') + \frac{1}{2c^2}x^ix^jn_in_j\,\partial^2_{t_{\text{ret}}}T_{kl}(t_{\text{ret}};\boldsymbol{x}')+\ldots
\end{aligned} \tag{2.33}$$

Thus (2.32) can be expressed as

$$h_{ij}^{TT}(t,\boldsymbol{x}) = \frac{1}{r}\frac{4G}{c^4}\Lambda_{ij,kl}(\hat{\boldsymbol{n}})\left[S^{kl} + \frac{n_m}{c}\dot{S}^{kl,m} + \frac{n_m n_p}{2c^2}\ddot{S}^{kl,mp} + \mathscr{O}\left(\frac{1}{c^3}\right)\right]\Bigg|_{t=t_{\rm ret}}, \tag{2.34}$$

where the momenta of T_{ij} are given by

$$S^{ij}(t) = \int \mathrm{d}^3x\, T^{ij}(t,\boldsymbol{x}), \qquad S^{ij,k}(t) = \int \mathrm{d}^3x\, T^{ij}(t,\boldsymbol{x})\, x^k, \qquad S^{ij,kl}(t) = \int \mathrm{d}^3x\, T^{ij}(t,\boldsymbol{x})\, x^k x^l, \tag{2.35}$$

and so on. One can also introduce the *mass momenta*, the momenta of T_{00}/c^2:

$$M = \frac{1}{c^2}\int \mathrm{d}^3x\, T^{00}(t,\boldsymbol{x}), \qquad M^i = \frac{1}{c^2}\int \mathrm{d}^3x\, T^{00}(t,\boldsymbol{x})\, x^i, \qquad M^{ij} = \frac{1}{c^2}\int \mathrm{d}^3x\, T^{00}(t,\boldsymbol{x})\, x^i x^j, \tag{2.36}$$

etc. It is interesting to observe that

$$\dot{M} = c\,\partial_0 M = \frac{1}{c}\int \mathrm{d}^3x\, \partial_0 T^{00} = -\frac{1}{c}\int \mathrm{d}^3x\, \partial_i T^{0i} = 0, \tag{2.37}$$

where $\partial_\nu T^{\mu\nu} = 0$ and the fact that $T^{\mu\nu}$ is compact has been used. It can also be shown that $\dot{M}^i$ and $\dot{M}^{ij}$ are the linear and angular momentum of the mass distribution, respectively, by using energy conservation and integration by parts. Moreover, $\ddot{M}^i = 0$. This means that the first two mass momenta cannot contribute to gravitational wave emission in GR. However,

$$\ddot{M}^{ij} = \partial_0^2\int \mathrm{d}^3x\, T^{00}\, x^i x^j = \int \mathrm{d}^3x\, (\partial_k\partial_l T^{kl})\, x^i x^j = 2\int \mathrm{d}^3x\, T^{ij} = 2S^{ij}. \tag{2.38}$$

This enables us to write the leading (quadrupole) term of the expansion (2.34) as

$$h_{ij}^{TT}(t,\boldsymbol{x}) \simeq \frac{1}{r}\frac{2G}{c^4}\Lambda_{ij,kl}(\hat{\boldsymbol{n}})\,\ddot{M}^{kl}(t-r/c) = \frac{1}{r}\frac{2G}{c^4}\Lambda_{ij,kl}(\hat{\boldsymbol{n}})\ddot{Q}^{kl}(t-r/c), \tag{2.39}$$

where we have introduced the traceless quadrupole moment

$$Q^{ij} \equiv M^{ij} - \frac{1}{3}\delta^{ij}M_{kk} = \int \mathrm{d}^3x\, \rho(t,\boldsymbol{x})\left(x^i x^j - \frac{1}{3}r^2\delta^{ij}\right), \tag{2.40}$$

with the mass distribution $\rho = \frac{1}{c^2}T^{00}$ (in the low-velocity limit). Notice that $\Lambda_{ij,kl}Q_{kl} = \Lambda_{ij,kl}M_{kl}$ since $\Lambda_{ij,kl}\delta_{kl} = 0$. We are then able to calculate in a straightforward way, by using the explicit form of $\Lambda_{ij,kl}$ in the direction of the z-axis:

$$\Lambda_{ij,kl}(\hat{\boldsymbol{z}})\ddot{M}_{kl} = \begin{pmatrix} \left(\ddot{M}_{11} - \ddot{M}_{22}\right)/2 & \ddot{M}_{12} & 0 \\ \ddot{M}_{21} & -\left(\ddot{M}_{11} - \ddot{M}_{22}\right)/2 & 0 \\ 0 & 0 & 0 \end{pmatrix}, \tag{2.41}$$

and thus the polarisation amplitudes for a wave propagating along $\hat{\boldsymbol{z}}$ are to leading quadrupole order

$$h_+\left(t-\frac{r}{c},\boldsymbol{x}\right) = \frac{1}{r}\frac{G}{c^4}\left[\ddot{M}_{11}\left(t-\frac{r}{c},\boldsymbol{x}\right)-\ddot{M}_{22}\left(t-\frac{r}{c},\boldsymbol{x}\right)\right], \tag{2.42}$$

$$h_\times\left(t-\frac{r}{c},\boldsymbol{x}\right) = \frac{2}{r}\frac{G}{c^4}\ddot{M}_{12}\left(t-\frac{r}{c},\boldsymbol{x}\right). \tag{2.43}$$

The acquired polarisation amplitudes can be generalised to a source at arbitrary spherical angles (Θ,ϕ) by rotating (2.42). For self-gravitating systems in the strong-field regime, as for example compact binary inspirals, it will not be enough to consider only a linearised version of Einstein's field equations; higher orders will have to be included. This can be done in a rigorous way in the so-called *post-Newtonian expansion* of GR that is introduced in the next section.

2.3 The post-Newtonian expansion of GR

The linearised equations computed in Section 2.2.2 give a useful insight into how GWs are generated. The equations are, however, only applicable in weak gravitational fields which inevitably produce weak gravitational waves. For actual detections, we are interested in the dynamical, strong field regime of GR where also higher order terms play a significant role. As all the involved gravitational physics are (presumably) governed by Einstein's field equations, one has to resort to either numerical methods or analytically expanded solutions. Numerical relativity has the advantage that it is as accurate as the resolution that is used in the codes; yet it is computationally extremely expensive: binary black hole simulations can last from a few days up to weeks. Numerical relativity can be very useful to improve our understanding of the physics behind binary black hole mergers, but it is in practice unfit to do parameter estimation where a large number of waveform templates are required. In this work we will solely rely on an analytical expansion of the field equations: the *post-Newtonian* (PN) expansion which is widely used to describe the orbital dynamics of gravitational wave sources and the associated GW generation.

The idea behind the PN expansion is that the typical velocities v in a self-gravitating system are always smaller than the speed of light c, and therefore the quantity $\epsilon \sim v/c$ (which is usually $\ll 1$) allows us to perform a Taylor expansion of Einstein's field equations. The virial theorem connects typical velocities to typical gravitational field strengths inside a self-gravitating system, namely $v/c \sim \sqrt{R_S/d}$, where d is the length scale of the system, $R_S = 2GM/c^2$ is its Schwarzschild radius and M its total mass.

In the following, a sketch of the ideas behind the PN expansion will be presented. Two equivalent approaches have been developed to this end, the *multipolar post-Minkowskian wave generation formalism* by Blanchet and Damour [8–11] as well as the *direct integration of the relaxed Einstein equations* (DIRE) by Will, Wiseman and Pati [12, 13]. As in practice the necessary mathematics are rather involved, we give here only a short introduction to the formalism by Blanchet and Damour.

2.3.1 Relaxed Einstein equations

For the purpose of a rigorous expansion of Einstein's equations, it is useful to work in so-called *harmonic coordinates* and to define the 'gothic' inverse metric $\mathfrak{g}^{\alpha\beta} = \sqrt{-\det g}\, g^{\alpha\beta}$ and the gravitational field amplitude $\mathfrak{h}^{\alpha\beta} = \eta^{\alpha\beta} - \mathfrak{g}^{\alpha\beta}$. By invoking the weak-field limit $g^{\alpha\beta} = \eta^{\alpha\beta} + h^{\alpha\beta}$ with $|h^{\alpha\beta}| \ll 1$ that has been introduced in Section 2.2.1, one can show that

$$\mathfrak{h}^{\alpha\beta} = \eta^{\alpha\beta} - \sqrt{1-h^\mu{}_\mu}\left(\eta^{\alpha\beta}+h^{\alpha\beta}\right) + \mathcal{O}(h^2) = -h^{\alpha\beta} + \frac{1}{2}\eta^{\alpha\beta}h^\mu{}_\mu + \mathcal{O}(h^2) \approx -\bar{h}^{\alpha\beta}, \tag{2.44}$$

where $\bar{h}^{\alpha\beta}$ is the trace-reversed metric defined in Section 2.2.1 and $\det(\eta+h) = -1+h^{\mu}{}_{\mu}+\mathcal{O}(h^2)$. Thus in the limit of weak fields, the metric perturbation $h^{\alpha\beta}$ can be recovered from the gravitational field amplitude $\mathfrak{h}^{\alpha\beta}$. By taking into account the harmonic gauge condition $\partial_\alpha\sqrt{-\det g}\, g^{\alpha\beta} = 0$, or equivalently $\partial_\alpha \mathfrak{h}^{\alpha\beta} = 0$, one can recast Einstein's field equations (2.1) to the form [11]

$$\Box \mathfrak{h}^{\alpha\beta} = \frac{16\pi G}{c^4}\tau^{\alpha\beta}, \tag{2.45}$$

where $\Box = \eta^{\mu\nu}\partial_\mu\partial_\nu$ is the d'Alembert operator in flat space and

$$\tau^{\alpha\beta} = |\det g| T^{\alpha\beta} + \frac{c^4}{16\pi G}\Lambda^{\alpha\beta}, \tag{2.46}$$

$$\begin{aligned}\Lambda^{\alpha\beta} = &-\mathfrak{h}^{\mu\nu}\mathfrak{h}^{\alpha\beta}{}_{,\mu\nu} + \mathfrak{h}^{\alpha\nu}{}_{,\mu}\mathfrak{h}^{\beta\mu}{}_{,\nu} + \frac{1}{2}g^{\alpha\beta}g_{\mu\nu}\mathfrak{h}^{\mu\tau}{}_{,\lambda}\mathfrak{h}^{\nu\lambda}{}_{,\tau} - g^{\alpha\mu}g_{\nu\tau}\mathfrak{h}^{\beta\tau}{}_{,\lambda}\mathfrak{h}^{\nu\lambda}{}_{,\mu} - g^{\beta\mu}g_{\nu\tau}\mathfrak{h}^{\alpha\tau}{}_{,\lambda}\mathfrak{h}^{\nu\tau}{}_{,\mu} \\ &+ g_{\mu\nu}g^{\lambda\tau}\mathfrak{h}^{\alpha\mu}{}_{,\lambda}\mathfrak{h}^{\beta\nu}{}_{,\tau} + \frac{1}{8}\left(2g^{\alpha\mu}g^{\beta\nu} - g^{\alpha\beta}g^{\mu\nu}\right)(2g_{\lambda\tau}g_{\epsilon\pi} - g_{\tau\epsilon}g_{\lambda\pi})\mathfrak{h}^{\lambda\pi}{}_{,\mu}\mathfrak{h}^{\tau\epsilon}{}_{,\nu},\end{aligned} \tag{2.47}$$

where $\Lambda^{\alpha\beta}$ is made of terms of at least quadratic order in $\mathfrak{h}^{\alpha\beta}$. Formally, Eq. (2.45) can be solved by

$$\mathfrak{h}^{\alpha\beta}(t,\boldsymbol{x}) = \frac{4G}{c^4}\int d^3x' \frac{\tau^{\alpha\beta}\left(t-\frac{|\boldsymbol{x}-\boldsymbol{x}'|}{c},\boldsymbol{x}';\mathfrak{h}^{\alpha\beta}\right)}{|\boldsymbol{x}-\boldsymbol{x}'|}, \tag{2.48}$$

but as $\tau^{\alpha\beta}$ is a functional of $\mathfrak{h}^{\alpha\beta}$, there is no easy way to compute (2.48). To this end, the PN expansion has to be employed, as introduced in the next subsection.

2.3.2 Expansion of the relaxed Einstein equations in the near and the far field zone

In order to solve the relaxed Einstein equations, two different approximations in two different regions of interest can be applied [10]. If $\lambda\!\!\!^{-} = \lambda/2\pi$ is the reduced wavelength of the GW that is produced by the source, then we find ourselves in the *near field zone* for distances $r \ll \lambda\!\!\!^{-}$ and in the *far field zone* for $r \gg \lambda\!\!\!^{-}$.

In the near field zone (inside the source), one can perform a PN expansion in terms of v/c. To this end, the gravitational field amplitude and the total energy-momentum tensor can be expanded in terms of $1/c$ as

$$\mathfrak{h}^{\mu\nu} = \sum_{n=2}^{\infty}\frac{1}{c^n}\mathfrak{h}_n^{\mu\nu}, \tag{2.49}$$

$$\tau^{\mu\nu} = \sum_{n=-2}^{\infty}\frac{1}{c^n}\tau_n^{\mu\nu}, \tag{2.50}$$

where it has been accounted for that the leading order component of the energy-momentum tensor $\tau^{\mu\nu}$ is of order c^2 and hence the leading order contribution to $\mathfrak{h}^{\alpha\beta}$ is of order $1/c^2$. Then, the relaxed Einstein equations become

$$\left(\nabla^2 - \frac{1}{c^2}\partial_t^2\right)\sum_{n=2}^{\infty}\frac{1}{c^n}\mathfrak{h}_n^{\mu\nu} = \frac{16\pi G}{c^4}\sum_{n=-2}^{\infty}\frac{1}{c^n}\tau_n^{\mu\nu}, \tag{2.51}$$

what allows to solve them iteratively through

$$\nabla^2 \mathfrak{h}_n^{\mu\nu} = 16\pi G \tau_{n-4}^{\mu\nu} + \partial_t^2 \mathfrak{h}_{n-2}^{\mu\nu}. \tag{2.52}$$

In the far field zone (outside the source), the gravitational field is weak and a *post-Minkowskian* (PM) expansion can be performed: the gravitational field amplitude can be expanded in terms of R_S/r or equivalently in terms of the gravitational constant G as

$$\mathfrak{h}^{\alpha\beta} = \sum_{n=1}^{\infty} G^n \mathfrak{h}_n^{\alpha\beta}, \tag{2.53}$$

and since we are outside of the source ($T^{\alpha\beta} = 0$), the relaxed Einstein equations reduce to

$$\Box \mathfrak{h}^{\alpha\beta} = \Lambda^{\alpha\beta}, \tag{2.54}$$

which by employing (2.53) can be solved iteratively through

$$\begin{aligned}
\Box \mathfrak{h}_1^{\alpha\beta} &= 0, \\
\Box \mathfrak{h}_2^{\alpha\beta} &= \Lambda^{\alpha\beta}\left[\mathfrak{h}_1^{\alpha\beta}\right], \\
&\vdots \qquad\quad \vdots \\
\Box \mathfrak{h}_n^{\alpha\beta} &= \Lambda^{\alpha\beta}\left[\mathfrak{h}_{n-1}^{\alpha\beta} \middle| \mathfrak{h}_1^{\alpha\beta}, \ldots, \mathfrak{h}_{n-2}^{\alpha\beta}\right].
\end{aligned} \tag{2.55}$$

Thus the problem of GW generation can be solved perturbatively using the PN expansion in the near field zone and the problem of GW propagation can be solved using the PM expansion in the far field zone. A GW detector will measure gravitational waves as they are in the far field zone; however, the PM expansion works with $T^{\mu\nu} = 0$, i.e. the source energy-momentum tensor does not enter the multipolar expansion. Yet one has to be able to refer the measured GWs to the characteristics of the source. This can be cured by considering an *overlap zone* with $r \sim \lambda$ where both the PM and the PN expansion are supposed to be valid. Denoting for PM[..] a multipolar post-Minkowskian expansion in G and for PN[..] a post-Newtonian expansion in $1/c$, in the overlap zone the *matching condition*

$$\mathrm{PN}[\mathrm{PM}[\mathfrak{h}^{\mu\nu}]] = \mathrm{PM}[\mathrm{PN}[\mathfrak{h}^{\mu\nu}]] \tag{2.56}$$

must hold. This associates the free parameters of the PM expansion to source parameters such as the total mass M. In a set of involved computations that require regularisation procedures, the waveforms for the sources considered in this work, compact binaries, can be derived. We shall not reproduce the calculations but only list the results in Section 3.3.

Chapter 3

Compact Binary Coalescence: Supermassive Black Hole Binary Inspirals

3.1 Astrophysical context

In Section 2.2.2 we have found that gravitational waves are produced by sources with a non-zero third time derivative of the quadrupole moment. The first sources that come to mind exhibiting this property are two masses on a close orbit. Although ordinary stars are in principle massive enough to produce gravitational radiation, they tend to be tidally disrupted long before reaching an orbital separation where the radiation is strong enough. However, there exist certain exotic astrophysical objects that can maintain their form as long until they reach the relativistic regime of gravity - so-called *compact objects* that are the end-product of a collapsed star: white dwarves, neutron stars and black holes (BHs). With a radius below the so-called *Schwarzschild radius*, BHs are the most compact objects that we know of. At the Schwarzschild radius $R_S = 2Gm/c^2$, an event horizon is located that lets nothing escape, not even light. Here m is the mass of the BH that is typically around the mass of our sun, corresponding to a Schwarzschild radius of $R_S \sim 3$km.

Many galaxies host a *supermassive black hole* (SMBH) in their center. SMBHs play a crucial role in the evolution of their host galaxy and their masses are usually in a well-established relation with the bulk mass of the galaxy. The center of the Milky Way galaxy is believed to harbour a SMBH with a mass of $4.3 \times 10^6 M_\odot$ [14]. As SMBHs have typical masses between $10^4 - 10^{10} M_\odot$, they are thought to have formed through successive mergers of so-called *seed black holes*. Such seeds could either be millions of stellar mass BHs that have formed out of collapsed stars or a few intermediate-mass BHs that could have formed through the direct collapse of a massive gaseous protogalactic disk. Both processes are still an open field of research which would greatly benefit from gravitational wave observations [15].

In this work, we are interested in binaries of compact objects, so called *compact binaries*, that lose energy and hence orbital separation through the emission of gravitational radiation, until they are deep in the relativistic, strong field regime and ultimately merge to one final remnant. As neutron star binaries (often so-called pulsars that emit electromagnetic pulses due to their strong rotation and magnetisation) usually show velocities of only $v/c \sim 10^{-3}$, they are still in the regime of GR where fields are relatively weak. On the other hand, SMBH binaries can have final velocities of up to $v/c \sim 0.3$ and are the strongest sources of gravitational waves that are currently known.

The coalescence process is usually divided into three stages (Fig. 3.1): The two BHs slowly approach each other on adiabatically evolving orbits (*inspiral*) until they reach the last stable orbit and plunge towards each other. After the *merger*, the final BH is still very excited and relaxes through emission of quasi-normal *ringdown* modes in the form of gravitational radiation.

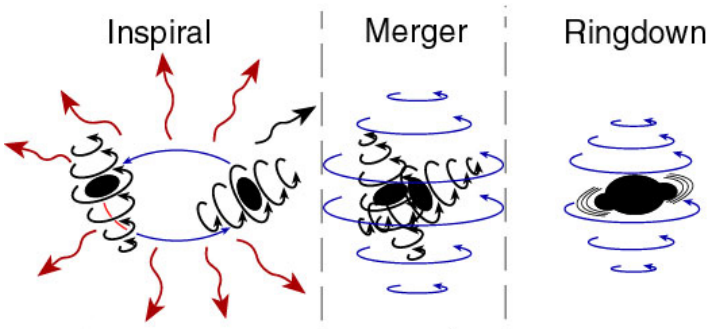

Figure 3.1: *The three stages of compact binary coalescence: inspiral, merger and ringdown.*[1]

In the following, we will concentrate on the inspiral part of coalescing SMBHs only. The inspiral is, especially for BH binaries, quite well-modelled in terms of an analytic PN expansion and shows a clean orbital evolution. We truncate the inspiral waveforms at orbital separations of $\sim 6-7\,GM/c^2$, as in this region the post-Newtonian expansion is expected to break down.

3.2 Anatomy of a non-spinning compact binary inspiral

In the rest of this work, we will only consider the pure mechanics of a compact binary inspiral, in particular the inspiral of two point masses due to the loss of energy through gravitational radiation. We will henceforth neglect all astrophysical effects, such as accretion disks, additional stars orbiting the binary, etc. According to [16], this can be done on a safe basis in the GW radiation dominated regime.

3.2.1 Position and orientation of the compact binary in space

The position of the center of mass (COM) of a compact binary in the sky can be expressed with a set of spherical angles (θ,ϕ) relative to a fixed frame tied to the distant stars with the Sun at its center (see Section 5.1). Equivalently, one can use a unit vector $\hat{\boldsymbol{n}}$ pointing from the Sun to the source with $\hat{\boldsymbol{n}} = (\cos\phi\cos\theta, \sin\phi\cos\theta, \sin\theta)$. Since we are considering cosmological distances between the sources and the detector, cosmological redshift affects the gravitational waves while they are travelling towards the detector. This requires the notion of the *luminosity distance* D_L, which is in the ΛCDM model as a function of the redshift z of a source given by

$$D_L = (1+z)\frac{c}{H_0}\int_0^z \frac{\mathrm{d}z'}{\sqrt{\Omega_R(1+z')^4+\Omega_M(1+z')^3+\Omega_\Lambda}}, \tag{3.1}$$

with $\Omega_R = 4.9\times10^{-5}$, $\Omega_M = 0.3086$, $\Omega_\Lambda = 0.6914$ and the Hubble constant $H_0 = 67.77$ km/s/Mpc as found by the Planck mission [17]. It is important to mention that for a pure gravitational wave observation, there is no way of discriminating mass and redshift. This is because we can only measure redshifted masses $m(1+z)$. Such a degeneracy could be broken with simultaneous electromagnetic observations.

Since the two point masses move on a plane, we need to indicate the tilting angles of this plane. This is usually done with the inclination angle $\cos\iota = \hat{\boldsymbol{L}}\cdot\hat{\boldsymbol{n}}$ and the polarisation angle [18]

$$\tan\psi = \frac{\hat{\boldsymbol{L}}\cdot\hat{\boldsymbol{z}} - (\hat{\boldsymbol{L}}\cdot\hat{\boldsymbol{n}})(\hat{\boldsymbol{z}}\cdot\hat{\boldsymbol{n}})}{\hat{\boldsymbol{n}}\cdot(\hat{\boldsymbol{L}}\times\hat{\boldsymbol{z}})}. \tag{3.2}$$

[1] Picture credit: Kip Thorne

Here, $\hat{\boldsymbol{L}}$ is the unit angular momentum vector of the the binary.

3.2.2 Inspiral dynamics

Having defined the COM position and the orientation of the plane of motion, the inspiral evolution is only governed by the BH masses m_1 and m_2. It will later be convenient to also have the notions of the total mass $M = m_1 + m_2$, the reduced mass $\mu = m_1 m_2/M$, the symmetric mass ratio $\eta = m_1 m_2/M^2$ and the chirp mass $\mathscr{M} = M\eta^{3/5}$.

If we set m_1 and m_2 free at a certain orbital separation r_0 and time t_0, their following orbital motion would be well-defined until they have successfully merged. This implies that there is a unique relation for $r = r(t)$. On the other hand, one can also describe the orbital evolution via the orbital phase $\Phi(t)$ that starts at an initial phase $\Phi_0 = \Phi(t_0)$. Initial time and phase are therefore enough to determine the inspiral of the masses m_1 and m_2. More commonly, one uses the time and phase at formal coalescence, t_c and Φ_c, respectively. The orbital phase as a function of time is then

$$\Phi(t) = \Phi_c - \int_t^{t_c} \omega(t')\,\mathrm{d}t', \tag{3.3}$$

where $\omega(t)$ is the angular orbital frequency of the compact binary that is a function of the binary masses only and has to be determined by post-Newtonian theory. A non-spinning compact binary inspiral can thus be described by a set of nine parameters:

$$\boldsymbol{\Theta} = \{m_1, m_2, t_c, \Phi_c, \theta, \phi, D_L, \iota, \psi\}\,. \tag{3.4}$$

3.2.3 Gravitational waveform structure

In the following we derive the gravitational waveform for a very basic example of a compact binary. Let us assume that two point-like masses m_1 and m_2 are orbiting each other with angular frequency ω at a separation R in the (x, y) plane. The motion is then described in terms of a one-body problem (reduced mass μ orbiting around total mass M) by $\boldsymbol{x}_0(t) = (R\cos\Phi(t), R\sin\Phi(t), 0)$, with $\Phi(t) = \Phi_c - \omega(t_c - t)$ and $\omega = \dot{\Phi}(t) = \text{const}$. Orbital separation and frequency can be related through Kepler's third law which states that $\omega^2 = GM/R^3$. The 00-component of the energy-momentum tensor of this particular problem is $T^{00}(t, \boldsymbol{x}) = \mu c^2 \delta^{(3)}(\boldsymbol{x} - \boldsymbol{x_0})$ and hence the quadrupole moment is $M^{ij} = \mu\, x_0^i(t) x_0^j(t)$, as given by (2.36). In terms of the coordinates chosen above,

$$M_{11} = \mu R^2 \cos^2\Phi(t), \qquad M_{12} = M_{21} = \mu R^2 \cos\Phi(t)\sin\Phi(t), \qquad M_{22} = \mu R^2 \sin^2\Phi(t), \tag{3.5}$$

and the second time derivatives are

$$\ddot{M}_{11} = -2\mu\omega R^2 \cos 2\Phi(t), \qquad \ddot{M}_{12} = \ddot{M}_{21} = -2\mu\omega R^2 \sin 2\Phi(t), \qquad \ddot{M}_{22} = 2\mu\omega R^2 \cos 2\Phi(t). \tag{3.6}$$

When looking face-on onto such a compact binary from a distance r, one thus measures the gravitational wave polarisation amplitudes (2.39)

$$h_+ = -\frac{4(G\mathscr{M})^{5/3}}{rc^4}\omega^{1/3}\cos 2\Phi(t), \qquad h_\times = -\frac{4(G\mathscr{M})^{5/3}}{rc^4}\omega^{1/3}\sin 2\Phi(t), \tag{3.7}$$

where we have used Kepler's law to rewrite $G\mu R^2\omega = (G\mathscr{M})^{5/3}\omega^{1/3}$. As an immediate conclusion, one should note that the phase of the gravitational wave is twice the orbital phase of the binary, hence the

dominant GW frequency comes in at $f_{\mathrm{GW}} = 2f_{\mathrm{orb}} = \omega/\pi$. By applying rotations to the result (3.7), one can include the effect of arbitrary source orientation angles (θ, ϕ), inclination ι and polarisation angle ψ.

In reality, the emission of gravitational radiation will lead to a loss of orbital energy and hence a loss of orbital separation. The distance between the two binaries will shrink more and more, the orbital frequency (and thus also the gravitational-wave frequency) will increase continuously until the two compact objects have merged. Towards the relativistic regime, where most of the power is emitted, the linearised approximation considered here will have failed already for some time; higher orders in terms of a post-Newtonian expansion will be necessary. In Section 3.3, post-Newtonian waveforms are presented that take this energy-loss into account.

3.3 Waveform models

In the following, let us introduce the waveform models in the PN expansion that have been established by the community. As in gravitational wave astronomy usually Fourier transforms of the time domain waveforms are needed, it can be favourable to work in the stationary phase approximation (SPA).

3.3.1 Time domain

For a non-spinning compact binary inspiral, one can write the orbital energy E and the gravitational wave flux $\mathscr{F}$ as a PN expansion in terms of the dimensionless frequency x, as has been done to 3.5PN for non-spinning compact binaries by [11, 19–23]:

$$E(x) = -\frac{\mu c^2 x}{2}\left[1 + \left(-\frac{3}{4} - \frac{1}{12}\eta\right)x + \left(-\frac{27}{8} + \frac{19}{8}\eta - \frac{1}{24}\eta^2\right)x^2 + \left(-\frac{675}{64} + \left(\frac{34445}{576} - \frac{205}{96}\pi^2\right)\eta - \frac{155}{96}\eta^2 - \frac{35}{5184}\eta^3\right)x^3\right] + \mathscr{O}\left(\frac{1}{c^8}\right), \tag{3.8}$$

and

$$\mathscr{F}(x) = \frac{32c^5}{5G}\eta^2 x^5\left[1 + \left(-\frac{1247}{336} - \frac{35}{12}\eta\right)x + 4\pi x^{3/2} + \left(-\frac{44711}{9072} + \frac{9271}{504}\eta + \frac{65}{18}\eta^2\right)x^2 + \left(-\frac{8191}{672} - \frac{583}{24}\eta\right)\pi x^{5/2} + \left(\frac{6643739519}{69854400} + \frac{16}{3}\pi^2 - \frac{1712}{105}\gamma_E - \frac{856}{105}\log(16x) + \left(-\frac{134543}{7776} + \frac{41}{48}\pi^2\right)\eta - \frac{94493}{3024}\eta^2 - \frac{775}{324}\eta^3\right)x^3\right] + \mathscr{O}\left(\frac{1}{c^8}\right), \tag{3.9}$$

where γ_E is Euler's constant. Note that the 3.5PN term in the energy function is zero. Energy conservation yields the *balance law* which states that

$$\frac{\mathrm{d}E}{\mathrm{d}t} + \mathscr{F} = 0, \tag{3.10}$$

i.e. all energy that is radiated away is removed from the potential energy governing the orbital motion of the two bodies. In the *adiabatic limit*, when the timescale for an orbit is much smaller than the typical timescale for the decrease of orbital separation, i.e. in other words $\dot{\omega}/\omega \ll 1$, one can assume that the inspiral is *quasi-circular*. This allows us to write down the system

$$\frac{\mathrm{d}\Phi}{\mathrm{d}t} = \frac{c^3}{GM}x^{3/2}, \tag{3.11}$$

$$\frac{\mathrm{d}x}{\mathrm{d}t} = \frac{\mathrm{d}E}{\mathrm{d}t}\left(\frac{\mathrm{d}E}{\mathrm{d}x}\right)^{-1} = -\frac{\mathscr{F}(x)}{\frac{\mathrm{d}E}{\mathrm{d}x}(x)}. \tag{3.12}$$

Since we work with Taylor expansions, there are multiple ways to go forward. A straightforward way would be to keep the ratio $F(x)/E'(x)$ as it is and solve the differential equations numerically with some initial values for t and x. This approach is called TaylorT1 (after the nomenclature of [24]). If we do not keep $F(x)/E'(x)$ as a fraction but expand it again as a Taylor series, we get a different solution, as for example given by the TaylorT2 formula

$$\Phi(x) = \Phi_{\mathrm{ref}} + \int \frac{\mathrm{d}\Phi}{\mathrm{d}t}\frac{\mathrm{d}t}{\mathrm{d}x}\mathrm{d}x = \Phi_{\mathrm{ref}} - \frac{c^3}{GM}\int x^{3/2}\left[\frac{E'(x)}{F(x)}\right]_{\mathrm{2PN}}\mathrm{d}x, \tag{3.13}$$

$$t(x) = t_{\mathrm{ref}} + \int \frac{\mathrm{d}t}{\mathrm{d}x}\mathrm{d}x = t_{\mathrm{ref}} - \int \left[\frac{E'(x)}{F(x)}\right]_{\mathrm{2PN}}\mathrm{d}x. \tag{3.14}$$

A third approach is the TaylorT3 formula where $t(x)$ is explicitly inverted to find $x(t)$ as a PN expansion. In order to simplify the expressions, one introduces the *dimensionless time* variable

$$\Theta = \frac{\eta c^3}{5GM}(t_{\mathrm{ref}} - t), \tag{3.15}$$

rewrites (3.14) as $\int \frac{E'(x)}{F(x)}\mathrm{d}x = \frac{5GM}{\eta c^3}\Theta$ and uses series inversion to find to 3.5PN

$$\begin{aligned} x(\Theta) = \frac{\Theta^{-1/4}}{4}\Bigg[1 &+ \left(\frac{743}{4032} + \frac{11}{48}\eta\right)\Theta^{-1/4} - \frac{\pi}{5}\Theta^{-3/8} + \left(\frac{19583}{254016} + \frac{24401}{193536}\eta + \frac{31}{288}\eta^2\right)\Theta^{-1/2} \\ &+ \left(-\frac{11891}{53760} + \frac{109}{1920}\eta\right)\pi\Theta^{-5/8} + \left(-\frac{10052469856691}{6008596070400} + \frac{\pi^2}{6} + \frac{107}{420}\gamma_E - \frac{107}{3360}\log\left(\frac{\Theta}{256}\right)\right. \\ &+ \left.\left(\frac{3147553127}{780337152} - \frac{451}{3072}\pi^2\right)\eta - \frac{15211}{442368}\eta^2 + \frac{25565}{331776}\eta^3\right)\Theta^{-3/4} \\ &+ \left(-\frac{113868647}{433520640} - \frac{31821}{143360}\eta + \frac{294941}{3870720}\eta^2\right)\pi\Theta^{-7/8}\Bigg] + \mathscr{O}\left(\frac{1}{c^8}\right). \end{aligned} \tag{3.16}$$

This enables us to compute

$$\Phi(\Theta) = \Phi_{\mathrm{ref}} - \frac{1}{\eta}\left[\Theta^{5/8} + \left(\frac{3715}{8064} + \frac{55}{96}\eta\right)\Theta^{3/8} - \frac{3\pi}{4}\Theta^{2/8} + \left(\frac{9275495}{14450688} + \frac{284875}{258048}\eta + \frac{1855}{2048}\eta^2\right)\Theta^{1/8}\right], \tag{3.17}$$

where we stopped at 2PN order. Through $\omega(\Theta) = \frac{\mathrm{d}\Phi}{\mathrm{d}t}\frac{\mathrm{d}t}{\mathrm{d}\Theta}$, the angular frequency evolution can easily be recovered as

$$\omega(\Theta) = \frac{c^3}{8GM}\left[\Theta^{-3/8} + \left(\frac{743}{2688} + \frac{11}{32}\eta\right)\Theta^{-5/8} - \frac{3\pi}{10}\Theta^{-6/8} + \left(\frac{1855099}{14450688} + \frac{56975}{258048}\eta + \frac{371}{2048}\eta^2\right)\Theta^{-7/8}\right]. \tag{3.18}$$

The two waveform polarisations can then be expressed as (following [11])

$$h_{+,\times}(t) = \frac{2GM\eta}{c^2 D_L} x(t)\left[H^{(0)}_{+,\times} + x^{1/2}H^{(1/2)}_{+,\times} + xH^{(1)}_{+,\times} + x^{3/2}H^{(3/2)}_{+,\times} + x^2 H^{(2)}_{+,\times}\right]. \tag{3.19}$$

The harmonic coefficients $H^{(n)}_{+,\times}$ are sums of cosines of multiples of the orbital phase. Explicit expressions for $H^{(n)}_{+,\times}$ can be found in [11]. The dominant contribution comes in at twice the orbital frequency: $H^{(0)}_{+} = -(1+\cos^2\iota)\cos 2\Phi$ and $H^{(0)}_{\times} = -2\cos\iota\sin 2\Phi$, where ι is the orbital inclination parameter.

A detector measures a strain $h(t)$ that is a linear combination of the above + and × polarisation modes, depending on the orientation of the source in the sky relative to the detector. As later introduced in Chapter 5, in the low-frequency approximation the individual polarisations can be projected onto the detector arms by using *antenna pattern functions* $F^{+,\times}(\theta,\phi,\psi)$,

$$h(t) = h_+(t)F^+(t) + h_\times(t)F^\times(t). \tag{3.20}$$

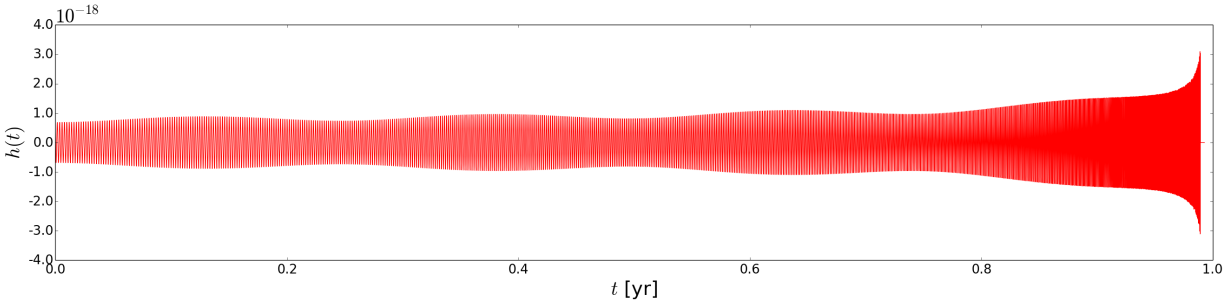

Figure 3.2: *Plot of a typical gravitational waveform originating from the inspiral of two compact objects, a so-called chirp. The Doppler modulation arising from the motion of the detector is already included and clearly visible.*

3.3.2 Frequency domain

As one usually evaluates the inner product (6.5) in matched filtering (Section 6.1), it is necessary to move the waveforms given in the previous section to the frequency domain. A Fourier transform of the waveform (3.19) can be computed either numerically or analytically. To perform the Fourier transform numerically, the time domain waveform has to be sampled at discrete points in time and a *Fast Fourier Transform* (FFT) algorithm has to be used. In appendix A, the signal processing tools needed for such a procedure are introduced. In general, there is no way of finding an analytical formula for a Fourier transform of (3.19); however, one can make use of the so-called *stationary phase approximation* (SPA) which shall be introduced here in terms of the dominant harmonic. An expansion for full harmonics can be found in Chapter 7.

The dominant harmonic of (3.20) is

$$h(t) = -\frac{2GM\eta}{c^2 D_L} x(t)\left[(1+\cos^2\iota)\cos 2\Phi(t)\,F^+(t) + 2\cos\iota\sin 2\Phi(t)\,F^\times(t)\right]$$
$$\equiv 2\,a_c(t)\cos 2\Phi(t) + 2\,a_s(t)\sin 2\Phi(t). \tag{3.21}$$

For simplicity, let us first look at the Fourier transform of the cosine part only:

$$\tilde{h}_c(f) = \int_{-\infty}^{\infty} h_c(t)\,e^{2\pi i f t}\,\mathrm{d}t = \int_{-\infty}^{\infty} a_c(t)\left[e^{i(2\pi f t - 2\Phi(t))} + e^{i(2\pi f t + 2\Phi(t))}\right]\mathrm{d}t$$
$$= \int_{-\infty}^{\infty} a_c(t)\,e^{i\psi_+}\,\mathrm{d}t + \int_{-\infty}^{\infty} a_c(t)\,e^{i\psi_-}\,\mathrm{d}t, \tag{3.22}$$

with $\psi_\pm(t) = 2\pi f t \pm 2\Phi(t)$. The SPA considers only the region of the integral where $\psi(t)$ is stationary, i.e. $\dot{\psi}_\pm = 2\pi f \pm 2\dot{\Phi} = 0$. The non-stationary part of the phase creates an oscillating term that is summed up by the integral and contributes only at subleading order. Since for compact binaries we demand that the orbital phase increases monotonically with time, we demand that $\dot{\Phi} > 0$ and hence $\psi_+(t)$ has no stationary point. We shall call $\psi_-(t)$ henceforth $\psi_f(t)$. Suppose that t_f solves $\dot{\psi}_f(t_f) = 0$. This is equivalent to $2F(t_f) = f$, where $F(t) = \dot{\Phi}/2\pi$ is the orbital frequency and f is the (dominant) gravitational wave frequency of the compact binary. Hence $t_f = t(f)$, where $t(f)$ is the timing function (3.14). Let us now expand the recovered phase around such a stationary point t_f. By definition, the first time derivative vanishes; one can compute the second to be

$$\left.\frac{\mathrm{d}^2\psi_f}{\mathrm{d}t^2}\right|_{t=t_f} = -4\pi\dot{F}(t_f), \tag{3.23}$$

and hence the phase can be approximated as

$$\psi_f(t) \approx \psi_f(t_f) - 2\pi\dot{F}(t_f)(t-t_f)^2. \tag{3.24}$$

Observing that the amplitude $a_c(t)$ is varying much more slowly than the gravitational wave phase, one can assume that $a(t_f) = \text{const}$ in the vicinity of the stationary point and therefore the Fourier integral (3.22) becomes

$$\tilde{h}_c(f) \approx a_c(t_f)\,e^{i\psi_f(t_f)}\int_{-\infty}^{\infty}\mathrm{d}t\,e^{-i\pi\dot{F}(t_f)(t-t_f)^2} = \frac{a_c(t_f)}{\sqrt{2i\dot{F}(t_f)}}e^{i\psi_f(t_f)} = \frac{a_c(t_f)}{\sqrt{2\dot{F}(t_f)}}e^{i\left(\psi_f(t_f)-\frac{\pi}{4}\right)}, \tag{3.25}$$

where we have solved the Gaussian integral and have used $i^{-1/2} = e^{-i\pi/4}$. Similarly, one finds $\tilde{h}_s(f) = i\frac{a_s(t_f)}{\sqrt{\dot{F}(t_f)}}e^{i\psi_f(t_f)-\frac{\pi}{4}}$ for the Fourier transform of the sine part of the waveform. This enables us to write

$$\tilde{h}(f) = \left[a_c(t_f) + i\,a_s(t_f)\right]\frac{e^{i\psi_f(t_f)-\frac{\pi}{4}}}{\sqrt{2\dot{F}(t_f)}} = \pi^{2/3}\frac{c}{D_L}\left(\frac{G\mathscr{M}}{c^3}\right)^{5/3}\frac{f^{2/3}}{\sqrt{2\dot{F}(t_f)}}\,a_{\mathrm{pol}}(t_f)\,e^{i\left(\psi_f(t_f)-\frac{\pi}{4}-\phi_{\mathrm{pol}}\right)}, \tag{3.26}$$

with

$$A_{\mathrm{pol}}(t) = \sqrt{(1+\cos^2\iota)^2[F^+(t)]^2 + \cos^2\iota[F^\times(t)]^2}, \qquad \phi_{\mathrm{pol}}(t) = \mathrm{atan2}\left[\frac{\cos\iota\,F^\times(t)}{(1+\cos^2\iota)\,F^+(t)}\right]. \tag{3.27}$$

The complex amplitude has been rewritten in terms of $z = |z|e^{i\arg(z)}$. The gravitational wave phase can be found using the PN expanded functions in Section 3.3.1 to be

$$\begin{aligned}\Psi(f) &= \psi_f(t_f) - \frac{\pi}{4} = 2\pi f\, t(f) - 2\Phi[t(f)] - \frac{\pi}{4} \\ &= 2\frac{t_c c^3}{GM}x^{3/2} - 2\phi_c - \frac{\pi}{4} + \frac{3x^{-5/2}}{128\eta}\left[1 + \left(\frac{3715}{756} + \frac{55\eta}{9}\right)x - 16\pi x^{3/2}\right. \\ &\left. + \left(\frac{15293365}{508032} + \frac{27145\eta}{504} + \frac{3085\eta^2}{72}\right)x^2\right],\end{aligned} \tag{3.28}$$

truncated at 2PN, where $\frac{\pi}{4}$ has been redefined into the phase. Here, in the so-called *restricted waveform* (RWF), the amplitude is only taken to leading order, in contrast to the *full waveform* (FWF) that takes the amplitude to full PN order. To compute the time derivative of $F(t)$, we use $F(\Theta) = \frac{\omega(\Theta)}{2\pi} = \frac{c^3}{16\pi GM}\Theta^{-3/8}$ (from (3.18)). Then,

$$\dot{F}|_{t=t(f)} = \frac{\mathrm{d}\Theta}{\mathrm{d}t}\frac{\mathrm{d}F}{\mathrm{d}\Theta}\bigg|_{t=t(f)} = \frac{3}{320}\frac{\eta}{2\pi}\left(\frac{c^3}{GM}\right)^2 \Theta^{-11/8}\bigg|_{t=t(f)}, \tag{3.29}$$

and, since through the inversion of $F(\Theta)$ one finds $\Theta(f)$, the waveform (3.26) can be expressed as

$$\tilde{h}(f) = \sqrt{\frac{5}{96}}\pi^{-2/3}\left(\frac{G\mathscr{M}}{c^3}\right)^{5/6}\frac{c}{D_L}f^{-7/6}A_{\mathrm{pol}}\, e^{i(\Psi(f)-\phi_{\mathrm{pol}})}. \tag{3.30}$$

The SPA is valid as long as the amplitude varies on a much slower timescale than the phase. This is enforced by the conditions [25, 26]

$$\frac{\mathrm{d}\log A}{\mathrm{d}t} \ll \frac{\mathrm{d}\Phi}{\mathrm{d}t}, \qquad \frac{\mathrm{d}^2\Phi}{\mathrm{d}t^2} \ll \left(\frac{\mathrm{d}\Phi}{\mathrm{d}t}\right)^2, \tag{3.31}$$

where $A(t)$ is the GW amplitude and $\Phi(t)$ is the orbital phase of the compact binary.

3.4 Spinning compact binaries

So far we have considered only non-spinning compact binaries. However, it is expected that most of the SMBHs have a non-negligible spin that they acquired either in their formation process or during accretion. This assigns spin vectors $\boldsymbol{S}_1$ and $\boldsymbol{S}_2$ to the two masses m_1 and m_2. In GR, $\boldsymbol{S}_1$ and $\boldsymbol{S}_2$ couple with the angular momentum $\boldsymbol{L}$ (spin-orbit) and with each other (spin-spin) through gravito-magnetic effects, what leads to a precession of both the spins and the angular momentum. The introduction of spins leaves us with six additional binary parameters that we have to consider in waveform templates: The inclination ι and the polarisation angle ψ as defined in Section 3.2.1 are relieved from their role and instead we introduce as binary parameters the orientation angles of the angular momentum unit vector $\hat{\boldsymbol{L}}$, ϕ_L and θ_L, and the magnitudes and the orientation angles of the individual spins, $\chi_1, \phi_1, \theta_1, \chi_2, \phi_2$ and θ_2. The spin magnitudes $\chi_i \in [0,1]$ are defined through the maximal spin that is possible in the Kerr solution of GR, in particular

$$|\boldsymbol{S}_i| = \chi_i \frac{Gm_i^2}{c}. \tag{3.32}$$

Hence the individual spins are given by $\boldsymbol{S}_i = \chi_i \frac{Gm_i^2}{c}(\cos\phi_i \cos\theta_i, \sin\phi_i \cos\theta_i, \sin\theta_i)$ and the orbital angular momentum is expressed as $\hat{\boldsymbol{L}} = (\cos\phi_L \cos\theta_L, \sin\phi_L \cos\theta_L, \sin\theta_L)$. In the following, we review how spin-precession affects GWs from compact binaries.

3.4.1 Spin-precession

To leading order in spin-orbit and spin-spin couplings, averaged over one orbit and neglecting radiation reaction, spin and angular momentum precession is governed by the *spin-precession equations* [18, 27]

$$\dot{\boldsymbol{L}} = \frac{G}{c^2}\frac{1}{r^3}\left[\left(2+\frac{3m_2}{2m_1}\right)\boldsymbol{S}_1 + \left(2+\frac{3m_1}{2m_2}\right)\boldsymbol{S}_2\right]\times\boldsymbol{L} - \frac{3G}{2c^2}\frac{1}{r^3}\left[(\boldsymbol{S}_2\cdot\hat{\boldsymbol{L}})\boldsymbol{S}_1 + (\boldsymbol{S}_1\cdot\hat{\boldsymbol{L}})\boldsymbol{S}_2\right]\times\hat{\boldsymbol{L}}, \quad (3.33)$$

$$\dot{\boldsymbol{S}}_i = \frac{G}{c^2}\frac{1}{r^3}\left[\left(2+\frac{3m_j}{2m_i}\right)\boldsymbol{L} + \frac{1}{2}\boldsymbol{S}_j - \frac{3}{2}(\boldsymbol{S}_j\cdot\hat{\boldsymbol{L}})\hat{\boldsymbol{L}}\right]\times\boldsymbol{S}_i, \quad (3.34)$$

where $i, j \in \{1,2\}$ and $i \neq j$. There are no closed-form solutions of this system; thus one has to resort to numerical methods to find $\boldsymbol{S}_{1,2}(t)$ and $\boldsymbol{L}(t)$. If one neglects radiation reaction, $\boldsymbol{S}_1$, $\boldsymbol{S}_2$ and $\boldsymbol{L}$ precess around the conserved total angular momentum vector $\boldsymbol{J} = \boldsymbol{S}_1 + \boldsymbol{S}_2 + \boldsymbol{L}$. Consequently, as soon as the spins precess, the orbital angular momentum is not conserved anymore, leading to a precession of the orbital plane. However, the magnitudes of the spins and the angular momentum are conserved, since it can easily be shown that $\frac{\mathrm{d}}{\mathrm{d}t}\boldsymbol{S}_i^2 = \frac{\mathrm{d}}{\mathrm{d}t}\hat{\boldsymbol{L}}^2 = 0$.

In the case of spins that are initially both aligned with the angular momentum vector, the spin-precession equations reduce to

$$\dot{\boldsymbol{L}} = 0, \qquad \dot{\boldsymbol{S}}_i = 0. \quad (3.35)$$

This represents a static equilibrium solution, hence the spins and the angular momentum remain constant and thus do not precess. It is considered to be quite likely that the spins of SMBHs are mostly nearly parallel, as accreting gas is thought to align them, resulting in minor misalignment angles of $10-30^\circ$ [28]. In this case, the spins and the angular momentum vectors are expected to precess smoothly around the total angular momentum (Fig. 3.3).

If one of the individual spins is zero, we choose $\boldsymbol{S}_2 = 0$ here, then we deal with so-called *simple precession* [18, 29]. There the precession equations simplify to

$$\dot{\boldsymbol{L}} = \frac{G}{c^2}\frac{1}{r^3}\left(2+\frac{3m_2}{2m_1}\right)\boldsymbol{L}\times\boldsymbol{S} = \boldsymbol{L}\times\boldsymbol{\Omega}, \quad (3.36)$$

$$\dot{\boldsymbol{S}} = -\dot{\boldsymbol{L}} = \boldsymbol{S}\times\boldsymbol{\Omega}, \quad (3.37)$$

where

$$\boldsymbol{\Omega} = \frac{G}{c^2}\frac{1}{r^3}\left(2+\frac{3m_2}{2m_1}\right)\boldsymbol{J}, \quad (3.38)$$

and $\boldsymbol{S} = \boldsymbol{S}_1 + \boldsymbol{S}_2$ is the total spin vector. The vectors $\hat{\boldsymbol{L}}$ and $\boldsymbol{S}_1$ precess thus around $\boldsymbol{J}$ with a precession frequency of $\omega_p = \frac{G}{c^2 r^3}\left(2+\frac{3m_2}{2m_1}\right)|\boldsymbol{J}|$.

In general, especially if the absolute values of the angular momentum and the spins are of comparable magnitude, the binary orbital plane can undergo strong precession (Fig. 3.4). Since the spin-precession equations are proportional to $1/r^3$, precession dominates particularly towards the last cycles of the inspiral.

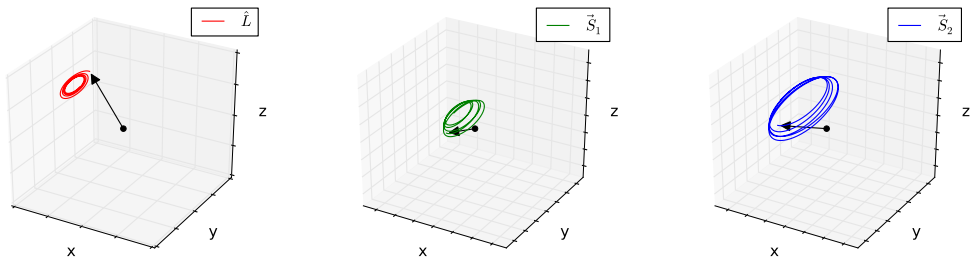

Figure 3.3: *Spin evolution for an equal mass binary with $m_1 = m_2 = 10^7 M_\odot$. The individual spins are small enough such that the spins and the angular momentum vectors all precess around the nearly fixed total angular momentum $\boldsymbol{J}$.*

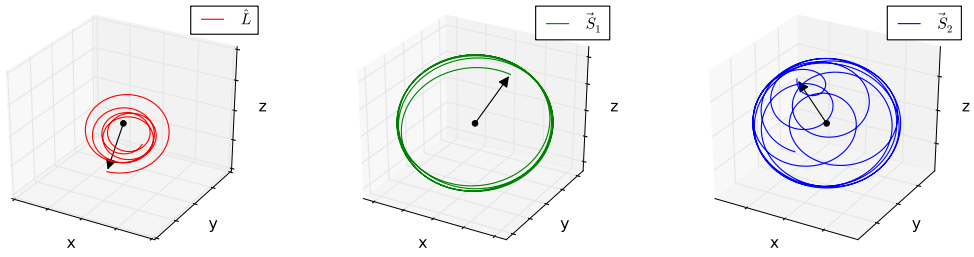

Figure 3.4: *Spin evolution for a binary with mass ratio of 1.6: $m_1 = 8 \times 10^6 M_\odot$, $m_2 = 5 \times 10^6 M_\odot$. Because of the large initial spins, the angular momentum and the individual spins undergo strong precession.*

3.4.2 Modified gravitational waveforms

The modification of the gravitational waveform due to non-zero spins and a precession thereof is twofold: The pure presence of spins alters the conservative orbital energy and the GW flux through gravito-magnetic effects, leading to an alternative frequency and orbital phase evolution. Spin-precession introduces an additional modulation to the waveform, as it implies a precession of the orbital plane.

Modified orbital energy and flux

For a binary of spinning compact objects, additional spin-orbit and spin-spin couplings enter the conservative orbital energy and the GW flux. In the following, we work in terms of the spin-orbit coupling parameter

$$\beta(a,b) = \frac{c}{G}\sum_{i=1}^{2}\left(\frac{a}{M^2} + \frac{b\eta}{m_i^2}\right)\boldsymbol{S}_i \cdot \hat{\boldsymbol{L}}, \tag{3.39}$$

and the spin-spin coupling parameter

$$\sigma(a,b) = \frac{c^2}{\eta M^4 G^2}\left(a\boldsymbol{S}_1 \cdot \boldsymbol{S}_2 - b(\boldsymbol{S}_1 \cdot \hat{\boldsymbol{L}})(\boldsymbol{S}_2 \cdot \hat{\boldsymbol{L}})\right). \tag{3.40}$$

The conservative (non-spinning, NS) orbital binding energy (3.8) is then modified by [30]

$$E(x) = E_{\rm NS}(x) + E_{\rm SO}(x) + E_{\rm SS}(x), \tag{3.41}$$

$$E_{\rm SO}(x) = -\frac{\mu c^2 x^{5/2}}{6}\,\beta\,(8,6)\,, \tag{3.42}$$

$$E_{\rm SS}(x) = -\frac{\mu c^2 x^3}{6}\,\sigma\,(1,3)\,, \tag{3.43}$$

truncated at 2PN order. It is worth noting that leading order spin-orbit effects enter here at 1.5PN order while spin-spin effects come in only at 2PN order. Similarly, accounting for non-zero spins leads to modifications of the GW flux (3.9)

$$\mathscr{F}(x) = \mathscr{F}_{\rm NS}(x) + \mathscr{F}_{\rm SO}(x) + \mathscr{F}_{\rm SS}(x), \tag{3.44}$$

$$\mathscr{F}_{\rm SO}(x) = -\frac{8}{5}\eta^2\frac{c^5}{G}x^{13/2}\,\beta\,(11,5)\,, \tag{3.45}$$

$$\mathscr{F}_{\rm SS}(x) = -\frac{2}{15}\eta^2\frac{c^5}{G}x^{7}\,\sigma\,(223,48)\,. \tag{3.46}$$

Assuming that β and σ are small and can be treated as constants (i.e. they vary on a much slower timescale than the orbital frequency), we approximate to 2PN order in the adiabatic approximation

$$\begin{aligned}\frac{\mathrm{d}x}{\mathrm{d}t} = -\mathscr{F}\left[\tfrac{\mathrm{d}E}{\mathrm{d}x}\right]^{-1} &= \frac{64\nu}{5}\frac{c^3}{GM}x^5\left[1-\left(\frac{743}{336}+\frac{11\nu}{4}\right)x+\left(4\pi-\frac{1}{12}\beta(113,75)\right)x^{3/2}\right.\\ &\left.+\left(\frac{34103}{18144}+\frac{13661\nu}{2016}+\frac{59\nu^2}{18}-\frac{1}{48}\sigma(247,721)\right)x^2\right].\end{aligned} \tag{3.47}$$

This expression can be used to compute the time-of-frequency relation $t(x)$, which allows us to find $x(t)$ through series inversion and consequently enables us to compute the orbital phase evolution $\Phi(t)$.

Treating β and σ as constants should be fine as long as spin-precession is considerably weak and the precession timescale is much larger than the orbital timescale (as assumed in the spin-precession equations). In the stationary phase approximation, one should test carefully whether the conditions (3.31) are violated, as spin-precession introduces another time-dependent term to the phase [31].

Phase modulation due to precession of the orbital plane

If the orbital angular momentum $\boldsymbol{L}$ undergoes a precession, then the plane of orbital motion moves around as well. This creates an additional modulation in the waveform which can be modelled by promoting the orbital phase to $\Phi(t) \to \Phi(t) + \delta\Phi(t)$ where $\delta\Phi(t)$ is an extra phase modulation term. This modulation is a function of all of the past history of the precessing spins and can be computed via [18]

$$\delta\Phi(t) = -\int_t^{t_c}\left(\frac{\hat{\boldsymbol{L}}\cdot\hat{\boldsymbol{n}}}{1-(\hat{\boldsymbol{L}}\cdot\hat{\boldsymbol{n}})^2}\right)(\hat{\boldsymbol{L}}\times\hat{\boldsymbol{n}})\cdot\dot{\hat{\boldsymbol{L}}}\,\mathrm{d}t, \tag{3.48}$$

where $\hat{\boldsymbol{n}}$ points to the source as introduced in Section 3.2.1.

In this section, we have established how spin-precession manifests in the phase evolution of the gravitational waveform. By taking such additional information on the orbital dynamics of the binary into account, the degeneracies introduced through the use of six additional spin parameters can partially be broken. This is applied in the context of tests of GR in Chapter 7.

Chapter 4

Alternative Theories of Gravity

Since the conception of GR, various alternatives to it have been proposed. Because of their large number, it is crucial to establish a framework to classify them. As our focus is to provide GW astronomy tools that let the data choose whether GR is the correct theory or not, we content ourselves here by giving only a very short review of proposed theories and their possible imprints on gravitational waves. Extensive reviews can be found in [32–34]. In the following, we motivate why it is a good idea to question GR although it has been tested very well in the past. We then discuss the imprints of alternative theories on GWs and introduce some examples of theories that are competing with GR. Going to a more general view, we then introduce tests that check the data for generic features that should be absent in GR. Instead of characterizing alternative models by a modified action or a particular physical phenomenon, data analysis procedures are only interested in the set of the PN coefficients provided by those models. As the PN coefficients are just real numbers, for the sake of testing GR it is therefore (at least in theory) sufficient to consider a linear space of deformations from the PN coefficients of GR. Such tests are crucial, for if we fail to do them, parameter estimation could suffer a fundamental bias [35].

4.1 Motivation - Why General Relativity should be questioned

The theory of general relativity has withstood various tests since its conception. Among such are the early, 'classical' tests that made it widely accepted among the community: the correct prediction of the deflection of light by the Sun and of Mercury's perihelion precession. Since then, plenty of tests for different aspects have been carried out that always ended up in favour of GR [32]. Nevertheless, GR has some theoretical 'shortcomings' that make it hard to fit it in the picture of cosmology and quantum theory.

On a cosmological scale, GR is not able to provide a mechanism for the process of inflation, i.e. the very rapid expansion that the universe is assumed to have undergone shortly after the big bang. Inflation is necessary to explain the origin of the large-scale structure in the universe and the isotropicity of the cosmic microwave background. Moreover, the rotation velocity curves of galaxies need the presence of additional invisible gravitational mass in order to be in accordance with theoretical predictions: so-called dark matter that responds only very weakly to non-gravitational forces. Because all attempts to detect the presence of any dark matter particle candidate have failed so far, some people would welcome it if GR incorporated such effects in an intrinsic way without having to rely on exotic forms of matter. Alternative theories such as Modified Newtonian Dynamics (MOND) have been proposed to account for this. In 1998, supernovae observations suggested that the known universe expands with an increasing instead of a decreasing velocity. The mass content of the universe was expected to stop its expansion eventually, but apparently a non-zero cosmological vacuum energy pushes against the gravitational pull. The simplest model that can account

for the presently observed acceleration introduces a cosmological constant to Einstein's equations that accounts for a non-zero cosmological vacuum energy.

Since quantum theory is very successful in the explanation of physical phenomena on the microscopic scale, demanding a common intersection with GR and that GR can be treated with the tools of quantum field theory can be justified. However, all attempts to quantise GR have hitherto turned out to be unsatisfactory. The fact that the vacuum energy predicted by quantum field theory is about fifty orders of magnitude higher than the vacuum energy that leads to the current acceleration of the known universe can be seen as a big clue that none of each theories is able to describe physical phenomena on both the microscopic and macroscopic scale. This has led to the conception of quantum gravity theories that try to propose a general relativistic theory that can be quantised.

Such arguments provide reason enough to test the predictions of GR carefully and to consider certain physically motivated alternative theories. However, it needs to be emphasised that, in contrast to GR, almost all competing theories considered here suffer from fundamental intrinsic problems [32] and are therefore to our current knowledge not viable theories. In the following, we shortly review what aspects of GR can be tested and reserve a special section for gravitational-wave tests.

The fundament of GR is the *equivalence principle*. Already Newton thought of the *weak equivalence principle* (WEP) when he stated that the inertial and the gravitational mass are the same. The WEP is equivalent to the principle of Universality of Free Fall which states that bodies freely falling in a gravitational field experience the same acceleration, independent of their mass. GR is based on the *Einstein equivalence Principle* (EEP) that incorporates the WEP but demands additionally that the outcome of any local non-gravitational experiment is independent of the velocity of the reference frame (local Lorentz invariance) and of the position of the reference frame (local position invariance). The *strong equivalence principle* (SEP) extends the EEP to self-gravitating systems. Various tests have constrained the WEP, local Lorentz invariance and local position invariance to a very high accuracy [32]. This suggests that we can assume that, even if GR might not be correct, we deal with a theory of gravitation where the motion of matter can be described through geodesics on a curved spacetime, i.e. with a metric tensor $g_{\mu\nu}$. In the rest of this chapter, we shall henceforth focus our attention only on *metric* theories that are endowed with a symmetric metric $g_{\mu\nu}$ which in a local inertial frame reduces to the Minkowski metric $\eta_{\mu\nu}$ and thus the laws of physics reduce to special relativity. However, GR seems to be the only theory that incorporates the SEP to its full extent. All other theories have been shown to violate either the WEP, local Lorentz invariance or local position invariance; the higher explanation power has to be traded for one of these beautiful fundamental principles. For example, quantum gravity incorporates the Planck length as a fundamental length scale; this is a violation of local Lorentz invariance, as there length is not an invariant quantity. In string theory, additional tensor, vector or scalar fields couple to matter and therefore also pose potential sources for Lorentz invariance violations. Since we expect GR to fail at the Planck scale, one should consider it to be quite likely that the SEP/EEP is violated at some level.

It is possible to incorporate violations of the SEP in terms of metric theories by including additional gravitational fields of tensor, vector or scalar nature that couple with matter and produce a different spacetime curvature than a theory with only a metric tensor $g_{\mu\nu}$. Such extra fields cannot act directly on test bodies, as matter couples still only to the metric tensor; the metric tensor is however influenced by the additional fields, providing a different spacetime curvature. As a standard approach to create an alternative to GR, one can therefore introduce additional fields to the Einstein-Hilbert action, as introduced in Section 4.3. In order to create a framework to categorise alternative theories, the *Parameterized Post-Newtonian* (PPN) formalism has been devised, that introduces a generalised 1PN expansion in order to classify the different theories by mapping them to a set of PPN parameters. Through constraints on the PPN parameters, many proposed theories have already been ruled out [32].

Various experiments, such as solar system tests, have been introduced to constrain the vast amount of alternative theories that sprouted up since the conception of GR. However, GR is the only one with no

adjustable parameters, all other theories provide at least one free parameter that has to be constrained with experiments. Since, especially on a cosmological scale, already small modifications can have a large impact, it is in general difficult to rule out a theory. It is hoped that by looking at the dynamical, strong-field regime of GR, we are able to place much more stringent constraints on the zoo of alternative theories.

4.2 Imprints on gravitational waves

There are two stages where gravitational waves can be altered under the influence of an alternative theory of gravity: *generation* and *propagation*. In GW generation, a different underlying theory implies different conservative orbital motion and a different loss of energy through GW emission. Conservative orbital motion can be changed because a modified spacetime curvature implies modified motion on modified geodesics. As a consequence of the introduction of e.g. additional tensor, vector or scalar fields, energy can be radiated away through additional channels such as dipolar radiation or additional degrees of freedom in terms of spacetime excitation - alternative polarisation modes. Consequently, the relations for flux (3.9) and orbital energy (3.8) are modified and hence lead to a modified orbital phase and frequency evolution; as these govern the gravitational waveform that is emitted, the phase of the resulting GW will differ from the one that is predicted by GR. We have already established that in GR gravitational waves travel at the speed of light, independent of their frequency. However, they could also follow a dispersion relation which would make the speed of a GW wave train a function of its frequency. This can e.g. be caused by a non-zero 'graviton mass' (see Section 4.4.1), where GWs move faster the higher their frequency is. As the frequency evolution of a compact binary inspiral increases monotonically, this results in a squeezing of the observed waveform. Four extra polarisations are allowed in addition to the plus and cross polarisation admitted by GR if one allows for alternative metric theories to exist: a transverse breathing mode and three longitudinal modes [32]. Although we will not consider such alternative modes in this work (except for their possible impact on the GW flux), we emphasise that, given a detector finds evidence for the existence of such an alternative polarisation, a smoking-gun evidence against GR would be provided. However, such a task is difficult for current detectors; possibly pulsar timing arrays that can be seen as a multiple arm detector will serve this task.

Although to date no direct detection of GWs could be claimed using state-of-the-art laser interferometers, the observation of the orbital decay of the binary pulsar PSR1913+16 provided indirect evidence for energy loss through gravitational radiation and allowed first tests of GR in stronger fields with $v/c \sim 10^{-3}$. Recently, the orbital decay of PSR1913+16 has been measured to be in accordance with GR with an error of less than 1% [32, 36].

4.3 The zoo of alternative theories - Particular examples

Scalar-Tensor, Brans-Dicke, Einstein-Aether, Hořava-Lifshitz, Pauli-Fierz, Lightman-Lee, Gauss-Bonnet, Einstein-Dilaton-Gauss-Bonnet, Horndeski, Braneworld, DGP, Kaluza-Klein, Will-Nordvedt, Hellings-Nordvedt, Khronometric, Randall-Sundrum, Einstein-Cartan-Sciama-Kibble, dynamical/non-dynamical Chern-Simons, Eddington-Inspired Born-Infeld Gravity, New Massive Gravity, Bi-Gravity, Tensor-Vector-Scalar, $f(R)$, Conformal gravity, Quintessence, Double Special Relativity Theory, Non-commutative geometry, Lovelock gravity, Cascading gravity, ...

This is an incomplete list of 30 alternative theories of gravity that are not ruled out and that aim to describe particular effects that GR is not able to. As introduced in Section 4.1, a first approach to classify this zoo of alternative theories is to map them to the PPN formalism. However, since the PPN formalism works in the weak-field regime and considers only terms up to 1PN order, the free parameters of such theories can

most likely not be constrained enough to rule the theory out. To this end, strong-field tests are required which can be performed best through the observation of gravitational waves from compact binaries.

In the following we introduce selected examples of alternative theories that have been proposed. Let us emphasise once more that a detailed review of alternative theories can be found in [32–34]; in this work we are not interested in a particular theory to be true or false, but rather in GR being consistent with the measured data or not. After possible evidence that GR is not the best theory to describe the data that has been gathered by our detectors, selected alternative theories could be investigated more closely.

Einstein's equations can be derived by variation of the Einstein-Hilbert action

$$S = \int R\,\sqrt{-g}\,\mathrm{d}^4x + S_M(\psi_M, g_{\mu\nu}), \tag{4.1}$$

where R represents the scalar curvature, g denotes the determinant of the metric and S_M is the matter action that universally couples a matter field ψ_M to the metric tensor. Any cosmological constant shall be ignored for the time being. Since S has to be scalar, R is the most-general scalar that can be formed from the metric in GR and $\sqrt{-g}\,d^4x$ is the invariant integration mass of GR, there are no alternative actions that could lead to Einstein's field equations. In the following, let us introduce some examples for alternative theories that modify this action.

4.3.1 Scalar-tensor theories

Scalar-tensor theories [37–39] are very popular in unification schemes such as string theory or quantum gravity. Moreover, scalar fields are used to provide a model for cosmological inflation. In addition to the metric tensor, such theories contain a scalar function $\varphi(x)$ that can be incorporated into the Einstein-Hilbert action using minimal coupling, where a potential $V(\varphi)$ and a coupling function $A(\varphi)$ are used:

$$S = \int \left[R - 2g^{\mu\nu}\partial_\mu\varphi\,\partial_\nu\varphi - V(\varphi)\right]\sqrt{-g}\,\mathrm{d}^4x + S_M(\psi_M, A^2(\varphi)g_{\mu\nu}). \tag{4.2}$$

This representation (in the so-called *Einstein frame*) is non-metric as here matter couples also to $A(\varphi)$. A metric representation can be found by defining the physical metric $\tilde{g}_{\mu\nu} \equiv A^2(\varphi)g_{\mu\nu}$ (*Jordan frame*), then,

$$S = \int \left[\phi\tilde{R} - \phi^{-1}\omega(\phi)\tilde{g}^{\mu\nu}\partial_\mu\phi\,\partial_\nu\phi - \phi^2 V\right]\sqrt{-\tilde{g}}\,\mathrm{d}^4x + S_M(\psi_M, \tilde{g}_{\mu\nu}), \tag{4.3}$$

with

$$\phi = A(\varphi)^{-2}, \qquad \omega(\phi) = \frac{1}{2}\left[\left(\frac{d(\log A(\varphi))}{d\varphi}\right)^{-2} - 3\right]. \tag{4.4}$$

The modified field equations in the Jordan frame are then found by the variation of the action to be

$$\tilde{\Box}\phi = \frac{1}{3+2\omega(\phi)}\left(8\pi T^M - \frac{d\omega}{d\phi}\tilde{g}^{\mu\nu}\partial_\mu\phi\,\partial_\nu\phi\right), \tag{4.5}$$

$$\tilde{G}_{\mu\nu} = \frac{8\pi G}{\phi}T^M_{\mu\nu} + \frac{\omega(\phi)}{\phi^2}\left(\partial_\mu\phi\,\partial_\nu\phi - \frac{1}{2}\tilde{g}_{\mu\nu}\tilde{g}^{\rho\sigma}\partial_\rho\phi\,\partial_\sigma\phi\right) + \frac{1}{\phi}\left(\partial_\mu\partial_\nu\phi - \tilde{g}_{\mu\nu}\tilde{\Box}\phi\right), \tag{4.6}$$

where $T^M_{\mu\nu}$ is the energy-momentum tensor constructed from $\tilde{g}_{\mu\nu}$. A special case is *Brans-Dicke* theory (or also referred to as *massless Jordan-Fierz-Brans-Dicke* theory) that assumes $\omega(\phi) \equiv \omega_{\mathrm{BD}}$ to be a constant.

Brans-Dicke theory reduces to GR for $\omega_{\rm BD} \to \infty$. The Brans-Dicke parameter could be constrained using the Cassini spacecraft to $\omega_{\rm BD} > 4 \times 10^4$ through measurements of the Shapiro time delay [40].

In the context of compact binaries and gravitational radiation, the dominant effects of scalar-tensor theories on GW generation are the introduction of an additional scalar breathing polarisation mode and the production of dipole radiation that arises through the non-trivial variation of the scalar field in the finite-sized bodies (see e.g. [34]). Thus the orbital energy of the binary is (to leading order) modified by a dipole term that enters one post-Newtonian order before the first contribution from GR. In terms of the gravitational waveform in the stationary phase approximation, this can be written as [41]

$$\tilde{h}(f) = \tilde{h}_{\rm GR}(f)\, e^{-i\beta_{\rm BD} u^{-7/3}}, \tag{4.7}$$

where

$$\beta_{\rm BD} = \frac{5}{3584}\frac{S^2}{\omega_{\rm BD}}\eta^{2/5}, \tag{4.8}$$

and we recall that $u = G\mathscr{M}\pi f/c^3 = \eta^{3/5}x^{3/2}$. Here, S compares the self-gravitational binding energy per unit mass for the two bodies and essentially depends on their equations of state: this is the point where the SEP is violated. For binary black hole systems, $S = 0$, and hence there is no dipolar radiation in the inspiral waveform [42]; we will therefore not go further into this theory, as it is irrelevant for the context of this work. Furthermore, scalar-tensor theories can be better constrained using weak-field experiments [34]. Nevertheless, they pose a nice pedagogical example of an alternative theory that has undergone a considerable amount of studies.

4.3.2 Vector-tensor theories

Similar to the previous approach, one can introduce an additional gravitational field with vectorial character to the Einstein-Hilbert action that will introduce Lorentz-violating preferred-frame effects to the theory. The most general such action up to quadratic derivatives in the vector is given by [32]

$$S = \int \left[(1+\omega u_\mu u^\mu)R - K^{\mu\nu}_{\alpha\beta}\nabla_\mu u^\alpha \nabla_\nu u^\beta + \lambda(u_\mu u^\mu + 1)\right]\sqrt{-g}\,{\rm d}^4x + S_M(\psi_M, g_{\mu\nu}), \tag{4.9}$$

where

$$K^{\mu\nu}_{\alpha\beta} = c_1 g^{\mu\nu}g_{\alpha\beta} + c_2\delta^\mu{}_\alpha\delta^\nu{}_\beta + c_3\delta^\mu{}_\beta\delta^\nu{}_\alpha - c_4 u^\mu u^\nu g_{\alpha\beta}. \tag{4.10}$$

The coefficients c_i can be chosen arbitrarily, while λ is a Lagrange multiplier that serves to incorporate constraints that are imposed by different subtheories, such as Will-Nordvedt theory, Hellings-Nordvedt theory and Khronometric theory. Einstein-Aether theory was introduced to account for the aether, a preferred frame for the propagation of light. However, vector-tensor theories suffer several serious defects [32]; consequently, to date nobody has computed their effect on gravitational waves.

It is possible to create a relativistic theory that reduces to MOND in the weak field by including a scalar gravitational field (tensor-vector-scalar theory, TeVeS). MOND [43] is a candidate to account for a correct description of galaxy rotation curves without resorting to dark matter by introducing short-range corrections to gravitational fields. TeVeS is not considered here since MOND-like modifications to strong-field binary dynamics seem to be negligibly small [35].

4.3.3 Modified quadratic gravity / Chern-Simons theory

Instead of incorporating additional fields, one can also account for higher powers of the Riemann curvature. This will introduce effects that manifest in the untested strong field of GR. The most general action for modified quadratic gravity reads [34, 44]

$$S = \int \Big[\kappa R + \alpha_1 f_1(\vartheta) R^2 + \alpha_2 f_2(\vartheta) R_{\mu\nu} R^{\mu\nu} + \alpha_3 f_3(\vartheta) R_{\mu\nu\rho\sigma} R^{\mu\nu\rho\sigma} + \alpha_4 f_4(\vartheta) R_{\mu\nu\rho\sigma} {}^*R^{\mu\nu\rho\sigma} - \frac{\beta}{2}\left[\nabla_\mu \vartheta \nabla^\mu \vartheta + 2V(\vartheta)\right] \Big] \sqrt{-g}\, \mathrm{d}^4x + S_M(\psi_M, g_{\mu\nu}), \tag{4.11}$$

where α_i, β and $\kappa = 1/(16\pi G)$ are coupling constants, f_i are functionals on the same field ϑ (which is a restriction; in general the f_i could act on different fields) and ${}^*R^{\mu\nu\rho\sigma} = (1/2)\,\epsilon_{\rho\sigma}{}^{\alpha\beta} R^{\mu}{}_{\nu\alpha\beta}$ is the dual Riemann tensor. The term proportional to β represents a potential and a kinetic energy term in order to achieve minimal coupling. By choosing different values for the coupling constants, one can construct different theory subspaces, such as *Einstein-Dilaton-Gauss-Bonnet gravity* with $(\alpha_1, \alpha_2, \alpha_3, \alpha_4) = (1, -4, 1, 0)\,\alpha_{\mathrm{EDGB}}$ [45] or *dynamical Chern-Simons gravity* with $(\alpha_1, \alpha_2, \alpha_3, \alpha_4) = (0, 0, 0, -1/4)\,\alpha_{\mathrm{dCS}}$ [34, 46]. Both of these theories arise when considering the low-energy expansion of string theory; dynamical Chern-Simons gravity appears also when one considers loop quantum gravity [47].

The effect of dynamical Chern-Simons gravity on gravitational-wave generation has recently been under deeper investigation [44]; to leading order, the GR waveform in the stationary phase approximation is modified to

$$\tilde{h}(f) = \tilde{h}_{\mathrm{GR}}(f)\, e^{-i\beta_{\mathrm{dCS}} u^{-1/3}}, \tag{4.12}$$

where

$$\beta_{\mathrm{dCS}} = \frac{1549225}{11812864} \frac{\zeta_4}{\eta^{14/5}}, \tag{4.13}$$

with the dynamical Chern-Simons coupling parameter $\zeta_4 = \alpha_4^2/(\beta\kappa M^4)$ and the total mass M. Through the R^*R term, dynamical Chern-Simons gravity leads to parity violation that can let the plus and the cross polarisation travel at different speeds. It is important to emphasise that, in contrast to the two types of theories introduced before, modified quadratic gravity has no physical motivation, but rather aims to describe higher-order corrections that enter by an even more complicated underlying theory. Modified quadratic gravity should therefore be interpreted as an effective theory of a more fundamental theory that is truncated at quadratic order.

4.3.4 f(R) theories

In $f(R)$ theories [48] the scalar curvature R in the Einstein-Hilbert action is replaced with a function of it:

$$S = \int f(R) \sqrt{-g}\, \mathrm{d}^4x + S_M(\psi_M, g_{\mu\nu}). \tag{4.14}$$

$f(R)$ theories are very popular in cosmology as they can be used to create models that explain inflation and late-time acceleration (dark energy) of the universe. It has to be emphasised here that $f(R)$ theories are rather mathematical toys instead of being physically motivated. Similar to modified quadratic gravity,

they could be seen as effective theories. We will not delve further into classes of $f(R)$ theories as they are formally equivalent to scalar-tensor theories, what can be shown by choosing the scalar field $\phi = \mathrm{d}f/\mathrm{d}R$ and the potential $V(\phi) = R\,\mathrm{d}f/\mathrm{d}R - f(R)$; it is then possible to map metric $f(R)$ theories to a Brans-Dicke theory with $\omega_{\mathrm{BD}} = 0$ and Palatini $f(R)$ theories to a Brans-Dicke theory with $\omega_{\mathrm{BD}} = -3/2$ [48].

4.4 Testing for generic features that are not present in GR

It is by construction that particular theories, as the ones introduced above, exhibit certain features that are not present in GR, such as a 'massive' graviton, emission of dipolar radiation, additional polarisation modes, Lorentz or parity violation, a gravitational constant that varies in time or space, etc. Instead of doing difficult and time-consuming computations for each individual from the zoo of alternatives introduced above, one could therefore check the impact of such generic features on gravitational wave generation and propagation. If a GR model extended with one or more of these features gives a better fit to the detector data, then this provides evidence against GR and gives us at least a clue which specific alternatives need more development to be able to test them more thoroughly against GR. This method has the disadvantage that one is often not able to relate measured quantities to coupling constants of a particular theory, yet we prefer such an approach since we are primarily interested in whether a modification of GR is necessary at all. In the following, let us introduce some examples of generic physical features that represent a deviation from GR.

4.4.1 Modified dispersion relation through massive gravity

In GR, gravitational waves propagate along null geodesics, i.e. they move with the speed of light. The first alternative theory that implied a 'massive' gravitational field was proposed by Pauli and Fierz [49]. Although all attempts to quantise GR have failed so far, such a massive field is commonly accounted for by a theory with a massive gauge boson: a massive graviton. Massive gravity is expected to produce significant differences from GR in the strong-field regime. Even though Pauli-Fierz theory suffers from a discontinuity in the limit of arbitrarily small graviton masses, the idea of a massive graviton has become a popular field of research. In the following, we consider the presence of massive gravity from a phenomenological point of view and show the consequences for GW measurements.

As in special relativity the energy of a massive particle is given by $E = mc^2(1-v^2/c^2)^{-1/2}$, the propagation velocity of the graviton can be expressed as

$$\frac{v^2}{c^2} = 1 - \frac{m_g^2 c^4}{E^2}, \tag{4.15}$$

where m_g represents the graviton mass. It is then possible to associate a Compton wavelength $\lambda_g = h/(m_g c)$ to the graviton where h is Planck's constant. Since the energy of a single graviton is frequency-dependent, $E = hf$, gravitational waves with higher frequencies travel faster, with a speed closer to the speed of light than for lower frequencies. This can be tested by comparing the arrival times of gravitational-wave signals with electromagnetic counterparts. In particular, Will [50] has computed the arrival time difference of two GWs emitted at times t_e and $t_e + \Delta t_e$ to be

$$\Delta t_a = (1+z)\left[\Delta t_e + \frac{D(z)}{2\lambda_g^2}\left(\frac{1}{f_e^2} - \frac{1}{f_e'^2}\right)\right], \tag{4.16}$$

where t_a and $t_a + \Delta t_a$ are the corresponding arrival times, z is the redshift, f_e, f_e' are the frequencies of the first and the second wave and $D(z)$ is the cosmological distance

$$D(z) = \frac{1+z}{H_0} \int_0^z \frac{\mathrm{d}z'}{(1+z'^2)\sqrt{\Omega_M (1+z')^3 + \Omega_\Lambda}}, \tag{4.17}$$

which should not be confused with the luminosity distance introduced in Eq. (3.1). As for the gravitational-wave signal from a compact binary chirp (as depicted in Fig. 3.2) the emitted frequencies increase monotonically with time, high-frequency wave trains travel faster than low-frequency wave-trains in massive gravity, what has the effect of squeezing the chirp together. Will [50] accounted for this by evaluating the SPA phase (3.28) with the different arrival times from (4.16). This amounts to a (leading order) modification of the 1PN GW phase coefficient of

$$\tilde{h} = \tilde{h}_{\mathrm{GR}}\, e^{-i\beta_{\mathrm{MG}} u^{-1}}, \tag{4.18}$$

with the massive gravity parameter

$$\beta_{\mathrm{MG}} = \frac{\pi^2 D(z) \mathscr{M}}{\lambda_g^2 (1+z)}. \tag{4.19}$$

It is therefore possible to extract effects originating from massive gravity only from detector data, without considering timing differences between gravitational waves and electromagnetic counterparts. However, as emphasised in Section 4.5, effects arising from a large set of different alternative theories or other systematic biases could also manifest in the 1PN phase coefficient, making the observation of electromagnetic counterparts an essential part of the investigation of massive gravity.

The Compton wavelength of the graviton has been bounded by solar system tests to $\lambda_g > 2.8 \times 10^{17}$ cm [51]; binary pulsar observations provide a more stringent bound of $\lambda_g > 1.5 \times 10^{19}$ cm [52]. Various studies have been published that compute bounds that can be achieved by space- or ground-based detectors [1, 50, 53, 54, 54–58]. For SMBH binaries, classic LISA is typically able to place a bound of $\lambda_g > (1-40) \times 10^{21}$cm [34], depending on whether spins, eccentricity, full inspiral-merger-ringdown, etc. are included and what algorithms are used for parameter error estimation.

4.4.2 Lorentz violation

Using a similar approach, one can incorporate Lorentz violation phenomenologically into GR waveforms. In special relativity, $m^2c^2 = p_\alpha p^\alpha$ ($m = 0$ for light) is a Lorentz invariant quantity. If this invariance is violated, additional terms will enter the dispersion relation $E^2 = m^2c^4 + p^2c^2$, where m is the potential mass of the graviton (in GR, $m = 0$). Mirshekari et al. [59] account for Lorentz violation by introducing an additional term to the dispersion relation:

$$E^2 = m^2c^4 + p^2c^2 + \mathbb{A} p^\alpha c^\alpha, \tag{4.20}$$

where $\mathbb{A}, \alpha$ are real numbers and $\mathbb{A}$ has the dimension of $[\text{energy}]^{2-\alpha}$. They find that this introduces corrections to the GR waveform in terms of a phase correction,

$$\tilde{h} = \tilde{h}_{\mathrm{GR}} e^{-i\beta_{\mathrm{MG}} u^{-1} - \zeta_\alpha u^{\alpha-1}}, \tag{4.21}$$

where β_{MG} is the massive gravity parameter from Section 4.4.1 and

$$\zeta_\alpha = \begin{cases} \frac{\pi^{2-\alpha}}{1-\alpha} \frac{D_\alpha \mathbb{A}}{h^{2-\alpha}} \frac{\mathscr{M}^{1-\alpha}}{(1+z)^\alpha} & \alpha \neq 1, \\ \frac{\pi D_1 \mathbb{A}}{h} & \alpha = 1, \end{cases} \tag{4.22}$$

with Plank's constant h and the generalised distance parameter

$$D_\alpha = \frac{(1+z)^{1-\alpha}}{H_0}\int_0^z \frac{(1+z')^{\alpha-2}}{\sqrt{\Omega_M(1+z')^3+\Omega_\Lambda}}\,\mathrm{d}z'. \tag{4.23}$$

Among modified-action theories that allow for Lorentz violation, one can find extra-dimensional theories [60], Hořava-Lifshitz gravity [61] and theories with non-commutative geometry [62]. Violations of Lorentz invariance are commonly found in loop quantum gravity and string theory where, however, the phase corrections are predicted to be of 5.5 or 7 PN order, what is difficult to test considering the fact that the PN expansion of GR is currently only known to 3.5PN.

4.4.3 Variable G(t) theories

Certain alternative theories predict a varying gravitational constant. For example in scalar-tensor theories, G is promoted to a function $G(\phi)$ which is time and position dependent (and thus violates local position invariance). If instead of being a constant, G was a function $G(t,x,y,z)$ depending on when and where a gravitational interaction takes place, GW emission would be modified. As a simple example, one can impose [63]

$$G(t,x,y,z) = G_c + \dot{G}_c\,(t_c - t), \tag{4.24}$$

where G_c and $\dot{G}_c$ are evaluated at the four-vector of the event of coalescence. Most probably, the time dependence would be more complicated, but this serves nevertheless as a first approximation and provides a nice toy example that illustrates the effect of a variable gravitational constant. As a consequence of the promotion of $G \to G_c + \dot{G}_c\,(t_c - t)$ in the orbital frequency evolution of GR, there arises the modification [63]

$$\dot{F} = \dot{F}_{\mathrm{GR}}\left[1 + \frac{65}{768}\dot{G}_c\mathscr{M}\,u^{-8/3}\right]. \tag{4.25}$$

This corresponds at leading order to a '−4PN' correction to the GR frequency frequency evolution and can be inverted to find $t(F)$ and hence the phase and amplitude of the stationary phase approximation. This implies an SPA waveform that is at leading order corrected to

$$\tilde{h}(f) = \tilde{h}_{\mathrm{GR}}(f)\left(1 - \frac{5}{512}\dot{G}_c\mathscr{M}\,u^{-8/3}\right)e^{-i\frac{25}{65536}\dot{G}_c\mathscr{M}\,u^{-13/3}}. \tag{4.26}$$

Measuring the variation of the gravitational constant with different sources at different redshifts would allow us to construct a constraint map that shows the bounds on $\dot{G}/G$ as a function of redshift.

4.5 Testing the post-Newtonian coefficients of GR

Let us summarise the impact of a theory that differs from GR on gravitational waves from compact binaries as we see them in the detector: the orbital evolution can be modified, maximum four additional polarisations can be brought into existence and the speed of gravitational waves can be frequency dependent. Except for the presence of alternative polarisation modes (where we refer the interested reader to [64, 65]), such effects can be tested through deformations of the PN coefficients of existing GR waveform templates that we are going to introduce in the following subsection.

4.5.1 Deformed GR templates

If the orbital evolution of compact binaries is different from GR, then this means that the orbital frequency and phase evolution have a different PN expansion, as established in Section 4.4. Particularly, the alternative theories and features introduced there yield leading order corrections to the PN expansion of the GW phase and amplitude. In the light of these findings, Yunes and Pretorius [35] devised the so called *parameterized post-Einsteinian (ppE) scheme*. There, waveform templates mimicking deformations to the PN coefficients of GR are introduced that can account for particular alternative theories. The simplest ppE waveform incorporates only leading order modifications and is given as a deformation of the $l = 2$ harmonic of the GR waveform in Fourier space as

$$\tilde{h}(f) = \tilde{h}_{\mathrm{GR}}(f)\,(1 + \alpha u^a)\, e^{i\beta u^b}, \tag{4.27}$$

where the ppE parameters (a, α, b, β) are real numbers and u is the reduced frequency. There are extensions to the ppE scheme for alternative polarisations [65] and full inspiral-merger-ringdown waveforms [35, 56, 66]. For the inclusion of higher orders, one can consider

$$\tilde{h}(f) = \tilde{h}_{\mathrm{GR}}(f) \left(1 + \sum_i \alpha_i u^{a_i}\right) e^{i \sum_k [\beta_k + \gamma_k \log u] u^{b_k}}, \tag{4.28}$$

with a broad choice of different ppE parameters and logarithmic terms in the phase. However, Sampson et al. [66] have shown that leading order corrections are already enough for discriminating GR from any competing theory through the use of Bayesian model selection with presently discussed detectors. The ppE framework is motivated from the observed fact that the metric theories and features considered in Sections 4.3 and 4.4 at leading order all lead to a deformation in the form of (4.27). Various studies exist that asses the prediction capabilities of the ppE scheme using advanced computational methods [66–69]. They find bounds that can be placed on the parameters (a, α, b, β) using Advanced LIGO or LISA that will allow to constrain the zoo of alternatives in the same way as the ppN scheme did. Moreover, Chatziioannou et al. [65] provide arguments that a and b are integer multiples of $1/3$ with $(a, b) > (-10/3, -15/3)$.

The four additional parameters (a, α, b, β) introduced by a simple ppE template can be treated in the same way as the binary parameters. The resulting parametrically deformed GR template can then be used together with data analysis algorithms to check whether it shows a higher overlap with the given detector data than an ordinary GR template. To this end it has to be made sure that the template does not just provide a better fit to the noise. Tools to perform model selection with modified waveforms are introduced in Chapter 6.

The ppE framework was preceded by a study by Arun, Qusailah and Sathyaprakash [70, 71], who changed the hitherto existing viewpoint of gravitational astronomy and took the PN coefficients of the SPA phase themselves as the parameters to be measured (Note: effects manifesting in the GW phase can be measured to a far better extent than amplitude effects). Considering only terms up to 2PN, the GW phase is in terms of the GW frequency f:

$$\Psi(f) = 2\pi f\, t_c - 2\Phi_c - \frac{\pi}{4} + \sum_{i=0}^{i=4} \psi_i\, f^{(i-5)/3}. \tag{4.29}$$

For higher PN orders, also terms logarithmic in f will enter the phase. For quasi-circular, non-spinning compact binaries, the ψ_i depend only on M and η. The first coefficient ψ_0 is proportional to $M^{-5/3}\eta^{-1}$ or in terms of the chirp mass to $\mathscr{M}^{5/3}$. Thus by using a leading PN order template, one can infer the chirp mass up to some error but not the total mass and the symmetric mass ratio individually. As the individual masses m_1 and m_2 are related to (M, η) by the relation $m_{1,2} = \frac{M}{2}(1 \pm \sqrt{1 - 4\eta})$, this means that

they are still totally correlated. This correlation can be broken by including the 1PN coefficient ψ_1 (the 0.5PN coefficient is zero for GR and leads only to something interesting if GR is wrong) which consists of a sum of two terms proportional to M^{-1} and $(M\eta)^{-1}$, respectively. This breaks the degeneracy between m_1 and m_2 and allows us to measure the individual masses apart from some errors. This procedure can be repeated for any possible combination of ψ_i and ψ_j, leading to different, individual estimates for m_1 and m_2 with corresponding error bars. Now, as a null test of GR, one demands that all individual measurements (m_1, m_2) lie within the error bars of all other combinations. If this is violated, then GR seems to have problems providing a waveform that is fit to describe the data in the detector. Arun et al. [71] find that the coefficients ψ_i can all be measured to a few percent at a redshift of $z = 1$; it is however unclear how much accuracy is needed, as it remains unknown as to what strength non-GR corrections should enter. One could in principle perform such a null test for every phase correction predicted by alternative theories in Sections 4.3 and 4.4, but the ppE scheme provides a much simpler test when combined with the concepts of Bayesian inference introduced in Section 6.4.

4.5.2 Fundamental questions

Having established models that account for the imprints of alternative theories on gravitational waves, different questions should be addressed [35]:

1. **Before the first detection:**
   (a) **The underlying theory is non-GR, GR templates are used:**
   To what extent can the signals still be detected, albeit with wrong templates? When are the biases that are introduced to the estimated binary parameters significant?
   (b) **The underlying theory is GR, ppE templates are used:**
   How well can the ppE parameters be measured, i.e. what is their error distribution around zero, and therefore how well can alternative theories be constrained? Since more parameters are introduced while the amount of information stays the same, what additional degeneracies are created among the parameters? Is there a way to break these correlations?
   (c) **The underlying theory is non-GR, ppE templates are used:**
   Given data from a particular underlying alternative theory, are we able to identify it using ppE templates? This question is at the given moment not as urgent as (a) and (b), as we do not have evidence for a failure of GR and do not expect that our currently discussed detectors will be fit for such a task.

2. **After the first detection:**
   (a) Given measured detector data, what are the betting odds for GR against any other theory? In other words, what are the betting odds that the PN coefficients of GR fit the data best?

4.5.3 Other effects than can modify the PN coefficients

In the previous sections we have established that a way to verify GR is to check whether its theoretically predicted PN expansion leads to waveforms that fit better with the measured detector data than for any other competing theory. However, what we see in our data can also be modified by other effects of either purely physical (astrophysical or instrumental) or theoretical nature (mismodelling) [34, 68].

During the generation of GWs, *astrophysical effects* can play a role: third bodies, accretion disks or other sources of matter or energy can 'pollute' the gravitational waveform, making it appear as if there was an

alternative theory of gravity at work. Although it has been shown that such effects are negligible on the time scale of the detector [16], they can always be removed by cross-correlating data from multiple sources to find what is individual 'astrophysical noise' and what particular effects are present for all the different sources. If one considers only quasi-circular, non-spinning orbits, then also spin-precession and eccentricity pose astrophysical systematics that alter the observed PN evolution.

Most certainly, the noise levels in ground and space-based GW detectors will neither be stationary nor follow a Gaussian probability distribution, as introduced as an idealisation in Section 5.3. Especially time-dependent noise could make parameter estimation much more difficult. Our lack of knowledge of the detector transfer function impacts which proposed template (GR or non-GR) reaches the best fit with the detector data and is therefore favoured. Also possibly some ununderstood instrumental glitches could mimic the presence of an alternative theory. Although such *instrumental effects* can in principle pose severe problems for tests of GR [72], they can be cured to a certain level by cross-correlating data from multiple detectors.

The third systematic, *mismodelling*, cannot be cured by cross-correlating data from different sources or detectors. Since we lack an exact solution of Einstein's equations and are only left with approximations thereof, there is always a possibility that Einstein's theory is correct but our models are wrong. In our case, we have to deal with the PN expansion for compact binary inspirals. The PN expansion has been shown to converge only slowly [73, 74], it is unclear how large the error introduced by truncating the true waveform is in reality. Moreover, it is hard to say what truncation order is sufficient for detection, as we have never dealt with real detector data. Many studies have adopted the convention of evolving black hole binaries up to the last stable orbit which is $R = 6\,GM/c^2$ in the case of a quasi-circular, non-spinning inspiral. It is however unclear, whether the PN expansion is sufficiently valid in this region. Even more complications regarding this problem arise when one considers spin-precession and eccentricity. Choosing the wrong point to stop the integration can bias the results [1]. Usually, only the dominant $l = 2, m = \pm 2$ quadrupole mode of the GW tensor field is considered; however, sub-dominant modes can alter the results significantly in some cases, especially for high masses [75] and lead to a mismodelled signal that could be misinterpreted as an effect coming from an alternative theory. Moreover, different ways of truncating the PN expressions have been introduced already in the time domain regime (Taylor T1-T4, Padé resummations, etc. [24]) which all yield different evolutions toward the last circular orbit; it is unclear which truncation is most appropriate. Due to the presence of the aforementioned potential sources for theoretical errors, thus, in order to avoid mismodelling, a lot of work will have to be invested into the analytic expansions of the Einstein equations. Especially comparisons of the PN expansion with numerical relativity have to be extended for a better understanding for when the PN approximation is supposed to have failed. Such investigations are particularly necessary for compact binaries with non-negligible spins, since there the resulting orbits can be much more complex. Also the failure of the fitting algorithm can pose mismodelling, e.g. if the MCMC algorithm (see Section 6.5) settles on a local but not global maximum.

Being aware of the above caveats, we assume for the rest of this work that they can be treated, i.e. if a template with PN coefficients that are different from the one in GR fits the data better, then we assume that this could be because GR is not the correct theory.

Our approach to testing GR has thus evolved from a theoretical perspective, by testing specific more or less well-defined features (Section 4.3), to tests of generic features that should not be present in GR (Section 4.4) and finally to a data analysis perspective by checking whether each PN coefficient matches the predictions by GR or whether there is a model consisting of a set of different PN coefficients that fits the data better. This allows us to test GR through only the possession of the detector data and the PN coefficients of GR, but without any specific information about possible alternative theories; in other words, we "remain agnostic as to which is the correct theory of Nature " [34]. If there is a set of PN coefficients that describes the data better than GR in a consistent way, we take this set to be our new model and check with the zoo of alternatives which theory matches best with this model: We let the data choose the correct theory.

Chapter 5

LISA-Like Detectors

The journey of the experimental detection of GWs started in the 1960s with *resonant-mass* detectors (or also called *bar* detectors). Such detectors consist of a material with piezo-electric properties that, under the strain of a passing GW, should give a measurable electrical potential difference. Although resonant-mass detectors are subject to strong noise and can observe only a very narrow band of frequencies, Joseph Weber claimed a detection in 1967, which was totally unrealistic and could never be reproduced but boosted experimental and theoretical research in the area of gravitational wave science significantly. In the 1970s, the use of *laser interferometers* was promoted and culminated in the foundation of the ground-based *Laser Interferometer Gravitational-wave Observatory* (LIGO). The simplest version of a laser interferometer consists of an input laser beam that is splitted into two perpendicular arms through the use of a semipermeable mirror. At the intended end of the laser arms, mirrors are positioned such that both beams are reflected and interfere at a photo detector back at the origin. If a GW passes through the detector, the photons in the two individual arms experience different travel times and arrive with different phases at the point of interference. The phase difference can be measured by a *phase meter* and, if we forget about noise for the moment, gives us information about the phasing of the gravitational wave. The delay of the photon travel time can also be seen as a fractional length change $h \sim \frac{\Delta L}{L}$ of the laser arms, where L is a typical arm length of the detector and h is the gravitational wave strain. The quantity h is a combination of the plus and the cross polarisation of the wave which depends on the orientation of the detector with respect to the propagation direction of the GW.

A unique way to observe events with frequencies around a few mHz is a space-based laser interferometer that is equipped with laser arms in the gigameter regime. The mHz frequency band is expected to be populated with the strongest existing GW sources: supermassive black hole binaries. A particular concept for such a detector that has been put forward is the *evolving Laser Interferometer Space Antenna* (eLISA). The European Space Agency (ESA) has recently selected the theme "The Gravitational Universe" for the ESA Cosmic Vision L3 mission to be launched in 2034 in order to promote a space-based GW detector. eLISA is a streamlined version of the classic LISA detector that fell out of NASA's space programme due to budget cuts in 2010. Both detectors share the concept of a drag-free constellation of three satellites that form a triangle and follow the Earth $10-20^\circ$ behind its orbit around the Sun (Fig. 5.1). The plane formed by the triangle is always tilted by 60° relative to the orbital plane. Each satellite contains a freely-falling test-mass that is shielded against solar radiation and magnetic fields by a disturbance reduction system (DRS) and is ensured to stay freely floating by a gravitational reference sensor (GRS) that adjusts the satellite's position through micro-Newton thrusters. In the following, we do without a detailed technical description, as the implementation is most certainly going to change again over the coming years (see [76–79] for technical details of particular mission proposals). Let us refer to this prototype concept of a space-based detector, without any specification of the number of arms or of their length, as a *LISA-like* detector. The

former NASA mission which we shall call *classic LISA* [79] was designed to have three arms (6 links) with a length of 5×10^6 km each, while *eLISA* [76, 77] (sometimes also referred to as 'New Gravitational-wave Observatory' (NGO)) is the mission that has been proposed to ESA by the European community, with only two arms (4 links) with lengths of 10^6 km each. A typical LISA-like detector is sensitive to frequencies between $\sim 10^{-5} - 1$ Hz.

Because laser frequency noise exceeds the GW signal and other noise sources excessively, plain arm length changes that are measured by the detector cannot be directly used for gravitational wave astronomy. Instead, one forms so-called *TDI* (Time-Delay Interferometry) observables [80–83]: linear combinations of the detector data of the individual arms where the time delays due to the different arrival times of the gravitational wave are accounted for. The simplest TDI observables are the *unequal-arm Michelson* observables X for a two-arm detector or X, Y, Z for a three-arm detector. Additionally, a three-arm detector allows to form TDI observables that have uncorrelated noise, in particular [84],

$$A = X, \qquad E = \frac{1}{\sqrt{3}}(X + 2Y) \tag{5.1}$$

is such a combination.

5.1 Different coordinate systems

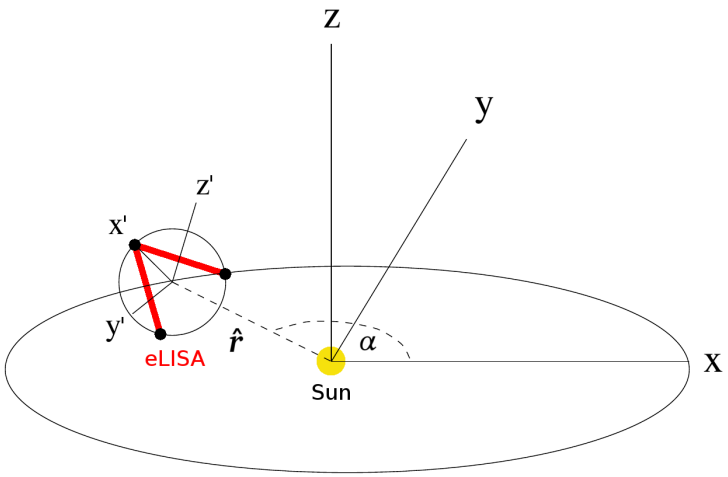

Figure 5.1: *The two different coordinate systems that are used in the context of gravitational wave astronomy. The barycentric frame is fixed with respect to the distant stars, with the Sun at its center, while the detector frame rotates around the Sun and around its own z-axis.*[1]

In order to describe the positions of sources in the sky, a *barycentric* coordinate system (x, y, z) with the Sun at its center that is tied to the fixed distant stars is most suitable. However, the detector measures gravitational waves in its own system (x', y', z') tied to the laser arm triangle that, since the triangle rotates around the Sun and around itself, follows a complicated motion in terms of barycentric coordinates (Fig. 5.1). To justify the use of the barycentric frame, let us thus establish a relation between the two frames. The detector's motion is in terms of an azimuthal and a polar angle by

$$\Theta = \frac{\pi}{2}, \qquad \alpha(t) = \alpha_0 + 2\pi\frac{t}{T}, \tag{5.2}$$

[1] Figure prototype adapted from C. Cutler [84]

where α_0 is the initial value of the orbital phase angle $\alpha(t)$ and T is the orbital period of one year. The unit vector pointing from the Sun to the detector is thus

$$\hat{\boldsymbol{r}} = \hat{\boldsymbol{x}}\cos\alpha(t) + \hat{\boldsymbol{y}}\sin\alpha(t). \tag{5.3}$$

As the $\hat{\boldsymbol{z}}'$ unit vector of the detector frame has always an angle of 60° (or $\frac{\pi}{3}$) with respect to $\hat{\boldsymbol{z}}$ and is inclined towards the Sun, it can be expressed as

$$\hat{\boldsymbol{z}}' = \cos\left(\frac{\pi}{2}+\frac{\pi}{3}\right)\hat{\boldsymbol{r}} + \sin\left(\frac{\pi}{2}+\frac{\pi}{3}\right)\hat{\boldsymbol{z}} = \frac{1}{2}\hat{\boldsymbol{z}} - \frac{\sqrt{3}}{2}\left[\hat{\boldsymbol{x}}\cos\alpha(t) + \hat{\boldsymbol{y}}\sin\alpha(t)\right]. \tag{5.4}$$

The choice of $\hat{\boldsymbol{x}}'(\hat{\boldsymbol{x}},\hat{\boldsymbol{y}},\hat{\boldsymbol{z}})$ and $\hat{\boldsymbol{y}}'(\hat{\boldsymbol{x}},\hat{\boldsymbol{y}},\hat{\boldsymbol{z}})$ can be arbitrary as long as $\hat{\boldsymbol{x}}'$ and $\hat{\boldsymbol{y}}'$ form a positive oriented system with $\hat{\boldsymbol{z}}'$ that rotates around $\hat{\boldsymbol{z}}'$ once per orbit. A possible choice is [31, 84]

$$\hat{\boldsymbol{x}}' = \left(\frac{3}{4} - \frac{1}{4}\cos 2\alpha(t)\right)\hat{\boldsymbol{x}} - \frac{1}{4}\sin 2\alpha(t)\,\hat{\boldsymbol{y}} + \frac{\sqrt{3}}{2}\cos\alpha(t)\,\hat{\boldsymbol{z}}, \tag{5.5}$$

$$\hat{\boldsymbol{y}}' = -\frac{1}{4}\sin 2\alpha(t)\,\hat{\boldsymbol{x}} + \left(\frac{3}{4} + \frac{1}{4}\cos 2\alpha(t)\right)\hat{\boldsymbol{y}} + \frac{\sqrt{3}}{2}\sin\alpha(t)\,\hat{\boldsymbol{z}}. \tag{5.6}$$

Having established such a relation, we will presume in the future that all detector data has already been transformed to the barycentric frame. To this end, let us establish a relation between the GW strains that are measured in the two frames. Depending on its orbital phase and the position of the source, the detector registers the GW before or after it reaches the barycenter. Assuming that the GW amplitude varies only slowly relative to the phase (adiabatic approximation) and that the finite size and rotational motion of the detector can be neglected for this particular treatment, the gravitational waveform at the barycenter can be found by moving the GW phase back or forth in time such that it matches the one in the detector. In terms of the 'barycentric time' t, this can be approximated by expressing the detector time ξ as

$$\xi(t) = t - \frac{R_\odot}{c}\sin\theta\cos(\alpha(t)-\phi), \tag{5.7}$$

where $R_\odot = 1\,\mathrm{AU}$ and (θ,ϕ) are the source angles in the sky. Consequently, if $h(t)$ is the waveform in the detector, then the corresponding waveform at the barycenter can be evaluated as $h[\xi(t)]$. In the SPA, this can be accounted for in a similar way by shifting the GW phase by $\Psi(f) \to \Psi(f) + \phi_D$, with

$$\phi_D = 2\pi f\frac{R_\odot}{c}\sin\theta\cos(\alpha(t)-\phi), \tag{5.8}$$

where f is the GW frequency.

5.2 Detector response and antenna patterns

A single detector channel of a LISA-like detector will give us a one-dimensional output: an electric signal $h_{\mathrm{out}}(t)$, the so-called *response function*. The GWs that reach the detector, however, come as a metric perturbation tensor $h_{ij}^{\mathrm{TT}}(t)$. In the following, let us summarise how one can relate these two quantities.

The induced relative length change $h(t)$ of a detector arm can be computed by a projection of $h_{ij}^{\mathrm{TT}}(t)$ onto the detector arm which is essentially a function of source and detector orientation. In the so-called *low-frequency approximation* (LFA) [82, 85], this can be achieved with a linear combination of the waveform

polarisations $h_{+,\times}$, weighted with the *antenna pattern functions* $F_k^{+,\times}$ (for detector channel k) that depend on the orientation of the source in the sky:

$$h_k(t;\mathbf{\Theta}) = h_+[\xi(t);\mathbf{\Theta}]\, F_k^+(t;\psi,\theta,\phi) + h_\times[\xi(t);\mathbf{\Theta}]\, F_k^\times(t;\psi,\theta,\phi), \tag{5.9}$$

with [82, 86]

$$F_k^+(t;\psi,\theta,\phi) = \frac{1}{2}\Big[\cos(2\psi)\, D^+(t;\psi,\theta,\phi,\lambda_k) - \sin(2\psi)\, D^\times(t;\psi,\theta,\phi,\lambda_k)\Big], \tag{5.10}$$

$$F_k^\times(t;\psi,\theta,\phi) = \frac{1}{2}\Big[\sin(2\psi)\, D^+(t;\psi,\theta,\phi,\lambda_k) + \cos(2\psi)\, D^\times(t;\psi,\theta,\phi,\lambda_k)\Big], \tag{5.11}$$

where $\lambda_1 = 0$ and $\lambda_2 = \pi/4$, and the detector motion is taken into account by

$$\begin{aligned}
D^+(t;\psi,\theta,\phi,\lambda) = \frac{\sqrt{3}}{64}\Big[&-36\sin^2(\theta)\sin(2\alpha(t)-2\lambda) + (3+\cos(2\theta)) \\
&\times (\cos(2\phi)\{9\sin(2\lambda) - \sin(4\alpha(t)-2\lambda)\} + \sin(2\phi)\{\cos(4\alpha(t)-2\lambda) - 9\cos(2\lambda)\}) \\
&-4\sqrt{3}\sin(2\theta)(\sin(3\alpha(t)-2\lambda-\phi) - 3\sin(\alpha(t)-2\lambda+\phi))\Big], \\
D^\times(t;\psi,\theta,\phi,\lambda) = \frac{1}{16}\Big[&\sqrt{3}\cos(\theta)(9\cos(2\lambda-2\phi) - \cos(4\alpha(t)-2\lambda-2\phi)) \\
&-6\sin\theta\,(\cos(3\alpha(t)-2\lambda-\phi) + 3\cos(\alpha(t)-2\lambda+\phi))\Big].
\end{aligned} \tag{5.12}$$

For a detector with arm length L, the LFA is valid for GW frequencies below the so-called *transfer frequency* $f_* = c/(2\pi L)$. When generating waveforms, one has therefore to make sure that the GW frequency stays below f_*: depending on L, the LFA breaks down for binaries with total masses below $\sim 10^5 M_\odot$. In the static limit, i.e. when the motion the detector with respect to the source is neglected, the above equations reduce to

$$\begin{aligned}
F_1^+(\theta,\phi,\psi) &= \frac{\sqrt{3}}{2}\left[\frac{1}{2}\left(1+\cos^2(\theta)\right)\cos(2\phi)\cos(2\psi) - \cos(\theta)\sin(2\phi)\sin(2\psi)\right], \\
F_1^\times(\theta,\phi,\psi) &= F_1^+\left(\theta,\phi,\psi-\frac{\pi}{4}\right), \\
F_2^+(\theta,\phi,\psi) &= F_1^+\left(\theta,\phi-\frac{\pi}{4},\psi\right), \\
F_2^\times(\theta,\phi,\psi) &= F_1^+\left(\theta,\phi-\frac{\pi}{4},\psi-\frac{\pi}{4}\right).
\end{aligned} \tag{5.13}$$

The detector translates $h(t)$ to the response function $h_{\rm out}(t)$. Most definitely, the detector will not be equally sensitive to all frequencies and will obey a *transfer function* $T(f)$ with

$$\tilde{h}_{\rm out}(f) = T(f)\,\tilde{h}(f). \tag{5.14}$$

In GW astronomy, we assume that the effects of $T(f)$ have already been removed from the data by multiplying $\tilde{h}_{\rm out}(f)$ with $T^{-1}(f)$ [6].

5.3 Modelling detector noise

In an actual experimental detector setup, there will not only be the gravitational wave signal present, but also a multitude of noise sources. If one does not treat noise at least as thoroughly as the generation of gravitational waves in Chapter 3, it will be impossible to recover the desired signals. Therefore it is of crucial importance to characterise how detector noise affects GW astronomy. The actual signal in the detector will be the gravitational-wave strain $h(t)$ superposed with noise,

$$s(t) = h(t) + n(t), \tag{5.15}$$

where $n(t)$ is the noise stream. In GW astronomy, the noise is usually assumed to be *stationary* and *Gaussian*. We will follow this assumption but emphasise that in real detections, we should be ready to face the challenge of understanding non-stationary non-Gaussian noise. Since noise is a stochastic process, let us introduce the *ensemble average* (or expectation value) $\langle..\rangle$ that averages its argument for multiple samples taken subsequently from the data stream. In the following, let us also assume that $\langle n(t)\rangle = 0$.

The behaviour of noise can be investigated through the autocorrelation function

$$R(\tau) = \langle n(t+\tau)\, n(t)\rangle, \tag{5.16}$$

which can be expressed through its Fourier transform $\tilde{R}(f)$ as $R(\tau) = \int_{-\infty}^{\infty} \mathrm{d}f\, \tilde{R}(f)\, e^{-2\pi i f\tau}$. Since

$$R(0) = \langle n^2(t)\rangle = \int_{-\infty}^{\infty} \mathrm{d}f\, \tilde{R}(f) = \int \mathrm{d}f \int \mathrm{d}f'\, \langle \tilde{n}^*(f)\, \tilde{n}(f')\rangle\, e^{2\pi i (f-f')t}, \tag{5.17}$$

$\tilde{R}(f)$ can be identified with the power spectral density of the noise. In the following we use the *one-sided power spectral density* $S_n(f) = \frac{1}{2}\tilde{R}(f)$, such that $\langle n^2(t)\rangle = \int_0^{\infty} \mathrm{d}f\, S_n(f)$. Moreover, we are able to identify

$$\langle \tilde{n}^*(f)\, \tilde{n}(f')\rangle = \delta(f-f')\, \frac{1}{2} S_n(f). \tag{5.18}$$

It is crucial to know the exact form of the power spectral density $S_n(f)$ of the noise appearing in a LISA-like detector. For such a detector, there are two main types of noise:

- *Instrumental noise* is an umbrella term for all the noise sources in the detector, such as laser shot noise and uncertainties in the position and acceleration of the spacecraft.
- Since a LISA-like detector will only detect a certain number of sources that are significantly stronger than the general background, sources that are below the detection threshold blend in with the background and form a noise floor of unresolvable sources, so called *confusion noise*.

The resulting power spectral density will be the sum of the spectral densities of these two individual noise sources,

$$S_n(f) = S_n^{\mathrm{instr}}(f) + S_n^{\mathrm{conf}}(f). \tag{5.19}$$

Different models for the representation of instrumental [87, 88] and confusion noise [89, 90] can be used, particular ones are introduced in Chapters 7 and 8. For an extensive review on the characterisation of noise, the interested reader shall be referred to [91]. We will make use of the Gaussian quality of noise in Chapter 6.

Chapter 6

Gravitational Wave Astronomy

In this chapter we review the tools that serve to analyze the data collected by gravitational-wave detectors and that can provide estimates of how accurately we will be able to measure the underlying parameters of compact binary inspirals. As GWs can be buried deep in noise, which is often considerably larger than the actual signal itself, the most suitable instrument to recover GWs from compact binaries is *matched filtering*. Matched filtering (Section 6.1) is the process of cross correlating the detector data with a set of signal templates. A template that matches (to some extent) a GW signal present in the data will lead to a signal-to-noise ratio that is above a certain detection threshold. Using matched filtering has the consequence that one has to know a priori what potential signals could be in the data and needs to have a bank of templates ready or generate them on the fly, what requires an immense amount of computation for compact binary model templates with 9-17 free parameters. It is therefore crucial that data analysis algorithms remain highly accurate, but are made the fastest possible. In the following we review the frequentist and the Bayesian approach to gravitational wave astronomy that allow us both, albeit with different methods, to assess the parameter estimation capabilities of a LISA-like detector. As our interest lies mainly in how a LISA-like detector will perform in doing astronomy with GWs and no detector data with confirmed GW signals is presently available, we use the notion 'gravitational wave astronomy' here instead of the commonly used term 'data analysis'.

6.1 Matched filtering

As introduced before, matched filtering is the cross correlation of a signal $s(t) = h(t) + n(t)$ in the detector with a filter $f(t)$:

$$o(\tau) = \int_{-\infty}^{\infty} s(t) f(t-\tau)\,\mathrm{d}t, \tag{6.1}$$

where $o(\tau)$ denotes the overlap for a filter that is shifted by τ, $h(t)$ is the GW signal and $n(t)$ is the noise stream. For conciseness, let us assume that the integral boundaries are always between $-\infty$ and ∞ in the following. The best match for the filter $f(t)$ is where $o(\tau)$ has its maximum. Let us assume that this maximum has been found at $\tau = \tau_0$ and let then $F(t) \equiv f(t-\tau_0)$ such that

$$o = \int s(t) F(t)\,\mathrm{d}t. \tag{6.2}$$

Given a signal $s(t)$ and a template $h(t)$, how can we know if the filter has found something? To this end, let us define the *signal-to-noise ratio* (SNR) under the action of the filter $F(t)$. For the nominator (signal) which we denote as S, let us take the average over many realisations of o when a signal is present:

$$\begin{aligned} S = \langle o \rangle &= \int \mathrm{d}t \, \langle s(t) \rangle F(t) \overset{\langle n(t) \rangle = 0}{=} \int \mathrm{d}t \, h(t) F(t) = \int \mathrm{d}t \int \mathrm{d}f \int \mathrm{d}f' \, e^{2\pi i (f - f')t} \, \tilde{h}(f) \tilde{F}^*(f') \\ &= \int \mathrm{d}f \int \mathrm{d}f' \, \delta(f - f') \tilde{h}(f) \tilde{F}^*(f') = \int \mathrm{d}f \, \tilde{h}(f) \tilde{F}^*(f), \end{aligned} \tag{6.3}$$

where we chose to work in frequency space and have used $F(t) = F^*(t)$. Note that since $h(t)$ is deterministic and has only one realisation, $\langle h(t) \rangle = h(t)$. Since $\langle n(t) \rangle = 0$, let us compute the denominator N through the variance of o in the absence of a gravitational-wave signal:

$$\begin{aligned} N^2 = \left[\langle o^2 \rangle - \langle o \rangle^2 \right]_{h=0} &= \int \mathrm{d}t \int \mathrm{d}t' \, \langle n(t) \, n(t') \rangle \, F(t) \, F(t') \\ &= \int \mathrm{d}t \int \mathrm{d}t' \int \mathrm{d}f \int \mathrm{d}f' \, e^{2\pi f t} \, e^{-2\pi f' t'} \langle \tilde{n}^*(f) \, \tilde{n}(f') \rangle \, F(t) \, F(t') \\ &= \int \mathrm{d}f \, S_n(f) \, |\tilde{F}(t)|^2, \end{aligned} \tag{6.4}$$

where (5.18) has been used. In order to write the SNR in a well-arranged way, let us introduce the inner product of two functions $g(t)$ and $h(t)$ as

$$(g|h) \equiv 2 \int_0^\infty \frac{\tilde{g}^*(f) \tilde{h}(f) + \tilde{g}(f) \tilde{h}^*(f)}{S_n(f)} \, \mathrm{d}f = 4 \, \mathrm{Re} \int_0^\infty \frac{\tilde{g}^*(f) \tilde{h}(f)}{S_n(f)} \, \mathrm{d}f, \tag{6.5}$$

where $S_n(f)$ in the denominator makes sure that contributions from frequencies where the detector noise level is higher are counted less. Using the definition $\tilde{k}(f) = S_n(f) \tilde{F}(f)$ allows us to write the SNR as

$$\rho = \frac{S}{N} = \frac{(h|k)}{\sqrt{(k|k)}}. \tag{6.6}$$

The quantity ρ is maximised if $k \propto h$, what leads us to the *optimal filter* $\tilde{F}(f) = \frac{\tilde{h}(f)}{S_n(f)}$. Plugging this into Eq. (6.6), one gets the optimal SNR of a single detector channel

$$\rho_{\mathrm{opt}} = \frac{(h|k)}{\sqrt{(k|k)}} = \sqrt{(h|h)}, \tag{6.7}$$

that can be achieved given that the parameter set $\boldsymbol{\Theta}$ of the template h is perfectly known. To compute the SNR of arbitrary data $d(t)$, one can evaluate

$$\rho = \frac{(d|h)}{\sqrt{(h|h)}} = \rho_{\mathrm{opt}} + \frac{(n|h)}{\sqrt{(h|h)}}. \tag{6.8}$$

Because of the presence of noise, $\rho(\boldsymbol{\Theta})$ will be maximised for a different parameter set $\boldsymbol{\Theta}$ than $\rho_{\mathrm{opt}}(\boldsymbol{\Theta})$, depending on the strength of the noise. More in-depth discussions of matched filtering can be found in [6] and [91]. Matched filtering is the basic tool used by the parameter estimation methods introduced in the following sections.

6.2 Frequentist statistics and likelihood maximisation

The frequentist approach to statistics regards probability as a long-run occurrence frequency. Through the conduction of a set of experiments, multiple random samples can be taken from the underlying probability distribution. If the underlying probability distribution depends on a set of parameters, then these parameters are considered to be fixed quantities that remain constant during the experiments. It is simply because we can only sample noisy instances of the truth that the true parameters remain hidden from our eyes. However, a large number of experiments will remove this noise and allow us to estimate the underlying parameters.

As in a gravitational-wave experiment we do not possess the power to set the binary black holes back to their initial position after they have merged, it is impossible to conduct the same experiment with similar initial conditions even twice. This renders the frequentist approach questionable and in general one should prefer a Bayesian approach as introduced in the next section. However, one can draw estimates for the true underlying parameter set $\boldsymbol{\Theta}_t$ through maximisation of the *likelihood function*:

Assuming Gaussian detector noise, the probability for a particular noise realisation n_0 to appear in the detector is given by $p(n_0)$, where $p(n)$ is defined through the Gaussian distribution

$$p(n) = C\,\exp\left[-\frac{1}{2}(n|n)\right], \tag{6.9}$$

with C being a normalisation constant. Since $n = d - h$, it is possible to express the probability distribution for the data $d(t)$ to appear in the detector given the GW signal $h(t;\boldsymbol{\Theta})$ as

$$p(d|\boldsymbol{\Theta}) = C\,\exp\left[-\frac{1}{2}(d-h(\boldsymbol{\Theta})|d-h(\boldsymbol{\Theta}))\right]. \tag{6.10}$$

The parameter estimation methods that are introduced in this work (maximum likelihood, MCMC) do not require the knowledge of the normalisation constant; this is a very useful property, as it is in general very difficult to compute.

One can define the *reduced log-likelihood* (reduced because the normalisation constant in (6.10) is dropped)

$$L(\boldsymbol{\Theta}) = -\frac{1}{2}(d-h(\boldsymbol{\Theta})|d-h(\boldsymbol{\Theta})). \tag{6.11}$$

The *maximum likelihood* method [6, 91, 92] provides us with an estimator $\hat{\boldsymbol{\Theta}}_{\mathrm{ML}}$ for the true underlying parameter set $\boldsymbol{\Theta}_t$ that can be found through

$$\left.\frac{\partial L(\boldsymbol{\Theta})}{\partial \Theta^i}\right|_{\boldsymbol{\Theta}=\hat{\boldsymbol{\Theta}}_{\mathrm{ML}}} = 0. \tag{6.12}$$

As $(d|d)$ is independent of $\boldsymbol{\Theta}$, an alternative definition of the log-likelihood that simplifies the computation of $\hat{\boldsymbol{\Theta}}_{\mathrm{ML}}$ is $\tilde{L}(\boldsymbol{\Theta}) = (d|h) - \frac{1}{2}(h|h)$. The (time-averaged) expectation value of $\tilde{L}$ can then also be expressed in terms of the signal-to-noise ratio (6.7) as $\langle\tilde{L}(\boldsymbol{\Theta})\rangle = \frac{1}{2}\rho^2$. Given a certain value of the log-likelihood, the SNR can thus easily be recovered with $\rho = \sqrt{2\langle\tilde{L}(\boldsymbol{\Theta})\rangle}$.

Due to the presence of noise in the data, $\hat{\boldsymbol{\Theta}}_{\mathrm{ML}}$ will in general be different from $\boldsymbol{\Theta}_t$ and show errors of $\Delta\Theta^i = \Theta^i_{\mathrm{ML}} - \Theta^i_t$. In the limit of high SNR, however, we expect that $\Delta\Theta^i \ll 1$. This allows us to expand the waveform template to quadratic order as

$$h(\hat{\boldsymbol{\Theta}}_{\mathrm{ML}}) \approx h(\boldsymbol{\Theta}_t) + \left.\frac{\partial h}{\partial \Theta^k}\right|_{\boldsymbol{\Theta}=\boldsymbol{\Theta}_t} \Delta\Theta^k + \frac{1}{2}\left.\frac{\partial^2 h}{\partial\Theta^k\partial\Theta^l}\right|_{\boldsymbol{\Theta}=\boldsymbol{\Theta}_t} \Delta\Theta^k\Delta\Theta^l, \tag{6.13}$$

and hence the reduced log-likelihood can be expressed as

$$L(\hat{\mathbf{\Theta}}_{\rm ML}) \approx -\frac{1}{2}\left[(n|n) - 2\Delta\Theta^k(n|h_k) - \Delta\Theta^k\Delta\Theta^l(n|h_{kl}) + \Delta\Theta^k\Delta\Theta^l(h_k|h_l)\right], \tag{6.14}$$

where $n = d - h(\mathbf{\Theta}_t)$ and the definitions $h_k = \frac{\partial h}{\partial\Theta^k}\big|_{\mathbf{\Theta}=\mathbf{\Theta}_t}$ and $h_{kl} = \frac{\partial^2 h}{\partial\Theta^k\partial\Theta^l}\big|_{\mathbf{\Theta}=\mathbf{\Theta}_t}$ have been used. In order to get a clearer understanding of how the SNR enters the calculations, let us define $h(\mathbf{\Theta}) = \rho\,\bar{h}(\mathbf{\Theta})$ with the optimal SNR $\rho = \sqrt{(h(\mathbf{\Theta}_t)|h(\mathbf{\Theta}_t))}$. Eq. (6.12) can then be expressed to first order in $\Delta\mathbf{\Theta}$ as [92]

$$\Delta\Theta^k\,(\bar{h}_k|\bar{h}_l) - \frac{1}{\rho}\left[(n|\bar{h}_l) + 2\Delta\Theta^k(n|\bar{h}_{kl})\right] = 0. \tag{6.15}$$

In the limit of large SNR, we expect the first term in the square brackets in Eq. (6.15) to dominate over the second one, leaving us with the error on the maximum likelihood estimator in the *linearised signal approximation*,

$$\Delta\Theta^k = \frac{1}{\rho}(\bar{h}_k|\bar{h}_l)^{-1}\,(n|\bar{h}_l). \tag{6.16}$$

The corresponding covariance matrix is then

$$\Sigma_{ij} = \langle\Delta\Theta^i\Delta\Theta^j\rangle = \frac{1}{\rho^2}(\bar{h}_i|\bar{h}_k)^{-1}\,\langle(n|\bar{h}_k)(n|\bar{h}_l)\rangle\,(\bar{h}_j|\bar{h}_l)^{-1} = \frac{1}{\rho^2}(\bar{h}_i|\bar{h}_j)^{-1} = \Gamma^{-1}_{ij}, \tag{6.17}$$

where it has been used that $\langle(g|n)\,(n|h)\rangle = (g|h)$ and

$$\Gamma_{ij} = \left(\frac{\partial h}{\partial\Theta^i}\middle|\frac{\partial h}{\partial\Theta^j}\right) \tag{6.18}$$

is the so called *Fisher information matrix* (FIM). In the limit of large SNR, the 1σ errors and the correlations among the parameters can therefore be estimated as

$$\Delta\Theta_i = \sqrt{\Gamma^{-1}_{ii}}, \quad C_{ij} = \frac{\Gamma^{-1}_{ij}}{\sqrt{\Gamma^{-1}_{ii}\Gamma^{-1}_{jj}}}, \tag{6.19}$$

respectively, with $C_{ij} \in [-1, 1]$. This goes together with a Gaussian approximation of the likelihood surface, as $L(\hat{\mathbf{\Theta}}_{\rm ML})$ is in the approximation considered above

$$\begin{aligned} L(\hat{\mathbf{\Theta}}_{\rm ML}) &\approx L(\mathbf{\Theta}_t) + \frac{\partial L}{\partial\Theta^i}\bigg|_{\mathbf{\Theta}=\mathbf{\Theta}_t}\Delta\Theta^i + \frac{1}{2}\frac{\partial^2 L}{\partial\Theta^i\partial\Theta^j}\bigg|_{\mathbf{\Theta}=\mathbf{\Theta}_t}\Delta\Theta^i\Delta\Theta^j \\ &\approx L(\mathbf{\Theta}_t) + \rho\,(n|\bar{h}_i)\,\Delta\Theta^i - \frac{1}{2}\rho^2\,(\bar{h}_i|\bar{h}_j)\,\Delta\Theta^i\Delta\Theta^j, \end{aligned} \tag{6.20}$$

what corresponds to

$$p(\Delta\mathbf{\Theta}) \propto \exp\left[-\frac{1}{2}\Gamma_{ij}\,\Delta\Theta^i\Delta\Theta^j\right]. \tag{6.21}$$

In the case of multiple detector channels, the resulting Fisher matrix is the sum of the ones for the individual detectors, $\Gamma_{ij} = \sum_k \Gamma^{(k)}_{ij}$.

The FIM is widely used in parameter estimation studies to assess the measurement accuracy of GW detectors. As it requires only the derivatives of the considered waveform model and no realistic simulation of noise, it can be computed very cheaply. However, the FIM suffers a couple of issues that should be handled with caution: For many considered sources, the limit of large SNR is not fulfilled. It is also quite unclear how large the SNR will have to be such that the assumption $\Delta\Theta^i \ll 1$ is justified. If the limit of large SNR is not reached, then the FIM might be a bad approximation of the covariance matrix. Consequently, errors found in parameter estimation studies may be under- or overestimated. Moreover, by apparent degeneracies in the parameter space of gravitational waves generated by black hole binaries, the FIM can often be ill-conditioned, making it very difficult to invert it numerically and harbouring potential errors [92]. Rodriguez et al. [93] found in the context of ground-based detectors that the FIM can greatly overestimate the errors (up to three orders of magnitude), even for considerably high SNR, leading to an underestimation of the science capabilities of GW detectors. Cornish and Porter [94] found that, for a classic LISA detector, the FIM overestimates the errors even for sources with an SNR as high as 450 by about a factor of two. They put this effect down to the fact that the FIM is unable to cope with the high correlations among the parameters.

It has to be emphasised again that the FIM is a frequentist tool, i.e. it considers the true underlying parameter set $\boldsymbol{\Theta}_t$ as fixed and treats the data as a random process. The FIM is not able to take prior information on the parameter set into account and provides no notion of how likely it is that a certain parameter set $\boldsymbol{\Theta}$ describes the measured data best; for such statements one has to resort to Bayesian techniques.

6.3 The Bayesian approach to parameter estimation

> *"A frequentist is a person whose long-run ambition is to be wrong 5% of the time. A Bayesian is one who, vaguely expecting a horse, and catching a glimpse of a donkey, strongly believes that he has seen a mule. "* — *Karl Pearson*

As mentioned before, frequentist statistics may not be the optimal tool for GW astronomy, as here we deal with single experiments that are non-repeatable and we may have prior information on the probability distribution at hand from previous astrophysical observations. In real life, we will ask ourselves how likely it is that a particular parameter set is the true one in the light of the detector data d. Frequentist statistics is by design not able to answer such questions.

The heart of Bayesian statistics is *Bayes' theorem*:

$$p(A|B) = \frac{p(B|A)\,p(A)}{p(B)}, \tag{6.22}$$

where A, B are two events and $p(A|B)$ is the conditional probability for A to take place given that B has already occurred. Taking for A the hypothesis that the set $\boldsymbol{\Theta}$ describes the parameters of the source best and for B the event that the particular data set d appears in the detector, we can write in terms of Bayes' theorem:

$$p(\boldsymbol{\Theta}|d) = \frac{p(d|\boldsymbol{\Theta})\,p(\boldsymbol{\Theta})}{p(d)}. \tag{6.23}$$

Here, $p(\boldsymbol{\Theta})$ is the *prior probability* for $\boldsymbol{\Theta}$ to be the true parameter set, i.e. what is known about $\boldsymbol{\Theta}$ before the experiment. In GW astronomy, these could e.g. be priors on the mass or distance distribution of black holes through astronomical observations. $p(d|\boldsymbol{\Theta})$ is the *likelihood* introduced in Eq. (6.10) and the quantity

$p(d) = \int \mathrm{d}\boldsymbol{\Theta}\, p(d|\boldsymbol{\Theta})$ is the so-called *evidence*, marginalised over all possible values of $\boldsymbol{\Theta}$. As before, $p(d)$ is just a normalisation constant that is not important for the tools we are going to use. The resulting distribution $p(\boldsymbol{\Theta}|d)$ is the *posterior probability* after considering the prior and the likelihood. $p(\boldsymbol{\Theta}|d)$ can be understood as the probability that $\boldsymbol{\Theta}$ gives the correct description of the measured data. In Bayesian statistics, the notion of probability is not that of an observed frequency but rather that of the possibility that an event is going to take place given also subjective expectations. In subsequent measurements, what has been the posterior before is promoted to the prior and a new posterior is gained with the new data.

Once the likelihood and the prior are defined, the posterior distribution can be explored with methods such as Markov Chain Monte Carlo, as introduced below. This is not an easy task, since $\boldsymbol{\Theta}$ can have from 9 to 17 dimensions in GR. In Bayesian statistics, one trades the intuitive notion of probability that is much closer to the human perception of reality for the fact that posterior probabilities are very expensive to compute.

To summarise, Bayesian statistics views the data as fixed and the underlying parameters as variable while frequentist statistics assumes that the underlying parameters are fixed and various experiments with a random component can be conducted. As Bayesian statistics requires a prior that shows the subjective expectation of an individual, different priors will lead to different posteriors. Hence it would be useful to check the robustness of acquired results by imposing different priors. It has to be emphasised that also a flat prior is a subjective prior.

The Bayesian viewpoint is more natural and intuitive than the frequentist viewpoint for GW astronomy. Yet it has been only recently that people started to incorporate Bayesian tools such as Markov Chain Monte Carlo algorithms, as we are just entering an era where computers and algorithms are getting fast enough to allow us to compute the desired probabilities in a reasonable time frame.

6.4 Bayesian inference for tests of GR

In Chapter 4 we introduced different alternatives to GR that are to date not ruled out using pulsar and solar system tests. Given some detector data d, how can we know if GR (and hence the waveform model in Section 3.3) is the true underlying theory? Might it be that an alternative to it, giving rise to a modified waveform model, provides a better answer? In other words: What theory fits the data best while keeping the number of possible parameters to a minimum? A good answer to this problem can be provided by Bayesian inference. Although the methods mentioned in this section have not been used in the studies conducted for this thesis, for future reference, let us give a brief review of how one can test hypotheses with Bayesian inference, with emphasis on alternative theories. More in-depth reviews can be found in [66, 67, 95].

Let us consider two different hypotheses in the following:

- $\mathscr{H}_{\mathrm{GR}}$: GR is the true underlying theory and the GW signal is described with the waveform model $h_{\mathrm{GR}}(\boldsymbol{\Theta})$ from Section 3.3.
- $\mathscr{H}_{\mathrm{NGR}}$: Any parametrized deviation from GR is a better fundamental theory of gravity, implying a modified waveform model $h_{\mathrm{NGR}}(\boldsymbol{\Theta}, \boldsymbol{\lambda})$, where $\boldsymbol{\lambda}$ is a set of additional theory parameters.

In the remainder of this section, for simplicity, we will always use the vector $\boldsymbol{\Theta}$ for the parameter set of the waveform model, regardless whether $\boldsymbol{\Theta}$ consists just of binary system parameters (GR) or contains also additional theory parameters (NGR).

Let us come back to the central question of this section: Given some detector data d, which of the above hypotheses is in favour and describes the data better?

As in Section 6.3 we start with Bayes' theorem:

$$p(\mathcal{H}_i|d) = \frac{p(d|\mathcal{H}_i)\,p(\mathcal{H}_i)}{p(d)}. \tag{6.24}$$

Here, the posterior $p(\mathcal{H}_i|d)$, the probability that $\mathcal{H}_i$ is the true hypothesis describing the data, can be computed through the evaluation of the likelihood $p(d|\mathcal{H}_i)$, the prior $p(\mathcal{H}_i)$ that can be placed on the hypothesis and the evidence $p(d) = \sum_i p(d|\mathcal{H}_i)\,p(\mathcal{H}_i)$ that takes again only the role of a normalisation constant. The likelihood is marginalised over the binary and theory parameters:

$$p(d|\mathcal{H}_i) = \int \mathrm{d}\mathbf{\Theta}\, p(d|\mathbf{\Theta}, \mathcal{H}_i)\, p(\mathbf{\Theta}|\mathcal{H}_i), \tag{6.25}$$

where $p(\mathbf{\Theta}|\mathcal{H}_i)$ are the priors that can be placed on the parameters in the specific case of where hypothesis $\mathcal{H}_i$ is assumed to be true. $p(d|\mathbf{\Theta}, \mathcal{H}_i)$ is the likelihood function discussed in Section 6.3 with a waveform model that assumes this particular hypothesis. If one aims to find the parameter set $\mathbf{\Theta}$ that describes the detector data best assuming that hypothesis $\mathcal{H}_i$ is true, it is straightforward to generalize Eq. (6.23) to

$$p(\mathbf{\Theta}|d, \mathcal{H}_i) = \frac{p(\mathbf{\Theta}|\mathcal{H}_i)\,p(d|\mathbf{\Theta}, \mathcal{H}_i)}{p(d|\mathcal{H}_i)}. \tag{6.26}$$

Once the waveform models are established for the different hypotheses, all the necessary quantities needed for Equation (6.24) are available. In practice, however, in order to compute the evidence $p(d)$, we would need to sum over all possible hypotheses (or theories); this is unfeasible because of the lack of our knowledge of all possible models. Yet we can compare different hypotheses and choose which one we are going to favour in the light of the measured data. A tool for such a comparison is the *odds ratio*

$$\mathcal{O}^{\mathrm{NGR}}_{\mathrm{GR}} = \frac{p(\mathcal{H}_{\mathrm{NGR}}|d)}{p(\mathcal{H}_{\mathrm{GR}}|d)} = \frac{p(\mathcal{H}_{\mathrm{NGR}})}{p(\mathcal{H}_{\mathrm{GR}})}\frac{p(d|\mathcal{H}_{\mathrm{NGR}})}{p(d|\mathcal{H}_{\mathrm{GR}})}, \tag{6.27}$$

which compares relative probabilities and represents the 'betting odds' for a certain hypothesis. The odds ratio has the advantage that the evidence $p(d)$ cancels out. More commonly, assuming flat prior odds, people use the *Bayes factor*

$$\mathrm{BF} = \frac{p(d|\mathcal{H}_{\mathrm{NGR}})}{p(d|\mathcal{H}_{\mathrm{GR}})}. \tag{6.28}$$

Large Bayes factors would thus imply a clear tendency towards an alternative theory describing the data much better than GR.

6.5 Exploring the posterior: The Markov Chain Monte Carlo algorithm

In the following, let us present a short introduction to the Markov Chain Monte Carlo (MCMC) algorithm - a particular computational tool that can be used to explore the probability distributions introduced in the previous sections. Comprehensive reviews can be found in [96, 97].

6.5.1 The Monte Carlo principle

The idea of Monte Carlo simulations is to draw an independent set of *random* samples $\left\{x^{(k)}\right\}_{k=1}^{N}$ from a target distribution $p(x)$. The acquired samples can then be used to construct an approximate version of the target distribution,

$$p(x) = \frac{1}{N}\sum_{k=1}^{N}\delta(x - x^{(k)}). \tag{6.29}$$

Thus, in the limit of large N, $p_N(x) \approx p(x)$. Expectation integrals can then be approximated by only considering samples $x^{(i)}$:

$$\int f(x)\,p(x)\,\mathrm{d}x = \lim_{N\to\infty}\int f(x)\,p_N(x)\,\mathrm{d}x = \lim_{N\to\infty}\frac{1}{N}\sum_{k=1}^{N} f(x^{(i)}). \tag{6.30}$$

Monte Carlo simulations are widely used in computational physics; we use one to assess the errors on the estimated theory parameters with Classic LISA in Chapter 7. If $p(x)$ follows a complicated structure with secondary maxima, is defined on a high-dimensional state space or is difficult to sample from at all, then Monte Carlo-based algorithms become very inefficient. A more appropriate method is the use of Markov Chains, as introduced in the next subsection.

6.5.2 A primer to Markov chain theory

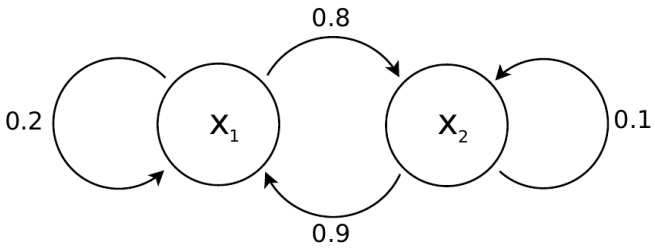

Figure 6.1: *A simple two-state system with assigned transition probabilities. After a large number of iterations, the probability distribution settles down to* $p(x_1) = 0.53$ *and* $p(x_2) = 0.47$.

Suppose we are to deal with a system of two different states x_1 and x_2, as visualised in Fig. 6.1. Let us choose x_1 as a starting point. To x_1, jump probabilities are assigned: in 20% of the jumps, we come back to x_1 and in the remaining 80% we reach x_2. Similarly, once we have reached x_2, we will reach x_1 only in 90% of the cases, in the rest we will fall back on x_2. Such jump probabilities can be formalised with a *transition matrix* $T(x_i|x_j)$, the probability to reach x_i given one sits on x_j. In the particular example, we are left with $T(x_1|x_1) = 0.2$, $T(x_1|x_2) = 0.9$, $T(x_2|x_1) = 0.8$ and $T(x_2|x_2) = 0.2$, or

$$T = \begin{pmatrix} 0.2 & 0.9 \\ 0.8 & 0.1 \end{pmatrix}. \tag{6.31}$$

T has, by definition, to follow the normalisation rule $\sum_i T(x_i|x_k) = 1$. After k jumps, the probability distribution is $p^{(k)}(x_i) = k_i/k$ where $x = \{x_1, x_2\}$ and k_i is the number of cases we ended up on x_i. In the limit of large k, the *invariant distribution* $p(x)$ is reached, with $\sum_i p(x_i) = 1$. In this particular example, one finds $p(x_1) = 0.53$ and $p(x_2) = 0.47$ for large k.

Using marginalisation over conditional probabilities (as done in Section 6.4), we are able to write

$$p(x_1) = T(x_1|x_1)\,p(x_1) + T(x_1|x_2)\,p(x_2) = \sum_{i=1}^{2} T(x_1|x_i)\,p(x_i),$$
$$p(x_2) = T(x_2|x_1)\,p(x_1) + T(x_2|x_2)\,p(x_2) = \sum_{i=1}^{2} T(x_2|x_i)\,p(x_i). \tag{6.32}$$

This relation must hold for the invariant distribution. Defining the vector $\boldsymbol{p} = (p(x_1), \ldots, p(x_n))$ allows us therefore to write relation (6.32) as the fix-point problem $\boldsymbol{p} = T\,\boldsymbol{p}$ (which is also the definition of the invariant distribution). Thus we can find the invariant distribution by evaluating $\boldsymbol{p}^{(k+1)} = T\,\boldsymbol{p}^{(k)}$ iteratively or, formally, $T^N\,\boldsymbol{p}^{(0)} \underset{N\to\infty}{\longrightarrow} \boldsymbol{p}$. For our particular example, one can indeed verify that $T\boldsymbol{p} = \boldsymbol{p}$ for $\boldsymbol{p} = (0.53, 0.47)$.

Definition: A *Markov chain* is a series of random variables $X^{(0)}, X^{(1)}, X^{(2)}, \ldots$ on a common *state space* where the probability distribution for $X^{(k+1)}$ only depends on $X^{(k)}$, in other words: the chain has no memory of its history. More formally, $p\left(X^{n+1}|X^{(n)}, X^{(n-1)}, \ldots, X^{(1)}, X^{(0)}\right) = p\left(X^{n+1}|X^{(n)}\right)$.

Markov chains are *ergodic*, i.e. $T^N\,\boldsymbol{p}^{(0)}(x) \to \boldsymbol{p}(x)$ in the limit of large N regardless of the initial condition $\boldsymbol{p}^{(0)}(x)$, as long as the transition matrix is *irreducible* and *aperiodic*. If the transition matrix is reducible, i.e. the matrix T can be reduced into separate smaller matrices, then not all states in the chain can be visited from within certain subsets of the state space. The requirement of aperiodicity makes sure that the Markov chain does not alternate between a set of final probability distributions, never converging on one invariant distribution.

In the multivariate and continuous case, where $\boldsymbol{x} \in \mathbb{R}^n$ and $p(\boldsymbol{x})$ is a real and continuous function with $\int p(\boldsymbol{x})\,\mathrm{d}^n x = 1$, the transition probabilities are expressed with the *transition function* $T(\boldsymbol{x}'|\boldsymbol{x}) = T(\boldsymbol{x}', \boldsymbol{x})$. The marginalisation (6.32) can then be expressed as

$$p(\boldsymbol{x}') = \int T(\boldsymbol{x}'|\boldsymbol{x})\,p(\boldsymbol{x})\,\mathrm{d}^n x, \tag{6.33}$$

allowing for the fix-point iteration

$$p^{(k+1)}(\boldsymbol{x}) = \int T(\boldsymbol{x}'|\boldsymbol{x})\,p^{(k)}(\boldsymbol{x})\,\mathrm{d}^n x. \tag{6.34}$$

Given a probability distribution $p(\boldsymbol{x})$, we wish to construct a Markov chain for which $p(\boldsymbol{x})$ is the invariant distribution. A *reversible* Markov chain satisfies the *detailed balance condition*

$$T(\boldsymbol{x}'|\boldsymbol{x})\,p(\boldsymbol{x}) = T(\boldsymbol{x}|\boldsymbol{x}')\,p(\boldsymbol{x}'), \tag{6.35}$$

i.e. if we pick a state from the target distribution $p(\boldsymbol{x})$ and jump with transition probability T, it is just as likely that we pick $\boldsymbol{x}$ and go from $\boldsymbol{x}$ to $\boldsymbol{x}'$ as it is that we choose $\boldsymbol{x}'$ and go from $\boldsymbol{x}'$ to $\boldsymbol{x}$. Then,

$$p(\boldsymbol{x}') = \int T(\boldsymbol{x}'|\boldsymbol{x})\,p(\boldsymbol{x})\,\mathrm{d}^n x = \int T(\boldsymbol{x}|\boldsymbol{x}')\,p(\boldsymbol{x}')\,\mathrm{d}^n x = p(\boldsymbol{x}') \int T(\boldsymbol{x}|\boldsymbol{x}')\,\mathrm{d}^n x = p(\boldsymbol{x}'). \tag{6.36}$$

This is an important result since if we are able to find a transition function that satisfies the detailed balance condition, then this will automatically ensure that $p(\boldsymbol{x})$ is its invariant distribution.

6.5.3 Using auxiliary proposal distributions - Rejection sampling

Some probability distributions $p(x)$ are very difficult to draw samples from. In order to prepare for the Metropolis-Hastings algorithm that is described in the next subsection, we introduce here the concept of adopting auxiliary distributions that are used instead for sampling. The basic idea of *rejection sampling* is to sample from an auxiliary distribution $q(x)$ that is easy to sample and satisfies $p(x) \leq Mq(x)$, where $M > 0$ is a constant (Fig. 6.2).

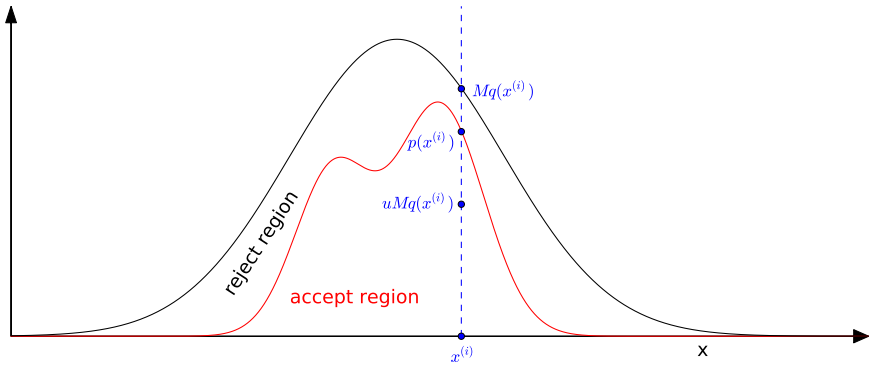

Figure 6.2: *In the rejection sampling algorithm, samples are drawn from an auxiliary distribution $q(x)$. By using a random value u drawn from an uniform distribution over $[0,1]$, certain samples can be rejected in order to correct for $p(x)$.*

In the following, samples $x^{(i)}$ are drawn from $q(x)$ while each time another random value u is chosen from a uniform probability distribution over $[0,1]$. If

$$u\,Mq(x^{(i)}) < p(x^{(i)}), \tag{6.37}$$

then we find ourselves in the area enclosed by $p(x)$ and accept the sample, otherwise we reject it. This method allows us to sample $p(x)$ without actually having to draw samples from it directly. In high-dimensional scenarios, however, rejection sampling is prone to fail, since

$$p(\boldsymbol{x} \text{ accepted}) = p\left(u^{(i)} < \frac{p(\boldsymbol{x}^{(i)})}{Mq(\boldsymbol{x}^{(i)})}\right) \sim \frac{1}{M}, \tag{6.38}$$

and M has usually to be quite large to allow $Mq(\boldsymbol{x})$ to enclose $p(\boldsymbol{x})$, leading to a very low acceptance rate.

6.5.4 Markov Chain Monte Carlo and the Metropolis-Hastings algorithm

Markov Chain Monte Carlo is a strategy to draw samples from a given probability distribution that is difficult to sample while exploring the state space using Markov chains. One of the most practical and most commonly used MCMC algorithms is the *Metropolis-Hastings* algorithm which is suitable especially for multi-dimensional problems. The Metropolis-Hastings algorithm is also particularly useful as it does not require the knowledge of the numerical value of a possible normalisation constant in front of the probability distribution.

As the invariant distribution $p(\boldsymbol{x})$ is difficult to sample from, we introduce the auxiliary, candidate-generating proposal density $q(\boldsymbol{x}'|\boldsymbol{x})$ which denotes the probability to jump to $\boldsymbol{x}'$ given that the current state is $\boldsymbol{x}$. Most

likely, $q(\boldsymbol{x}'|\boldsymbol{x})$ does not satisfy the detailed balance condition introduced in Section 6.5.2. However, we can restore detailed balance by constructing a proposal distribution $\mathscr{A}(\boldsymbol{x}'|\boldsymbol{x})\,q(\boldsymbol{x}'|\boldsymbol{x})$, where $\mathscr{A}(\boldsymbol{x}'|\boldsymbol{x})$ is an arbitrary function and can be interpreted as the *acceptance probability* for a jump that has been proposed by $q(\boldsymbol{x}'|\boldsymbol{x})$. The detailed balance condition is thus

$$\mathscr{A}(\boldsymbol{x}'|\boldsymbol{x})\,q(\boldsymbol{x}'|\boldsymbol{x})\,p(\boldsymbol{x}) = \mathscr{A}(\boldsymbol{x}|\boldsymbol{x}')\,q(\boldsymbol{x}|\boldsymbol{x}')\,p(\boldsymbol{x}'). \tag{6.39}$$

In order to ensure reversibility, it is convenient to choose $\mathscr{A}(\boldsymbol{x}|\boldsymbol{x}') = 1$ for the acceptance probability to jump back. Hence we end up with $\mathscr{A}(\boldsymbol{x}'|\boldsymbol{x}) = [q(\boldsymbol{x}|\boldsymbol{x}')p(\boldsymbol{x}')]/[q(\boldsymbol{x}'|\boldsymbol{x})p(\boldsymbol{x})]$, or at iteration i,

$$\mathscr{A}\left(\boldsymbol{x}^{(i+1)}|\boldsymbol{x}^{(i)}\right) = \min\left[1, \frac{p\left(\boldsymbol{x}^{(i+1)}\right)\,q\left(\boldsymbol{x}^{(i)}|\boldsymbol{x}^{(i+1)}\right)}{p\left(\boldsymbol{x}^{(i)}\right)\,q\left(\boldsymbol{x}^{(i+1)}|\boldsymbol{x}^{(i)}\right)}\right], \tag{6.40}$$

where the maximum acceptance probability has been limited to one. Given a sample $\boldsymbol{x}^{(i)}$ that has been reached previously, the next sample $\boldsymbol{x}^{(i+1)}$ is drawn from the auxiliary probability distribution $q(\boldsymbol{x}^{(i+1)}|\boldsymbol{x}^{(i)})$. The sample $\boldsymbol{x}^{(i+1)}$ is then accepted with the probability $\mathscr{A}\left(\boldsymbol{x}^{(i+1)}|\boldsymbol{x}^{(i)}\right)$. Here, the ratio $p(\boldsymbol{x}^{(i+1)})/p(\boldsymbol{x}^{(i)})$ represents the reality, i.e. the probability distribution of the observed process as it is in nature. However, the ratio $q(\boldsymbol{x}^{(i)}|\boldsymbol{x}^{(i+1)})/q(\boldsymbol{x}^{(i+1)}|\boldsymbol{x}^{(i)})$ can be adjusted by the choice of $q(\boldsymbol{x}|\boldsymbol{x}')$, allowing us to optimise for speed and acceptance rate of the chain.

The Metropolis-Hastings algorithm has two main disadvantages: First, since every sample is chosen according to the previous one, the samples are correlated; a set of nearby samples will not reflect the correct distribution. As a solution, only every nth sample can be stored. However, this will substantially increase the number of samples that have to be acquired. Another solution would be to increase the width of $q(\boldsymbol{x}'|\boldsymbol{x})$ allowing for larger jumps; this can lead to very high rejection probabilities and therefore can take the chain a long time to run. Secondly, although the chain eventually converges to the invariant distribution, it needs some time to get from the initial state to the states where the probabilities are high and lurks around in one particular low-probability region of the state space which thus appears to have higher probabilities at the end. Such initial samples in the so-called *burn-in phase* do not represent the probability distribution well and should be thrown away.

Concluding, the Metropolis-Hastings algorithm works as follows:

- Choose an initial value $\boldsymbol{x}^{(0)}$.
- For $i = 0$ to $N-1$:
  - Randomise $u \in [0,1]$ uniformly.
  - Sample $\boldsymbol{x}'$ from $q(\boldsymbol{x}'|\boldsymbol{x})$.
  - If $u < \mathscr{A}\left(\boldsymbol{x}'\middle|\boldsymbol{x}^{(i)}\right)$: $\boldsymbol{x}^{(i+1)} = \boldsymbol{x}'$, else: $\boldsymbol{x}^{(i+1)} = \boldsymbol{x}^{(i)}$.

6.5.5 Simulated annealing

Instead of sampling from a distribution, especially for the search of the underlying parameters of gravitational wave sources, one can also be interested in finding its global maximum, in order to do a maximum a posteriori estimate. Such a task could in principle be accomplished by an MCMC where the state $\boldsymbol{x}^{(i)}$ leading to the highest $p(\boldsymbol{x}_i)$ is fetched from the chain at the end of the run. This is however quite inefficient, because only a few samples might come from the very vicinity of the maximum. Moreover, if the chain starts away from the maximum, it can very easily get stuck on one of the secondary or tertiary maxima that are distributed around the maximum [98]. A strategy to explore the maximum of a given probability distribution is *simulated annealing* which introduces a *non-homogeneous* (time-varying) Markov chain where the invariant distribution is modified to depend on iteration i:

$$p(i; \boldsymbol{x}) \propto p^{1/T_i}(\boldsymbol{x}), \tag{6.41}$$

with a 'temperature' T_i that decreases with i according to a certain cooling schedule which has the asymptotic property $\lim_{i\to\infty} T_i = 1$. As illustrated in Fig. 6.3, large temperatures render the invariant distribution smoothed out and low temperatures narrow the peak around the global maximum. This allows the chain to move easily between all local maxima in the beginning in order to find the approximate region of the global maximum and, as the cooling schedule goes forward and the temperature is decreased more and more, it settles around the global maximum and explores only its local surrounding. If one aims to explore the global maximum with a Metropolis-Hastings algorithm, one could replace the usual burn-in phase with a simulated annealing algorithm.

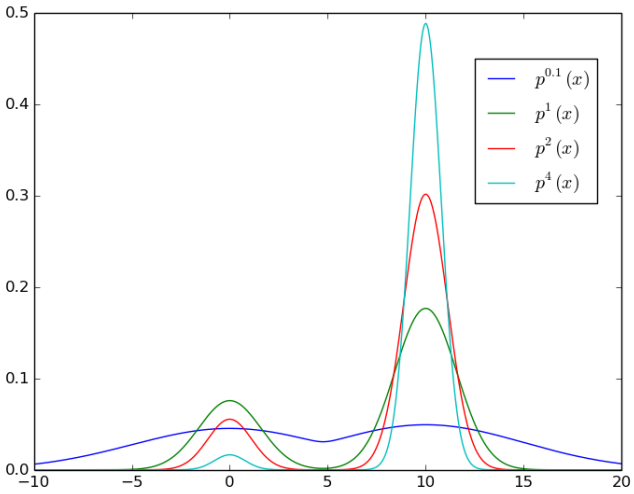

Figure 6.3: *In simulated annealing, a temperature decreasing with the number of iterations is assigned to the invariant distribution, as in Eq.* (6.41)*. It is interesting to observe how the probability distribution is smoothed out for large temperatures and is then successively narrowed for low temperatures. The probability distributions are all normalised to one.*

6.5.6 Choosing a good proposal distribution for gravitational-wave parameter estimation

The proposal distribution $q(\boldsymbol{x}^{(i+1)}|\boldsymbol{x}^{(i)})$ is usually chosen to follow a Gaussian distribution centered around $\boldsymbol{x}^{(i)}$ with a certain width parameter σ. A proposed jump will therefore preferably stay in the σ-vicinity of $\boldsymbol{x}^{(i)}$. Choosing the correct width parameter is crucial; if it is too small, then the corresponding jumps are too small and the samples can be strongly correlated, perhaps not allowing to jump from one local maximum to another. Conversely, if σ is too large, most of the jumps will be rejected as they are usually placed far away from a local maximum, rendering the Markov chain very inefficient. In Figs. 6.4-6.6, a Metropolis-Hastings algorithm is used to explore a bimodal target distribution by using a Gaussian distribution with a width parameter that is too narrow, just right or too wide.

In GW astronomy, we explore the posterior probability distribution (6.23)

$$p(\boldsymbol{\Theta}|d) \propto p(\boldsymbol{\Theta})\, e^{-\frac{1}{2}(d-h(\boldsymbol{\Theta})|d-h(\boldsymbol{\Theta}))}. \tag{6.42}$$

We saw in Section 6.2 that this distribution can be approximated using the Fisher matrix Γ_{ij}. This approximation is not perfect, but can nevertheless be used to form a good proposal distribution. We do this by

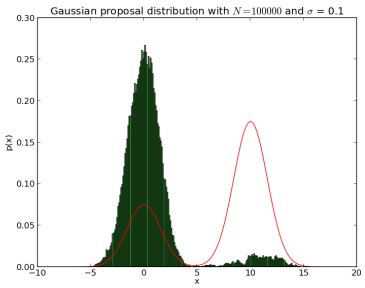

Figure 6.4: *Metropolis-Hastings algorithm where the width parameter of the proposal distribution is too narrow: the global maximum is missed and the chain stays mostly in the subdominant mode.*

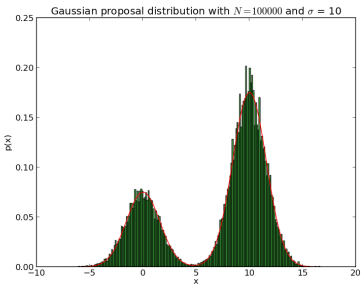

Figure 6.5: *Here, the width parameter seems to be optimally chosen: the chain moves well through the whole state space.*

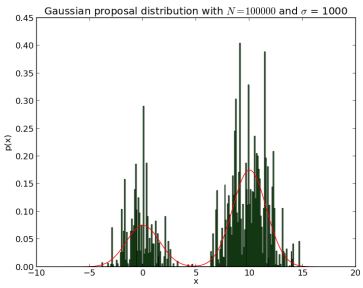

Figure 6.6: *In this case, the σ parameter was too wide: the allowed jumps are too large and rejected most of the time, leaving us with a sparsely filled chain.*

taking a multivariate Gaussian distribution (with nine dimensions for the non-spinning case) with a width parameter of $\sigma_i = 1/\sqrt{DE_i}$ in each eigendirection of Γ_{ij} [94, 99]. Here, E_i is the eigenvalue corresponding to the chosen eigendirection and D is the number of dimensions that makes sure that typical jumps are about 1σ of the full distribution. Cornish and Porter [94] find that the resulting acceptance rate is lower than expected due to the Fisher matrix slightly overestimating uncertainties in the magnitude of the eigenvalues and in the orientation of the eigenvectors.

Chapter 7

Testing General Relativity with LISA including Spin Precession and Higher Harmonics in the Waveform

C. Huwyler, A. Klein, Ph. Jetzer

Published in Physical Review D, Volume **86***, 084028 (2012)*

Abstract

We compute the accuracy at which a LISA-like space-based gravitational wave detector will be able to observe deviations from General Relativity in the low frequency approximation. To do so, we introduce six correction parameters that account for modified gravity in the second post-Newtonian gravitational wave phase for inspiralling supermassive black hole binaries with spin precession on quasi-circular orbits. Our implementation can be regarded as a subset of the ppE formalism developed by Yunes and Pretorius, being able to investigate also next-to-leading order effects. In order to find error distributions for the alternative theory parameters, we use the Fisher information formalism and carry out Monte Carlo simulations for 17 different binary black hole mass configurations in the range $10^5 M_\odot < M < 10^8 M_\odot$ with 10^3 randomly distributed points in the parameter space each, comparing the full (FWF) and restricted (RWF) version of the gravitational waveform. We find that the binaries can roughly be separated into two groups: one with low ($\lesssim 10^7 M_\odot$) and one with high total masses ($\gtrsim 10^7 M_\odot$). The RWF errors on the alternative theory parameters are two orders of magnitude higher than the FWF errors for high-mass binaries while almost comparable for low-mass binaries. Due to dilution of the available information, the accuracy of the binary parameters is reduced by factors of a few, except for the luminosity distance which is affected more seriously in the high-mass regime. As an application and to compare our research with previous work, we compute an optimal lower bound on the graviton Compton wavelength which is increased by a factor of ~ 1.6 when using the FWF.

7.1 Introduction

Although General Relativity (GR) has so far passed all experimental and observational tests [32], some unsatisfactorily explained phenomena still remain which could be more elegantly described by alternative gravity theories. Among these theories are the proposed inflationary epoch of the universe shortly after the big bang which explains the temperature homogeneity of the cosmic microwave background, dark matter which should account for the missing 23% of the mass in the universe and dark energy introduced as an attempt to drive the observed late accelerated expansion of the universe. Moreover, attempts to quantize GR or to unify gravitation with the other three fundamental forces are as yet incomplete. Consequently, several modifications to GR have been proposed. Certain alternative theories work by introducing additional fields to the Einstein-Hilbert action of GR. Scalar-tensor field theories such as Brans-Dicke theory [100] are candidates for reproducing inflation. Modified Newtonian Dynamics (MOND) [101] attempts to get rid of dark matter by modifying the $1/r^2$ behavior of the gravitational potential; a relativistic version introducing scalar and vector fields called Tensor-Vector-Scalar gravity (TeVeS) has also been proposed [102]. The class of $f(R)$ theories [103] modify the Einstein-Hilbert action by replacing the Riemann scalar by a function of it. More phenomenological approaches such as Massive Graviton theories [50, 54] study the wave propagation of a 'massive' gravitational field.

Since alternatives to GR can be heavily constrained by the observation of Solar System effects and pulsar binaries [32], viable alternative theory candidates should reduce to GR in the limit of weak fields. In spacetime regions with strong dynamical gravity, such as binary black holes (BBHs), comparable constraints do not yet exist and should be tested for. A good review of currently discussed alternatives to GR can be found in the appendix of [35].

Among the most popular gravitational wave detectors are laser interferometers. Several ground-based interferometers such as LIGO (USA), Virgo (Italy) and GEO600 (Germany) have been built and are already operating, being sensitive to high frequencies between 10 Hz and 1 kHz. Currently LIGO is being upgraded to *Advanced LIGO* with a sensitivity ten times better, and is expected to observe several events per year and make gravitational wave detection likely within the next five years. Hence gravitational waves could finally be observed directly a hundred years after their theoretical prediction by Einstein.

Complementary to ground-based detectors restricted by their short arm-length and seismic noise at low frequencies, the spaceborne, low frequency detector eLISA/NGO (evolved Laser Interferometer Space Antenna / Next Gravitational Wave Observatory) has been proposed, sensitive in a range of $\sim 10^{-5} - 1$ Hz. The mission was originally planned as an ESA/NASA collaboration, consisting of three spacecrafts separated by five million km, forming an equilateral triangle of laser arms. In 2011, NASA discontinued their participation in the LISA project; the European Space Agency planned to realize the project on their own with a reduced, affordable mission design called eLISA/NGO [77]. Although not selected as the first large L1 mission, there is a high chance that eLISA/NGO will be selected within the next few years as an L2 mission. In this paper we perform calculations for the originally planned LISA-like detector, as this enables us to compare our results to other studies and also since it is currently unknown with what technical specifications eLISA will fly. We will use the term 'LISA' for a classic LISA-like mission throughout this paper.

Among the strongest sources which LISA will detect are supermassive black hole binaries with masses between $10^5 - 10^7 M_\odot$. After a long inspiral phase, such binaries could merge into one single Kerr black hole which rings down from its excited state by emitting gravitational radiation. Compact binary inspirals produce a very clean and long-lasting gravitational signal which may be accurately described by harmonics of the orbital phase using the post-Newtonian (PN) formalism. Inspiralling BBHs emit gravitational radiation carrying information about binary parameters such as the individual black hole masses and spins in its amplitude and phase. By using matched filtering techniques [104, 105], the binary parameters can be extracted from the noisy signal measured by the detector. Alternative gravity theories will also leave their imprints on gravitational waves, since they modify the strong-field dynamics of the BBH, resulting in a

different orbital phase evolution. Also a possible 'graviton mass' will influence gravitational waves on their way to us by making their velocity frequency dependent. Since alternative theories are heavily constrained and LISA is expected to observe signals with very high signal-to-noise ratio (SNR), a signal from a BBH will be detected with GR waveform templates regardless whether or not GR is true. This could create a fundamental bias [35] in parameter extraction if the signal is fitted with an incorrect GR waveform template, leading to incorrect parameter estimation. To fix this bias, additional parameters controlling deviations from GR can be introduced. Adding parameters while having the same information from the detectors increases the correlation between the extracted parameters and thus decreases the accuracy in the recovered parameter values.

Previous papers computed bounds which LISA could place on the Brans-Dicke parameter $\omega_{\rm BD}$ (see e.g. [106, 107]) or on the graviton Compton wavelength λ_g (see e.g. [50]) using matched filtering. Due to the no hair theorem, for BBHs, scalar field effects in Brans-Dicke theory arising from the inner structure of compact objects cannot be distinguished; however, such massive binaries are an excellent environment to test massive gravity effects. The effects of 'massive' propagation have been investigated by various authors, considering different source and detector models. After a first analysis of massive graviton propagation by Will [50], Berti et al. [53] introduced spin parameters and spin-orbit/spin-spin couplings, finding a loss of accuracy due to the extra parameters included in the model. Stavridis and Will [54] considered the full precession of the spins and discovered that the resulting phase modulation restores the lost accuracy on λ_g. Yagi and Tanaka [57] included eccentricity to the system and found that the additional structure through both precession and eccentricity increases the measurement accuracy by an order of magnitude. Arun and Will [55] showed that the bounds on λ_g are improved by almost an order of magnitude for non-spinning BBHs when using the full waveform (FWF) instead of the restricted waveform (RWF) which takes the phase up to full PN order but considers the amplitude only to leading order. Taking higher harmonics into consideration increases the time during which the signal stays in the frequency window of LISA and shows a richer structure in the gravitational wave, leading to less correlation in the parameter space. Keppel and Ajith [56] used hybrid inspiral-merger-ringdown waveforms and found that they lead to a ~ 10 times higher accuracy than for inspiral-only waveforms. Moreover, Berti et al. [58] pointed out that the combination of the bounds on λ_g from individually observed inspirals in a two-year running time can again raise the accuracy by an order of magnitude. Tables summarizing lower bounds on λ_g and upper bounds on $\omega_{\rm BD}$ found by previous works are e.g. provided by [56, 57]. Arun et al. [70] re-interpreted the matched filtering method and fitted the post-Newtonian coefficients to the waveform instead of the parameters usually extracted from them. They discussed to what extent LISA will be able to measure deviations from the 3.5PN gravitational wave phase parameters in General Relativity. Yunes and Pretorius [35] generalized this approach to a *parameterized post-Einsteinian (ppE)* formalism which maps different types of alternative theories to the gravitational waveform of a compact binary merger. Cornish et al. [67] used Markov Chain Monte Carlo simulations to investigate parameter biases and possible bounds on the ppE parameters.

In this work we parametrize alternative theories by introducing corrections to the post-Newtonian coefficients of the orbital phase for a BBH inspiral, including the full 2PN precession of spins and angular momentum. We add higher harmonics to the waveform by considering the full 2PN amplitude. We postpone the discussion of eccentric orbits to later work and restrict our calculations to quasi-circular orbits. Since matched filtering is far more sensitive to the gravitational wave phase than to the amplitude, we do not consider corrections to the amplitude of the wave. We evaluate the measurement accuracy with which a LISA-like mission will be able to detect such corrections for BBHs. To estimate the errors on the parameters, we make use of the Fisher information formalism which is legitimate in the limit of high SNR which LISA will provide.

The organization of this paper is as follows. In Sec. 7.2 we shortly introduce the necessary equations to describe the evolution of the inspiral phase, the spins and the angular momentum of a BBH up to 2PN. In Sec. 7.3 we introduce small departures from GR into the post-Newtonian frequency evolution equation. We

then compute the modified orbital phase evolution in this scheme, incorporate it into a modified waveform template in Sec. 7.4, taking the waveform to be the sum of harmonics of the orbital phase, compute the Fourier transformed waveform including alternative theory parameters and compare it with the ppE formalism in sec. 7.5. In Sec. 7.6 we review the Fisher information formalism in order to estimate the errors on the parameters. In sec. 7.7 we explain the details of the Monte Carlo simulations we carried out. We discuss the resulting error distributions on selected parameters in Sec. 7.8 to see to what extent we can measure deviations from the 2PN gravitational wave phase predicted by GR and how strongly the binary parameters are affected by the introduction of six new parameters to the model. We discuss two representative BBH systems in Secs. 7.8.1) and 7.8.2). In sec. 7.8.3 we have a closer look at correlations between the newly-introduced parameters. Because systems at higher redshifts experience higher errors, we plot the maximal redshifts for different upper error limits of the alternative theory parameters in Section 7.8.4. As an example, we calculate the resulting optimal lower bounds on the Compton wavelength of the graviton in Sec. 7.8.5. We summarize our work and discuss possible extensions in Sec. 7.9. In Appendix 7.11.1 we discuss the breakdown of three approximations used in this work and where the integrations should be stopped. The expressions we used for the 2.5PN and 3PN frequency evolution are given in appendix 7.11.2. We give tables with best-case, worst-case and median measurement errors of both the binary and alternative theory parameters in Appendix 7.11.3.

7.2 Evolution of black hole binaries with precessing spins

A complete description of the inspiral evolution of two spinning black holes on a quasi-circular orbit with two individual masses $m_{1,2}$ and the corresponding spin vectors $\boldsymbol{S}_{1,2}(t)$ is given by the angular momentum unit vector $\hat{\boldsymbol{L}}(t)$, the orbital angular frequency $\omega(t)$ and an initial value for the orbital phase $\varphi(t_0)$. Further characteristics such as the orbital separation can be related to ω using post-Newtonian expressions. Therefore a quasi-circular BBH inspiral can be described by 12 intrinsic parameters. In order to relate the binary with a detector, a unit vector $\hat{\boldsymbol{n}}$ pointing from the detector to the barycenter, and a luminosity distance d_L between the two can be introduced, bringing an additional set of 3 extrinsic parameters into play. Thus, to describe a BBH inspiral on quasi-circular orbit, 15 parameters are required.

Since a description of the motion of such a system with full General Relativity is only possible with numerical methods and at high computational cost, an analytic expansion of the Einstein equations in powers of v/c has been studied: the post-Newtonian (PN) formalism. Currently, the equations of motion for spinning objects are known up to 2.5PN, while spin-spin and spin-orbit coupling terms are only known up to 2PN [19]. Therefore we take all the relevant expressions up to 2PN, i.e. $\mathcal{O}[(v/c)^4]$ away from leading order. The evolution equation for the angular frequency of a BBH system is [30]

$$\begin{aligned}\frac{\mathrm{d}x}{\mathrm{d}t} = \frac{64\nu}{5}\frac{c^3}{GM}x^5\Bigg[1-\left(\frac{743}{336}+\frac{11\nu}{4}\right)x+\left(4\pi-\frac{1}{12}\beta(113,75)\right)x^{3/2} \\ +\left(\frac{34103}{18144}+\frac{13661\nu}{2016}+\frac{59\nu^2}{18}-\frac{1}{48}\sigma(247,721)\right)x^2\Bigg],\end{aligned} \tag{7.1}$$

where

$$x \equiv \left(\frac{GM\omega}{c^3}\right)^{2/3} \tag{7.2}$$

is the dimensionless orbital frequency parameter, $M = m_1 + m_2$ is the total mass and $\nu = m_1 m_2/M^2$ is the symmetric mass ratio. The spin-orbit and spin-spin couplings are given by

$$\beta(a,b) = \frac{c}{G}\sum_{i=1}^{2}\left(\frac{a}{M^2} + \frac{b\,\nu}{m_i^2}\right)\boldsymbol{S}_i \cdot \hat{\boldsymbol{L}}, \tag{7.3}$$

and

$$\sigma(a,b) = \frac{c^2}{\nu M^4 G^2}(a\;\boldsymbol{S}_1 \cdot \boldsymbol{S}_2 - b(\boldsymbol{S}_1 \cdot \hat{\boldsymbol{L}})(\boldsymbol{S}_2 \cdot \hat{\boldsymbol{L}})), \tag{7.4}$$

respectively. The precession of $\hat{\boldsymbol{L}}$ and $\boldsymbol{S}_{1,2}$ induces a time dependence for these couplings, and thus a modulation of the gravitational wave phase. The orbit-averaged evolution equations without radiation reaction ($\dot{\boldsymbol{L}} + \dot{\boldsymbol{S_1}} + \dot{\boldsymbol{S_2}} = 0$) at 2PN order are [18]

$$\dot{\boldsymbol{L}} = \frac{G}{c^2}\frac{1}{r^3}\left(\left(2+\frac{3m_2}{2m_1}\right)\boldsymbol{S}_1 + \left(2+\frac{3m_1}{2m_2}\right)\boldsymbol{S}_2\right)\times\boldsymbol{L} - \frac{3G}{2c^2}\frac{1}{r^3}\left(\left(\boldsymbol{S}_2\cdot\hat{\boldsymbol{L}}\right)\boldsymbol{S}_1 + \left(\boldsymbol{S}_1\cdot\hat{\boldsymbol{L}}\right)\boldsymbol{S}_2\right)\times\hat{\boldsymbol{L}}, \tag{7.5}$$

$$\dot{\boldsymbol{S}}_i = \frac{G}{c^2}\frac{1}{r^3}\left[\left(2+\frac{3m_j}{2m_i}\right)\boldsymbol{L} + \frac{1}{2}\boldsymbol{S}_j - \frac{3}{2}\left(\boldsymbol{S}_j\cdot\hat{\boldsymbol{L}}\right)\hat{\boldsymbol{L}}\right]\times\boldsymbol{S}_i, \tag{7.6}$$

with $i \neq j$ and $i, j \in \{1,2\}$. The orbital separation r and the angular momentum are related to the orbital frequency by the Newtonian relations

$$L = \mu\left(\frac{G^2M^2}{\omega}\right)^{1/3}, \tag{7.7}$$

$$r = \left(\frac{GM}{\omega^2}\right)^{1/3}, \tag{7.8}$$

since higher-order corrections would exceed the 2PN order. Eqs. (7.1) and (7.7) enable us to express the evolution equations (7.6) in terms of the frequency ω:

$$\frac{\mathrm{d}\boldsymbol{S}_i}{\mathrm{d}\omega} = \frac{5}{96}\frac{c^3}{GM}\omega^{-2}\left[\hat{\boldsymbol{L}}\times\boldsymbol{\Sigma}_i + \frac{1}{2L}\left(\boldsymbol{S}_j - 3\left(\boldsymbol{S}_j\cdot\hat{\boldsymbol{L}}\right)\hat{\boldsymbol{L}}\right)\times\boldsymbol{S}_i\right], \tag{7.9}$$

$$\frac{\mathrm{d}\hat{\boldsymbol{L}}}{\mathrm{d}\omega} = \frac{5}{96}\frac{c^3}{GM}\omega^{-2}\frac{1}{L}\left[\boldsymbol{\Sigma}_1 + \boldsymbol{\Sigma}_2 - \frac{3}{2L}\left(\boldsymbol{\sigma}_1 + \boldsymbol{\sigma}_2\right)\right]\times\hat{\boldsymbol{L}} = -\frac{1}{L}\left(\frac{\mathrm{d}\boldsymbol{S}_1}{\mathrm{d}\omega} + \frac{\mathrm{d}\boldsymbol{S}_2}{\mathrm{d}\omega}\right), \tag{7.10}$$

with

$$\boldsymbol{\Sigma}_i = \left(2+\frac{3m_j}{2m_i}\right)\boldsymbol{S}_i, \tag{7.11}$$

and

$$\boldsymbol{\sigma}_i = \left(\boldsymbol{S}_j\cdot\hat{\boldsymbol{L}}\right)\boldsymbol{S}_i. \tag{7.12}$$

We express the gravitational wave phase in terms of the "principal + direction" [108] defined as the direction of the vector $\hat{\boldsymbol{L}}\times\hat{\boldsymbol{n}}$. A precession of the angular momentum vector changes the principal + direction. The resulting modulation of the gravitational waveform can be expressed by modifying the phase by

$$\delta\varphi = -\int_t^{t_c}\frac{\hat{\boldsymbol{L}}\cdot\hat{\boldsymbol{n}}}{1-\left(\hat{\boldsymbol{L}}\cdot\hat{\boldsymbol{n}}\right)^2}\left(\hat{\boldsymbol{L}}\times\hat{\boldsymbol{n}}\right)\cdot\dot{\hat{\boldsymbol{L}}}\,\mathrm{d}t = \delta\varphi_0 + \int_{\omega_0}^{\omega}\frac{\hat{\boldsymbol{L}}\cdot\hat{\boldsymbol{n}}}{1-\left(\hat{\boldsymbol{L}}\cdot\hat{\boldsymbol{n}}\right)^2}\left(\hat{\boldsymbol{L}}\times\hat{\boldsymbol{n}}\right)\cdot\frac{\mathrm{d}\hat{\boldsymbol{L}}}{\mathrm{d}\omega}\,\mathrm{d}\omega, \tag{7.13}$$

where ω_0 is the orbital frequency at time t_0, $\delta\varphi_0 = -\int_{t_0}^{t_c}(\mathrm{d}\delta\varphi/\mathrm{d}t)\,\mathrm{d}t$, and $\mathrm{d}\hat{\mathbf{L}}/\mathrm{d}\omega$ is given in Eq. (7.10). The resulting 2PN orbital phase is then, expressed in terms of the orbital angular frequency: $\phi(\omega) = \varphi(\omega) + \delta\varphi(\omega)$.

A signal observed from a BBH at cosmological distance is redshifted, i.e. the observed frequency is $f_\mathrm{o} = f_\mathrm{e}/(1+z)$, where f_e is the frequency of the gravitational waves emitted by the binary. The relation between redshift and luminosity distance in a ΛCDM cosmology without radiation and with $\Omega_\Lambda = 0.72$, $\Omega_m = 0.28$ and $H_0 = 70.1$ km/s/Mpc [109] is

$$d_L(z) = (1+z)\frac{c}{H_0}\int_0^z \frac{\mathrm{d}z'}{\sqrt{\Omega_m(1+z')^3+\Omega_\Lambda}}. \tag{7.14}$$

For binaries at cosmological distance, the redshifted signal can be expressed as one coming from a binary with 'redshifted' masses $\tilde{m}_{1,2} = (1+z)\,m_{1,2}$ at luminosity distance $d_L(z)$. Unfortunately, for gravitational wave experiments, it is not possible to disentangle redshift, mass and distance: only two parameters out of these three can be inferred. Simultaneous observations of electromagnetic counterparts, through which the actual redshift could be measured, could break this correlation and lead to interesting astrophysical insights.

7.3 Modifications to the 2PN orbital phase

Matched filtering techniques are more sensitive to the gravitational wave phase than to the amplitude. The signal from a BBH inspiral can be described as a sum of harmonics of its orbital phase; to find the imprints of alternative gravity theories on gravitational waves it is therefore reasonable to look at how the orbital phase evolution of a BBH changes for small departures from GR. In the 2PN expansion, the orbital phase evolution can be found by integrating the frequency evolution equation (see Eq. (7.1) for the PN coefficients b_i)

$$\frac{\mathrm{d}x}{\mathrm{d}t} = \frac{64\nu}{5}\frac{c^3}{GM}x^5\left[1 + b_1 x + b_{3/2}x^{3/2} + b_2 x^2\right]. \tag{7.15}$$

As thoroughly discussed by Yunes and Pretorius in the derivation of their ppE formalism [35], in the adiabatic approximation the dimensionless frequency can be expressed as

$$\frac{\mathrm{d}x}{\mathrm{d}t} = \frac{\dot{E}}{\mathrm{d}E/\mathrm{d}x}. \tag{7.16}$$

E is the total binding energy or Hamiltonian (conservative part) of the system while $\dot{E}$ stands for the energy loss through gravitational waves or other physical degrees of freedom of energy loss (dissipative part). Considering the impact of alternative theories on these two quantities leads to modifications of the gravitational wave phase. Certain theories such as Brans-Dicke theory introduce scalar fields which lead to a difference in the self-gravitational binding energy $\mathcal{G}$ per unit mass [110], producing additional dipole radiation. The energy loss formula including dipole contributions can be expressed to leading quadrupole order as [35, 110, 111]:

$$\dot{E} = -\frac{\mu^2 G^3 M^2}{c^5 r^4}\left[\frac{8}{15}(\kappa_1 v^2 - \kappa_2 \dot{r}^2) + \frac{1}{3}\kappa_D \mathcal{G}^2\right] - \mathscr{L}_\mathrm{other}. \tag{7.17}$$

Here, v and r are the orbital velocity and separation of the system, respectively, while κ_1 and κ_2 are so-called Peter-Mathews parameters and κ_D is a coefficient for the dipole contribution. $\mathscr{L}_\mathrm{other}$ stands for any other energy loss channel, either through other polarizations or as yet unknown physical processes. Since

we do not have any good parametrization for $\mathscr{L}_{\rm other}$ so far, we do not consider it. In terms of dimensionless frequency, the dipole radiation term in Eq. (7.17) leads to an additional x^{-1} term in the PN expansion (7.15).

We introduce a general parametrization where the effects on the phase are emphasized and no corrections to the wave amplitude are considered. The calculations are done for quasi-circular binaries with precession of both black hole spins described by the full 2PN waveform (2PN expansion of both the phase and the amplitude). We start by introducing corrections to the 2PN orbital frequency evolution dx/dt which will lead to a corrected version of the 2PN orbital phase. To do that, we introduce a correction term a_i for every 2PN coefficient b_i and an additional x^{-1} and $x^{1/2}$ term. Products of a correction term $a_{-1}x^{-1}$ with a PN expanded expression such as $1 + b_1 x + b_{3/2}x^{3/2} + b_2 x^2$ result in b_2 featuring already at 1PN order. Hence for the final result to be consistent at 2PN order, we need to do all the calculations up to 3PN, truncating at 2PN only at the very end. The current 2.5PN expansion accounts for spin-orbit effects while the 3PN expansion does not consider spin effects at all. Nevertheless, these higher order expansions can be used as approximations. The 3PN evolution equations of the dimensionless orbital angular frequency are, motivated from [23, 30] (see appendix 7.11.2)

$$\left(\frac{\mathrm{d}x}{\mathrm{d}t}\right)_{\rm 3PN} = \frac{64\nu}{5}\frac{c^3}{GM}x^5\left[1 + b_1 x + b_{3/2}x^{3/2} + b_2 x^2 + b_{5/2}x^{5/2} + b_3 x^3 + b_{3,\log}x^3\log(x)\right],$$

with

$$\begin{aligned}
b_1 &= -\left(\frac{743}{336} + \frac{11\nu}{4}\right),\\
b_{3/2} &= \left(4\pi - \frac{1}{12}\beta(113,75)\right),\\
b_2 &= \left(\frac{34103}{18144} + \frac{13661\nu}{2016} + \frac{59\nu^2}{18} - \frac{1}{48}\sigma(247,721)\right),\\
b_{5/2} &= \pi\left(-\frac{4159}{672} - \frac{189\nu}{8}\right) + \frac{1}{c}\left(-\frac{40127}{1008} + \frac{1465\nu}{28}\right)\\
&\quad \times\beta(1,0) + \frac{1}{c}\left(-\frac{583}{42} + \frac{3049\nu}{168}\right)\beta(-1,1),\\
b_3 &= \frac{16447322263}{139708800} - \frac{1712\gamma_e}{105} + \frac{16\pi^2}{3} - \frac{56198689\nu}{217728}\\
&\quad + \frac{451\pi^2\nu}{48} + \frac{541\nu^2}{896} - \frac{5605\nu^3}{2592} - \frac{856}{105}\log(16),\\
b_{3,\log} &= -\frac{856}{105},
\end{aligned} \tag{7.18}$$

where β and σ are the spin-orbit and spin-spin couplings, respectively. To account for alternative theories, we generalize the frequency evolution to

$$\left(\frac{\mathrm{d}x}{\mathrm{d}t}\right)_{\rm mod} = \left(\frac{\mathrm{d}x}{\mathrm{d}t}\right)_{\rm 3PN} + \frac{64\nu}{5}\frac{c^3}{GM}x^5\left[a_{-1}x^{-1} + a_0 + a_{1/2}x^{1/2} + a_1 x + a_{3/2}x^{3/2} + a_2 x^2 + a_{2,\log}\,x^2\log(x)\right], \tag{7.19}$$

including corrections to every existing PN parameter and an additional x^{-1} and $x^{1/2}$ term. The reason why $x^2\log(x)$ appears is that a term proportional to $x^3\log(x)$ enters the 3PN phase which has to be included

in 2PN corrections because of couplings with x^{-1} terms. Note that we treat the a_i as constants, i.e. we disregard any dependencies on binary parameters such as masses and spins, since we do not know how they look like in general.

We now follow the steps for the derivation of the gravitational waveform presented in [112], introducing these additional corrections, keeping them at first order, and truncating at 3PN. By inverting and integrating Eq. (7.19) we find the time $t(x)$ as a function of the frequency to be of the form:

$$t - t_c \approx t(x)\big|_{\text{3PN}} - t_c - \frac{5}{256\nu}\frac{GM}{c^3}x^{-4}\left[T_{-1}x^{-1} + T_0 + T_{1/2}x^{1/2} + T_1 x + T_{3/2}x^{3/2} + T_2 x^2 + T_{2,\log}x^2\log(x)\right]. \tag{7.20}$$

The coefficients T_i are functions of a_i. To find the orbital phase as function of frequency, we need to recast $t(x)$ into a series expansion for $x(t)$; we are then able to find the phase by integrating $\omega \propto x^{3/2}$ over time:

$$[\varphi(x)]_{\text{mod}} = [\varphi(x)]_{\text{2PN}} + \frac{1}{32\nu}x^{-5/2}\left[A_{-1}x^{-1} + A_0 + A_{1/2}x^{1/2} + A_1 x + A_{3/2}x^{3/2} + A_2 x^2 + A_{2,\log}x^2\log(x)\right], \tag{7.21}$$

with the phase corrections $A_i(\{a_k\})$ as functions of the orbital frequency evolution corrections introduced in Eq. (7.19):

$$\begin{aligned}
A_{-1} &= \frac{5a_{-1}}{7},\\
A_0 &= a_0 - 2a_{-1}b_1,\\
A_{1/2} &= \frac{5}{4}(a_{1/2} - 2a_{-1}b_{3/2}),\\
A_1 &= \frac{5}{3}(a_1 - 2a_0 b_1 + 3a_{-1}b_1^2 - 2a_{-1}b_2),\\
A_{3/2} &= \frac{5}{2}\left(a_{3/2} - 2(a_{1/2}b_1 + a_0 b_{3/2} - 3a_{-1}b_1 b_{3/2} + a_{-1}b_{5/2})\right),\\
A_2 &= 5\big(a_2 + 2a_{2,\log} - 2a_1 b_1 + 3a_0 b_1^2 - 4a_{-1}b_1^3 - 2a_0 b_2 + 6a_{-1}b_1 b_2 b_{3/2}\\
&\quad -2a_{-1}b_3 - 2a_{1/2} + 3a_{-1}b_{3/2}^2 - 4a_{-1}b_{3,\log}\big),\\
A_{2,log} &= 5a_{2,\log} - 10a_{-1}b_{3,\log}.
\end{aligned} \tag{7.22}$$

At this point we choose not to consider the correction term $A_{2,log}$ in our implementation for simplicity and thus set $A_{2,log} = 0$ in the following.

7.4 Modifications to the 2PN waveform

Having found a 2PN expression for the orbital phase corrections, we are able to construct the gravitational waveform as a series of harmonics of the orbital frequency:

$$h_{+,\times} = \frac{2GM\nu x}{D_L c^2}\left[\sum_{n\geq 0}\left(A_{+,\times}^{(n)}\cos(n\phi) + B_{+,\times}^{(n)}\sin(n\phi)\right)\right]. \tag{7.23}$$

Here, ϕ is the orbital phase of the binary with spin precession included: $\phi(t) = [\varphi(t)]_{mod} + \delta\varphi(t)$. The coefficients $A^{(n)}_{+,\times}$, $B^{(n)}_{+,\times}$ are both post-Newtonian series in x:

$$A^{(n)}_{+,\times} = \sum_{i\geq 0} a^{(n,i/2)}_{+,\times} x^{i/2}, \qquad B^{(n)}_{+,\times} = \sum_{i\geq 0} b^{(n,i/2)}_{+,\times} x^{i/2}. \tag{7.24}$$

Explicit expressions for $A^{(n)}_{+,\times}$ and $B^{(n)}_{+,\times}$ can be found in [112]. A three arm classic LISA will form two different detectors with uncorrelated noise: for a detector k with antenna pattern functions F^+_k and $F^\times_k$, the response function can be written in the low frequency approximation (LFA) as

$$h_k = \frac{\sqrt{3}}{2}\left(F^+_k h_+ + F^\times_k h_\times\right) = \frac{\sqrt{3}GM\nu x}{D_L c^2}\sum_{n\geq 0}\left[A_{k,n}\cos(n\psi) + B_{k,n}\sin(n\psi)\right], \tag{7.25}$$

with the antenna pattern functions

$$F^+_1(\theta_N,\phi_N,\psi_N) = \frac{1}{2}\left(1+\cos^2\theta_N\right)\cos 2\phi_N\cos 2\psi_N - \cos\theta_N \sin 2\phi_N \sin 2\psi_N, \tag{7.26}$$
$$F^\times_1(\theta_N,\phi_N,\psi_N) = F^+_1(\theta_N,\phi_N,\psi_N - \pi/4), \tag{7.27}$$
$$F^+_2(\theta_N,\phi_N,\psi_N) = F^+_1(\theta_N,\phi_N - \pi/4,\psi_N), \tag{7.28}$$
$$F^\times_2(\theta_N,\phi_N,\psi_N) = F^+_1(\theta_N,\phi_N - \pi/4,\psi_N - \pi/4). \tag{7.29}$$

θ_N and ϕ_N are the spherical angles of the position of the binary in the detector frame, and ψ_N is defined through

$$\tan\psi_N \equiv \frac{\hat{\boldsymbol{L}}\cdot\hat{\boldsymbol{z}} - (\hat{\boldsymbol{L}}\cdot\hat{\boldsymbol{n}})(\hat{\boldsymbol{z}}\cdot\hat{\boldsymbol{n}})}{\hat{\boldsymbol{n}}\cdot(\hat{\boldsymbol{L}}\times\hat{\boldsymbol{z}})}, \tag{7.30}$$

with $\psi = [\varphi]_{mod} + \delta\varphi + \phi_D$, including the LISA Doppler phase $\phi_D(t) = (\omega R/c)\sin\bar{\theta}_N\cos(\bar{\Phi}(t) - \bar{\phi}_N)$, where $R = 1$ AU and $\bar{\phi}(t) = 2\pi t/1$ yr as explained in [112]. The harmonic coefficients are

$$A_{k,n} = \sum_{i\geq 0}\left(F^+_k a^{(n,i/2)}_+ + F^\times_k a^{(n,i/2)}_\times\right)x^{i/2}. \tag{7.31}$$
$$B_{k,n} = \sum_{i\geq 0}\left(F^+_k b^{(n,i/2)}_+ + F^\times_k b^{(n,i/2)}_\times\right)x^{i/2}. \tag{7.32}$$

By changing the cosine+sine representation into a cosine+phase representation, we can write Eq. (7.25) as

$$h_k = \frac{\sqrt{3}GM\nu x}{D_L c^2}\left[A^{(0)}_+ F^+_k + A^{(0)}_\times F^\times_k + \sum_{n\geq 1} A^{\rm pol}_{k,n}\cos\left(n\psi + \phi^{\rm pol}_{k,n}\right)\right], \tag{7.33}$$

with

$$\tan\phi^{\rm pol}_{k,n} = -\frac{B_{k,n}}{A_{k,n}}, \qquad A^{\rm pol}_{k,n} = {\rm sgn}(A_{k,n})\sqrt{A^2_{k,n} + B^2_{k,n}}. \tag{7.34}$$

The Fourier transform of the response function is then, writing the cosine as an exponential and defining the new phase $\psi_{k,n} \equiv n([\varphi]_{mod} + \delta\varphi + \phi_D) + \phi^{\rm pol}_{k,n}$:

$$\tilde{h}_k(f) = \frac{\sqrt{3}GM\nu}{2D_L c^2}\int_{-\infty}^{\infty}\left(\sum_{n\geq 1} xA_{k,n}^{\rm pol}\left[e^{i(2\pi f t-\psi_{k,n})} + e^{i(2\pi f t+\psi_{k,n})}\right] + 2x\left(A_+^{(0)}F_k^+ + A_\times^{(0)}F_k^\times\right)\times e^{2\pi i f t}\right)\mathrm{d}t. \tag{7.35}$$

The $n=0$ integral accumulates around frequencies different from the gravitational wave frequency and $e^{i(2\pi f t+\psi_{k,n})}$ around negative frequencies, so both can be neglected. Then the Fourier transform reduces to

$$\tilde{h}_k(f) = \frac{\sqrt{3}GM\nu}{2D_L c^2}\sum_{n\geq 1}\left[\int_{-\infty}^{\infty} xA_{k,n}^{\rm pol}e^{i(2\pi f t-\psi_{k,n})}\mathrm{d}t\right]. \tag{7.36}$$

In the stationary phase approximation (SPA, see e.g. [25, 26]), $\tilde{h}_k(f)$ is approximated by

$$\tilde{h}_k(f) \sim \frac{\sqrt{6\pi}GM\nu}{4D_L c^2}\sum_{n\geq 1} x(t_n)A_{k,n}^{\rm pol}(t_n)\,e^{i(2\pi f t_n-\psi_{k,n}-\frac{\pi}{4})}\times\sqrt{\frac{1}{\left|\frac{\mathrm{d}^2\psi_{k,n}}{\mathrm{d}t^2}\right|}}, \tag{7.37}$$

evaluated at the stationary points $t_n = t_{\rm 2PN}(f/n)$. The square root of the reciprocal of the second derivative of $\psi_{k,n}$ is found to be

$$\sqrt{\frac{1}{\left|\frac{\mathrm{d}^2\psi_{k,n}}{\mathrm{d}t^2}\right|}} = \frac{\sqrt{5}\,GM}{4\sqrt{6\nu}\,c^3x^{11/4}}[S(f)]_{\rm mod}, \tag{7.38}$$

with $[S(f/n)]_{\rm mod} = S_{\rm 2PN}(f/n) + \Delta S$ being a 2PN function with

$$\begin{aligned} S_{\rm 2PN}(f) &= \left[1+\left(\frac{743}{336}+\frac{11\nu}{8}\right)x+\left(\frac{1}{24}\beta(113,75)-2\pi\right)x^{3/2}\right. \\ &+ \left.\left(\frac{7266251}{8128512}+\frac{18913\nu}{16128}+\frac{1379\nu^2}{1152}+\frac{1}{96}\sigma(247,721)\right)x^2\right], \\ \Delta S &= S_{-1}x^{-1}+S_0+S_{1/2}x^{1/2}+S_1x+S_{3/2}x^{3/2}+S_2x^2+S_{2,\log}x^2\log(x). \end{aligned} \tag{7.39}$$

The S_i are functions of the orbital phase corrections A_i. The waveform can then be written as

$$\begin{aligned} \tilde{h}_k(f) &\sim \frac{\sqrt{5\pi\nu}G^2M^2}{8D_L c^5}\sum_{n\geq 1}A_{k,n}^{\rm pol}(t(f/n))x_n^{-7/4}[S(f/n)]_{\rm mod} \\ &\times \exp\left\{i[n([\Psi(f/n)]_{\rm mod}-\delta\varphi(f/n)-\phi_D[t(f/n)])-\phi_{k,n}^{\rm pol}[t(f/n)]]\right\}, \end{aligned} \tag{7.40}$$

where the modified phase is defined as $[\Psi(f/n)]_{\rm mod} = [\Psi(f/n)]_{\rm 2PN} + \Delta\Psi$, with

$$\begin{aligned}
\Psi_{\rm 2PN} &= \left(\frac{t_c c^3}{GM}\right)x^{3/2} - \phi_c - \frac{\pi}{4} + \frac{3x^{-5/2}}{256\nu}\left[1 + \left(\frac{3715}{756} + \frac{55\nu}{9}\right)x + \left(\frac{1}{3}\beta(113,75) - 16\pi\right)x^{3/2}\right. \\
&\quad \left. + \left(\frac{15293365}{508032} + \frac{27145\nu}{504} + \frac{3085\nu^2}{72} + \frac{5}{24}\sigma(247,721)\right)x^2\right], \\
\Delta\Psi &= \frac{3}{256\nu}x^{-5/2}\left(\Psi_{\text{-}1}x^{-1} + \Psi_0 + \Psi_{1/2}x^{1/2} + \Psi_1 x + \Psi_{3/2}x^{3/2} + \Psi_2 x^2\right). \qquad (7.41)
\end{aligned}$$

The Ψ_i are also functions of the orbital phase corrections A_i. It makes thus sense to work only with the phase correction parameters Ψ_i from now on. The coefficients of ΔS are then, given as functions of Ψ_i:

$$\begin{aligned}
S_{\text{-}1} &= -\frac{7}{24}\Psi_{\text{-}1}, \\
S_0 &= -\frac{35}{48}b_1\Psi_{\text{-}1} - \frac{1}{2}\Psi_0, \\
S_{1/2} &= -\frac{49}{48}b_{3/2}\Psi_{\text{-}1} - \frac{7}{15}\Psi_{1/2}, \\
S_1 &= -\frac{21}{16}\left(\frac{b_1^2}{4} - b_2\right)\Psi_{\text{-}1} + -\frac{7}{12}b_1\Psi_0 - \frac{3}{8}\Psi_1, \\
S_{3/2} &= \left(\frac{77}{96}b_1 b_{3/2} - \frac{49}{24}b_{5/2}\right)\Psi_{\text{-}1} - \frac{3}{4}b_{3/2}\Psi_0 \\
&\quad -\frac{7}{15}b_1\Psi_{1/2} - \frac{1}{4}\Psi_{3/2}, \\
S_2 &= \left(-\frac{91}{384}b_1^3 + \frac{91}{96}b_1 b_2 - \frac{7}{3}b_3 + \frac{91}{192}b_{3/2}^2\right. \\
&\quad \left. - \frac{7}{12}b_{3,\log}\right)\Psi_{\text{-}1} + \left(\frac{11}{48}b_1^2 - \frac{11}{12}b_2\right) \\
&\quad \Psi_0 - \frac{7}{12}b_{3/2}\Psi_{1/2} - \frac{27}{80}b_1\Psi_1 - \frac{7}{60}\Psi_2, \\
S_{2,\log} &= -\frac{7}{3}b_{3,\log}\Psi_{\text{-}1}. \qquad (7.42)
\end{aligned}$$

All the alternative theory parameters Ψ_i are treated as constants. They will most probably depend on other binary parameters such as masses and spins, but it is not possible at this point to find a general parametrization in terms of binary parameters. In practice this could lead to further covariances between the alternative theory and binary parameters. Since in the PN expansion of the gravitational wave phase usually coefficients depending on the symmetric mass ratio of the form $\alpha_1 + \alpha_2\nu + \alpha_3\nu^2 + \ldots$ appear, one could theoretically introduce a new set of parameters, as an attempt to disentangle binary and alternative theory parameters, but it would increase the number of parameters drastically, therefore reducing the accuracy of a single measurement. Since such a parametrization would not induce time varying couplings, and this study focuses on the measurement accuracy for individual systems, we chose not to take the mass ratio into account. However, the spins might lead to time varying modifications; we chose not to take them into account either, because of the lack of theoretical predictions for their form.

7.5 Connection to the ppE formalism

The idea of this work is based on the ppE formalism by Yunes and Pretorius [35]. To look for deviations from GR, they introduce modifications to the amplitude and phase of the gravitational wave in the frequency domain [67]:

$$\begin{aligned} A(f) &= \left(1+\sum_k \alpha_k\, u^{a_k}\right) A^{\mathrm{GR}}(f), \\ \Psi(f) &= \Psi^{\mathrm{GR}}(f) + \sum_k \beta_k\, u^{b_k}. \end{aligned} \tag{7.43}$$

Here, $u = x^{3/2}\nu^{3/5}$ is the reduced frequency and α_k, β_k are alternative theory parameters which could depend on the binary parameters, such as on the symmetric mass ratio or on some spin/angular-momentum quantities. These deviations results in a modification for the n-th harmonic of the gravitational waveform (in the frequency domain) of the form

$$\tilde{h}_n(f) = \tilde{h}_n^{\mathrm{GR}}(f)\,[1+\Delta A_n(f/n)]\, e^{in\Delta\Psi(f/n)}, \tag{7.44}$$

where ΔA_n and $\Delta\Psi$ are power series in the frequency arising from the above modifications, and the overall waveform is the sum $\tilde{h}(f) = \sum_n \tilde{h}_n(f)$. Previous studies [67, 113] used the restricted waveform ($n = 2$) and investigated leading order deviations using a waveform template of the form

$$\tilde{h}(f) = \tilde{h}^{\mathrm{GR}}(f)\left[1+\alpha(4\nu)^A u^a\right] e^{i\beta(4\nu)^B u^b}, \tag{7.45}$$

where a dependency on the symmetric mass ratio ν is introduced. Let us relate this to our parametrization given in Eq. (7.40):

$$\tilde{h}_n(f) = \tilde{h}_n^{\mathrm{GR}}(f)\left(1+\frac{\Delta S(f/n)}{S(f/n)}\right) e^{in\Delta\Psi(f/n)}. \tag{7.46}$$

Since in our implementation we start from the frequency evolution (7.19), the amplitude correction term $\Delta S/S$ entering through the stationary phase approximation is only a pseudo correction, as it can be expressed with phase correction parameters Ψ_i (7.42). Thus our implementation does not consider real amplitude modifications, only the phase parameters Ψ_i can be put into relation with the ppE formalism. The phase modifications $\Delta\Psi$ are, for the ppE formalism and our implementation respectively:

$$\begin{aligned} \Delta\Psi_{\mathrm{ppE}} &= \sum_k \beta_k\,(4\nu)^{B_k}\, u^{b_k}, \\ \Delta\Psi_{\text{this work}} &= \frac{3}{256\nu}\sum_i \Psi_i\, x^{i-5/2}. \end{aligned} \tag{7.47}$$

Because of the special treatment of the symmetric mass ratio prefactor with a parameter B_k and since the symmetric mass ratio enters the conversion between u and x, there is no clear way how to put the parameter sets $\{\beta_k, B_k, b_k\}$ and $\{\Psi_i, i\}$ into relation. Only the frequency powers b_k and i where the corrections enter can be compared: they relate as $b_k = \frac{2}{3}(i_k - \frac{5}{2})$, where the i_k are our summation indices. Our implementation is thus a subset of the ppE formalism with $b_k = \{-7/3, -5/3, -4/3, -1, -2/3, -1/3\}$.

This subset with fixed frequency does not cover the leading order contributions of every alternative to GR currently proposed. While it is able to catch leading order deviations originating from Brans-Dicke, massive graviton and quadratic curvature-type theories, it will not see the leading order imprints of Dynamical Chern-Simons gravity, Variable $G(t)$ theories and theories including extra dimensions (see [67] for an overview table of the leading order contributions of alternative theories). On the other hand, our implementation is able to investigate next-to-leading order effects and can quantify how the inclusion of alternative theory parameters with more than just one frequency power affects the measurement accuracy of a LISA-type detector, including the effects of spin precession and higher harmonics.

7.6 Parameter estimation

To estimate how accurately LISA can measure deviations from the 2PN gravitational wave phase predicted by General Relativity, we use the standard Fisher information formalism for gravitational wave experiments, as reviewed in [92, 114]. The Fisher information formalism holds only in the limit of high SNR; this is true for a LISA-type mission, for which SNRs of a few thousands are expected. For low SNR, advanced Bayesian techniques exploring the whole parameter space such as Markov Chain Monte Carlo methods, (see e.g. [67, 115]) are needed. Also, once data will become available, Bayesian statistics taking into account prior probability distributions will be the preferred framework [116].

We assume the gravitational wave signal to be buried in stationary Gaussian noise $n(t)$ such that the different Fourier components $\tilde{n}(f)$ are uncorrelated. Moreover, we presume that the noise of the two detectors is totally uncorrelated. Assuming flat priors, for a signal $h(t)$ described by a true parameter set $\boldsymbol{\theta}_t$, with noise with spectral density $S_n(f)$, the probability for the measured data $d(t) = n(t) + h(t;\boldsymbol{\theta}_t)$ to take this specific form is proportional to

$$p(d|\boldsymbol{\theta}_t) \propto e^{-(d-h(\boldsymbol{\theta}_t)|d-h(\boldsymbol{\theta}_t))}, \tag{7.48}$$

where the inner product $(g|h)$ is defined as

$$(g|h) = 4\,Re\int_0^\infty \frac{\tilde{g}^*(f)\tilde{h}(f)}{S_n(f)}\mathrm{d}f. \tag{7.49}$$

The use of a waveform template with the parameter set $\boldsymbol{\theta}$ is inaccurate by $\Delta\theta^i = \theta^i_t - \theta^i$. The errors $\Delta\theta^i$ are then approximately given by maximizing the above likelihood distribution, expanding it in the errors assumed to be small and keeping only first derivatives [92]:

$$\langle \Delta\theta_i \Delta\theta_j \rangle = \Sigma_{ij} = (\Gamma^{-1})_{ij} + \mathcal{O}\left(\frac{1}{\mathrm{SNR}}\right), \tag{7.50}$$

where Σ is the covariance matrix and

$$\Gamma_{ij} = \left(\frac{\partial h}{\partial\theta^i}\middle|\frac{\partial h}{\partial\theta^j}\right) \tag{7.51}$$

is the so-called *Fisher matrix*. The expected measurement errors on the parameters θ^i can be expressed as

$$\Delta\theta^i = \sqrt{(\Gamma^{-1})^{ii}}. \tag{7.52}$$

We chose the same noise curve for classic LISA as in [112], namely the piecewise fit used by the LISA parameter estimation community [88] given by the instrumental noise

$$S_n(f) = \frac{1}{L^2}\left\{\left[1+\frac{1}{2}\left(\frac{f}{f_*}\right)^2\right]S_p + \left[1+\left(\frac{10^{-4}}{f}\right)^2\right]\frac{4S_a}{(2\pi f)^4}\right\}, \tag{7.53}$$

and the confusion noise

$$S_{\rm conf}(f) = \begin{cases} 10^{-44.62} f^{-2.3} & (f \leqslant 10^{-3}), \\ 10^{-50.92} f^{-4.4} & (10^{-3} < f \leqslant 10^{-2.7}), \\ 10^{-62.8} f^{-8.8} & (10^{-2.7} < f \leqslant 10^{-2.4}), \\ 10^{-89.68} f^{-20} & (10^{-2.4} < f \leqslant 10^{-2}), \\ 0 & (10^{-2} < f), \end{cases} \tag{7.54}$$

where $L = 5\times10^9$ m is the arm length of classic LISA, $S_p = 4\times10^{-22}$ m^2 Hz^{-1} is the white position noise level, $S_a = 9\times10^{-30}$ m^2 s^{-4} Hz^{-1} is the white acceleration noise level, and $f_* = c/(2\pi L)$ is the arm transfer frequency. The total noise curve is then $S_h(f) = S_n(f) + S_{\rm conf}(f)$.

7.7 Simulations

For our simulations, 21 parameters are needed: 15 GR parameters plus 6 alternative theory parameters. We use

(i) $\log_{10} m_1/M_\odot$ and $\log_{10} m_2/M_\odot$, for the masses of the two black holes.

(ii) $\mu_l = \cos\theta_l$ and ϕ_l, for the spherical angles of the orbital angular momentum $\boldsymbol{L}$ at $\gamma = \frac{1}{6}$.

(iii) $\mu_1 = \cos\theta_1$ and ϕ_1 for the spherical angles of the spin of the first black hole $\boldsymbol{S}_1$ at $\gamma = \frac{1}{6}$.

(iv) $\chi_1 = \frac{c}{Gm_1^2}|\boldsymbol{S}_1|$ for the dimensionless strength of the spin of the first black hole, which has to satisfy $0 \leqslant \chi_1 < 1$.

(v) $\mu_2 = \cos\theta_2$, ϕ_2, and χ_2 for the second black hole, defined equivalently as for the first one.

(vi) $\log t_c$, for the time of coalescence.

(vii) φ_c, the phase at coalescence. As this phase is random and its determination is not of any astrophysical interest, we can safely neglect constants in the orbital phase, in particular $\delta\varphi_0$ from Eq. (7.13).

(viii) $\mu_n = \cos\theta_n$ and ϕ_n, the spherical angles of the position of the binary in the sky.

(ix) $\log d_L$, for the luminosity distance between the source and the Solar System.

(x) Ψ_i with $i \in \{-1, 0, 1/2, 1, 3/2, 2\}$, the 6 alternative theory parameters defined in section 7.4

All angles are taken in the frame tied to the distant stars. Moreover, we set $t = 0$ to be at the time when LISA will start operating.

We perform Monte Carlo simulations, keeping the masses $m_{1,2}$, the redshift z and the alternative theory parameters Ψ_i fixed, and randomizing all other parameters using a flat probability distribution. The spin

precession equations (7.9) are integrated using a fourth order adaptive Runge-Kutta algorithm to find the evolution of $\hat{\boldsymbol{L}}(\omega)$ and $\boldsymbol{S}_{1,2}(\omega)$, going backwards in frequency. As generic starting point for ω, we chose the frequency at the Schwarzschild ISCO (innermost stable circular orbit) $r_{\rm ISCO} = 6\,GM/c^2$. Even though such a clear ISCO does not exist for black hole binaries with comparable mass and precessing spins, we find that this limit is a good cut-off criterion, avoiding unphysical results. For more information about our considerations, the reader is referred to section 7.11.1 in the appendix. We stop the evolution either at $t = 0$ or when the frequency of the highest harmonic goes below the LISA band ($6\omega < 3 \times 10^{-5}$ Hz). The upper and lower bounds on all the randomized parameters of the simulation are straightforward (d_L is just a function of the redshift z, defined in (7.14)), except for t_c for which we set a lower bound of $t_c = t_{\rm 2PN}(\omega(r = r_{\rm ISCO}))$ using Eq. (7.20) and an upper bound of $t_c = 2$yr, which is the minimum science requirement for the LISA mission running time.

Using the angular momentum, spin and orbital time evolution we are able to compute the Fisher matrix elements (7.51), taking the analytical derivatives with respect to $\log t_c$, $\log d_L$, ϕ_c, μ_n, ϕ_n and all the GR correction parameters Ψ_i. The first three derivatives are easy to compute:

$$\frac{\partial \tilde{h}_k(\theta^j, f)}{\partial \log t_c} = 2\pi i f\, t_c\, \tilde{h}_k(\theta^j, f), \tag{7.55}$$

$$\frac{\partial \tilde{h}_k(\theta^j, f)}{\partial \log d_L} = -\tilde{h}_k(\theta^j, f), \tag{7.56}$$

$$\frac{\partial \tilde{h}_k(\theta^j, f)}{\partial \varphi_c} = -i \sum_n n \tilde{h}_{k,n}(\theta^j, f), \tag{7.57}$$

where $\tilde{h}_{k,n}$ is the nth harmonic of $\tilde{h}_k$. The derivatives with respect to the corrections Ψ_i are of the form

$$\begin{aligned}\frac{\partial \tilde{h}_k}{\partial \Psi_i}(f) &= \frac{\sqrt{5\pi\nu} G^2 M^2}{8 D_L c^5} \sum_{n\geq 1} A^{\rm pol}_{k,n} x_n^{-7/4} \times e^{i\left[n(\Psi_{\rm GR} + \Delta\Psi - \delta\varphi - \phi_D) - \phi^{\rm pol}_{k,n}\right]} \\ &\quad \times \left(i\, n\, (S_{\rm 2PN} + \Delta S) \frac{\partial \Delta\Psi}{\partial \Psi_i} + \frac{\partial \Delta S}{\partial \Psi_i} \right),\end{aligned} \tag{7.58}$$

and can be calculated in a straightforward way. The derivatives which we could not compute analytically are approximated by

$$\frac{\partial \tilde{h}_k(\theta^j, f)}{\partial \theta^i} \approx \frac{\tilde{h}_k(\theta^j + \frac{1}{2}\epsilon\delta^{ij}, f) - \tilde{h}_k(\theta^j - \frac{1}{2}\epsilon\delta^{ij}, f)}{\epsilon}, \tag{7.59}$$

where ϵ is a small displacement of the parameter θ_i which we chose to be of the constant value $\epsilon = 10^{-7}$ for every parameter, except for ϕ_l for which ϵ was divided by $2 - 2|\mu_l|$, μ_i ($i \in \{1, 2\}$) for which ϵ was divided by $5\chi_i$, and ϕ_i for which ϵ was divided by $10\chi_i(1 - |\mu_i|)$. The formula is accurate up to $O(\epsilon^2)$. For each set of parameters we then compute the Fisher matrix using *Clenshaw-Curtis quadrature* and then invert it in order to find the corresponding errors on the parameters which we analyze in section 7.8. In order to avoid matrix inversion problems, we use a normalization of the Fisher-Matrix so that all diagonal elements are $A_{ii} = 1$ and all off-diagonal elements are in the range $A_{ij} \in [-1; 1]$:

$$A_{ij} \equiv \frac{1}{\sqrt{\Gamma_{ii}\Gamma_{jj}}}\, \Gamma_{ij}. \tag{7.60}$$

After inversion, the covariance matrix can then be recovered with

$$\Sigma_{ij} = \frac{1}{\sqrt{\Gamma_{ii}\Gamma_{jj}}} A^{-1}_{ij}. \tag{7.61}$$

In situations where $\hat{\boldsymbol{L}} \cdot \hat{\boldsymbol{n}}$ is close to 1, the Runge Kutta method fails to converge because

$$\frac{\mathrm{d}\delta\varphi}{\mathrm{d}\omega} = \frac{\hat{\boldsymbol{L}} \cdot \hat{\boldsymbol{n}}}{1 - \left(\hat{\boldsymbol{L}} \cdot \hat{\boldsymbol{n}}\right)^2} \left(\hat{\boldsymbol{L}} \times \hat{\boldsymbol{n}}\right) \cdot \frac{\mathrm{d}\hat{\boldsymbol{L}}}{\mathrm{d}\omega} \underset{\hat{\boldsymbol{L}}\cdot\hat{\boldsymbol{n}}\to 1}{\longrightarrow} \infty. \tag{7.62}$$

Whenever this happens, we take the approximate value

$$\delta\varphi(\omega + \delta\omega)\delta\varphi(\omega) + \mathrm{angle}\left[\left(\hat{\boldsymbol{L}}(\omega + \delta\omega) \times \hat{\boldsymbol{n}}\right), \left(\hat{\boldsymbol{L}}(\omega) \times \hat{\boldsymbol{n}}\right)\right], \tag{7.63}$$

as explained in [112].

7.8 Results

We performed simulations for 17 different mass configurations, with total masses between $10^5 M_\odot$ and $10^8 M_\odot$, mass ratios varying between 1:1 and 1:10, and using 10^3 points in the parameter space for each configuration. The redshift has been kept fixed to $z = 1$ since it is not possible to disentangle redshift, mass and distance. The signal coming from a binary with masses $m_{1,2}$ at redshift z and luminosity distance $d_L(z)$ can be expressed with one from an apparent binary with $\tilde{m}_{1,2} = \frac{1+z}{1+z_0} m_{1,2}$ at redshift z_0 and luminosity distance $d_L(z_0)$ multiplied by an overall factor of $d_L(z_0)/d_L(z)$. Thus every BBH inspiral producing a signal at redshift z can be described with a waveform template at redshift z_0. The Fisher matrix scales as

$$\begin{aligned} \Gamma^{(z)}_{ij} &= \left(\frac{\partial h}{\partial \theta^i}(m_1, m_2, z) \middle| \frac{\partial h}{\partial \theta^j}(m_1, m_2, z)\right) = \left(\frac{d_L(z_0)}{d_L(z)}\right)^2 \left(\frac{\partial h}{\partial \theta^i}(\tilde{m}_1, \tilde{m}_2, z_0) \middle| \frac{\partial h}{\partial \theta^j}(\tilde{m}_1, \tilde{m}_2, z_0)\right) \\ &= \left(\frac{d_L(z_0)}{d_L(z)}\right)^2 \Gamma^{(z_0)}_{ij}. \end{aligned} \tag{7.64}$$

The errors on the parameters scale then with (Fig. 7.1)

$$\Delta\theta^i(z) = \frac{d_L(z)}{d_L(z_0)} \Delta\theta^i(z_0). \tag{7.65}$$

Since we choose to work in a picture where General Relativity is the theory assumed to be true and we are keen to know how well LISA will be able to measure deviations from its post-Newtonian expansion terms ψ_i, we fixed the alternative theory parameters to the fiducial values $\Psi_i = 0$.

For each of the 17 binaries we computed the best-case measurement error (5% quantile), the typical error (median) and the worst-case error (95% quantile) for the full (FWF) and restricted waveforms (RWF) and present them in tables 7.1-7.14. For each BBH parameter we are interested in, we give an error table with (21 parameters in total) and without (15 parameters in total) including the alternative theory parameters Ψ_i. We do this to show how much accuracy is lost by introducing alternative theory corrections into a GR waveform template. For binaries where no signal can be extracted from the dataset, we fix the error to infinity. We give the errors on the sky localization not in terms of errors on μ_n and ϕ_n but instead in terms of an error ellipse with principal axes $2a$ and $2b$, enclosing the region outside of which there is an $1/e$ probability of finding the binary, following [117]. Moreover, in tables 7.15-7.20 we give measurement errors on the alternative theory parameters, using both the RWF and FWF.

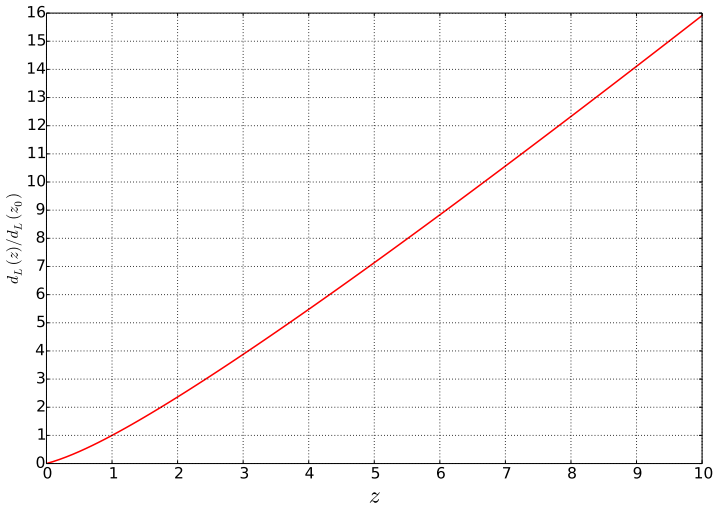

Figure 7.1: *Multiplication factor $d_L(z)/d_L(z_0)$ that scales the errors on the individual parameters computed at redshift $z = 1$.*

We roughly divide the binaries into two classes: low-mass binaries ($M \lesssim 10^7 M_\odot$) and high-mass binaries ($M \gtrsim 10^7 M_\odot$). Below we discuss these two cases, using BBHs with $m_1 = 10^6 M_\odot$, $m_2 = 3 \times 10^5 M_\odot$ and $m_1 = 3 \times 10^7 M_\odot$, $m_2 = 10^7 M_\odot$ as representative examples for low-mass and high-mass binaries respectively. We find when using both the RWF and the FWF, the error distributions of the mass and spin parameters behave similarly, losing a factor $1.2-5$ of accuracy when alternative theory parameters are included. The error on the sky location of the binary $2a$ and $2b$ is at maximum an order of magnitude worse. For high-mass binaries, factors of ~ 10 and ~ 100 are lost in the determination of the luminosity distance d_L, using the FWF and RWF respectively. While the RWF/FWF errors on the alternative theory parameters are almost equal for low-mass binaries, the RWF errors are about 100 times higher for high-mass binaries

7.8.1 Low-mass binaries

For low-mass binaries with total masses below $10^7 M_\odot$ we find that in general, using the FWF instead of the RWF improves the measurement errors $\Delta\Psi_i$ on the alternative theory parameters by a factor of $\sim 1.5-3$. The correlation with the new parameters causes a decrease in the accuracy of the 15 binary parameters. For both the FWF and the RWF, the errors on the mass and spin parameters are typically worse by a factor of $2-5$ while the luminosity distance is approximately half as accurate. The sky location errors increase only by $\sim 10\%$; this is reasonable, since we do not expect alternative theories to correlate strongly with rotations on a large scale. Therefore it is not necessary to use the FWF instead of the RWF for the sole purpose of measuring alternative gravity parameters in the low-mass regime. We present selected distributions of the measurement errors $\Delta m_1/m_1$, $\Delta\chi_1/\chi_1$, $2a$, $\Delta d_L/d_L$ and all the six $\Delta\Psi_i$ in figures 7.2-7.15. The error distributions of $\Delta m_2/m_2$, $\Delta\chi_2/\chi_2$ and $2b$ are similar to the ones of $\Delta m_1/m_1$, $\Delta\chi_1/\chi_1$ and $2a$.

It is important to recall that we used the low frequency approximation (LFA) [82, 84, 85, 118] to generate the LISA detector response. This approximation holds as long as the wavelength of the gravitational wave is much larger than the arm length L of the LISA-type detector, in other words: as long as $f_{GW} \ll f_* = \frac{c}{2\pi L}$, where c is the speed of light and f_* is the so called *transfer frequency*. As soon as the wavelength is comparable to the arm length, the detector response function begins to depend strongly on the sky location

and orientation of the source. Effects neglected before, such as the cartwheel motion of LISA, become important, resulting in a modulation of the the waveforms: more information about orientation and sky location is encoded in the signal. Consequently, the errors on extrinsic parameters such as the angles μ_n, ϕ_n, the luminosity distance d_L and the angular momentum orientation μ_l, ϕ_l effectively decrease compared to the LFA, while the intrinsic parameter errors differ only slighly. Usually, the problems with the approximation start around 3 mHz [82, 85, 119]: in our case the first three mass configurations with total masses of 3.3×10^5, 4×10^5 and $6\times10^5 M_\odot$ are above this limit, with frequencies (at $f_{\rm ISCO}=6\,GM/c^2$ and redshift z=1) of 6.6, 5 and 3.6 mHz, respectively. Following Fig. 2 in [85], this means that our results for these three configurations should be too pessimistic, the relative errors on the luminosity distance would in general be smaller by $\sim$ 10%, 20% and 50% for the respective configurations. Also the errors on sky location and angular momentum orientation will be better by up to $\sim$ 50% for the 3.3×10^5 binary.

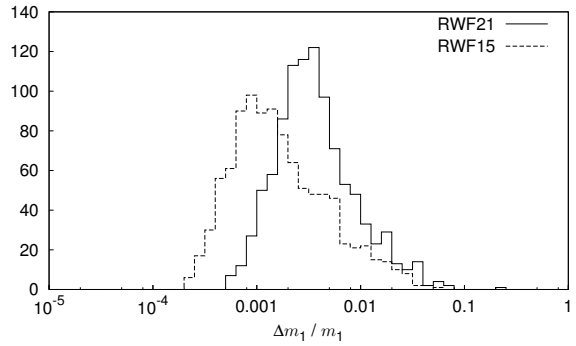

Figure 7.2: *Comparison between the estimated distributions of the measurement error on m_1 for a low-mass binary system $m_1 = 1\times10^6 M_\odot$ and $m_2 = 3\times10^5 M_\odot$ with (RWF21) and without (RWF15) including alternative theory parameters, using only the restricted waveform.*

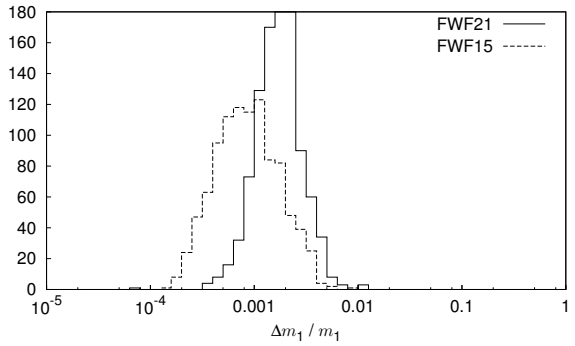

Figure 7.3: *Comparison between the estimated distributions of the measurement error on m_1 for a low-mass binary system $m_1 = 1\times10^6 M_\odot$ and $m_2 = 3\times10^5 M_\odot$ with (FWF21) and without (FWF15) including alternative theory parameters and using the full waveform.*

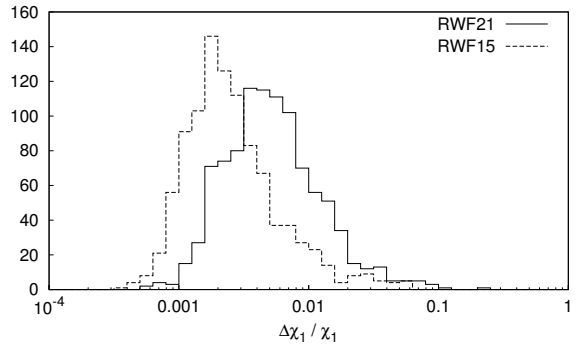

Figure 7.4: *Comparison between the estimated distributions of the measurement error on χ_1 for a low-mass binary system $m_1 = 1\times10^6 M_\odot$ and $m_2 = 3\times10^5 M_\odot$ with (RWF21) and without (RWF15) including alternative theory parameters, using only the restricted waveform.*

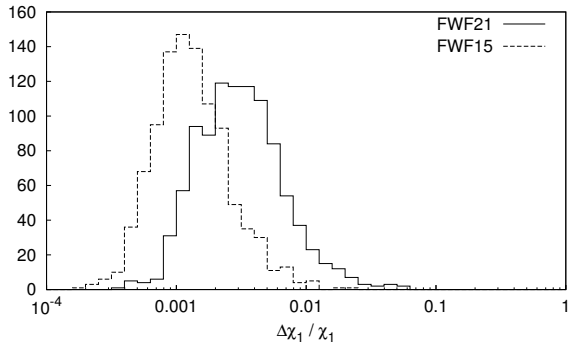

Figure 7.5: *Comparison between the estimated distributions of the measurement error on χ_1 for a low-mass binary system $m_1 = 1\times10^6 M_\odot$ and $m_2 = 3\times10^5 M_\odot$ with (FWF21) and without (FWF15) including alternative theory parameters and using the full waveform.*

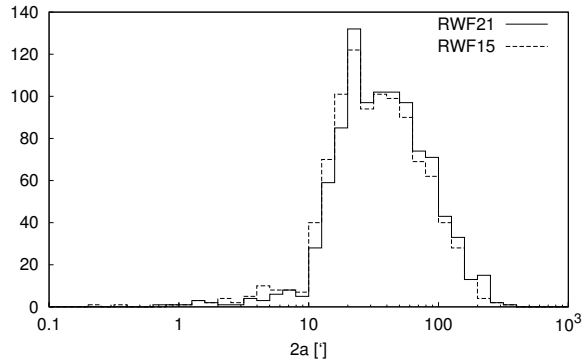

Figure 7.6: *Comparison between the estimated distributions of the major axis of the positioning error ellipse for a low-mass binary system $m_1 = 1 \times 10^6 M_\odot$ and $m_2 = 3 \times 10^5 M_\odot$ with (RWF21) and without (RWF15) including alternative theory parameters, using only the restricted waveform.*

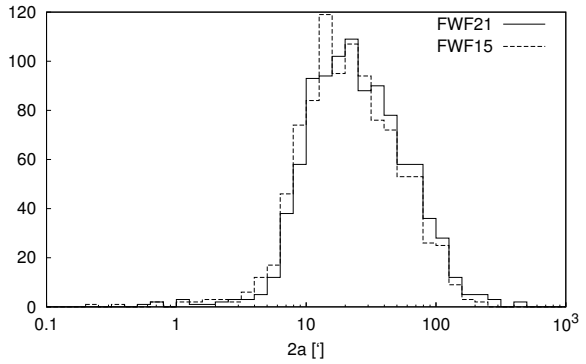

Figure 7.7: *Comparison between the estimated distributions of the major axis of the positioning error ellipse for a low-mass binary system $m_1 = 1 \times 10^6 M_\odot$ and $m_2 = 3 \times 10^5 M_\odot$ with (FWF21) and without (FWF15) including alternative theory parameters and using the full waveform.*

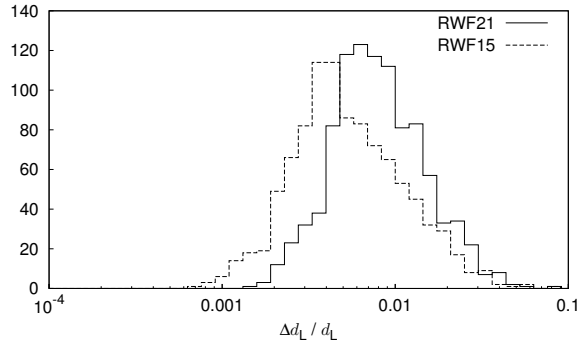

Figure 7.8: *Comparison between the estimated distributions of the measurement error on d_L for a low-mass binary system $m_1 = 1 \times 10^6 M_\odot$ and $m_2 = 3 \times 10^5 M_\odot$ with (RWF21) and without (RWF15) including alternative theory parameters, using only the restricted waveform.*

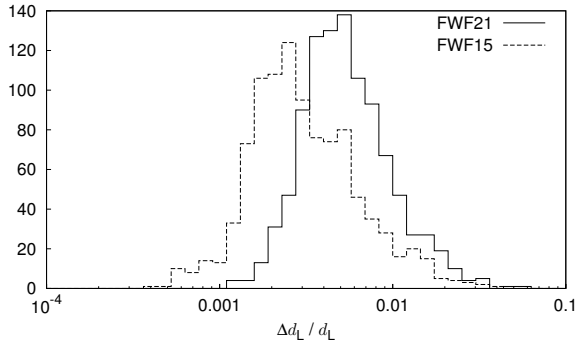

Figure 7.9: *Comparison between the estimated distributions of the measurement error on d_L for a low-mass binary system $m_1 = 1 \times 10^6 M_\odot$ and $m_2 = 3 \times 10^5 M_\odot$ with (FWF21) and without (FWF15) including alternative theory parameters, using only the restricted waveform.*

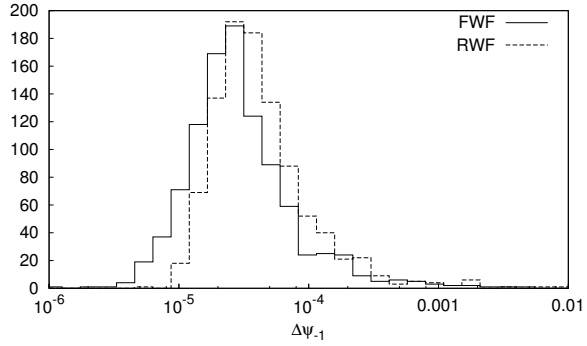

Figure 7.10: *Comparison between the estimated distributions of the measurement error on the alternative theory parameter Ψ_{-1} for a low-mass binary system $m_1 = 1 \times 10^6 M_\odot$ and $m_2 = 3 \times 10^5 M_\odot$, using the restricted waveform (RWF) and the full waveform (FWF).*

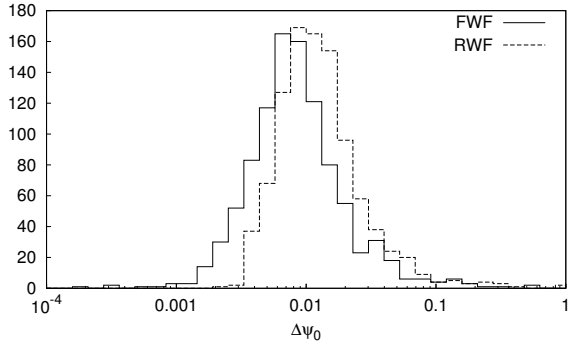

Figure 7.11: *Comparison between the estimated distributions of the measurement error on the alternative theory parameter Ψ_0 for a low-mass binary system $m_1 = 1 \times 10^6 M_\odot$ and $m_2 = 3 \times 10^5 M_\odot$, using the RWF and the FWF.*

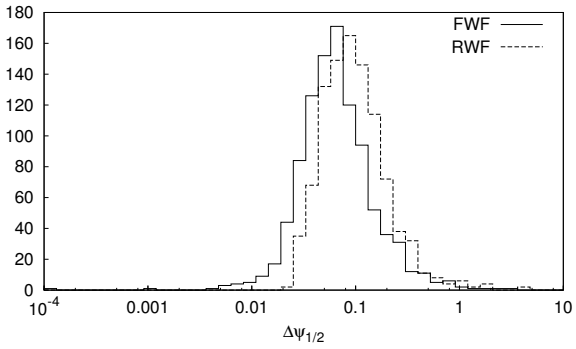

Figure 7.12: *Comparison between the estimated distributions of the measurement error on the alternative theory parameter $\Psi_{1/2}$ for a low-mass binary system $m_1 = 1\times10^6 M_\odot$ and $m_2 = 3\times10^5 M_\odot$, using the RWF and the FWF.*

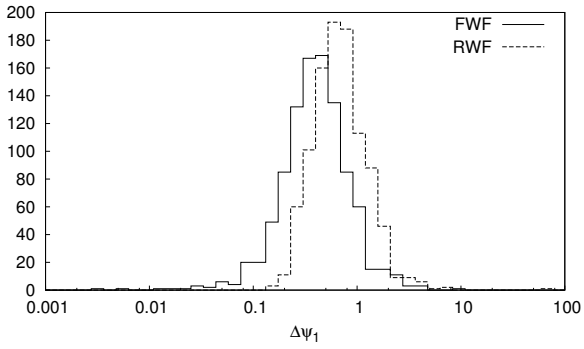

Figure 7.13: *Comparison between the estimated distributions of the measurement error on the alternative theory parameter Ψ_1 for a low-mass binary system $m_1 = 1\times10^6 M_\odot$ and $m_2 = 3\times10^5 M_\odot$, using the RWF and the FWF.*

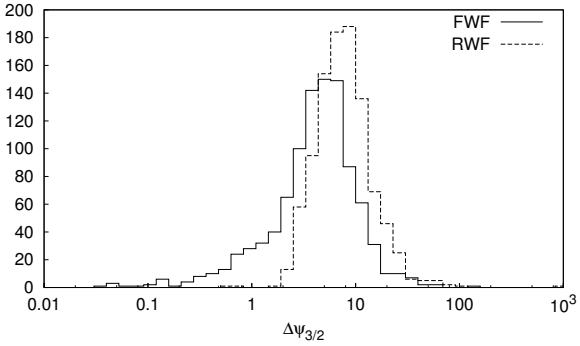

Figure 7.14: *Comparison between the estimated distributions of the measurement error on the alternative theory parameter $\Psi_{3/2}$ for a low-mass binary system $m_1 = 1\times10^6 M_\odot$ and $m_2 = 3\times10^5 M_\odot$, using the RWF and the FWF.*

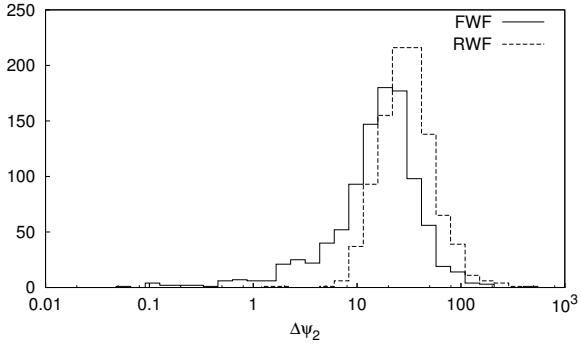

Figure 7.15: *Comparison between the estimated distributions of the measurement error on the alternative theory parameter Ψ_2 for a low-mass binary system $m_1 = 1\times10^6 M_\odot$ and $m_2 = 3\times10^5 M_\odot$, using the RWF and the FWF.*

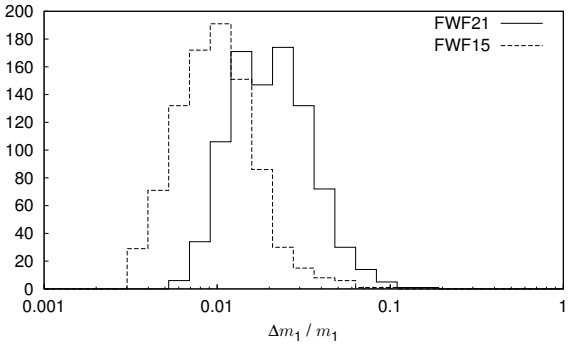

Figure 7.16: *Comparison between the estimated distributions of the measurement error on m_1 for a high-mass binary system $m_1 = 3\times10^7 M_\odot$ and $m_2 = 1\times10^7 M_\odot$ with (FWF21) and without (FWF15) including alternative theory parameters and using the full waveform.*

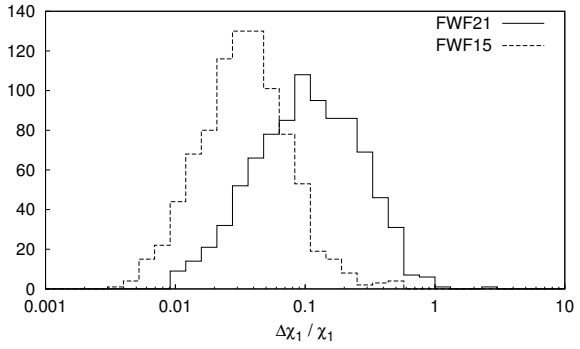

Figure 7.17: *Comparison between the estimated distributions of the measurement error on χ_1 for a high-mass binary system $m_1 = 3\times10^7 M_\odot$ and $m_2 = 1\times10^7 M_\odot$ with (FWF21) and without (FWF15) including alternative theory parameters and using the full waveform.*

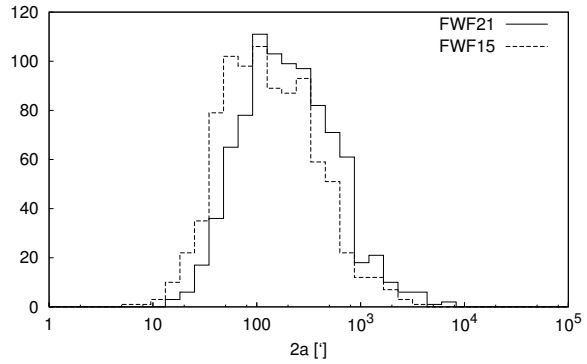

Figure 7.18: *Comparison between the estimated distributions of the major axis of the positioning error ellipse for a high-mass binary system $m_1 = 3 \times 10^7 M_\odot$ and $m_2 = 1 \times 10^7 M_\odot$ with (FWF21) and without (FWF15) including alternative theory parameters and using the full waveform.*

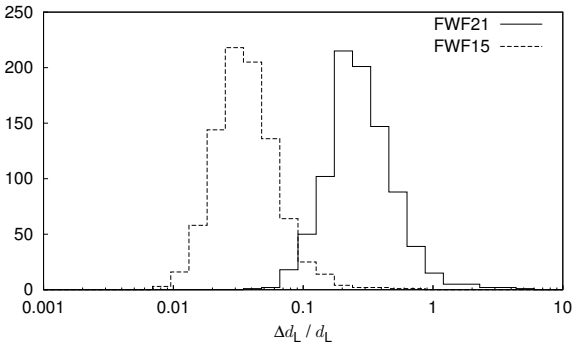

Figure 7.19: *Comparison between the estimated distributions of the measurement error on d_L for a high-mass binary system $m_1 = 3 \times 10^7 M_\odot$ and $m_2 = 1 \times 10^7 M_\odot$ with (FWF21) and without (FWF15) including alternative theory parameters, using only the restricted waveform.*

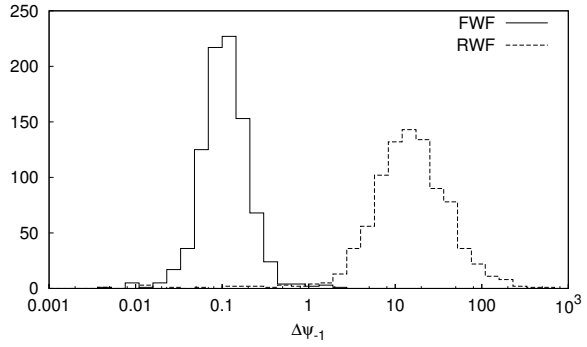

Figure 7.20: *Comparison between the estimated distributions of the measurement error on the alternative theory parameter Ψ_{-1} for a high-mass binary system $m_1 = 3 \times 10^7 M_\odot$ and $m_2 = 1 \times 10^7 M_\odot$, using the RWF and the FWF.*

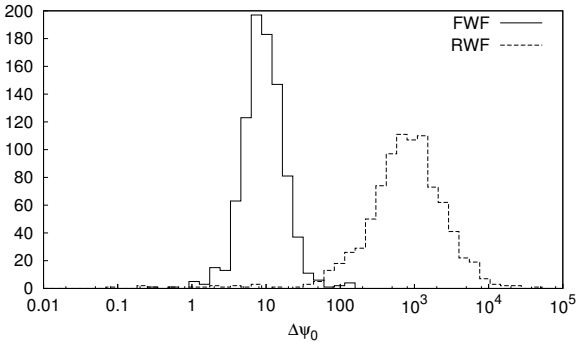

Figure 7.21: *Comparison between the estimated distributions of the measurement error on the alternative theory parameter Ψ_0 for a high-mass binary system $m_1 = 3 \times 10^7 M_\odot$ and $m_2 = 1 \times 10^7 M_\odot$, using the RWF and the FWF.*

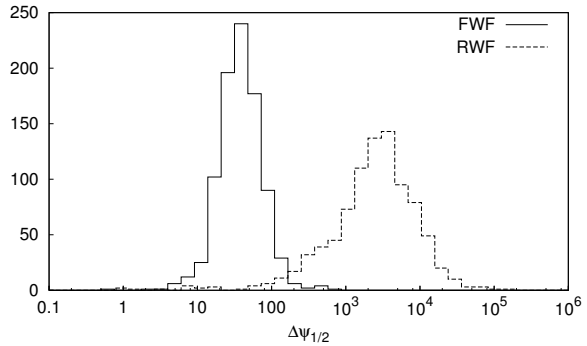

Figure 7.22: *Comparison between the estimated distributions of the measurement error on the alternative theory parameter $\Psi_{1/2}$ for a high-mass binary system $m_1 = 3 \times 10^7 M_\odot$ and $m_2 = 1 \times 10^7 M_\odot$, using the RWF and the FWF.*

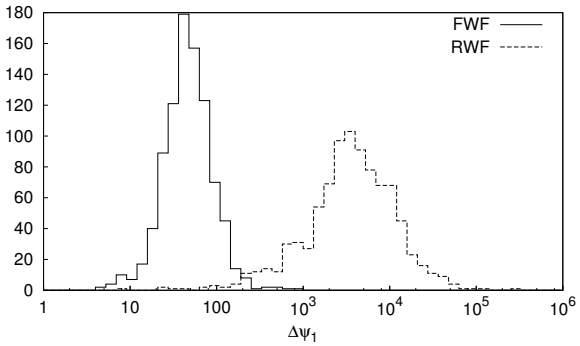

Figure 7.23: *Comparison between the estimated distributions of the measurement error on the alternative theory parameter Ψ_1 for a high-mass binary system $m_1 = 3 \times 10^7 M_\odot$ and $m_2 = 1 \times 10^7 M_\odot$, using the RWF and the FWF.*

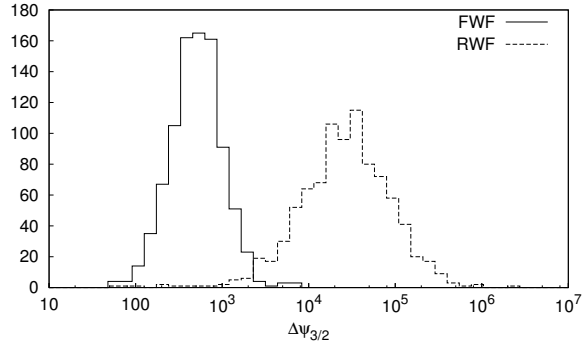

Figure 7.24: *Comparison between the estimated distributions of the measurement error on the alternative theory parameter $\Psi_{3/2}$ for a high-mass binary system $m_1 = 3\times10^7 M_\odot$ and $m_2 = 1\times10^7 M_\odot$, using the RWF and the FWF.*

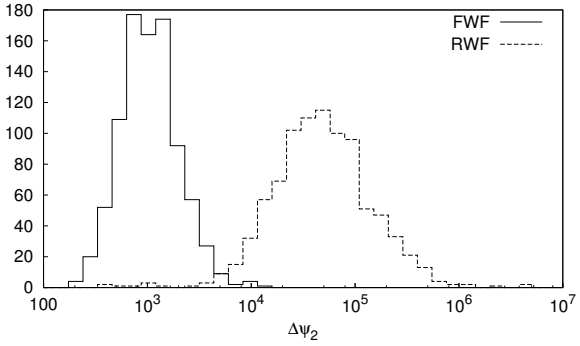

Figure 7.25: *Comparison between the estimated distributions of the measurement error on the alternative theory parameter Ψ_2 for a high-mass binary system $m_1 = 3\times10^7 M_\odot$ and $m_2 = 1\times10^7 M_\odot$, using the RWF and the FWF.*

7.8.2 High-mass binaries

By using the FWF instead of the RWF for high-mass binaries with total masses $\gtrsim 10^7 M_\odot$, we find significant improvements for the measurement errors of the alternative theory parameters by factors of $\sim 100-1000$ for $\Delta\Psi_{-1}$, $\sim 30-60$ for $\Delta\Psi_0$ and $\Delta\Psi_{1/2}$, and $\sim 10-100$ for $\Delta\Psi_1$, $\Delta\Psi_{3/2}$ and $\Delta\Psi_2$. This makes it clear that it is inevitable to use the FWF in the high-mass regime to perform precision tests of GR. In any case, since the second harmonic spends only a few orbits in the LISA band, the use of the RWF is not trustworthy. Moreover, for BBHs with total masses higher than $10^8 M_\odot$, LISA will not be able to see the second harmonic at all and so the RWF cannot be used. For both the FWF and the RWF, the errors on the mass and spin parameters are typically worse by a factor of $\sim 1.2-4$ when accounting for alternative gravity parameters. The luminosity distance is about $50-1000$ times less accurate for the RWF while for the FWF it is only $\sim 10-100$ times worse. For the FWF, the sky location error is at maximum 5 times worse while the RWF loses up to a factor of ~ 10 in accuracy.

We present selected distributions of the measurement errors $\Delta m_1/m_1$, $\Delta\chi_1/\chi_1$, $2a$, $\Delta d_L/d_L$ and all the six $\Delta\Psi_i$ in figures 7.16-7.25.

7.8.3 Correlations between alternative theory parameters

The correlation coefficients for two parameters θ_i and θ_j are given by the normalized covariance matrix as

$$C_{ij} = \frac{\Sigma_{ij}}{\sqrt{\Sigma_{ii}\Sigma_{jj}}}, \tag{7.66}$$

and are in a range between -1 (perfectly anti-correlated) and 1 (perfectly correlated). Since we are only interested in the mere presence of correlations, we will focus on the absolute value $|C_{ij}|$ varying in the range between 0 (no correlation) and 1.

Because of their simple form in the gravitational wave phase, the alternative theory parameters are expected to correlate highly among each other and with the rest of the phase parameters, especially with the ones which have a similar simple dependency on frequency (and are already highly correlated) like the phase or time at coalescence, ϕ_c and t_c. Often, the use of higher harmonics makes the resulting errors and correlations more complicated and unpredictable: the mostly narrow and symmetric RWF distribution is

smeared out over the whole range of possible correlations, usually with a long tail. Also, higher harmonics can in principle introduce new correlations among certain parameters that have not been there before. Below we shortly investigate correlations among the alternative theory parameters and between alternative theory and binary parameters.

Correlations between alternative theory parameters

We find that the alternative theory parameters can be subdivided into two sets: $\Psi_{\rm low} \equiv \{\Psi_{\text{-}1}, \Psi_0, \Psi_{1/2}\}$ and $\Psi_{\rm high} \equiv \{\Psi_1, \Psi_{3/2}, \Psi_2\}$. The parameters in every set show very high correlations among each other, but less correlation with the parameters of the other set. The parameters in $\Psi_{\rm low}$ have either no fiducial GR phase equivalent with the same frequency power ($\Psi_{\text{-}1}$ and $\Psi_{1/2}$) or one which is fixed to 1 (Ψ_0). In contrast, every parameter in $\Psi_{\rm high}$ can correlate to intrinsic binary parameters with the same frequency dependency, such as masses and spins. Since one integrates over the frequency to compute the Fisher matrix, two parameters have higher correlation if the frequency powers proportional to which they appear in the phase or amplitude are close. So we expect parameters from $\Psi_{\rm high}$ to have higher correlation with the intrinsic binary parameters appearing in the GR phase with the same frequency power than with the $\Psi_{\rm low}$ parameters appearing with lower frequency powers. Consequently, we expect high correlations among the parameters within both sets and also high, but slightly lower correlations between parameters belonging to a different set each. In Fig. 7.30, we plotted the median FWF correlations for selected parameters of both sets against the total mass to illustrate this finding. For two parameters drawn from different sets, the mass ratio also plays an important role for the resulting correlations, while for parameters from the same set, the correlations mainly depend on the total mass.

Within the set $\Psi_{\rm low}$, the FWF is not very effective in breaking the correlations that are present using the RWF model, in some cases it even introduces further correlation. Among theory parameters from the set $\Psi_{\rm high}$, there is a modest correlation breaking for high total masses while for low masses the FWF model stretches out the nearly symmetric RWF correlation distributions by providing them with a long tail on the left-hand side and slightly shifting the peak to the right-hand side (Fig. 7.26). For correlations between two parameters coming out from different sets, there is the same stretching effect and modest correlation breaking for high-masses as for parameters in $\Psi_{\rm high}$, but only for parameters from $\Psi_{\rm low}$ in combination with Ψ_2, a stronger breaking of correlations is achieved by the FWF (Fig. 7.27).

Correlations between binary and theory parameters

Although there are mass and spin-dependent terms that are proportional to the same frequency power as the alternative theory parameters, mass, spin and angular momentum parameters show only absolute correlations of $\lesssim 0.5$ with the theory parameters, because they enter non-linearly and in several different frequency powers. The phase and time at coalescence ϕ_c and t_c are formally equivalent to $\Psi_{5/2}$ and Ψ_4, respectively, and are therefore highly correlated with the theory parameters. Especially for tightly correlated parameters, correlations can be broken easily through the introduction of extra structure with higher harmonics. Also the correlations with the sky position parameters μ_n and ϕ_n can be strongly broken for high masses (Fig. 7.28) when using higher harmonics. Interestingly, correlations with the luminosity distance parameter d_L increase for low masses (extra structure can in principle also introduce additional correlations), while there is a modest breaking for high masses (Fig. 7.29).

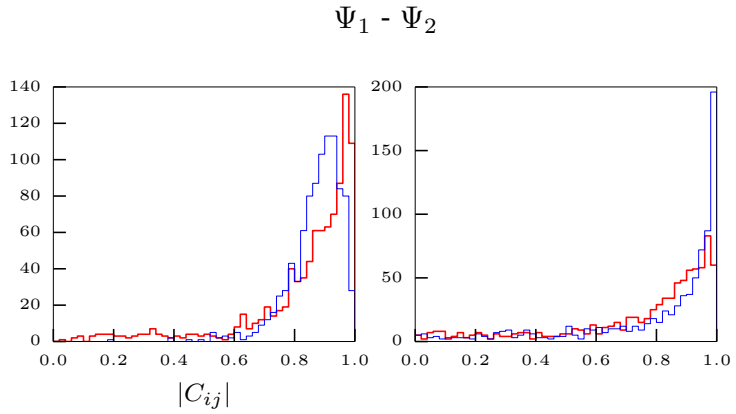

Figure 7.26: *Correlation breaking for a low-mass $m_1 = 10^6 M_\odot$, $m_2 = 3 \times 10^5 M_\odot$ binary (left) and a $m_1 = 3 \times 10^7 M_\odot$, $m_2 = 10^7 M_\odot$ binary (right). The results of the RWF are indicated with the (thin) blue line and the results for the FWF with the (bold) red line. For this selected combination of theory parameters, there is modest breaking for high masses.*

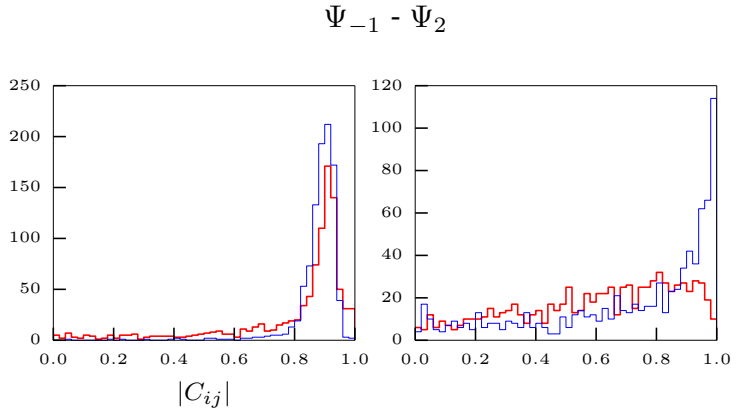

Figure 7.27: *Correlation breaking for a low-mass $m_1 = 10^6 M_\odot$, $m_2 = 3 \times 10^5 M_\odot$ binary (left) and a $m_1 = 3 \times 10^7 M_\odot$, $m_2 = 10^7 M_\odot$ binary (right). The results of the RWF are indicated with the (thin) blue line and the results for the FWF with the (bold) red line. For this selected combination of theory parameters, there is stronger correlation breaking for high masses.*

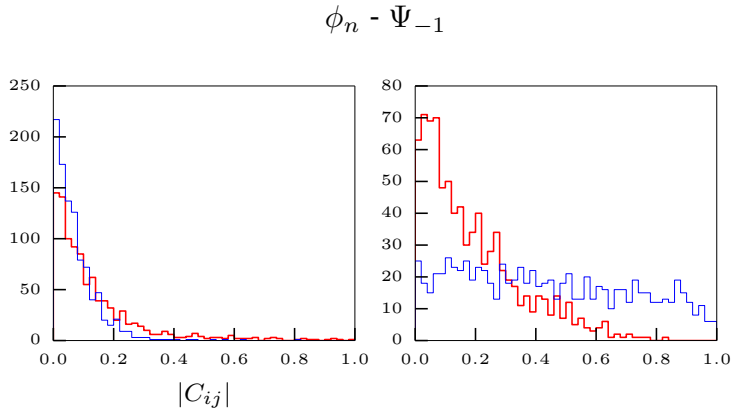

Figure 7.28: *Correlation breaking for a low-mass $m_1 = 10^6 M_\odot$, $m_2 = 3 \times 10^5 M_\odot$ binary (left) and a $m_1 = 3 \times 10^7 M_\odot$, $m_2 = 10^7 M_\odot$ binary (right). The results of the RWF are indicated with the thin (blue) line and the results for the FWF with the bold (red) line. When accounting for higher harmonics, correlations of ϕ_n with alternative theory parameters are strongly broken for high masses.*

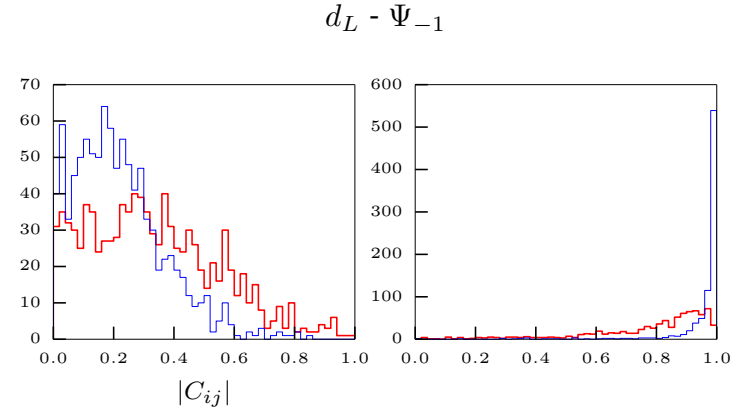

Figure 7.29: *Correlation breaking for a low-mass $m_1 = 10^6 M_\odot$, $m_2 = 3 \times 10^5 M_\odot$ binary (left) and a $m_1 = 3 \times 10^7 M_\odot$, $m_2 = 10^7 M_\odot$ binary (right). The results of the RWF are indicated with the thin (blue) line and the results for the FWF with the bold (red) line. For low masses, the correlation with the luminosity distance parameter increases while there is modest breaking for high masses when introducing higher harmonics.*

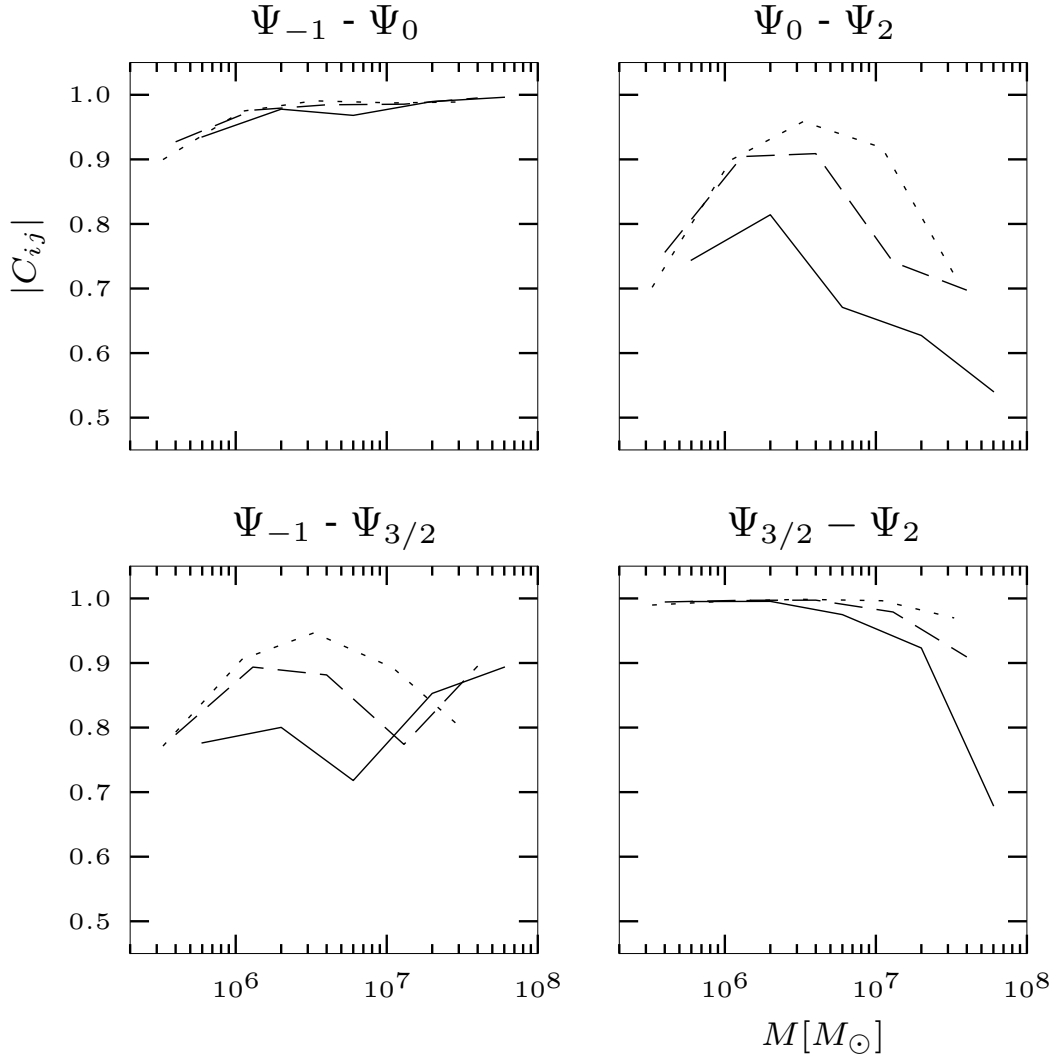

Figure 7.30: *Median correlations (FWF) between selected alternative theory parameters varying with total mass and shown for each mass ratio independently (1:1 - solid line, 1:3 - dashed line, 1:10 - dotted line). The sets* $\{\Psi_{-1}, \Psi_0, \Psi_{1/2}\}$ *and* $\{\Psi_1, \Psi_{3/2}, \Psi_2\}$ *show very high correlations among themselves (top-left, bottom-right) while correlations between theory parameters belonging to different sets are lower (top-right, bottom-left).*

7.8.4 Upper limits for redshifted masses

All the errors tabularized in appendix 7.11.3 are given for the fixed redshift $z = 1$. Some of them in the high-mass regime are apparently too high at $z = 1$. Nevertheless, since the measurement accuracy of the parameters is correlated with the redshift as given in Eq. (7.65), for an equivalent mass configuration at a lower redshift the errors should reduce to reasonable values. Since the actual values of the alternative theory parameters are not known, we cannot fix the accuracy with which we want to measure $\Psi_i(z)$. For this reason, we introduce the relative accuracy parameter α such that $\Delta\Psi_i(z)/\psi_i < \alpha$ where ψ_i is the fiducial 2PN phase coefficient from $\Psi_{\rm 2PN}$ in Eq. (7.41). The maximal redshift is then given as

$$z_{\rm max} = z\left(\alpha\, d_L(z_0)\, |\Delta\Psi_i(z_0)/\psi_i|^{-1}\right), \tag{7.67}$$

where $z(d_L)$ is the inverse of (7.14) and can be computed numerically. We use here the 5%-quantile for $\Delta\Psi_i(z_0 = 1)$ as given in the tables in appendix 7.11.3, i.e. we define the (optimistic) maximal redshift as the redshift where 5% of the binaries in the sample can still be seen with relative accuracy less than α. Since we expect corrections to the 2PN phase parameters of GR to be small (at least for the lower PN orders), we focus here on a relative accuracy below 10%. At redshift $z = 1$ this accuracy is already difficult to reach for binaries with masses above $10^6 M_\odot$ (see also [70]). It is important to emphasize that we concentrate here on actually measuring the alternative theory parameters instead of just setting bounds upon them. In figures 7.31-7.34 we present the maximal redshifts at which LISA can still measure the alternative theory parameters Ψ_0, Ψ_1, $\Psi_{3/2}$ and Ψ_2 for certain mass configurations with relative accuracies of $\alpha = 10\%$ and $\alpha = 1\%$. Since for Ψ_{-1} and $\Psi_{1/2}$ the fiducial 2PN phase coefficients are zero, we do not consider them. We checked that the error roughly scales with the redshift. For a relative accuracy of 1%, Ψ_0 is measurable up to redshifts of $z \sim 1-10$ for low-mass binaries and up to redshifts of $z \sim 0.01-0.1$ for high-mass binaries. Ψ_1, $\Psi_{3/2}$ and Ψ_2 can all be detected with a relative accuracy of 1% up to redshifts of $z \sim 0.1-1$ for low masses and $z \sim 0.01-0.1$ for high masses. For Ψ_0, the use of the FWF improves the maximal redshifts by about a factor of 2 for low masses and up to a factor of 10 for high masses, while the maximal redshifts are improved by almost an order of magnitude for the rest of the alternative theory parameters. If we were lucky and LISA could find a low-mass black hole binary at very low redshift $z = 0.1$, we would be able to recover the alternative theory parameters with ~ 10 times smaller errors than given in tables 7.15-7.20.

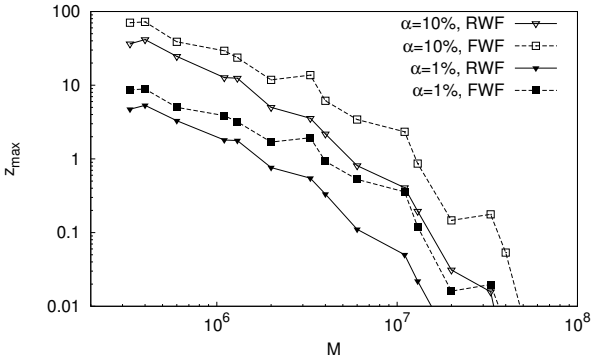

Figure 7.31: *Maximal redshifts for the alternative theory parameter Ψ_0 such that the relative error $\Delta\Psi_0/\psi_0$ is smaller than α. ψ_0 is the corresponding fiducial 2PN phase coefficient. For a relative error of 1%, low-mass binaries are suitable up to redshifts $z \sim 1-10$ while high-mass binaries can be observed up to $z \sim 0.01-0.1$.*

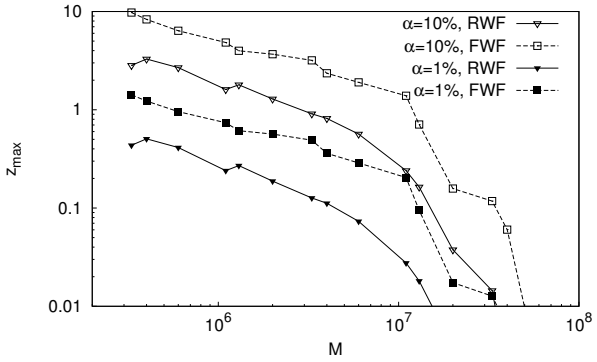

Figure 7.32: *Maximal redshifts for the alternative theory parameter Ψ_1 such that the relative error $\Delta\Psi_1/\psi_1$ is smaller than α. ψ_1 is the corresponding fiducial 2PN phase coefficient. For a relative error of 1%, low-mass binaries are suitable up to redshifts $z \sim 0.1-1$ while high-mass binaries can be observed up to $z \sim 0.01-0.1$.*

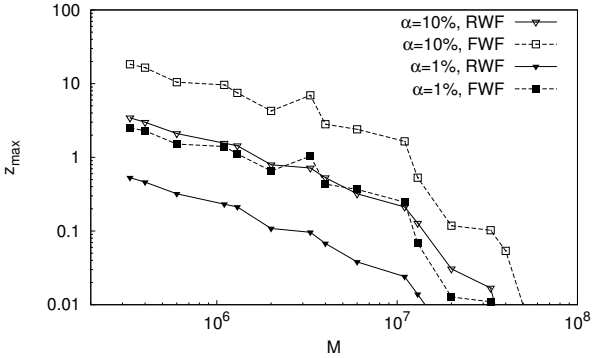

Figure 7.33: *Maximal redshifts for the alternative theory parameter $\Psi_{3/2}$ such that the relative error $\Delta\Psi_{3/2}/\psi_{3/2}$ is smaller than α. ψ_1 is the corresponding fiducial 2PN phase coefficient. For a relative error of* 1%*, low-mass binaries are suitable up to redshifts $z \sim 0.1-1$ while high-mass binaries can be observed up to $z \sim 0.01-0.1$.*

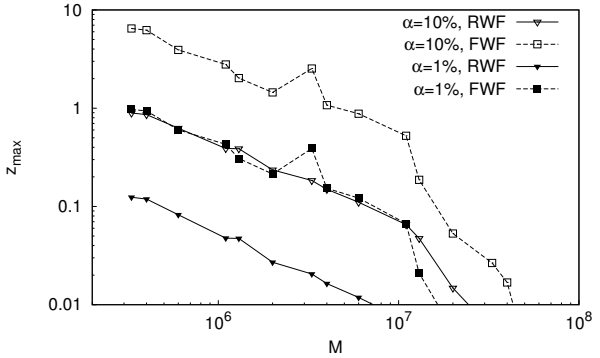

Figure 7.34: *Maximal redshifts for the alternative theory parameter Ψ_2 such that the relative error $\Delta\Psi_2/\psi_2$ is smaller than α. ψ_2 is the corresponding fiducial 2PN phase coefficient. For a relative error of* 1%*, low-mass binaries are suitable up to redshifts $z \sim 0.1-1$ while high-mass binaries can be observed up to $z \sim 0.01-0.1$.*

7.8.5 Example: Lower bound on graviton Compton wavelength

In order to compare our results with previous work in the field, we present here a lower bound on a possible graviton Compton wavelength from our results at redshift $z = 1$. The term 'massive graviton' is commonly used to state that the speed of gravitational waves depends on frequency rather than being constant. According to [50], the effect of a 'massive graviton' can be accounted for by introducing a gravitational wave phase correction

$$\Delta\Psi_{\rm MG}(z) = -\beta(z)\,\nu^{-3/5}\,x^{-3/2}, \tag{7.68}$$

where x is the dimensionless frequency, ν is the symmetric mass ratio and the parameter $\beta(z)$ is defined as

$$\beta(z) = \frac{G}{c^2}\frac{\pi^2 D(z)\mathscr{M}}{\lambda_g^2(1+z)}. \tag{7.69}$$

Here λ_g is the Compton wavelength of the graviton, z is the redshift, $\mathscr{M} = (1+z)M\,\nu^{3/5}$ is the *measured* chirp mass affected by redshift, and $D(z)$ is the distance given as

$$D(z) = (1+z)\frac{c}{H_0}\int_0^z \frac{{\rm d}z'}{(1+z')^2\sqrt{\Omega_M(1+z')^3+\Omega_\Lambda}}, \tag{7.70}$$

where H_0, Ω_M and Ω_Λ are defined as in section 7.2. In our implementation, this is similar to the correction in Eq. (7.41):

$$\Delta\Psi_{\rm MG}(z) = \frac{3}{256\nu}x^{-3/2}\Psi_1(z). \tag{7.71}$$

Hence the errors on β and Ψ_1 can be related with

$$\Delta\beta(z) = \frac{3}{256}\,\nu^{-2/5}\Delta\Psi_1(z). \tag{7.72}$$

We take the fiducial value $\beta = 0$, thus the error $\Delta\beta$ sets an upper bound on possible values for β. A lower bound on the Compton wavelength of the graviton can then be calculated at redshift z as

$$\lambda_g(z) > \sqrt{\frac{256}{3}\frac{G}{c^2}\frac{\pi^2 D(z) M \nu}{(1+z)\Delta\Psi_1(z)}}, \tag{7.73}$$

where M is the redshifted total mass of the binary. At redshift $z = 1$ we find that optimal lower bounds on λ_g originate from a $(3 \times 10^6 + 1 \times 10^7)M_\odot$ binary for the FWF and from a $(1 \times 10^6 + 1 \times 10^6)M_\odot$ binary for the RWF. Including all six alternative theory parameters Ψ_i, the resulting average bounds are $\lambda_g > 1.2 \times 10^{21}$ cm (FWF) and $\lambda_g > 7.8 \times 10^{20}$ cm (RWF). These bounds are both lower than the one Yagi and Tanaka [57] found ($\lambda_g > 4.9 \times 10^{21}$ cm) using the RWF and simple precession at a distance of 3 Gpc; this is because the presence of the other five alternative theory parameters increases correlations among the parameters. If we consider only one correction parameter Ψ_1 which among other things accounts for massive gravity, the bounds increase to $\lambda_g > 7.6 \times 10^{21}$ cm (FWF) and $\lambda_g > 4.9 \times 10^{21}$ cm (RWF). The RWF bound is slightly higher than the one by Yagi and Tanaka for a $(10^6 + 10^7)M_\odot$ binary; for this mass configuration we found a lower RWF bound of $\lambda_g > 2.8 \times 10^{21}$ cm. Cornish et al. [67] found a similar optimal RWF bound of $\lambda_g > 3.8 \times 10^{21}$ cm. The use of the FWF improves the bound on the graviton Compton wavelength by a factor of ~ 1.6 with respect to the RWF, regardless whether only one or all the alternative theory parameters are included into the simulations. Approximately this factor of accuracy will be lost when going from classic LISA to eLISA/NGO [58].

7.9 Conclusion and outlook

We analyzed the expected measurement error distributions of 17 different mass configurations of supermassive black hole binaries with masses between $10^5 - 10^8 M_\odot$. We found that the black hole binaries can roughly be divided into two groups: low-mass binaries with $M \lesssim 10^7 M_\odot$ and high-mass binaries with $M \gtrsim 10^7 M_\odot$. Comparing the results of the simulations using the FWF and the RWF, we found that the RWF errors on the alternative theory parameters Ψ_i are a factor of ~ 100 times higher than the FWF errors for high-mass binaries, while they are almost comparable for low-mass binaries. Due to the dilution of the available information through the introduction of six extra parameters, the original parameters lose accuracy. For masses and spins this is only a factor of 1.2-5 for both low- and high-mass binaries regardless of whether the FWF or RWF is used. The loss of accuracy on the position of the black hole binary on the sky is at maximum 10% for low-mass binaries and up to a factor of 5 for high-mass binaries. However, the accuracy of the luminosity distance is affected more seriously for high-mass binaries, using the RWF results in a loss of a factor of $\sim 50 - 1000$ while using the FWF reduces it to factors of $\sim 10 - 100$. For low-mass binaries it is only about a factor of 2 worse. The use of the FWF is therefore mandatory for high-mass binaries, while the parameter estimation is more efficient for low-mass binaries and only up to a factor of 5 times worse when the RWF is used instead of the FWF.

Since the error distributions were all calculated at fixed redshift $z = 1$ but the errors increase with redshift, we computed typical maximal redshifts up to which the alternative theory parameters are detectable with a relative accuracy smaller than 1% for the best 5% of the binaries in the sample. We found that for a deviation of 1% from the fiducial value, Ψ_0 is detectable up to redshifts of $z \sim 1 - 10$ for low total masses and up to $z \sim 0.01 - 0.1$ for high total masses. The rest of the alternative theory parameters Ψ_1, $\Psi_{3/2}$ and Ψ_2 with a fiducial 2PN phase coefficient unequal zero are detectable up to redshifts of $z \sim 0.1 - 1$ for low-mass binaries and $z \sim 0.01 - 0.1$ for high-mass binaries with the same relative accuracy. The use of the FWF improves the maximal redshifts up to a factor of 10 for high total masses.

The FWF enables us to increase the optimal lower bound on the Compton wavelength of the graviton by about a factor of 1.6 compared to the one reached by the RWF. We achieve an optimal lower bound of $\lambda_g > 7.6 \times 10^{21}$ cm for the classic LISA detector design if only the alternative theory parameter Ψ_1 is considered.

Since the proposed eLISA/NGO mission will most certainly fly as a reduced variant of classic LISA, it is important to investigate the reassessment of certain aspects of the mission. A broad range of LISA variants are currently reviewed by the community. To account for the technical 'shortcomings' it is thus of great importance to use as accurate waveform templates as possible to restore the lost accuracy with computational power on Earth. The use of the FWF improves the accuracy of the alternative theory parameters by at least an order of magnitude compared to the RWF. As shown by [55], the use of hybrid inspiral-merger-ringdown templates instead of inspiral-only templates improves the accuracy by an order of magnitude for the RWF; it would be interesting to find out how much such templates are improved when the FWF is used. The accuracy can further be enhanced by about an order of magnitude when considering combined observations instead of just extracting alternative theory parameters from individual black hole binaries [58]. Also effects of eccentric orbits should be accounted for to make the model more realistic.

Future work could include the introduction of amplitude corrections such as in [35], since certain alternative theories have dominant contributions in the gravitational wave amplitude (e.g. Chern-Simons-modified gravity [46]). Also, the underlying mechanism of spin precession should be analyzed for effects originating from possible alternative theories. In this paper we neglected the energy loss of black hole binaries through unexpected physical effects such as further degrees of freedom in the propagation of gravitational waves arising from additional polarizations (e.g. longitudinal modes). It would be interesting to introduce a parametrized model for these effects [65] into our simulations. Also, since we studied a search for modifications at different PN orders at the same time, one could use the results of this work to investigate how the use of next-to-leading order modifications of GR could affect the determination of alternative theory parameters. The impact of turning off and on correction parameters also needs further studies (following e.g. [116]).

7.10 Acknowledgements

C. H. would like to thank Sylvain Marsat for interesting discussions about the post-Newtonian expansion and Ed Porter for his suggestions for improvements on our code. The authors appreciate the valuable comments by the anonymous referee. C. H. and A. K. are supported by the Swiss National Science Foundation.

7.11 Appendix

7.11.1 Breakdown conditions

Since in previous work different viewpoints are taken on the choice of a critical orbit at which the integrations need to be stopped for binary black holes with precessing spins, we give here a quick summary of the approximations we used for the gravitational wave signal generation and indicate at which point we consider them to have failed. The three major assumptions are that orbits can be considered to be quasi-circular (adiabatic approximation), the spins can be treated as constants over one orbit (orbit-averaged spin precession) and the weak field or post-Newtonian approximation, which assumes typical velocities to be smaller than the speed of light, which enables us to perform a PN expansion in terms of powers of v/c. We shall discuss below how to estimate at which point the breakdown of these assumptions occurs; in particular, the breakdown of the PN approximation can be estimated using different methods, among which the use of the minimum energy circular orbit (MECO) or the PN energy flux is common.

We decided to stop our integrations always at the ISCO of $6\,GM/c^2$, since orbit-averaged spin precession can already start to be inaccurate at this point and the authors do not trust the PN expansion below this limit. Also we did not find any binary system with a minimum energy circular orbit, flux or adiabatic breakdown

higher than this radius. In the following subsection we list four different approximations criteria and discuss the limits of their validity.

Adiabatic approximation

The adiabatic approximation assumes that the time needed for one orbit is much smaller than the timescale for orbit shrinkage. In other words, the orbit shrinkage velocity $\dot{r} = \frac{\mathrm{d}r}{\mathrm{d}t}$ is required to be much smaller than the orbital velocity ωr, then the orbits can be considered to be quasi-circular. The orbital separation is given (expanded in terms of the dimensionless frequency x up to 2PN order) by

$$r(x) = \frac{GM}{c^2 x}\left[1 + \frac{1}{3}(-3+\nu)x - \frac{1}{3}\beta(2,3)x^{3/2} + \left(\frac{19}{4}\nu + \frac{1}{9}\nu^2 - \frac{1}{2}\sigma(1,3)\right)x^2\right], \tag{7.74}$$

where β and σ (expected to vary only slowly on one orbit) have been treated as constants. As an indicator for the faithfulness of the adiabatic approximation, we choose the expression

$$\frac{|\dot{r}|}{\omega r} < \kappa_{\mathrm{adiab}}. \tag{7.75}$$

The quantities ωr and $\dot{r} = \frac{\mathrm{d}r}{\mathrm{d}x}\frac{\mathrm{d}x}{\mathrm{d}t}$ can be computed to stop the integration when a certain adiabatic breakdown limit κ_{adiab} of our choice is reached. The breakdown radius for constant κ_{adiab} shows almost linear dependency on the initial value of $\hat{\boldsymbol{L}} \cdot \boldsymbol{S}_{\mathrm{eff}}$ (when the binary enters the LISA band). In Figs. 7.35 and 7.36, the adiabatic breakdown limits for $\kappa_{\mathrm{adiab}} = 0.1, 0.3$ and 1.0 are plotted for 10^3 randomly distributed systems in the parameter space with equal masses and a mass ratio of 1:10 respectively. The figures indicate that the adiabatic approximation is still quite reasonable ($\kappa_{\mathrm{adiab}} < 0.1$) for orbital separations larger than $r = 5\,GM/c^2$, so we do not have to consider it since we already stop before this limit.

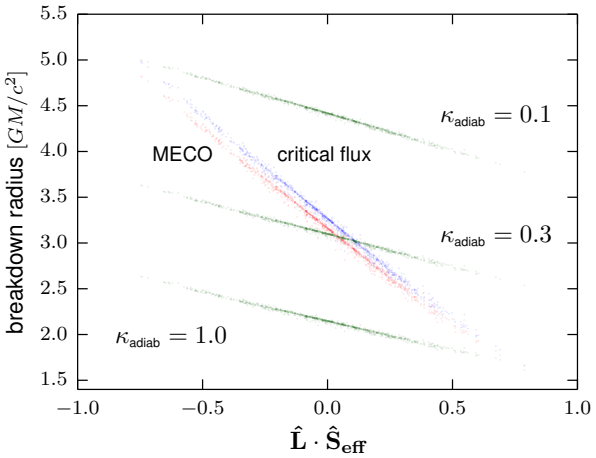

Figure 7.35: *Plot of MECO radius (red), critical flux radius (blue) and adiabatic breakdown radii (green, for different limits κ_{adiab}) against the initial effective spin orientation for 1000 simulated systems with two equal mass $2 \times 10^6 M_\odot$ black holes (binary of two $10^6 M_\odot$ black holes seen at redshift $z = 1$).*

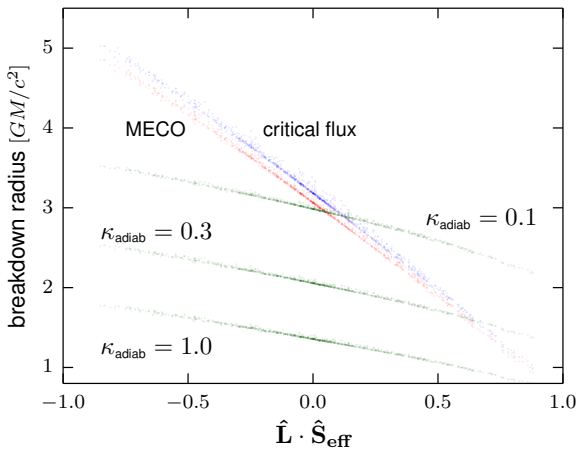

Figure 7.36: *Plot of MECO radius (red), critical flux radius (blue) and adiabatic breakdown radii (green, for different limits κ_{adiab}) against the initial effective spin orientation for 1000 simulated systems with black hole binaries of mass ratio 1:10 ($m_1 = 2 \times 10^7 M_\odot$, $m_2 = 2 \times 10^6 M_\odot$).*

MECO

The last stable circular orbit (ISCO) for test masses orbiting a non-spinning, Schwarzschild black hole takes place at the minimum of the effective gravitational potential $\frac{dV_{\rm eff}}{dr} = 0$, corresponding to an orbital separation of $6\,GM/c^2$. This is of course different for black hole binaries with comparable masses and non-zero spins; there, the total energy is only known in terms of a PN expansion [120–122]

$$\begin{aligned} E &= -\frac{\mu c^2}{2} x \left(1 - \frac{1}{12}(9+\nu)x + \frac{c}{G}\frac{4}{3M^2}\hat{\boldsymbol{L}}\cdot\boldsymbol{S}_{\rm eff}\,x^{3/2} \right. \\ &+ \left. \left[\frac{1}{24}(-81+57\nu-\nu^2) + \frac{c^2}{G^2}\frac{1}{\nu M^4}(\boldsymbol{S}_1\cdot\boldsymbol{S}_2 - 3(\hat{\boldsymbol{L}}\cdot\boldsymbol{S}_1)(\hat{\boldsymbol{L}}\cdot\boldsymbol{S}_2))\right]x^2\right), \end{aligned} \tag{7.76}$$

including leading order spin-spin and spin-orbit couplings. The effective spin $\boldsymbol{S}_{\rm eff}$ is defined as the combination

$$\boldsymbol{S}_{\rm eff} = \left(2 + \frac{3m_2}{2m_1}\right)\boldsymbol{S}_1 + \left(2 + \frac{3m_1}{2m_2}\right)\boldsymbol{S}_2. \tag{7.77}$$

The last stable circular orbit is then thought to take place at the point where

$$\frac{\mathrm{d}E}{\mathrm{d}x} = 0,$$

the *minimum energy circular orbit* (MECO). Afterwards the binaries are thought to plunge and quasi-circular orbit approximations will certainly fail. In figures 7.35 and 7.36, the MECO radii for 10^3 randomly distributed systems in the parameter space are plotted for mass ratios of 1:1 and 1:10 respectively. The MECO radius is always below the radius where the gravitational wave energy flux reaches a critical limit (defined in the next subsection), so we do not consider the MECO as a breakdown criterion for our simulations but instead use the flux condition worked out in the next subsection.

Flux

The energy flux of a gravitational wave can be expressed as [19]

$$\mathscr{L} = -\frac{\mathrm{d}E}{\mathrm{d}t} = -\frac{\mathrm{d}x}{\mathrm{d}t}\frac{\mathrm{d}E}{\mathrm{d}x} = \frac{32c^5}{5G}\nu^2 x^5 \left[1 - \left(\frac{1247}{336} + \frac{35}{12}\nu\right)x + \alpha_{3/2}x^{3/2} + \alpha_2 x^2\right], \tag{7.78}$$

where $\frac{dx}{dt}$ and E are the 2PN expressions used in this paper. For the expressions $\alpha_{3/2}$ and α_2 containing spin-orbit and spin-spin couplings, the reader is referred to [19]. As long as x is small, this flux will stay close to its leading order contribution. As soon as x gets close to 1, the 1PN term will grow stronger, decrease the flux and eventually make it negative [123]. One can thus infer that the PN series tends to breakdown if $\mathscr{L}$ deviates significantly from its leading order contribution and has for sure broken down if the flux is negative.

We decided to stop the integrations if the flux is smaller than 10% of its leading order contribution (with spin-angular momentum and spin-spin terms included). The plots in figures 7.35 and 7.36 show that the critical flux is never reached above $r = 5\,GM/c^2$, which means that there are no black hole binaries with a MECO higher than $r = 6\,GM/c^2$ in our mass range which could potentially lead to unphysical results. Nevertheless, we use a catch in our code to stop the integration if the flux gets by an unforeseen chance

smaller than 10% of its leading order contribution. Especially for parallel spins, one could theoretically try to go even down to $2-4\,GM/c^2$. In these regions a lot more SNR could be accumulated, resulting in a $\sim$ 10 times higher overall SNR and sometimes several orders of magnitude smaller errors. This is very dangerous, since we do not expect post-Newtonian theory to be physically accurate enough in these regions and one should be suspicious of such small errors.

Orbit-averaged spin precession

Since we use orbit-averaged spin precession equations [18], we need to assure that the underlying assumption of the timescale for precession always being smaller than the orbital time still holds. Like other recent studies (see e.g. [119]), we do not consider the breakdown of this approximation in our integrations, since both timescales are comparable only around $2-3\ GM/c^2$. We are however not sure, how strongly errors in the spin precession affect the matched filtering process. Since large spin precession occurs only in the late inspiral (where the largest part of the SNR is accumulated), an improper treatment of orbit-averaged spin precession creates a theoretical error in the waveform template and thus could result in a significant loss of SNR, despite the fact that the Fisher matrix gave an optimistic error estimate. We plan to quantify this theoretical error in a future publication.

In this subsection, we present the breakdown radii corresponding to certain limits on the angular momentum precession timescale, i.e. the critical orbits where the integration should be stopped. The timescale for one full orbit is

$$T_{\rm orb} = 2\pi\sqrt{\frac{r^3}{GM}}. \tag{7.79}$$

Ignoring spin-spin terms, the precession of the angular momentum unit vector can then be written as (see e.g. [124])

$$\dot{\hat{\boldsymbol{L}}} = \frac{G}{c^2 r^3}\boldsymbol{S}_{\rm eff}\times\hat{\boldsymbol{L}}, \tag{7.80}$$

with the effective spin vector $\boldsymbol{S}_{\rm eff}$ defined in (7.77). Thus $\hat{\boldsymbol{L}}$ precesses with an angular frequency of approximately $\omega_{\rm prec} = \frac{G}{c^2 r^3}|\boldsymbol{S}_{\rm eff}|$ which corresponds to a time of

$$T_{\rm prec} = 2\pi\frac{c^2 r^3}{G|\boldsymbol{S}_{\rm eff}|}, \tag{7.81}$$

for one precession. A good indicator for the breakdown of orbit-averaged spin precession is thus the fraction

$$\frac{T_{\rm orb}}{T_{\rm prec}} < \kappa_{\rm prec}, \tag{7.82}$$

where $\kappa_{\rm prec}$ is the critical limit of our choice. In the case where the two timescales are equal ($\kappa_{\rm prec} = 1$), this corresponds to a full precession in one orbit. At this point one certainly cannot speak of 'orbit-averaged' spin precession anymore.

The maximum absolute value which the effective spin is able to reach can be found to be $|\boldsymbol{S}_{\rm eff}| = \frac{GM^2}{c}(2-\nu)$, for two aligned, maximally spinning black holes. Hence we can write the effective spin introducing a dimensionless strength $0 \leq \chi_{\rm eff} < 1$ as

$$|\boldsymbol{S}_{\rm eff}| = \chi_{\rm eff}\frac{GM^2}{c}(2-\nu). \tag{7.83}$$

From Eqs. (7.79) - (7.82) we can then infer the critical radius where the orbit-averaged precession equations break down (slightly perturbed by fluctuations coming from neglected spin-spin terms):

$$r = \left(\frac{(2-\nu)\chi_{\rm eff}}{\kappa_{\rm prec}} \right)^{2/3} \frac{GM}{c^2}. \tag{7.84}$$

In figures 7.37 and 7.38, numerical simulations (including spin-spin terms) are shown, where 10^3 binary systems with mass ratios 1:1 and 1:10 (and uniformly distributed parameters) are used, respectively. The simulations match with the predictions by Eq. (7.84). For high effective spins, the integrations should be stopped already around $r = 6GM/c^2$ in the conservative limit ($\kappa_{\rm prec} = 0.1$) and $r = 2GM/c^2$ in a very optimistic limit ($\kappa_{\rm prec} = 1$). Since we stop at $r = 6GM/c^2$, we chose to ignore the breakdown of orbit-averaged spin precession in the current work, but emphasize that theoretical errors arising from this assumption should be investigated in the future.

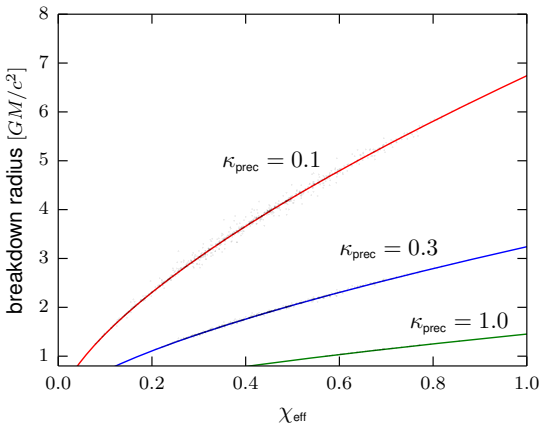

Figure 7.37: *Plot of orbit-averaged precession breakdown radii (for different limits κ_{prec}) against the initial effective spin strength for 1000 simulated systems with two equal mass $2\times10^6 M_\odot$ black holes. Spin-spin effects lead to a scattering around the analytical spin-orbit-only prediction from Eq.* (7.84) *represented by the coloured lines.*

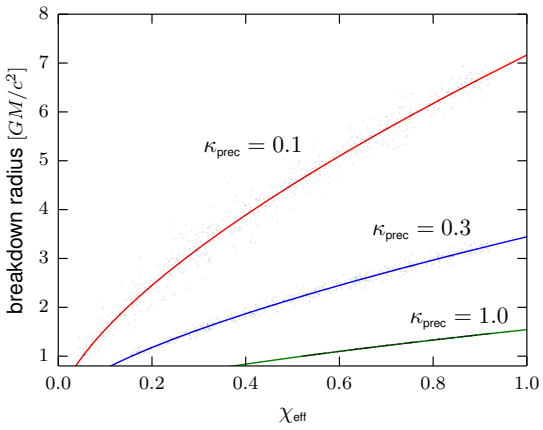

Figure 7.38: *Plot of orbit-averaged precession breakdown radii (for different limits κ_{prec}) against the initial effective spin strength for 1000 simulated systems with black hole binaries of mass ratio 1:10 ($m_1 = 2\times10^7 M_\odot$, $m_2 = 2\times10^6 M_\odot$). Spin-spin effects lead to a scattering around the analytical spin-orbit-only prediction from Eq.* (7.84) *represented by the coloured lines.*

7.11.2 The 2.5PN and 3PN orbital frequency evolution equations

The inclusion of dipole radiation corrections proportional to x^{-1} requires the knowledge of higher PN orders to be consistent to 2PN order, namely 2.5PN and 3PN contributions. Since the current 2.5PN expansion just considers spin-orbit contributions and no spin-spin effects, and the 3PN expansion does not account for any spin coupling effects at all, these are of course only approximations.

2.5PN from Blanchet et al. 2006

Blanchet et al. 2006 [30] compute the angular frequency evolution for a binary with symmetric mass ratio ν as

$$\begin{aligned}\frac{\dot{\omega}}{\omega^2} &= \frac{96}{5}\nu x^{5/2}\left\{1+x\left(-\frac{743}{336}-\frac{11}{4}\nu\right)+4\pi x^{3/2}+x^2\left(\frac{34103}{18144}+\frac{13661}{2016}\nu+\frac{59}{18}\nu^2\right)\right.\\ &+\pi x^{5/2}\left(-\frac{4159}{672}-\frac{189}{8}\nu\right)+\frac{x^{3/2}}{Gm^2}\left[-\frac{47}{3}S_l-\frac{25}{4}\frac{\delta m}{m}\Sigma_l\right]\\ &\left.+\frac{x^{5/2}}{Gm^2}\left[\left(-\frac{40127}{1008}+\frac{1465}{28}\nu\right)S_l+\left(-\frac{583}{42}+\frac{3049}{168}\nu\right)\frac{\delta m}{m}\Sigma_l\right]+O\left(\frac{1}{c^6}\right)\right\}, \end{aligned} \tag{7.85}$$

where $\omega = c^3/(GM)\, x^{3/2}$, $\delta m = m_1 - m_2$ is the mass difference and $m = m_1 + m_2$ is the total mass. The spin interaction terms are expressed with

$$\boldsymbol{\Sigma} = m\left[\frac{\boldsymbol{S}_2}{m_2}-\frac{\boldsymbol{S}_1}{m_1}\right], \qquad S_l = \boldsymbol{S}\cdot\boldsymbol{l}, \qquad \Sigma_l = \boldsymbol{\Sigma}\cdot\boldsymbol{l}, \tag{7.86}$$

where $\boldsymbol{S} = \boldsymbol{S}_1 + \boldsymbol{S}_2$ is the total spin and $\boldsymbol{l} = \frac{\boldsymbol{L}}{|\boldsymbol{L}|}$ is the angular momentum unit vector. This enables us to write Eq. (7.85) in the same form as Eq. (7.18), and we recover

$$b_{5/2} = \pi\left(-\frac{4159}{672}-\frac{189}{8}\nu\right)+\frac{1}{Gm^2}\left[\left(-\frac{40127}{1008}\frac{1465}{28}\nu\right)S_l+\left(-\frac{583}{42}+\frac{3049}{168}\nu\right)\frac{\delta m}{m}\Sigma_l\right]. \tag{7.87}$$

3PN without spin terms from Blanchet et al. 2002

In Luc Blanchet's living review [19] (see also [20–22]), the 3PN expression for the total energy of non-spinning compact binaries can be found to be

$$\begin{aligned}E &= -\frac{1}{2}\mu c^2 x\left\{1+\left(-\frac{3}{4}-\frac{1}{12}\nu\right)x+\left(-\frac{27}{8}+\frac{19}{8}\nu-\frac{1}{24}\nu^2\right)x^2\right.\\ &\left.+\left(-\frac{675}{64}+\left[\frac{34445}{576}-\frac{205}{96}\pi^2\right]\nu-\frac{155}{96}\nu^2-\frac{35}{5184}\nu^3\right)x^3\right\}, \end{aligned} \tag{7.88}$$

and the energy flux is

$$\begin{aligned}\frac{\mathrm{d}E}{\mathrm{d}t} &= -\frac{32c^5}{5G}\nu^2x^5\left\{1+\left(-\frac{1247}{336}-\frac{35}{12}\nu\right)x+4\pi x^{3/2}+\left(-\frac{44711}{9072}+\frac{9271}{504}\nu+\frac{65}{18}\nu^2\right)x^2\right.\\ &+\left(-\frac{8191}{672}-\frac{535}{24}\nu\right)\pi x^{5/2}+\left(\frac{6643739519}{69854400}+\frac{16}{3}\pi^2-\frac{1712}{105}C-\frac{856}{105}\log(16x)\right.\\ &\left.\left.+\left[-\frac{134543}{7776}+\frac{41}{48}\pi^2\right]\nu-\frac{94403}{3024}\nu^2-\frac{775}{324}\nu^3\right)x^3+\left(-\frac{16285}{504}+\frac{176419}{1512}\nu+\frac{19897}{378}\nu^2\right)\pi x^{7/2}\right\}. \end{aligned} \tag{7.89}$$

Here ν is the symmetric mass ratio and $C = 0.577..$ is the Euler constant. The logarithm in $\mathrm{d}E/\mathrm{d}t$ will lead to a logarithmic term in the 3PN expansion. The PN coefficients b_i can be recovered by computing the frequency evolution as a series in the dimensionless frequency x in the adiabatic approximation:

$$\frac{\mathrm{d}x}{\mathrm{d}t} = \frac{\mathrm{d}E}{\mathrm{d}t}\left(\frac{dE}{dx}\right)^{-1} = \frac{64\nu}{5}\frac{c^3}{Gm}x^5\left[b_1x+b_{3/2}x^{3/2}+b_2x^2+b^{5/2}x^{5/2}+b_3x^3+b_{3,\log}x^3\log(x)\right], \tag{7.90}$$

with

$$b_3 = \frac{16447322263}{139708800} - \frac{1712\gamma_e}{105} + \frac{16\pi^2}{3} - \frac{56198689\nu}{217728} + \frac{451\pi^2\nu}{48} + \frac{541\nu^2}{896} - \frac{5605\nu^3}{2592} - \frac{856}{105}\log(16), \tag{7.91}$$

$$b_{3,\log} = -\frac{856}{105}. \tag{7.92}$$

7.11.3 Tables

Table 7.1: *Median, 5% and 95% quantiles of the estimated measurement errors on m_1 for different mass configurations at redshift $z = 1$ with alternative theory parameters included.*

$m_1[M_\odot]$	$m_2[M_\odot]$	$\Delta m_1/m_1$ with corrections					
		5%-quantile		Median		95%-quantile	
		RWF	FWF	RWF	FWF	RWF	FWF
3×10^5	3×10^4	5.2×10^{-4}	4.0×10^{-4}	1.4×10^{-3}	1.1×10^{-3}	7.1×10^{-3}	2.7×10^{-3}
3×10^5	1×10^5	5.1×10^{-4}	4.0×10^{-4}	1.6×10^{-3}	8.8×10^{-4}	1.1×10^{-2}	2.3×10^{-3}
3×10^5	3×10^5	6.4×10^{-4}	4.1×10^{-4}	2.4×10^{-3}	1.0×10^{-3}	1.5×10^{-2}	2.7×10^{-3}
1×10^6	1×10^5	1.2×10^{-3}	7.9×10^{-4}	2.8×10^{-3}	1.8×10^{-3}	1.4×10^{-2}	4.4×10^{-3}
1×10^6	3×10^5	1.1×10^{-3}	7.5×10^{-4}	3.3×10^{-3}	1.7×10^{-3}	1.9×10^{-2}	4.0×10^{-3}
1×10^6	1×10^6	1.3×10^{-3}	8.9×10^{-4}	6.2×10^{-3}	2.7×10^{-3}	6.6×10^{-2}	6.6×10^{-3}
3×10^6	3×10^5	2.3×10^{-3}	1.4×10^{-3}	6.0×10^{-3}	2.8×10^{-3}	3.3×10^{-2}	6.5×10^{-3}
3×10^6	1×10^6	2.5×10^{-3}	1.2×10^{-3}	1.1×10^{-2}	2.9×10^{-3}	6.6×10^{-2}	7.8×10^{-3}
3×10^6	3×10^6	4.9×10^{-3}	2.1×10^{-3}	3.2×10^{-2}	9.0×10^{-3}	0.33	2.7×10^{-2}
1×10^7	1×10^6	1.1×10^{-2}	2.1×10^{-3}	3.7×10^{-2}	4.0×10^{-3}	0.12	9.6×10^{-3}
1×10^7	3×10^6	2.1×10^{-2}	1.9×10^{-3}	9.0×10^{-2}	4.9×10^{-3}	0.34	1.5×10^{-2}
1×10^7	1×10^7	0.17	1.6×10^{-2}	0.83	3.4×10^{-2}	4.2	7.5×10^{-2}
3×10^7	3×10^6	0.14	5.6×10^{-3}	0.37	1.1×10^{-2}	1.1	2.2×10^{-2}
3×10^7	1×10^7	0.42	9.2×10^{-3}	1.1	2.0×10^{-2}	3.6	5.0×10^{-2}
3×10^7	3×10^7	3.7	5.8×10^{-2}	29	0.15	250	0.5
1×10^8	1×10^7	∞	0.13	∞	0.36	∞	1.5
1×10^8	3×10^7	∞	1.3	∞	3.8	∞	40

Table 7.2: *Median, 5% and 95% quantiles of the estimated measurement errors on m_1 for different mass configurations at redshift $z = 1$ without considering alternative theory parameters.*

$m_1[M_\odot]$	$m_2[M_\odot]$	$\Delta m_1/m_1$ without corrections					
		5%-quantile		Median		95%-quantile	
		RWF	FWF	RWF	FWF	RWF	FWF
3×10^5	3×10^4	1.1×10^{-4}	8.2×10^{-5}	3.2×10^{-4}	2.4×10^{-4}	2.5×10^{-3}	2.5×10^{-3}
3×10^5	1×10^5	1.8×10^{-4}	1.4×10^{-4}	7.7×10^{-4}	4.5×10^{-4}	8.2×10^{-3}	8.2×10^{-3}
3×10^5	3×10^5	2.1×10^{-4}	1.4×10^{-4}	1.2×10^{-3}	2.9×10^{-4}	9.1×10^{-3}	9.1×10^{-3}
1×10^6	1×10^5	2.2×10^{-4}	1.5×10^{-4}	7.0×10^{-4}	4.2×10^{-4}	5.1×10^{-3}	5.1×10^{-3}
1×10^6	3×10^5	3.9×10^{-4}	2.7×10^{-4}	1.4×10^{-3}	8.6×10^{-4}	1.3×10^{-2}	1.3×10^{-2}
1×10^6	1×10^6	3.6×10^{-4}	2.6×10^{-4}	2.5×10^{-3}	6.9×10^{-4}	3.2×10^{-2}	3.2×10^{-2}
3×10^6	3×10^5	4.1×10^{-4}	2.3×10^{-4}	1.2×10^{-3}	6.6×10^{-4}	1.4×10^{-2}	1.4×10^{-2}
3×10^6	1×10^6	9.1×10^{-4}	5.0×10^{-4}	3.9×10^{-3}	1.2×10^{-3}	4.0×10^{-2}	4.0×10^{-2}
3×10^6	3×10^6	1.0×10^{-3}	3.8×10^{-4}	8.5×10^{-3}	8.3×10^{-4}	0.11	0.11
1×10^7	1×10^6	1.1×10^{-3}	4.0×10^{-4}	4.1×10^{-3}	1.3×10^{-3}	4.8×10^{-2}	4.8×10^{-2}
1×10^7	3×10^6	3.4×10^{-3}	7.9×10^{-4}	1.6×10^{-2}	1.8×10^{-3}	0.16	0.16
1×10^7	1×10^7	2.4×10^{-2}	2.1×10^{-3}	0.2	5.5×10^{-3}	1.6	1.6
3×10^7	3×10^6	1.4×10^{-2}	1.6×10^{-3}	9.0×10^{-2}	5.0×10^{-3}	0.55	0.55
3×10^7	1×10^7	0.38	4.4×10^{-3}	0.97	9.8×10^{-3}	3.1	3.1
3×10^7	3×10^7	3.2	5.1×10^{-2}	22	0.13	120	120
1×10^8	1×10^7	∞	0.1	∞	0.26	∞	∞
1×10^8	3×10^7	∞	0.92	∞	2.8	∞	∞

Table 7.3: *Median, 5% and 95% quantiles of the estimated measurement errors on m_2 for different mass configurations at redshift $z = 1$ with alternative theory parameters included.*

$m_1[M_\odot]$	$m_2[M_\odot]$	$\Delta m_2/m_2$ with corrections					
		5%-quantile		Median		95%-quantile	
		RWF	FWF	RWF	FWF	RWF	FWF
3×10^5	3×10^4	1.6×10^{-4}	1.2×10^{-4}	5.6×10^{-4}	4.0×10^{-4}	4.8×10^{-3}	2.2×10^{-3}
3×10^5	1×10^5	3.2×10^{-4}	2.2×10^{-4}	1.1×10^{-3}	7.6×10^{-4}	9.2×10^{-3}	2.3×10^{-3}
3×10^5	3×10^5	6.4×10^{-4}	4.2×10^{-4}	2.4×10^{-3}	1.0×10^{-3}	1.6×10^{-2}	2.6×10^{-3}
1×10^6	1×10^5	3.4×10^{-4}	2.3×10^{-4}	1.3×10^{-3}	8.7×10^{-4}	1.3×10^{-2}	4.5×10^{-3}
1×10^6	3×10^5	7.1×10^{-4}	4.9×10^{-4}	2.3×10^{-3}	1.5×10^{-3}	1.7×10^{-2}	4.1×10^{-3}
1×10^6	1×10^6	1.2×10^{-3}	8.8×10^{-4}	6.4×10^{-3}	2.7×10^{-3}	6.5×10^{-2}	6.6×10^{-3}
3×10^6	3×10^5	7.5×10^{-4}	4.8×10^{-4}	2.6×10^{-3}	1.5×10^{-3}	3.2×10^{-2}	7.8×10^{-3}
3×10^6	1×10^6	1.7×10^{-3}	8.4×10^{-4}	6.6×10^{-3}	3.0×10^{-3}	5.5×10^{-2}	1.0×10^{-2}
3×10^6	3×10^6	4.5×10^{-3}	2.1×10^{-3}	3.2×10^{-2}	9.0×10^{-3}	0.33	2.7×10^{-2}
1×10^7	1×10^6	3.0×10^{-3}	1.1×10^{-3}	1.2×10^{-2}	3.8×10^{-3}	9.6×10^{-2}	1.8×10^{-2}
1×10^7	3×10^6	6.1×10^{-3}	1.7×10^{-3}	2.9×10^{-2}	6.6×10^{-3}	0.27	2.6×10^{-2}
1×10^7	1×10^7	0.17	1.6×10^{-2}	0.8	3.4×10^{-2}	4.2	7.5×10^{-2}
3×10^7	3×10^6	7.5×10^{-2}	5.5×10^{-3}	0.38	1.8×10^{-2}	2.3	6.4×10^{-2}
3×10^7	1×10^7	1.2	1.5×10^{-2}	4.7	3.6×10^{-2}	22	0.11
3×10^7	3×10^7	3.3	5.8×10^{-2}	26	0.15	240	0.51
1×10^8	1×10^7	∞	0.83	∞	2.6	∞	12
1×10^8	3×10^7	∞	5.0	∞	17	∞	260

Table 7.4: *Median, 5% and 95% quantiles of the estimated measurement errors on m_2 for different mass configurations at redshift $z = 1$ without considering alternative theory parameters.*

$m_1[M_\odot]$	$m_2[M_\odot]$	$\Delta m_2/m_2$ without corrections					
		5%-quantile		Median		95%-quantile	
		RWF	FWF	RWF	FWF	RWF	FWF
3×10^5	3×10^4	8.0×10^{-5}	5.9×10^{-5}	2.3×10^{-4}	1.7×10^{-4}	1.7×10^{-3}	1.7×10^{-3}
3×10^5	1×10^5	1.5×10^{-4}	1.2×10^{-4}	6.3×10^{-4}	3.7×10^{-4}	6.7×10^{-3}	6.7×10^{-3}
3×10^5	3×10^5	2.1×10^{-4}	1.3×10^{-4}	1.2×10^{-3}	2.9×10^{-4}	9.2×10^{-3}	9.2×10^{-3}
1×10^6	1×10^5	1.6×10^{-4}	1.1×10^{-4}	5.0×10^{-4}	3.0×10^{-4}	3.6×10^{-3}	3.6×10^{-3}
1×10^6	3×10^5	3.1×10^{-4}	2.2×10^{-4}	1.1×10^{-3}	6.9×10^{-4}	1.1×10^{-2}	1.1×10^{-2}
1×10^6	1×10^6	3.6×10^{-4}	2.7×10^{-4}	2.5×10^{-3}	6.9×10^{-4}	3.2×10^{-2}	3.2×10^{-2}
3×10^6	3×10^5	3.1×10^{-4}	1.7×10^{-4}	8.5×10^{-4}	4.7×10^{-4}	1.0×10^{-2}	1.0×10^{-2}
3×10^6	1×10^6	7.8×10^{-4}	4.2×10^{-4}	3.2×10^{-3}	9.7×10^{-4}	3.2×10^{-2}	3.2×10^{-2}
3×10^6	3×10^6	1.0×10^{-3}	3.7×10^{-4}	8.5×10^{-3}	8.2×10^{-4}	0.11	0.11
1×10^7	1×10^6	1.1×10^{-3}	4.0×10^{-4}	3.3×10^{-3}	1.0×10^{-3}	3.3×10^{-2}	3.3×10^{-2}
1×10^7	3×10^6	3.1×10^{-3}	7.3×10^{-4}	1.4×10^{-2}	1.5×10^{-3}	0.13	0.13
1×10^7	1×10^7	2.4×10^{-2}	2.1×10^{-3}	0.2	5.5×10^{-3}	1.6	1.6
3×10^7	3×10^6	3.5×10^{-2}	2.5×10^{-3}	0.13	5.0×10^{-3}	0.53	0.53
3×10^7	1×10^7	0.43	5.9×10^{-3}	1.5	1.3×10^{-2}	5.1	5.1
3×10^7	3×10^7	2.9	5.1×10^{-2}	19	0.13	130	130
1×10^8	1×10^7	∞	0.36	∞	1.0	∞	∞
1×10^8	3×10^7	∞	3.4	∞	9.9	∞	∞

Table 7.5: *Median, 5% and 95% quantiles of the estimated measurement errors on χ_1 for different mass configurations at redshift $z = 1$ with alternative theory parameters included.*

$m_1[M_\odot]$	$m_2[M_\odot]$	$\Delta\chi_1$ with corrections					
		5%-quantile		Median		95%-quantile	
		RWF	FWF	RWF	FWF	RWF	FWF
3×10^5	3×10^4	3.3×10^{-4}	2.2×10^{-4}	9.7×10^{-4}	6.7×10^{-4}	4.3×10^{-3}	2.6×10^{-3}
3×10^5	1×10^5	8.3×10^{-4}	5.6×10^{-4}	3.1×10^{-3}	2.0×10^{-3}	1.6×10^{-2}	1.0×10^{-2}
3×10^5	3×10^5	2.1×10^{-3}	1.6×10^{-3}	1.3×10^{-2}	8.9×10^{-3}	0.24	0.14
1×10^6	1×10^5	6.6×10^{-4}	4.3×10^{-4}	1.9×10^{-3}	1.2×10^{-3}	7.9×10^{-3}	4.4×10^{-3}
1×10^6	3×10^5	1.6×10^{-3}	1.0×10^{-3}	4.9×10^{-3}	3.0×10^{-3}	2.3×10^{-2}	1.2×10^{-2}
1×10^6	1×10^6	3.5×10^{-3}	2.6×10^{-3}	3.4×10^{-2}	2.0×10^{-2}	0.61	0.21
3×10^6	3×10^5	1.3×10^{-3}	7.1×10^{-4}	3.5×10^{-3}	1.9×10^{-3}	1.7×10^{-2}	6.7×10^{-3}
3×10^6	1×10^6	3.1×10^{-3}	1.3×10^{-3}	1.4×10^{-2}	5.1×10^{-3}	6.9×10^{-2}	2.5×10^{-2}
3×10^6	3×10^6	1.5×10^{-2}	6.5×10^{-3}	0.17	5.2×10^{-2}	2.8	0.65
1×10^7	1×10^6	5.0×10^{-3}	1.4×10^{-3}	1.7×10^{-2}	4.4×10^{-3}	6.9×10^{-2}	1.5×10^{-2}
1×10^7	3×10^6	1.2×10^{-2}	2.3×10^{-3}	6.4×10^{-2}	9.5×10^{-3}	0.32	4.9×10^{-2}
1×10^7	1×10^7	0.68	8.6×10^{-2}	4.2	0.47	23	2.9
3×10^7	3×10^6	9.6×10^{-2}	6.1×10^{-3}	0.41	2.2×10^{-2}	2.0	6.5×10^{-2}
3×10^7	1×10^7	1.6	2.1×10^{-2}	4.6	0.11	17	0.44
3×10^7	3×10^7	14	2.9	79	11	780	61
1×10^8	1×10^7	∞	0.75	∞	2.6	∞	9.0
1×10^8	3×10^7	∞	8.9	∞	25	∞	240

Table 7.6: *Median, 5% and 95% quantiles of the estimated measurement errors on χ_1 for different mass configurations at redshift $z = 1$ without considering alternative theory parameters.*

$m_1[M_\odot]$	$m_2[M_\odot]$	$\Delta\chi_1$ without corrections					
		5%-quantile		Median		95%-quantile	
		RWF	FWF	RWF	FWF	RWF	FWF
3×10^5	3×10^4	1.8×10^{-4}	1.1×10^{-4}	4.2×10^{-4}	2.5×10^{-4}	1.6×10^{-3}	1.6×10^{-3}
3×10^5	1×10^5	4.6×10^{-4}	2.8×10^{-4}	1.4×10^{-3}	8.1×10^{-4}	9.3×10^{-3}	9.3×10^{-3}
3×10^5	3×10^5	1.0×10^{-3}	7.8×10^{-4}	6.0×10^{-3}	3.6×10^{-3}	8.8×10^{-2}	8.8×10^{-2}
1×10^6	1×10^5	3.6×10^{-4}	1.9×10^{-4}	8.7×10^{-4}	4.4×10^{-4}	2.9×10^{-3}	2.9×10^{-3}
1×10^6	3×10^5	8.6×10^{-4}	4.8×10^{-4}	2.2×10^{-3}	1.2×10^{-3}	1.2×10^{-2}	1.2×10^{-2}
1×10^6	1×10^6	1.6×10^{-3}	1.2×10^{-3}	1.2×10^{-2}	6.6×10^{-3}	0.19	0.19
3×10^6	3×10^5	4.8×10^{-4}	2.3×10^{-4}	1.2×10^{-3}	5.6×10^{-4}	5.8×10^{-3}	5.8×10^{-3}
3×10^6	1×10^6	1.3×10^{-3}	6.2×10^{-4}	4.2×10^{-3}	1.7×10^{-3}	3.2×10^{-2}	3.2×10^{-2}
3×10^6	3×10^6	4.4×10^{-3}	2.5×10^{-3}	4.0×10^{-2}	1.4×10^{-2}	0.92	0.92
1×10^7	1×10^6	1.3×10^{-3}	4.4×10^{-4}	3.5×10^{-3}	1.0×10^{-3}	1.5×10^{-2}	1.5×10^{-2}
1×10^7	3×10^6	3.5×10^{-3}	1.1×10^{-3}	1.5×10^{-2}	3.0×10^{-3}	0.1	0.1
1×10^7	1×10^7	0.12	2.1×10^{-2}	1.1	0.12	9.3	9.3
3×10^7	3×10^6	3.4×10^{-2}	2.7×10^{-3}	0.15	6.8×10^{-3}	0.63	0.63
3×10^7	1×10^7	0.46	9.4×10^{-3}	1.8	3.4×10^{-2}	7.5	7.5
3×10^7	3×10^7	12	1.3	63	5.1	520	520
1×10^8	1×10^7	∞	0.3	∞	1.3	∞	∞
1×10^8	3×10^7	∞	4.0	∞	14	∞	∞

Table 7.7: *Median, 5% and 95% quantiles of the estimated measurement errors on χ_2 for different mass configurations at redshift $z = 1$ with alternative theory parameters included.*

$m_1[M_\odot]$	$m_2[M_\odot]$	$\Delta\chi_2$ with corrections					
		5%-quantile		Median		95%-quantile	
		RWF	FWF	RWF	FWF	RWF	FWF
3×10^5	3×10^4	1.4×10^{-3}	8.9×10^{-4}	1.3×10^{-2}	9.0×10^{-3}	0.13	7.2×10^{-2}
3×10^5	1×10^5	2.0×10^{-3}	1.3×10^{-3}	9.7×10^{-3}	6.7×10^{-3}	8.9×10^{-2}	5.0×10^{-2}
3×10^5	3×10^5	2.0×10^{-3}	1.5×10^{-3}	1.4×10^{-2}	9.0×10^{-3}	0.25	0.13
1×10^6	1×10^5	3.3×10^{-3}	1.9×10^{-3}	2.7×10^{-2}	1.7×10^{-2}	0.32	0.15
1×10^6	3×10^5	3.4×10^{-3}	2.2×10^{-3}	1.8×10^{-2}	1.2×10^{-2}	0.13	5.7×10^{-2}
1×10^6	1×10^6	3.9×10^{-3}	2.7×10^{-3}	3.1×10^{-2}	1.9×10^{-2}	0.76	0.23
3×10^6	3×10^5	5.4×10^{-3}	2.7×10^{-3}	4.4×10^{-2}	2.4×10^{-2}	0.59	0.2
3×10^6	1×10^6	6.0×10^{-3}	2.6×10^{-3}	3.9×10^{-2}	1.9×10^{-2}	0.31	0.11
3×10^6	3×10^6	1.4×10^{-2}	6.7×10^{-3}	0.18	5.2×10^{-2}	2.7	0.66
1×10^7	1×10^6	1.9×10^{-2}	5.5×10^{-3}	0.17	5.1×10^{-2}	1.5	0.35
1×10^7	3×10^6	2.5×10^{-2}	4.8×10^{-3}	0.16	3.5×10^{-2}	1.4	0.26
1×10^7	1×10^7	0.72	9.6×10^{-2}	4.3	0.49	25	2.9
3×10^7	3×10^6	0.31	2.3×10^{-2}	4.0	0.24	33	1.3
3×10^7	1×10^7	2.6	4.3×10^{-2}	15	0.34	75	1.7
3×10^7	3×10^7	15	3.3	79	11	670	51
1×10^8	1×10^7	∞	3.0	∞	25	∞	140
1×10^8	3×10^7	∞	27	∞	120	∞	1.2×10^3

Table 7.8: *Median, 5% and 95% quantiles of the estimated measurement errors on χ_2 for different mass configurations at redshift $z = 1$ without considering alternative theory parameters.*

$m_1[M_\odot]$	$m_2[M_\odot]$	$\Delta\chi_2$ without corrections					
		5%-quantile		Median		95%-quantile	
		RWF	FWF	RWF	FWF	RWF	FWF
3×10^5	3×10^4	7.6×10^{-4}	4.5×10^{-4}	2.7×10^{-3}	1.6×10^{-3}	1.5×10^{-2}	1.5×10^{-2}
3×10^5	1×10^5	8.2×10^{-4}	5.3×10^{-4}	3.3×10^{-3}	1.9×10^{-3}	1.9×10^{-2}	1.9×10^{-2}
3×10^5	3×10^5	1.0×10^{-3}	8.2×10^{-4}	6.3×10^{-3}	3.7×10^{-3}	7.9×10^{-2}	7.9×10^{-2}
1×10^6	1×10^5	1.6×10^{-3}	7.7×10^{-4}	5.6×10^{-3}	2.9×10^{-3}	3.3×10^{-2}	3.3×10^{-2}
1×10^6	3×10^5	1.4×10^{-3}	8.6×10^{-4}	5.0×10^{-3}	2.9×10^{-3}	2.9×10^{-2}	2.9×10^{-2}
1×10^6	1×10^6	1.6×10^{-3}	1.1×10^{-3}	1.2×10^{-2}	6.4×10^{-3}	0.23	0.23
3×10^6	3×10^5	2.3×10^{-3}	1.2×10^{-3}	7.6×10^{-3}	3.9×10^{-3}	5.8×10^{-2}	5.8×10^{-2}
3×10^6	1×10^6	2.2×10^{-3}	1.1×10^{-3}	7.9×10^{-3}	3.7×10^{-3}	6.4×10^{-2}	6.4×10^{-2}
3×10^6	3×10^6	4.0×10^{-3}	2.4×10^{-3}	4.1×10^{-2}	1.4×10^{-2}	0.88	0.88
1×10^7	1×10^6	6.2×10^{-3}	2.0×10^{-3}	3.1×10^{-2}	9.1×10^{-3}	0.19	0.19
1×10^7	3×10^6	7.8×10^{-3}	2.5×10^{-3}	3.4×10^{-2}	9.5×10^{-3}	0.17	0.17
1×10^7	1×10^7	0.13	2.1×10^{-2}	1.2	0.12	9.6	9.6
3×10^7	3×10^6	0.13	8.6×10^{-3}	1.3	6.5×10^{-2}	6.9	6.9
3×10^7	1×10^7	0.59	2.0×10^{-2}	4.5	0.1	24	24
3×10^7	3×10^7	14	1.2	66	5.1	450	450
1×10^8	1×10^7	∞	1.4	∞	13	∞	∞
1×10^8	3×10^7	∞	8.1	∞	48	∞	∞

Table 7.9: *Median, 5% and 95% quantiles of the estimated measurement errors on 2a for different mass configurations at redshift $z = 1$ with alternative theory parameters included.*

$m_1[M_\odot]$	$m_2[M_\odot]$	$2a[']$ with corrections					
		5%-quantile		Median		95%-quantile	
		RWF	FWF	RWF	FWF	RWF	FWF
3×10^5	3×10^4	7.5	4.5	21	13	83	67
3×10^5	1×10^5	5.3	3.3	24	15	99	81
3×10^5	3×10^5	6.9	4.3	29	21	110	100
1×10^6	1×10^5	12	8.2	37	22	130	96
1×10^6	3×10^5	11	7.2	36	23	140	100
1×10^6	1×10^6	11	6.7	47	34	180	140
3×10^6	3×10^5	16	8.0	40	21	160	100
3×10^6	1×10^6	15	7.3	51	27	220	150
3×10^6	3×10^6	15	7.6	74	40	420	260
1×10^7	1×10^6	27	8.9	87	28	440	130
1×10^7	3×10^6	26	8.8	130	41	700	190
1×10^7	1×10^7	58	18	459	130	4.4×10^3	930
3×10^7	3×10^6	160	23	640	77	7.5×10^3	350
3×10^7	1×10^7	459	43	5.0×10^3	190	8.1×10^4	1.2×10^3
3×10^7	3×10^7	1.6×10^4	670	3.8×10^5	3.9×10^3	7.9×10^6	2.3×10^4
1×10^8	1×10^7	∞	2.3×10^3	∞	8.4×10^3	∞	5.0×10^4
1×10^8	3×10^7	∞	1.7×10^4	∞	8.7×10^4	∞	6.6×10^5

Table 7.10: *Median, 5% and 95% quantiles of the estimated measurement errors on 2a for different mass configurations at redshift $z = 1$ without considering alternative theory parameters.*

$m_1[M_\odot]$	$m_2[M_\odot]$	$2a[']$ without corrections					
		5%-quantile		Median		95%-quantile	
		RWF	FWF	RWF	FWF	RWF	FWF
3×10^5	3×10^4	7.2	4.4	20	13	77	77
3×10^5	1×10^5	5.0	3.1	21	14	91	91
3×10^5	3×10^5	6.0	3.7	26	18	100	100
1×10^6	1×10^5	8.5	7.6	35	20	120	120
1×10^6	3×10^5	8.5	6.2	33	21	120	120
1×10^6	1×10^6	8.3	5.6	38	26	150	150
3×10^6	3×10^5	9.6	6.8	35	19	140	140
3×10^6	1×10^6	11	6.3	41	23	190	190
3×10^6	3×10^6	11	5.7	51	28	280	280
1×10^7	1×10^6	18	7.6	64	24	300	300
1×10^7	3×10^6	20	7.8	87	32	420	420
1×10^7	1×10^7	34	13	220	83	1.8×10^3	1.8×10^3
3×10^7	3×10^6	100	20	380	64	3.0×10^3	3.0×10^3
3×10^7	1×10^7	180	27	1.3×10^3	120	1.5×10^4	1.5×10^4
3×10^7	3×10^7	4.7×10^3	400	1.3×10^5	2.2×10^3	2.2×10^6	2.2×10^6
1×10^8	1×10^7	∞	1.4×10^3	∞	4.5×10^3	∞	∞
1×10^8	3×10^7	∞	7.1×10^3	∞	3.3×10^4	∞	∞

Table 7.11: *Median, 5% and 95% quantiles of the estimated measurement errors on $2b$ for different mass configurations at redshift $z = 1$ with alternative theory parameters included.*

$m_1[M_\odot]$	$m_2[M_\odot]$	$2b[']$ with corrections					
		5%-quantile		Median		95%-quantile	
		RWF	FWF	RWF	FWF	RWF	FWF
3×10^5	3×10^4	0.98	0.57	4.7	2.7	13	7.3
3×10^5	1×10^5	0.9	0.52	4.1	2.4	17	9.3
3×10^5	3×10^5	1.5	0.89	5.8	3.4	22	15
1×10^6	1×10^5	2.3	1.0	11	5.0	28	13
1×10^6	3×10^5	1.8	1.1	9.0	4.8	30	17
1×10^6	1×10^6	2.0	1.1	9.7	5.8	39	27
3×10^6	3×10^5	2.4	1.2	11	5.4	31	14
3×10^6	1×10^6	2.1	1.0	10	4.9	34	16
3×10^6	3×10^6	2.2	1.1	12	5.7	56	30
1×10^7	1×10^6	3.4	1.1	17	5.6	66	16
1×10^7	3×10^6	3.9	1.4	19	6.1	87	25
1×10^7	1×10^7	14	4.3	64	18	310	93
3×10^7	3×10^6	29	3.8	110	15	919	56
3×10^7	1×10^7	88	10	600	34	6.1×10^3	140
3×10^7	3×10^7	1.2×10^3	93	2.9×10^4	530	6.3×10^5	3.0×10^3
1×10^8	1×10^7	∞	490	∞	1.8×10^3	∞	8.2×10^3
1×10^8	3×10^7	∞	3.2×10^3	∞	1.3×10^4	∞	9.2×10^4

Table 7.12: *Median, 5% and 95% quantiles of the estimated measurement errors on $2b$ for different mass configurations at redshift $z = 1$ without considering alternative theory parameters.*

$m_1[M_\odot]$	$m_2[M_\odot]$	$2b[']$ without corrections					
		5%-quantile		Median		95%-quantile	
		RWF	FWF	RWF	FWF	RWF	FWF
3×10^5	3×10^4	0.95	0.55	4.6	2.6	12	12
3×10^5	1×10^5	0.82	0.44	3.8	2.1	15	15
3×10^5	3×10^5	1.2	0.69	5.1	3.0	19	19
1×10^6	1×10^5	2.1	0.91	10	4.7	25	25
1×10^6	3×10^5	1.5	0.92	8.4	4.4	27	27
1×10^6	1×10^6	1.6	0.97	8.7	5.1	34	34
3×10^6	3×10^5	2.3	1.1	11	5.1	27	27
3×10^6	1×10^6	1.9	0.89	9.0	4.3	29	29
3×10^6	3×10^6	1.7	0.83	9.7	4.6	38	38
1×10^7	1×10^6	2.8	0.91	15	4.9	41	41
1×10^7	3×10^6	2.7	0.99	14	4.9	54	54
1×10^7	1×10^7	6.1	2.3	27	10	130	130
3×10^7	3×10^6	15	2.5	60	12	260	260
3×10^7	1×10^7	43	4.8	170	18	919	919
3×10^7	3×10^7	550	49	4.2×10^3	250	7.1×10^4	7.1×10^4
1×10^8	1×10^7	∞	270	∞	890	∞	∞
1×10^8	3×10^7	∞	1.4×10^3	∞	4.9×10^3	∞	∞

Table 7.13: *Median, 5% and 95% quantiles of the estimated measurement errors on d_L for different mass configurations at redshift $z = 1$ with alternative theory parameters included.*

$m_1[M_\odot]$	$m_2[M_\odot]$	$\Delta d_L/d_L$ with corrections					
		5%-quantile		Median		95%-quantile	
		RWF	FWF	RWF	FWF	RWF	FWF
3×10^5	3×10^4	2.4×10^{-3}	1.5×10^{-3}	4.8×10^{-3}	3.0×10^{-3}	1.4×10^{-2}	8.8×10^{-3}
3×10^5	1×10^5	2.3×10^{-3}	1.5×10^{-3}	4.9×10^{-3}	3.3×10^{-3}	1.8×10^{-2}	1.2×10^{-2}
3×10^5	3×10^5	2.7×10^{-3}	2.0×10^{-3}	7.0×10^{-3}	5.1×10^{-3}	2.1×10^{-2}	1.7×10^{-2}
1×10^6	1×10^5	3.7×10^{-3}	2.5×10^{-3}	8.0×10^{-3}	5.0×10^{-3}	2.2×10^{-2}	1.4×10^{-2}
1×10^6	3×10^5	3.0×10^{-3}	2.3×10^{-3}	7.6×10^{-3}	5.1×10^{-3}	2.4×10^{-2}	1.6×10^{-2}
1×10^6	1×10^6	3.8×10^{-3}	2.7×10^{-3}	1.1×10^{-2}	7.6×10^{-3}	3.4×10^{-2}	2.6×10^{-2}
3×10^6	3×10^5	4.9×10^{-3}	3.3×10^{-3}	9.9×10^{-3}	6.3×10^{-3}	3.1×10^{-2}	1.6×10^{-2}
3×10^6	1×10^6	5.3×10^{-3}	3.2×10^{-3}	1.2×10^{-2}	7.5×10^{-3}	4.0×10^{-2}	2.4×10^{-2}
3×10^6	3×10^6	6.9×10^{-3}	4.1×10^{-3}	2.3×10^{-2}	1.3×10^{-2}	7.6×10^{-2}	4.1×10^{-2}
1×10^7	1×10^6	1.6×10^{-2}	6.4×10^{-3}	3.7×10^{-2}	1.4×10^{-2}	0.11	3.2×10^{-2}
1×10^7	3×10^6	2.8×10^{-2}	6.9×10^{-3}	7.1×10^{-2}	1.7×10^{-2}	0.23	5.2×10^{-2}
1×10^7	1×10^7	0.23	4.3×10^{-2}	0.71	9.4×10^{-2}	3.1	0.23
3×10^7	3×10^6	0.89	3.5×10^{-2}	4.4	8.0×10^{-2}	21	0.18
3×10^7	1×10^7	9.3	0.11	43	0.26	210	0.73
3×10^7	3×10^7	1.3×10^3	4.2	2.8×10^4	11	3.0×10^5	50
1×10^8	1×10^7	∞	16	∞	78	∞	560
1×10^8	3×10^7	∞	229	∞	1.0×10^3	∞	1.9×10^4

Table 7.14: *Median, 5% and 95% quantiles of the estimated measurement errors on d_L for different mass configurations at redshift $z = 1$ without considering alternative theory parameters.*

$m_1[M_\odot]$	$m_2[M_\odot]$	$\Delta d_L/d_L$ without corrections					
		5%-quantile		Median		95%-quantile	
		RWF	FWF	RWF	FWF	RWF	FWF
3×10^5	3×10^4	1.1×10^{-3}	7.8×10^{-4}	2.5×10^{-3}	1.5×10^{-3}	9.4×10^{-3}	9.4×10^{-3}
3×10^5	1×10^5	9.2×10^{-4}	6.1×10^{-4}	2.8×10^{-3}	1.7×10^{-3}	1.4×10^{-2}	1.4×10^{-2}
3×10^5	3×10^5	1.2×10^{-3}	7.7×10^{-4}	4.3×10^{-3}	2.8×10^{-3}	1.8×10^{-2}	1.8×10^{-2}
1×10^6	1×10^5	1.9×10^{-3}	9.8×10^{-4}	5.0×10^{-3}	2.5×10^{-3}	1.8×10^{-2}	1.8×10^{-2}
1×10^6	3×10^5	1.7×10^{-3}	1.1×10^{-3}	4.9×10^{-3}	2.8×10^{-3}	2.0×10^{-2}	2.0×10^{-2}
1×10^6	1×10^6	1.8×10^{-3}	1.1×10^{-3}	6.8×10^{-3}	4.4×10^{-3}	2.7×10^{-2}	2.7×10^{-2}
3×10^6	3×10^5	2.0×10^{-3}	1.2×10^{-3}	5.1×10^{-3}	2.7×10^{-3}	2.2×10^{-2}	2.2×10^{-2}
3×10^6	1×10^6	2.0×10^{-3}	1.2×10^{-3}	5.9×10^{-3}	3.2×10^{-3}	2.9×10^{-2}	2.9×10^{-2}
3×10^6	3×10^6	2.1×10^{-3}	1.3×10^{-3}	8.7×10^{-3}	4.9×10^{-3}	4.6×10^{-2}	4.6×10^{-2}
1×10^7	1×10^6	3.1×10^{-3}	1.3×10^{-3}	8.4×10^{-3}	3.4×10^{-3}	4.0×10^{-2}	4.0×10^{-2}
1×10^7	3×10^6	4.0×10^{-3}	2.0×10^{-3}	1.2×10^{-2}	4.8×10^{-3}	7.2×10^{-2}	7.2×10^{-2}
1×10^7	1×10^7	1.4×10^{-2}	6.9×10^{-3}	6.2×10^{-2}	2.2×10^{-2}	0.31	0.31
3×10^7	3×10^6	3.0×10^{-2}	4.9×10^{-3}	8.0×10^{-2}	1.0×10^{-2}	0.49	0.49
3×10^7	1×10^7	0.23	1.6×10^{-2}	0.76	3.5×10^{-2}	3.2	3.2
3×10^7	3×10^7	3.3	0.21	21	0.5	380	380
1×10^8	1×10^7	∞	0.44	∞	1.1	∞	∞
1×10^8	3×10^7	∞	3.1	∞	9.4	∞	∞

Table 7.15: *Median, 5% and 95% quantiles of the estimated measurement errors on Ψ_{-1} for different mass configurations at redshift $z = 1$*

$m_1[M_\odot]$	$m_2[M_\odot]$	$\Delta\Psi_{-1}$					
		5%-quantile		Median		95%-quantile	
		RWF	FWF	RWF	FWF	RWF	FWF
3×10^5	3×10^4	3.0×10^{-6}	1.8×10^{-6}	7.3×10^{-6}	5.4×10^{-6}	7.0×10^{-5}	4.9×10^{-5}
3×10^5	1×10^5	2.8×10^{-6}	1.8×10^{-6}	7.3×10^{-6}	6.0×10^{-6}	5.2×10^{-5}	4.6×10^{-5}
3×10^5	3×10^5	5.3×10^{-6}	3.2×10^{-6}	1.5×10^{-5}	1.1×10^{-5}	1.2×10^{-4}	8.2×10^{-5}
1×10^6	1×10^5	1.4×10^{-5}	5.9×10^{-6}	3.3×10^{-5}	2.2×10^{-5}	2.9×10^{-4}	2.2×10^{-4}
1×10^6	3×10^5	1.4×10^{-5}	7.8×10^{-6}	3.6×10^{-5}	2.6×10^{-5}	2.3×10^{-4}	1.8×10^{-4}
1×10^6	1×10^6	5.3×10^{-5}	2.2×10^{-5}	1.4×10^{-4}	8.8×10^{-5}	6.3×10^{-4}	4.0×10^{-4}
3×10^6	3×10^5	9.8×10^{-5}	3.1×10^{-5}	2.1×10^{-4}	1.1×10^{-4}	1.2×10^{-3}	6.1×10^{-4}
3×10^6	1×10^6	1.9×10^{-4}	3.1×10^{-5}	4.2×10^{-4}	1.6×10^{-4}	1.1×10^{-3}	6.1×10^{-4}
3×10^6	3×10^6	8.2×10^{-4}	1.4×10^{-4}	2.6×10^{-3}	7.0×10^{-4}	8.0×10^{-3}	2.1×10^{-3}
1×10^7	1×10^6	2.9×10^{-3}	3.8×10^{-4}	6.4×10^{-3}	9.3×10^{-4}	1.6×10^{-2}	2.8×10^{-3}
1×10^7	3×10^6	7.3×10^{-3}	3.4×10^{-4}	1.9×10^{-2}	1.9×10^{-3}	5.5×10^{-2}	4.8×10^{-3}
1×10^7	1×10^7	6.1×10^{-2}	1.0×10^{-2}	0.18	2.4×10^{-2}	0.77	6.3×10^{-2}
3×10^7	3×10^6	0.25	8.3×10^{-3}	1.3	1.7×10^{-2}	7.6	4.5×10^{-2}
3×10^7	1×10^7	2.9	4.3×10^{-2}	15	0.11	74	0.29
3×10^7	3×10^7	459	1.5	9.1×10^3	4.0	9.1×10^4	18
1×10^8	1×10^7	∞	4.6	∞	24	∞	210
1×10^8	3×10^7	∞	75	∞	400	∞	7.5×10^3

Table 7.16: *Median, 5% and 95% quantiles of the estimated measurement errors on Ψ_0 for different mass configurations at redshift $z = 1$*

$m_1[M_\odot]$	$m_2[M_\odot]$	$\Delta\Psi_0$					
		5%-quantile		Median		95%-quantile	
		RWF	FWF	RWF	FWF	RWF	FWF
3×10^5	3×10^4	1.4×10^{-3}	7.0×10^{-4}	3.1×10^{-3}	2.1×10^{-3}	1.7×10^{-2}	1.3×10^{-2}
3×10^5	1×10^5	1.3×10^{-3}	8.1×10^{-4}	3.2×10^{-3}	2.4×10^{-3}	1.4×10^{-2}	1.3×10^{-2}
3×10^5	3×10^5	2.2×10^{-3}	1.2×10^{-3}	5.9×10^{-3}	4.1×10^{-3}	3.1×10^{-2}	2.3×10^{-2}
1×10^6	1×10^5	4.7×10^{-3}	1.7×10^{-3}	1.0×10^{-2}	6.2×10^{-3}	6.3×10^{-2}	4.7×10^{-2}
1×10^6	3×10^5	4.6×10^{-3}	2.4×10^{-3}	1.2×10^{-2}	7.9×10^{-3}	5.3×10^{-2}	3.9×10^{-2}
1×10^6	1×10^6	1.5×10^{-2}	5.4×10^{-3}	3.8×10^{-2}	2.3×10^{-2}	0.13	9.1×10^{-2}
3×10^6	3×10^5	2.1×10^{-2}	5.7×10^{-3}	4.6×10^{-2}	2.5×10^{-2}	0.21	0.11
3×10^6	1×10^6	3.7×10^{-2}	4.7×10^{-3}	8.5×10^{-2}	3.5×10^{-2}	0.22	0.11
3×10^6	3×10^6	0.13	1.1×10^{-2}	0.38	0.11	1.1	0.34
1×10^7	1×10^6	0.31	4.6×10^{-2}	0.76	0.14	2.1	0.38
1×10^7	3×10^6	0.73	2.7×10^{-2}	2.0	0.25	5.8	0.66
1×10^7	1×10^7	4.8	0.96	14	2.3	60	6.2
3×10^7	3×10^6	8.4	0.73	71	1.8	530	4.4
3×10^7	1×10^7	96	3.5	800	9.1	4.4×10^3	26
3×10^7	3×10^7	1.1×10^4	110	2.7×10^5	290	3.3×10^6	1.2×10^3
1×10^8	1×10^7	∞	160	∞	1.2×10^3	∞	1.4×10^4
1×10^8	3×10^7	∞	2.6×10^3	∞	2.2×10^4	∞	4.6×10^5

Table 7.17: *Median, 5% and 95% quantiles of the estimated measurement errors on $\Psi_{1/2}$ for different mass configurations at redshift $z = 1$*

$m_1[M_\odot]$	$m_2[M_\odot]$	$\Delta\Psi_{1/2}$ 5%-quantile		Median		95%-quantile	
		RWF	FWF	RWF	FWF	RWF	FWF
3×10^5	3×10^4	1.5×10^{-2}	5.7×10^{-3}	3.6×10^{-2}	2.0×10^{-2}	0.13	9.6×10^{-2}
3×10^5	1×10^5	1.4×10^{-2}	7.0×10^{-3}	3.3×10^{-2}	2.3×10^{-2}	0.13	0.11
3×10^5	3×10^5	1.8×10^{-2}	1.0×10^{-2}	5.0×10^{-2}	3.6×10^{-2}	0.24	0.18
1×10^6	1×10^5	3.9×10^{-2}	1.5×10^{-2}	8.7×10^{-2}	4.8×10^{-2}	0.4	0.3
1×10^6	3×10^5	3.5×10^{-2}	2.0×10^{-2}	9.1×10^{-2}	6.2×10^{-2}	0.35	0.27
1×10^6	1×10^6	0.1	3.4×10^{-2}	0.27	0.16	0.9	0.59
3×10^6	3×10^5	0.13	4.0×10^{-2}	0.29	0.16	1.2	0.66
3×10^6	1×10^6	0.22	3.6×10^{-2}	0.52	0.21	1.3	0.67
3×10^6	3×10^6	0.65	6.3×10^{-2}	2.0	0.6	6.0	1.9
1×10^7	1×10^6	1.3	0.23	3.6	0.78	10	2.1
1×10^7	3×10^6	3.2	0.15	9.0	1.3	28	3.5
1×10^7	1×10^7	19	4.0	56	10	250	29
3×10^7	3×10^6	21	2.9	240	7.7	2.0×10^3	22
3×10^7	1×10^7	200	14	2.6×10^3	37	1.4×10^4	110
3×10^7	3×10^7	1.9×10^4	409	5.7×10^5	1.1×10^3	6.8×10^6	5.0×10^3
1×10^8	1×10^7	∞	330	∞	3.5×10^3	∞	5.1×10^4
1×10^8	3×10^7	∞	5.6×10^3	∞	7.1×10^4	∞	1.5×10^6

Table 7.18: *Median, 5% and 95% quantiles of the estimated measurement errors on Ψ_1 for different mass configurations at redshift $z = 1$*

$m_1[M_\odot]$	$m_2[M_\odot]$	$\Delta\Psi_1$ 5%-quantile		Median		95%-quantile	
		RWF	FWF	RWF	FWF	RWF	FWF
3×10^5	3×10^4	0.14	3.6×10^{-2}	0.32	0.16	0.91	0.61
3×10^5	1×10^5	0.15	4.5×10^{-2}	0.33	0.21	1.0	0.74
3×10^5	3×10^5	0.19	6.0×10^{-2}	0.48	0.29	1.6	1.4
1×10^6	1×10^5	0.3	7.5×10^{-2}	0.65	0.34	2.0	1.3
1×10^6	3×10^5	0.27	0.11	0.67	0.4	1.8	1.2
1×10^6	1×10^6	0.49	0.13	1.3	0.68	4.4	2.9
3×10^6	3×10^5	0.61	0.16	1.4	0.74	4.0	2.4
3×10^6	1×10^6	0.79	0.13	1.9	0.84	5.0	2.7
3×10^6	3×10^6	1.3	0.2	4.0	1.4	15	5.9
1×10^7	1×10^6	3.1	0.5	8.8	2.4	25	6.0
1×10^7	3×10^6	5.2	0.34	14	2.4	45	8.1
1×10^7	1×10^7	28	5.5	76	13	320	36
3×10^7	3×10^6	62	6.1	560	15	3.6×10^3	35
3×10^7	1×10^7	400	17	3.7×10^3	46	2.0×10^4	120
3×10^7	3×10^7	4.2×10^4	440	7.1×10^5	1.1×10^3	1.2×10^7	5.1×10^3
1×10^8	1×10^7	∞	1.0×10^3	∞	8.0×10^3	∞	8.3×10^4
1×10^8	3×10^7	∞	8.5×10^3	∞	9.0×10^4	∞	1.8×10^6

Table 7.19: *Median, 5% and 95% quantiles of the estimated measurement errors on $\Psi_{3/2}$ for different mass configurations at redshift $z = 1$*

$m_1[M_\odot]$	$m_2[M_\odot]$	$\Delta\Psi_{3/2}$ 5%-quantile		$\Delta\Psi_{3/2}$ Median		$\Delta\Psi_{3/2}$ 95%-quantile	
		RWF	FWF	RWF	FWF	RWF	FWF
3×10^5	3×10^4	1.1	0.13	2.5	1.4	8.2	6.3
3×10^5	1×10^5	1.3	0.16	3.0	1.9	8.7	7.3
3×10^5	3×10^5	2.0	0.22	5.1	2.9	16	14
1×10^6	1×10^5	2.8	0.24	6.1	3.4	23	15
1×10^6	3×10^5	3.0	0.63	7.5	4.5	21	14
1×10^6	1×10^6	6.8	0.71	17	8.9	47	32
3×10^6	3×10^5	7.5	0.71	18	9.7	53	33
3×10^6	1×10^6	11	0.42	27	11	66	33
3×10^6	3×10^6	20	1.1	54	18	160	63
1×10^7	1×10^6	35	3.7	110	32	330	77
1×10^7	3×10^6	58	1.5	180	34	600	110
1×10^7	1×10^7	250	61	770	150	3.6×10^3	459
3×10^7	3×10^6	450	66	3.7×10^3	190	3.1×10^4	459
3×10^7	1×10^7	3.4×10^3	160	2.8×10^4	500	1.7×10^5	1.5×10^3
3×10^7	3×10^7	3.5×10^5	3.6×10^3	3.2×10^6	1.0×10^4	4.1×10^7	4.7×10^4
1×10^8	1×10^7	∞	8.7×10^3	∞	5.4×10^4	∞	6.5×10^5
1×10^8	3×10^7	∞	7.2×10^4	∞	6.8×10^5	∞	1.4×10^7

Table 7.20: *Median, 5% and 95% quantiles of the estimated measurement errors on Ψ_2 for different mass configurations at redshift $z = 1$*

$m_1[M_\odot]$	$m_2[M_\odot]$	$\Delta\Psi_2$ 5%-quantile		$\Delta\Psi_2$ Median		$\Delta\Psi_2$ 95%-quantile	
		RWF	FWF	RWF	FWF	RWF	FWF
3×10^5	3×10^4	4.0	0.35	8.9	5.3	30	23
3×10^5	1×10^5	5.1	0.6	12	7.6	34	28
3×10^5	3×10^5	8.2	0.83	21	12	63	52
1×10^6	1×10^5	10	0.76	23	13	86	55
1×10^6	3×10^5	12	2.1	30	18	85	54
1×10^6	1×10^6	26	2.7	65	33	180	120
3×10^6	3×10^5	26	1.9	63	35	180	110
3×10^6	1×10^6	38	1.3	97	40	250	120
3×10^6	3×10^6	60	3.0	170	58	520	210
1×10^7	1×10^6	84	9.3	320	110	1.0×10^3	240
1×10^7	3×10^6	130	3.9	450	100	1.7×10^3	340
1×10^7	1×10^7	509	130	1.6×10^3	350	8.8×10^3	1.1×10^3
3×10^7	3×10^6	890	190	7.5×10^3	490	6.3×10^4	1.2×10^3
3×10^7	1×10^7	9.5×10^3	380	4.6×10^4	1.0×10^3	2.9×10^5	3.1×10^3
3×10^7	3×10^7	5.4×10^5	5.7×10^3	5.5×10^6	1.7×10^4	8.3×10^7	8.7×10^4
1×10^8	1×10^7	∞	2.8×10^4	∞	1.3×10^5	∞	1.3×10^6
1×10^8	3×10^7	∞	2.0×10^5	∞	1.2×10^6	∞	2.4×10^7

Chapter 8

Supermassive Black Hole Tests of General Relativity with eLISA

C. Huwyler, E. Porter, Ph. Jetzer

In preparation

Abstract

Motivated by the parameterized post-Einsteinian (ppE) scheme devised by Yunes and Pretorius, which introduces corrections to the post-Newtonian coefficients of the frequency domain gravitational waveform in order to emulate alternative theories of gravity, we compute analytical time domain waveforms that, after a numerical Fourier transform, aim to represent (phase corrected only) ppE waveforms. In this formalism, alternative theories manifest themselves via corrections to the phase and frequency, as predicted by General Relativity (GR), at different post-Newtonian (PN) orders. In order to present a generic test of alternative theories of gravity, we assume that the coupling constant of each alternative theory is manifestly positive, allowing corrections to the GR waveforms to be either positive or negative. By exploring the capabilities of massive black hole binary GR waveforms in the detection and parameter estimation of corrected time domain ppE signals, using the current eLISA configuration (as presented for the ESA Cosmic Vision L3 mission), we demonstrate that for corrections arising at higher than 1PN order in phase and frequency, GR waveforms are sufficient for both detecting and estimating the parameters of alternative theory signals. However, for theories introducing corrections at the 0 and 0.5 PN order, GR waveforms are not capable of covering the entire parameter space, requiring the use of non-GR waveforms for detection and parameter estimation.

8.1 Introduction

General Relativity (GR) has been tested rigorously in the recent past [32]; so far, no evidence has been observed in the macroscopic regime that suggests any failure of GR. Nevertheless, various alternative theories of gravity have been proposed in order to account for effects that are currently otherwise explained, or for the lack of a common intersection between GR and quantum field theory. A few of these theories can be ruled out by solar system and binary pulsar observations. However, many of them are still essentially unconstrained since GR has never been tested in the true strong field regime where v/c approaches unity or where $\Phi/c^2 = GM/rc^2 \sim 1$, where G is Newton's gravitational constant, c is the speed of light, r is the effective distance of measurement and M is the mass of the system.

Gravitational Waves (GWs) will provide a unique opportunity to test GR in the strong field, dynamical regime. A ground-based network of detectors (i.e. Advanced LIGO, Advanced Virgo, KAGRA etc.) is currently being enhanced, with the aim of going online in 2015 and providing the first direct detection of astrophysical sources of GWs in the Hz-kHz regime within the next decade. Simultaneously, pulsar timing array analysis is expected to improve to a point where detection in the nHz regime should be possible within the same time frame. On a longer time scale, ESA has recently chosen the theme of the "Gravitational Wave Universe" for the ESA Cosmic Vision L3 mission in order to nourish the development of a space-based GW mission. The mission, called eLISA, consists of a triangle of three spacecrafts in a heliocentric orbit, interconnected with two laser arms. This single channel laser interferometer will operate at frequencies between $\sim 10^{-5} - 1$ Hz, and will be sensitive to supermassive black hole binaries (SMBHBs) with total redshifted masses between $10^4 - 10^8 M_\odot$. SMBHBs provide excellent strong-field tests of GR, as the waveform models for such objects are quite well understood [11]. The waveforms are composed of three phases: inspiral, merger and ringdown. The inspiral phase is adequately described by post-Newtonian theory, while the ringdown phase is known from perturbation theory. Incredible advances in numerical relativity now mean that we have a much more complete idea of how the merger phase works. In the next few years as this field improves even further, we will rapidly approach a point where we may have complete analytical waveforms involving all three phases.

Tests of GR can be performed from a number of different viewpoints [34]. For *direct* tests, one takes a certain alternative model to GR with known action, e.g. a scalar-tensor theory, computes the modified gravitational waveforms and checks (in a post detection manner) whether or not they achieve a higher correlation with the recorded data than GR waveforms. The advantage of such a top-down approach is that it is possible to directly constrain the coupling constant(s) of the theory through evaluating the detector data. At the same time, there is of course the disadvantage that GR can only be tested against this specific theory. Since it requires an intense effort to perform such steps for every imaginable alternative to GR, one can think of performing more *generic* tests. Certain features of GR can be tested in this more phenomenological manner: what if the 'graviton' has a mass? What if Lorentz invariance is violated? What if Newton's gravitational constant changed with time? Such features could be exhibited by a certain subset of alternative theories; and while a generic test will not be able to reveal which particular alternative is the true underlying theory, it could certainly provide evidence against GR and point us in the right direction.

As a simple example, consider a class of theories that exhibit massive gravity. There have been several studies assessing the ability of ground and space-based gravitational-wave detectors to see whether such an effect is manifested in the detector data [1, 50, 53, 54, 54–58]. Will [50] has computed the effect of a GW dispersion relation through the different arrival times of wave trains with different frequencies (to leading order) as a 1PN correction to the frequency domain GR phase, namely

$$\Psi_{\rm MG}(f) = \Psi_{\rm GR} - \beta_{\rm MG}\, u^{-1}, \tag{8.1}$$

$$\beta_{\rm MG} = \frac{\pi^2 D(z)\, G\mathscr{M}}{c^2 \lambda_g^2 (1+z)}, \tag{8.2}$$

where f is the GW frequency, $u = \frac{G\mathscr{M}}{c^3}\pi f$ is the reduced GW frequency, and $\mathscr{M} = m\eta^{3/5}$ is the chirp mass of the binary. In this last expression $m = m_1 + m_2$ and $\eta = m_1 m_2/m^2$ are the total mass and the symmetric mass ratio of the source. Finally, z is the redshift of the source, and the distance parameter is given by $D(z) = \frac{1+z}{a_0}\int_{t_e}^{t_a} a(t)\,dt$, where t_e and t_a are the times of signal emission and arrival, respectively, and $a(t)$ is the cosmic scale factor with present value $a_0 = a(t_a)$. $\beta_{\rm MG}$ is in functional relation to the coupling constant of the massive gravity correction, the gravition's Compton wavelength λ_g. From an analysis perspective, in the remainder of this paper we call $\beta_{\rm MG}$ the coupling constant of this particular physical effect.

Being interested in whether or not GR is the correct theory, it is reasonable to perform as many such tests as possible, without having to assume a certain alternative theory or a particular physical effect. This can be done with a waveform model that aims to catch any possible deformation of the expected GR waveform. Among such are tests that introduce perturbations to the post-Newtonian (PN) coefficients of the GR inspiral waveform [35, 71]; similarly, the ringdown part of the waveform can be checked [35, 125–127]. One has to be careful here, as one de-facto tests only the PN coefficients of GR or the perturbed Kerr metric, respectively, but not directly GR itself. Although it has been shown that phenomenological inspiral-merger-ringdown (IMR) waveforms can in principle decrease parameter estimation errors by almost an order of magnitude [56], we consider only the inspiral part in this work due to the lack of a full theoretical model for the merger phase. A framework to test the PN coefficients of the inspiral waveform that has been studied recently is the ppE scheme devised by Yunes and Pretorius [35, 67, 69, 128] that is motivated by the stationary phase approximation (SPA) and works in the frequency domain. There, leading order corrections to the amplitude and the phase of the waveform are introduced:

$$\tilde{h}_{\rm ppE}(f) = \tilde{h}_{\rm GR}(f)\,(1 + \alpha u^a)\, e^{i\beta u^b}, \tag{8.3}$$

where $\{\alpha, a, \beta, b\}$ is the set of ppE parameters with $\alpha, \beta \in \mathbb{R}$ and a, b being integer multiples of $-1/3$. Sampson et al. [66] have shown that leading order corrections are sufficient to discriminate between GR and any alternative to it, while higher order corrections play only a subdominant role.

The existing ppE scheme has been developed in the frequency domain for a number of reasons: GW astronomy is mainly conducted using the concept of optimal Wiener or 'matched' filtering. Here, one assumes a theoretical waveform model based on a number of physical parameters, and correlates this template with a data set to test the viability of the choice of parameters. Matched filtering works extremely well in the case where we are tasked with extracting a coherent signal buried in noise (which is almost always the case in GW astronomy). By carrying out the analysis in the Fourier domain, it is possible to 'lift' the signal above the noise. The important results in GW astronomy for both detection and parameter estimation require the evaluation of noise-weighted inner products of the form

$$(g|h) = 2\int_0^\infty \frac{\tilde{g}^*(f)\tilde{h}(f) + \tilde{g}(f)\tilde{h}^*(f)}{S_n(f)}\,\mathrm{d}f, \tag{8.4}$$

where $\tilde{g}(f)$ and $\tilde{h}(f)$ are the Fourier transforms of the time domain waveforms $g(t)$ and $h(t)$, and $S_n(f)$ is the noise spectral density of the detector (which we will define at a later stage). If $S_n(f)$ is constant across the frequency band of the detector, we could use Parseval's theorem to evaluate these inner products in the time domain. As it is not constant for the sources we consider in this work, there is no closed form solution to the above integrals, and they must then be evaluated numerically in the Fourier domain. When GW algorithms were first developed, one had the option of generating a time domain waveform and then carry out a numerical Fast Fourier Transform (FFT). However, due to the efficiency to the algorithm and the available computers, the FFT accounted for a large fraction of the total waveform generation time. In this case it was clearly more advantageous to generate the waveforms directly in the Fourier domain. This lead to the widespread use of the SPA in GW parameter estimation due its low computational cost. In most cases it has been shown to perform reasonably well for ground based detectors such as LIGO, although it should

be pointed out that some modifications are necessary in the high mass regime [129–131]. Nowadays, the FFT accounts for a small quantity of the total waveform generation time (normally on the order of between 3-8%). Therefore, as the modelling of the binary system is conducted in the time domain, and as the GW waveforms are initially derived in the time domain, there seems to be little point in expending the extra theoretical energy to derive either higher order approximation or alternative theory SPA waveforms. Furthermore, several studies have shown issues with the simple (unextended) SPA waveform, especially at the high mass end and close to the last stable orbit [129–131]. For these reasons, we chose to work in a framework of perturbed GR time domain waveforms. In order to establish a common base with the frequency domain ppE scheme, we compute an approximate relation between both schemes.

As matched filtering is highly sensitive to phase corrections, in this work we neglect amplitude corrections to the ppE waveforms and set $\alpha = a = 0$ in Eqn (8.3). In terms of the phase correction parameters $\{b, \beta\}$ as used in (8.3), we work with the general form corrected orbital phase

$$\Phi^{(\pm)}_{\rm NGR}(\Theta; b, \beta) = \Phi_{\rm GR}(\Theta) \pm \Phi_c(\Theta; b, \beta), \tag{8.5}$$

where NGR stands for 'non-GR', Θ represents the dimensionless time (to be defined) and $\Phi_c(\Theta; b, \beta)$ is a corrective term to the GR phase that will also be defined at a later stage. As we stated earlier, our goal is to work in the most general context possible, allowing for all possible deviations to GR. Therefore, in constructing our theoretical framework, we always assume that the coupling constant β is manifestly positive, allowing us to distinguish between positive and negative corrections to the GR waveform.

This paper is structured as follows: In section 8.2 we review time and frequency domain (SPA) waveform models as they are in GR. Then, in section 8.3, we introduce modifications to both waveform models and set them into approximate relation. In section 8.4 we introduce the methodology to detect non-GR signals and carry out a parameter estimation for the different systems. Finally the results are presented in section 8.5.

8.2 Waveform models

8.2.1 Time domain waveform

If we consider the quasi-circular inspiral of two non-spinning supermassive black holes with masses m_1 and m_2, with respect to a fixed detector frame, we can define the binary unit angular momentum vector $\hat{\boldsymbol{L}}$ and the unit vector pointing from the detector to the source $\hat{\boldsymbol{n}}$. The position of the source in the sky can then be indicated with spherical angles (θ, ϕ). The orientation of the binary relative to the detector can be described by the inclination $\iota = \arccos\left[\hat{\boldsymbol{L}} \cdot \hat{\boldsymbol{n}}\right]$ and polarisation angle

$$\psi = \arctan\left[\frac{\hat{\boldsymbol{L}} \cdot \hat{\boldsymbol{z}} - (\hat{\boldsymbol{L}} \cdot \hat{\boldsymbol{n}})(\hat{\boldsymbol{z}} \cdot \hat{\boldsymbol{n}})}{\hat{\boldsymbol{n}} \cdot (\hat{\boldsymbol{L}} \times \hat{\boldsymbol{z}})}\right]. \tag{8.6}$$

The gravitational wave strain of the eLISA detector is, in the low frequency approximation [84], a linear combination of $h_{+,\times}$ polarisations, weighed with the antenna patterns $F^{+,\times}$:

$$h(t) = h_+[\xi(t)]F^+_k + h_\times[\xi(t)]F^\times. \tag{8.7}$$

Because of the detector motion relative to the source, a Doppler shift is introduced via a phase shifted time parameter $\xi(t) = t - \frac{R_\oplus}{c}\sin\theta\cos(\alpha(t) - \phi)$, where $R_\oplus = 1$AU is the Earth-Sun distance and $\alpha(t) = 2\pi f_m t + \alpha_0$ with LISA modulation frequency $f_m = 1/\text{yr}$ is the orbital phase of the detector.

The antenna patterns depend on position and orientation of the source in the sky and are given for an eLISA-like detector by [82, 86]

$$F_k^+(t;\psi,\theta,\phi) = \frac{1}{2}\left[\cos(2\psi)D^+(t;\psi,\theta,\phi,\lambda_k) - \sin(2\psi)D^\times(t;\psi,\theta,\phi,\lambda_k)\right], \tag{8.8}$$

$$F_k^\times(t;\psi,\theta,\phi) = \frac{1}{2}\left[\sin(2\psi)D^+(t;\psi,\theta,\phi,\lambda_k) + \cos(2\psi)D^\times(t;\psi,\theta,\phi,\lambda_k)\right], \tag{8.9}$$

with $\lambda_1 = 0$ and $\lambda_2 = \pi/4$. Expressions for the detector patterns $D^{+,\times}(t;\psi,\theta,\phi,\lambda_k)$ will not be printed here, but can be found in [86].

Many previous studies on detection and parameter estimation have used "restricted" post-Newtonian waveforms, i.e. the amplitude of the waveform is kept at the dominant order, while the phase of the waveform is expanded to higher post-Newtonian orders. However, a large body of work has demonstrated that the inclusion of higher harmonic corrections to the waveform are extremely important in both the breaking of parameter correlations and the improvement of parameter estimation [88, 132–136]. In fact, in some cases the estimation of luminosity distance, sky resolution and mass determination have been shown to be improved by at least an order of magnitude due to the inclusion of the harmonic corrections [132]. With this in mind, we will use higher harmonic corrected gravitational wave polarisations up to second post-Newtonian (2PN) order[11, 137], i.e.

$$h_{+,\times} = \frac{2GM\eta}{c^2 D_L} x\left[H_{+,\times}^{(0)} + x^{1/2}H_{+,\times}^{(1/2)} + xH_{+,\times}^{(1)} + x^{3/2}H_{+,\times}^{(3/2)} + x^2 H_{+,\times}^{(2)}\right], \tag{8.10}$$

where the post-Newtonian parameter $x = (GM\omega/c^3)^{2/3}$ is a function of the orbital frequency ω. The luminosity distance D_L is given as a function of redshift z in terms of the ΛCDM model by

$$D_L = (1+z)\frac{c}{H_0}\int_0^z \frac{dz'}{\sqrt{\Omega_R(1+z')^4 + \Omega_M(1+z')^3 + \Omega_\Lambda}}, \tag{8.11}$$

using the concurrent Planck values of $\Omega_R = 4.9\times10^{-5}$, $\Omega_M = 0.3086$, $\Omega_\Lambda = 0.6914$ and the Hubble constant $H_0 = 67.77$ km s^{-1} Mpc^{-1} [17]. The waveform evolution is governed by the orbital phase and frequency of the binary, which can be expressed to 2PN order using the dimensionless time variable $\Theta(t) = \frac{\eta c^3}{5GM}(t_c - t)$ as [11, 24]

$$\begin{aligned}\omega(\Theta) &= \frac{c^3}{8GM}\left[\Theta^{-3/8} + \left(\frac{743}{2688} + \frac{11}{32}\eta\right)\Theta^{-5/8} - \frac{3\pi}{10}\Theta^{-6/8}\right.\\ &\quad\left. + \left(\frac{1855099}{14450688} + \frac{56975}{258048}\eta + \frac{371}{2048}\eta^2\right)\Theta^{-7/8}\right],\end{aligned} \tag{8.12}$$

$$\begin{aligned}\Phi(\Theta) &= \Phi_C - \frac{1}{\eta}\left[\Theta^{5/8} + \left(\frac{3715}{8064} + \frac{55}{96}\eta\right)\Theta^{3/8} - \frac{3\pi}{4}\Theta^{2/8}\right.\\ &\quad\left. + \left(\frac{9275495}{14450688} + \frac{284875}{258048}\eta + \frac{1855}{2048}\eta^2\right)\Theta^{1/8}\right].\end{aligned} \tag{8.13}$$

Multiples of the orbital phase are then manifest in the harmonic coefficients $H_{+,\times}^{(n)}(\Phi,\iota,m_1,m_2)$.

8.2.2 Stationary phase approximation

To work directly in the Fourier domain, one requires an analytic form of the Fourier transform $\tilde{h}(f) = \int e^{2\pi i f t}h(t)\,\mathrm{d}t$. Many previous studies in the field of GW data analysis have employed the stationary phase

approximation which gives a reasonable approximation of the Fourier integral, respecting some limitations towards high masses and close to the last stable orbit. In constructing the SPA, one assumes that because of the rapid oscillatory nature of the integrand, the Fourier integral averages to zero, except at points where the phase function has an extremum. By expanding the phase in a Taylor series around the stationary point, the integral takes on the form of a Fresnel integral with a standard solution.

Only considering the dominant harmonic of Eqn (8.7) with the corresponding non-zero coefficients $H_+^{(0)} = -(1+\cos^2\iota)\cos 2\Phi$ and $H_\times^{(0)} = -2\cos\iota\sin 2\Phi$, one ends up with (see e.g. [25, 117])

$$\tilde{h}(f) = \sqrt{\frac{5}{96}}\frac{\pi^{-2/3}}{D_L}\left(\frac{G\mathscr{M}}{c^3}\right)^{5/6} A_{\rm pol}[t(f)]\, f^{-7/6}\, e^{i(\Psi(f)-\varphi_{\rm pol}[t(f)]-\varphi_D[t(f)])}, \tag{8.14}$$

with the SPA phase given by

$$\Psi(f) = 2\pi f\, t(f) - 2\Phi[t(f)] - \frac{\pi}{4}, \tag{8.15}$$

and polarisation amplitude and phase

$$A_{\rm pol} = \sqrt{(1+\cos^2\iota)^2 F^+(t)^2 + 4\cos^2\iota\, F^\times(t)^2}, \tag{8.16}$$

$$\varphi_{\rm pol} = \text{atan2}\left[\frac{2\cos\iota\, F^\times(t)}{(1+\cos^2\iota)^2 F^+(t)}\right]. \tag{8.17}$$

The Doppler phase correction caused by detector motion is given by

$$\varphi_D = 2\pi f \frac{R_\oplus}{c}\sin\theta\cos(\alpha[t(f)] - \phi)]. \tag{8.18}$$

Finally, the time evolution $t(f)$ is given by the TaylorT2 timing function which up to 2PN order is defined by [24]

$$t(f) = t_c - \frac{5GM}{256\eta c^3 x^4}\left[1 + \left(\frac{743}{252}+\frac{11}{3}\nu\right)x - \frac{32}{5}\pi x^{3/2} + \left(\frac{3058673}{508032}+\frac{5429}{504}\eta+\frac{617}{72}\eta^2\right)x^2\right]. \tag{8.19}$$

The SPA has been shown to be reasonably accurate as long as the binary inspiral is in the adiabatic regime, i.e. as long as $\frac{d(\log a(t))}{dt} \ll \frac{d\Phi}{dt}$ and $\frac{d^2\Phi}{dt^2} \ll \left(\frac{d\Phi}{dt}\right)^2$, where $a(t)$ is the amplitude of the GW [26, 138].

8.3 Relating time and frequency domain waveforms

8.3.1 A relation between modified waveforms in time and frequency domains

To derive the perturbed time domain waveform, we start in the same manner as [35] and introduce a leading order correction to the time domain orbital phase, albeit based a little bit more on the general form of the GR orbital phase given by Eqn (8.13):

$$\Phi_{\rm NGR}(\Theta) = \Phi_{\rm GR}(\Theta) \pm \frac{1}{\eta}\kappa_i(b,\beta)\Theta^{\frac{5-2i}{8}}, \tag{8.20}$$

where $\kappa_i(b,\beta) \in \mathbb{R}$ and $i \in \{0, 1/2, 1, 3/2, 2\}$ allow the corrections to enter somewhere between 0PN and 2PN. We choose not to consider corrections above 2PN and below 0PN in this work: we disregard 'negative' PN terms such as a '-1PN' dipole moment correction for simplicity and because for the main class of theories exhibiting dipole radiation (scalar-tensor theories), SMBHB inspirals are not expected to emit dipole radiation [39]. Furthermore, corrections coming in below 1PN order are better constrained

using solar system tests and binary pulsar observations [67, 113]. In order to compare our results with the considerable effort that has already been done in the field, we relate Eqn (8.20) to a leading order phase-only correction ppE scheme. Eqn (8.3) implies the phase correction

$$\Psi_{\rm NGR}(b,\beta;u) = \Psi_{\rm GR}(u) \mp \beta\, u^b. \tag{8.21}$$

To relate Eqns (8.20) and (8.21), we construct a time domain waveform, that, after a numerical Fourier transform, approximately reproduces a frequency domain waveform with a modified phase as in Eqn (8.21). To this end, we introduce sub-leading terms to Eqn (8.20) which then becomes

$$\Phi_{\rm NGR}(\Theta) = \Phi_{\rm GR}(\Theta) \pm \frac{1}{\eta}\sum_i \kappa_i \Theta^{\frac{5-2i}{8}}. \tag{8.22}$$

The next question to answer is what set of $\{\kappa_i\}$ leads to a time domain waveform that is consistent with a modified SPA waveform with phase (8.21) . The necessary relations can be found by reconsidering the steps that led us to the SPA waveform. Eqn (8.15) can, in terms of the reduced frequency u, be written as

$$\Psi(u) = 2\left[\frac{c^3}{G\mathscr{M}} t(u)\, u - \Phi(u)\right] - \frac{\pi}{4}. \tag{8.23}$$

Since the frequency derivative of the orbital phase can be expressed as

$$\frac{d\Phi}{du}(u) = \frac{dt}{du}(u)\frac{d\Phi}{dt}[t(u)] = \frac{dt}{du}\frac{c^3}{G\mathscr{M}} u, \tag{8.24}$$

the frequency derivative of the SPA phase reduces then to the simple expression

$$\frac{d\Psi}{du} = 2\frac{c^3}{G\mathscr{M}}\, t(u). \tag{8.25}$$

This enables us to write the time-of-frequency function in the simple form

$$t(u) = \frac{1}{2}\frac{G\mathscr{M}}{c^3}\frac{d\Psi}{du}. \tag{8.26}$$

Similarly, we can write the inverse relation as

$$u(t) = \frac{G\mathscr{M}}{c^3}\frac{d\Phi}{dt}. \tag{8.27}$$

One should remember that for Eqn (8.26) we have only considered the dominant harmonic, while Eqn (8.27) uses no such assumption. The functions $t(u)$ and $u(t)$ inherit the corrections applied to Ψ and Φ in the previous section in a simple manner. Since we require $u[t(u)] = u$, relations between the time domain and the SPA phase coefficients can be computed at ease. In terms of Θ the above expressions can be written as

$$u(\Theta) = \frac{G\mathscr{M}}{c^3}\frac{d\Theta}{dt}\frac{d\Phi}{d\Theta}, \qquad \Theta(u) = \Theta[t(u)].$$

The coefficients of $\Psi(u)$, given the coefficients for $\Phi(\Theta)$, can thus be computed by evaluating the equation

$$u[\Theta(u)]_{\rm 2PN} = u\left(1 + \sum_{k=0}^{4} u^{k/3}\mathscr{A}_k\right) = u, \tag{8.28}$$

expanded up to 2PN order in u. For the non-GR time domain and SPA phases, we do this at linear order in κ_i and β, assuming that the corrections are small enough. Setting the $\mathscr{A}_k$ to zero, the resulting system can then be solved for $\kappa_i(b,\beta)$.

Table 8.1: *Impact of different frequency domain corrections to the phase on the parameter space of time domain corrections $\kappa_i(b,\beta)$.*

b	-5/3	-4/3	-1	-2/3	-1/3
κ_0	16β	0	0	0	0
$\kappa_{1/2}$	0	$8\beta\eta^{1/5}$	0	0	0
κ_1	$-16\beta\Phi_1$	0	$4\beta\eta^{2/5}$	0	0
$\kappa_{3/2}$	$-\frac{32}{3}\beta\Phi_{3/2}$	$-\frac{32}{5}\beta\Phi_1\eta^{1/5}$	0	$2\beta\eta^{3/5}$	0
κ_2	$16\beta\left(\frac{4}{5}\Phi_1^2-\frac{1}{3}\Phi_2\right)$	$-\frac{64}{15}\beta\Phi_{3/2}\eta^{1/5}$	$-\frac{12}{5}\beta\Phi_1\eta^{2/5}$	0	$\beta\eta^{4/5}$

We restrict b and i such that corrections can come in only between 0PN and 2PN order, in detail $b \in \{-5/3,-4/3,-1,-2/3,-1/3\}$ and $i \in \{0,1/2,1,3/2,2\}$; this corresponds to 0PN, 0.5PN, 1PN, 1.5PN, 2PN corrections, respectively. While we fix one particular value of b, we always allow the full sum of corrections proportional to κ_i in the time domain phase. This enables us to compute $\kappa_i(b,\beta)$ for each value of b; the results are listed in table 8.1. As expected, the κ_i are always proportional to β. If the frequency domain phase correction enters at nPN order, $n=(3b+5)/2$, then $\kappa_{i<n}=0$ and the remaining κ_i are proportional to $\eta^{2n/5}$. Also one can see that the lowest order correction κ_i then has the numeric prefactor 2^{4-2i}. Moreover, in each diagonal term, the coefficients are proportional to $\Phi_0=1$, in the first off-diagonal to $\Phi_{1/2}=0$, in the second off-diagonal to Φ_1 and in the third off-diagonal to $\Phi_{3/2}$. In the fourth off-diagonal element, terms proportional both to Φ_1^2 and Φ_2 can appear.

It is important to stress that these are approximate relations, i.e. we do not expect the time domain waveform to match the SPA waveform perfectly. This is because we expect time domain and SPA waveforms to differ near the last stable orbit due to approximation errors in the SPA. However, the waveform match is more than good enough to accomplish our task of constraining the 'coupling constant' β.

By the same argument as in [69], we assume that leading order corrections to the time domain phase are already enough to discriminate between GR and competing theories. This can be justified through the fact that the next-to-leading order term is in always of order 1PN away from the leading order term (see table 8.1), hence we usually end up with $\left[\kappa_{i+1}\Theta^{\frac{5-2(i+1)}{8}}\right]/\left[\kappa_i\Theta^{\frac{5-2i}{8}}\right]\sim\Theta^{-\frac{1}{4}}$. At an orbital separation of $R_{\max}=7GM/c^2$, $\Theta^{-1/4}$ usually takes a numerical value of around 0.7, while away from the last stable orbit it will be much smaller.

Therefore, to leading order, taking only the diagonal terms in table 8.1 into account, we can write our non-GR corrected phase as

$$\Phi^{(\pm)}_{\rm NGR}(b,\beta;\Theta)=\Phi_{\rm GR}(\Theta)\pm 2^{-1-3b}\beta\,\eta^{\frac{3b}{5}}\Theta^{-\frac{3b}{8}}, \tag{8.29}$$

where $i=\frac{3b+5}{2}$ has been used. This expression corresponds to the modified SPA phase

$$\Psi^{(\pm)}_{\rm NGR}(b,\beta;u)=\Psi_{\rm GR}(u)\mp\beta u^b. \tag{8.30}$$

We should note here that the sign of the corrections in the time domain are reversed from those in the frequency domain.

In our study, we assume that β is manifestly positive for two reasons. The first is that we would like to be able to differentiate between positive and negative corrections to the GR phase. The second is a numerical reason: when carrying out a parameter estimation study, we will need to calculate the Fisher Information Matrix (FIM). As we expect β to be quite small for certain theories, the FIM is numerically more stable if we chose $\ln(\beta)$ as the working parameter rather than β itself, thus requiring a positive value.

Given the non-GR corrected phase, we can now also write down the modified orbital frequency evolution

$$\omega^{(\pm)}_{\rm NGR}(b,\beta;\Theta) = \omega_{\rm GR}(\Theta) \pm 2^{-4-3b}\frac{3\beta}{5}\frac{c^3}{GM}\eta^{\frac{3b}{5}+1}\Theta^{-\frac{3b}{8}-1}. \tag{8.31}$$

Using these expressions, our next goal is to compute for what size of β the eLISA detector is able to distinguish between GR and a competing theory. This is done in section 8.5 for a total of ten different cases: five values of b (as defined above) and for $\Phi^{(+)}_{\rm NGR}$ and $\Phi^{(-)}_{\rm NGR}$ individually. In the next subsection, we discuss the limits that we choose to set on β, which will further be used as priors in our study.

8.3.2 Suggested limits to correction parameters

The possible values of β, and hence $\kappa_i(b,\beta)$, have to be limited for two reasons: firstly, due to the fact that we make the assumption that we are working with a perturbed GR waveform. By doing so, one can then, after successful detection, conduct a further analysis of the recovered signal and check it against different theories. If the corrections to the GR waveforms are too large (which they could well be after 1PN order corrections where they there they are essentially unconstrained), then GR waveforms will fail to detect the signal. Secondly, in the upcoming chapters, we use a Markov Chain Monte Carlo algorithm (MCMC) to not only confirm detection, but also to conduct a Bayesian inference. For the MCMC to work, we need to place priors on β, as a function of the theory described by different values of b.

In order to limit the perturbation of the GR waveform, one should demand that κ_i is small with respect to the fiducial orbital phase coefficients (let us call them Φ_i) in Eqn (8.13). One issue is that not every correction has its own fiducial GR coefficient. Since there is no 0.5PN term in the GR phase evolution, we have no way of constraining the corresponding $\kappa_{1/2}$ coefficient. In this case, we simply make sure that all the other non-zero subleading coefficients in Eqn (8.22) (i.e. $\kappa_{3/2}$ and κ_2) stay within a certain limit. For this study, we choose the limit to be 50% of the GR coefficient value:

$$\max_i \left|\frac{\kappa_i}{\Phi_i}\right| < 0.5. \tag{8.32}$$

This results in a limit on β as a function of mass ratio q, depending on what order of approximation a correction enters due to a theory with a particular value of b. We found that for all cases, regardless of whether the corrections have a positive or negative sign, except for $b = -4/3$, the first non-zero $\frac{\kappa_i}{\Phi_i}$ dominates the others. Interestingly, for $b = -4/3$, $\frac{\kappa_2}{\Phi_2}$ dominates $\frac{\kappa_{3/2}}{\Phi_{3/2}}$. The resulting upper limits on β are plotted as a function of the mass ratio in Fig 8.1.

In cell (a) we plot the limits on β for theories with positive sign corrections, while in cell (b) we have the maximum values of β for theories with negative corrections. In Table 8.2 we also provide an analytic form for the limit of $|\beta|$ for the different values of b. As these values are correct for the magnitude of the coupling constant, it would suggest that the limits plotted in Fig 8.1 should be identical regardless of the sign of the corrections. However, we can clearly see that this is not the case. The reason for the discrepancy between the plot and the table is due to pathologies in the evolution of the non-GR orbital frequency. For all cases, our goal is to evolve the binary systems to a minimum separation of $R = 7GM/c^2$. This works in all cases when we consider positive corrections to the phase. However, when we introduce a negative sign correction, the gradient of the non-GR orbital frequency changes sign before reaching $7GM/c^2$. As a consequence, we are then required to terminate the waveform evolution at the point where $\mathrm{d}\omega_{NGR}/\mathrm{d}t = 0$. Thus, the maximum limits for $\beta(q)$ plotted in cell (b) correspond to waveforms terminated at a separation of $R(\mathrm{d}\omega_{NGR}/\mathrm{d}t = 0)$. We should point out that as we go to smaller values of β in each theory, we do recover a situation where the waveforms are once more terminated at $R = 7GM/c^2$.

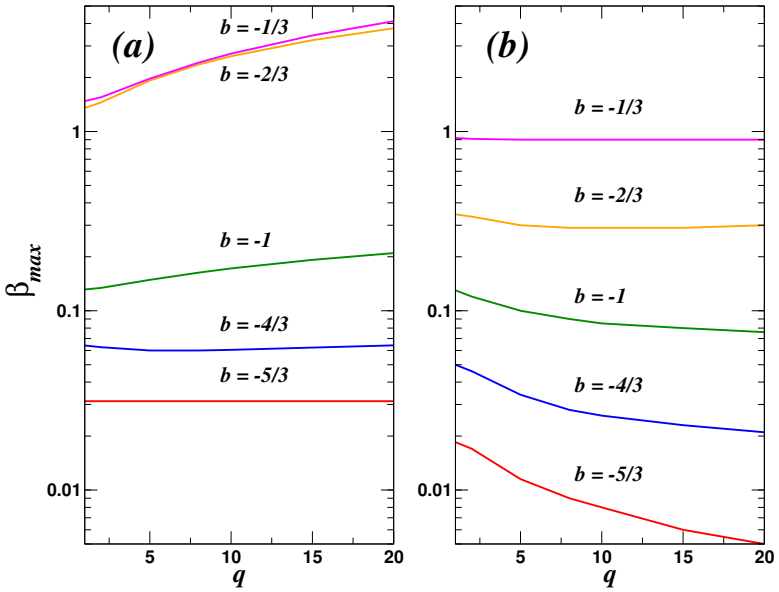

Figure 8.1: *Maximum allowed values for β as a function of mass ratio q given the constraint of $\kappa_i/\Phi_i \leq 0.5$ for different alternative theories. Cell (a) represents non-GR corrections with positive sign, while cell (b) represents non-GR corrections with negative sign.*

$b = -5/3$ (0PN)	$\|\beta\| < 0.03125$
$b = -4/3$ (0.5PN)	$\|\beta\| < \frac{15}{128\eta^{1/5}} \left\|\frac{\Phi_2(\eta)}{\Phi_{3/2}}\right\|$
$b = -3/3$ (1PN)	$\|\beta\| < \frac{\|\Phi_1(\eta)\|}{8\eta^{2/5}}$
$b = -2/3$ (1.5PN)	$\|\beta\| < \frac{\|\Phi_{3/2}\|}{4\eta^{3/5}}$
$b = -1/3$ (2PN)	$\|\beta\| < \frac{\|\Phi_2(\eta)\|}{2\eta^{4/5}}$

Table 8.2: *Upper limits on β for different powers of b, assuming that the $\kappa_i(b,\beta)$ are at maximum 50% of the fiducial GR orbital phase parameters Φ_i.*

8.4 Detecting non-GR signals

8.4.1 Detector configuration

For this study we assume an eLISA configuration, where the space-craft are separated by 10^6 kms and operate using four laser links. In this configuration, the observatory can be interpreted as a single channel Michelson interferometer. This corresponds to the eLISA configuration accepted as a candidate for the ESA Cosmic Vision L3 mission concept [76, 77]. The noise power spectral density for the eLISA observatory can be modelled using the form

$$\begin{aligned} S_n^{\rm instr}(f) &= \frac{1}{4L^2}\left[S_n^{fxd} + 2S_n^{\rm pos}\left(2+\cos^2\left(\frac{f}{f_*}\right)\right)\right. \\ &\left. +8S_n^{\rm acc}\left(1+\cos^2\left(\frac{f}{f_*}\right)\right)\left(\frac{1}{(2\pi f)^4}+\frac{(2\pi 10^{-4})^2}{(2\pi f)^6}\right)\right], \end{aligned} \tag{8.33}$$

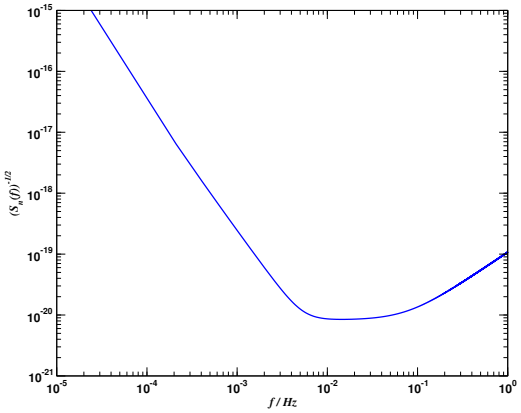

Figure 8.2: *Instrumental noise model for a 10^6m arm eLISA configuration.*

where $L = 10^6$m is the arm-length of the particular LISA configuration, $S_n^{\rm pos}(f) = 1.21 \times 10^{-22}\mathrm{m}^2/\mathrm{Hz}$ is the position noise, $S_n^{\rm acc}(f) = 9 \times 10^{-30}\mathrm{m}^2/(\mathrm{s}^4\mathrm{Hz})$ is the acceleration noise, $S_n^{fxd} = 6.28 \times 10^{-23}\mathrm{m}^2/\mathrm{Hz}$ is a frequency independent fixed level noise in the detector and $f_* = 1/(2\pi L)$ is the mean transfer frequency. We plot this noise curve in Fig. 8.2.

8.4.2 Bayesian inference and MCMC

Our goal in this work is twofold: we are first of all interested in testing the capability of GR templates in detecting non-GR signals for differing values of (b, β). Once we have confirmed the regions of "detectability", the next question to answer is to what values of β are we capable of resolving the system parameters without having to resort to using non-GR templates for different values of b. In each case, we inject a non-GR signal into random Gaussian instrumental noise. Given a detector response $s(t) = h_{NGR}(t; \boldsymbol{\lambda}, b, \beta) + n(t)$, where h_{NGR} is our corrected signal and $n(t)$ is random instrumental noise, and a GR template $h(t; \boldsymbol{\lambda})$ with the 9-dimensional binary physical parameter vector $\boldsymbol{\lambda} = (m_1, m_2, \theta, \phi, \iota, \psi, D_L, t_c, \Phi_c)$, we define the likelihood function

$$\mathscr{L}(\boldsymbol{\lambda}) = C \exp\left[-\frac{1}{2}(s - h(\boldsymbol{\lambda})|s - h(\boldsymbol{\lambda}))\right], \tag{8.34}$$

where C is a normalisation constant. The posterior distribution for the parameters $\boldsymbol{\lambda}$ is then given by Bayes' theorem

$$p(\boldsymbol{\lambda}|s) = \frac{\pi(\boldsymbol{\lambda})\mathscr{L}(\boldsymbol{\lambda})}{p(s)}. \tag{8.35}$$

where $\pi(\boldsymbol{\lambda})$ is the prior distribution of the binary parameters, and $p(s)$ is the marginal likelihood or model evidence.

Markov Chain Monte Carlo

As it is not our goal to conduct a full search over the entire possible parameter space for massive black hole binaries, we make the fundamental assumption that we have been able to narrow the search region by some other means. At this point we use a non-Markovian Metropolis-Hastings Markov Chain Monte Carlo (MCMC) to narrow the search space even further. When using a standard MCMC, one picks a starting point in the parameter space, and by using a tailored proposal distribution, proposes a jump to another part of the parameter space with parameters $\boldsymbol{\lambda}'$ using a proposal distribution of choice $q(|)$. One then compares

the new and old points in parameter space by evaluating the Metropolis-Hastings ratio

$$H = \frac{\pi(\boldsymbol{\lambda}')\,\mathscr{L}(\boldsymbol{\lambda}')q(\boldsymbol{\lambda}|\boldsymbol{\lambda}')}{\pi(\boldsymbol{\lambda})\,\mathscr{L}(\boldsymbol{\lambda})q(\boldsymbol{\lambda}'|\boldsymbol{\lambda})}. \tag{8.36}$$

If we work with a Hessian MCMC, we can use a multivariate Gaussian based on the Fisher information matrix (FIM) as our proposal distribution [139]. The FIM is defined as

$$\Gamma_{\mu\nu} = \left\langle \frac{\partial h_{GR}}{\partial \lambda^{\mu}} \middle| \frac{\partial h_{GR}}{\partial \lambda^{\nu}} \right\rangle, \tag{8.37}$$

where we explicitly specify that we are constructing the FIM using GR templates. We call the MCMC *Hessian* because the Hessian matrix of the log-likelihood is set equal to the FIM.

As we expect there to be a difference between the GR and non-GR waveforms for some particular theories, even if we inject GR templates with the true parameter values, we do not expect the starting points to be close to the final solution due to the mismatch between the two waveform models. This will be especially evident in the investigation of the $b = -5/3$ and $b = -4/3$ theories. In Fig. 8.3 we plot the power spectra for both the GR waveforms and for the non-GR waveforms in the $b = -5/3$ theory, assuming a SMBHB with masses of $10^7 - 10^6\,M_{\odot}$ at $z = 1$. The top image corresponds to positive corrections, while the bottom image represents negative corrections. In each case we plot a range of different values of the coupling constant β, with the maximum value corresponding to the limits derived earlier. If we first investigate the positive corrections, we can see that the increased values of β shift the waveforms to lower frequencies. In the case of $\beta = 0.03$, we can see that the dominant harmonic has started to drift below the lower frequency cutoff of the detector at $f = 10^{-5}$ Hz. For a GR template to detect this signal, it would first have to move it's total mass to a higher value, and then change it's mass ratio to fit the spread of the power spectrum. An investigation of the corresponding time domain waveforms shows that the higher the value of a positive β correction, the faster the waveform reaches the termination radius of $R = 7\,GM/c^2$.

In the lower image, we observe that the higher the value of β, the more the waveforms are shifted to higher frequencies as compared with the GR waveform. Again an investigation of the corresponding time domain waveforms demonstrates that it takes longer in the case of negative corrections for the waveforms to reach $R = 7\,GM/c^2$. For other theories, while the patterns are the same for both positive and negative corrections, the correction at each lower value of b induces a correction into the GR phase and frequency at higher PN orders. This implies that the deviations from a GR waveform become smaller as we go to lower values of b.

Due to the large possible mis-match between the GR and non-GR waveforms, it turns out that the final "detection" parameters for many of these systems lie many hundreds of sigma away from the input parameters. Therefore, while we are starting relatively close to the final solution in the parameter space, a short search phase is required for the MCMC to converge. To achieve convergence, we use two types of annealing schemes. The goal of annealing is to smoothen irregularities in the likelihood surface allowing the Metropolis-Hastings chain to converge on a solution quicker. To accomplish this, we replace the factor of $1/2$ in Eqn (8.34) by an inverse temperature. When the temperature is large, the likelihood surface is smoother and flatter. One then slowly cools the temperature back to a value of $1/2$ with the hope that the chain has now converged to the global solution. A problem with this method is choosing firstly, the initial temperature and secondly, the cooling rate. It was shown that the first of these problems can be overcome by allowing the chain to control the injected heat itself. This method, called thermostated annealing [139] injects a heat according to the rule

$$\gamma = \begin{cases} \frac{1}{2} & 0 \leq \rho \leq \rho_0 \\ \\ \frac{1}{2}\left(\frac{\rho}{\rho_0}\right)^2 & \rho > \rho_0 \end{cases}, \tag{8.38}$$

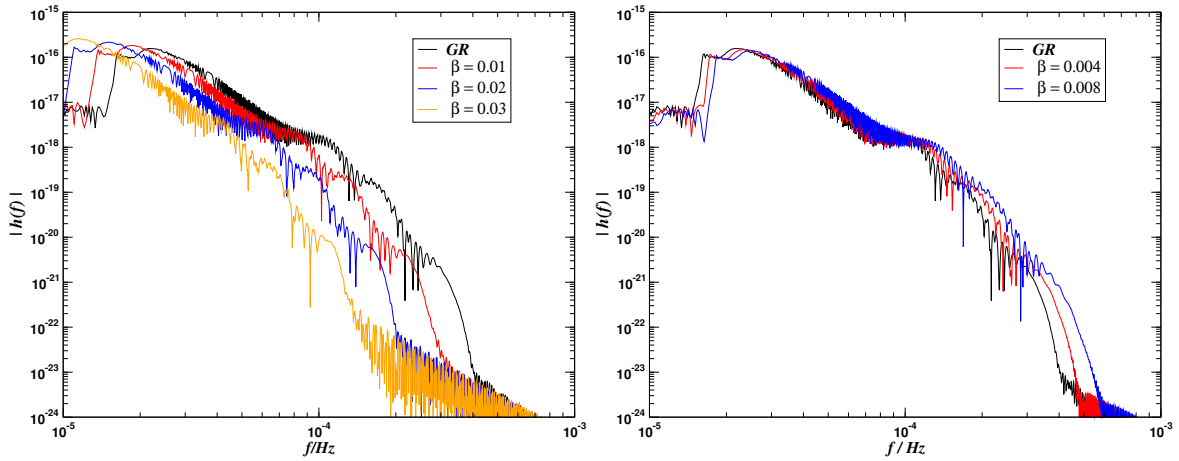

Figure 8.3: *Power spectra for both GR and non-GR waveforms assuming a SMBHB with individual source-frame masses of $10^7 - 10^6\,M_\odot$ at $z = 1$, for an alternative theory with $b = -5/3$, and for differing values of β. The top figure represents positive non-GR corrections, while the bottom figure displays negative non-GR corrections.*

where we define the signal to noise ratio (SNR) ρ as

$$\rho = \frac{\langle s|h\rangle}{\sqrt{\langle s|h\rangle}}, \tag{8.39}$$

and ρ_0 is a SNR threshold value of choice. As $\ln \mathscr{L} \propto \rho^2$, the second quantity in Eqn (8.38) is nothing more than a normalised likelihood. For this study, we choose $\rho_0 = 5$. We run the thermostated annealing phase for the first 2×10^4 iterations, whereupon we use a standard simulated annealing phase [140, 141]

$$\gamma = \begin{cases} \frac{1}{2} 10^{-\xi\left(1-\frac{i}{T_c}\right)} & 0 \leq i \leq T_c \\ \\ \frac{1}{2} & i > T_c \end{cases}, \tag{8.40}$$

to cool the surface over the next 10^4 iterations. At this point we begin a standard Hessian MCMC to estimate the recovered parameters.

As the starting point of the chain, even though it represents the true input parameters, may lie many hundreds of sigma from the final solution, the chain may start in a deep valley in the parameter space. In this situation, the log-likelihood is negative and it takes a long time for the chain to move onto a peak. To accelerate this process, we use a maximisation over the time of arrival t_c. This is done by calculating the correlation between the data and template, and searching for the maximum of the correlation. During the annealing phases of the algorithm, we maximise over t_c at every iteration while $\ln \mathscr{L} \leq 0$. Once the log-likelihood is positive, we then carry out a maximisation every ten iterations.

Setting priors for the MCMC

Finally, we impose the following priors on a subset of the physical parameters: using a flat prior, we constrain the maximum possible redshifted mass to be less than $1.163 \times 10^8\,M_\odot$. This ensures that the minimum last stable orbit frequency for higher harmonic waveforms is approximately at 5×10^{-5} Hz. For the symmetric mass ratio, we confine our search to the flat prior between $0.01 \leq \eta \leq 0.25$, corresponding to a mass ratio domain of $100 \leq q \leq 1$. As the mass distribution as a function of distance is one of the goals of

any space observatory, we use a flat prior on the luminosity distance given by $7.7\times10^{-4} \leq D_L/\mathrm{Gpc} \leq 110$. The lower bound on this prior assumes that the closest a SMBHB can exist is in the M31 (Andromeda) galaxy. The upper bound corresponds to a redshift of $z \sim 10$. Finally, as we assume an observation period of one year, we restrict the search over time of coalescence to $0.2 \leq t_c/\mathrm{yrs} \leq 0.99$. All angular parameters are allowed to vary over their natural ranges.

In each run, we start the MCMC algorithm at the true input values as our goal is not only detection of the non-GR signal, but also an estimation of parameters.

To investigate the capabilities of the eLISA detector, we chose five test sources with mass combinations of $(m_1, m_2) = \{(1.1,1)\times10^6, (5,1)\times10^6, (10^7, 10^6), (8\times10^6, 5.333\times10^5), (8\times10^6, 4\times10^5)\}\, M_\odot$. These mass combinations correspond to mass ratios of $q = \{1.1, 5, 10, 15, 20\}$. In all cases, the sources were placed at a redshift of $z = 1$ and the time to coalescence was set at $t_c = 0.89$ yrs. The input angular values were set as $\{\theta, \phi, \iota, \varphi_c, \psi\} = \{2.054, 4.5, 0.256, 3.707, 1.794\}$.

8.4.3 Setting a detection threshold

Before investigating the detection possibilities of the GR waveforms, we need to set a detection threshold for the eLISA observatory. To do this, we conduct a null-signal test by assuming that the output of the detector is composed of instrumental noise only, i.e. $o(t) = n(t)$. It is known that when a galaxy of white dwarf binaries is also included in the data stream, an algorithm can be fooled into a false detection. This is commonly known as the white-dwarf transform, where the SMBHB signal is able to match power from the multitude of white dwarves at different frequencies and returns a $\rho > 0$. While we do not include a galactic foreground in this study, in the same manner, it is also possible for a SMBHB template to match the random fluctuations of a Gaussian instrumental noise and also return a positive SNR.

To set our threshold for detection, we ran fifteen algorithms, as described above, from different starting positions in the parameter space. In all cases, the algorithms returned "detections" with SNRs of $9 \leq \rho \leq 9.5$. To account for the possibility of slightly higher values, we thus decided to take $\rho = 10$ as our threshold for detection.

8.5 Results

8.5.1 Detection horizons for non-GR theories

Given the SNR threshold calculated in the previous section, our first objective is to calculate the detection horizons for the different possible theories (i.e. the maximum redshift a system of a certain mass can be detected with $\rho \geq 10$). To arrive at the various detection horizons, we use a Monte Carlo simulation based on an astrophysical distribution of sources [142]. For the Monte Carlo, we impose two restrictions: the first is that the maximum allowed redshifted total mass corresponds to the MCMC limit of $m(z) = 1.163\times10^8\, M_\odot$. The second is, for computational purposes, to restrict the maximum array length for waveform generation to 2^{23} elements. This second restriction will automatically exclude the investigation of some lower mass systems. For each system, the angular values are drawn from standard ranges, while the time of coalescence is chosen to be between $0.3 \leq t_c/\mathrm{yrs} \leq 0.99$. Finally, β is chosen from a uniform distribution given the limits provided in Fig 8.1 for each value of b.

In Fig 8.4 we plot the detection horizons for both positive (upper panel) and negative (lower panel corrections). The various theories are represented by: GR (solid black line), $b = -1/3$ (red dotted line), $b = -2/3$ (blue dashed line), $b = -1$ (green dot-dashed line), $b = -4/3$ (orange double dot-dashed line), $b = -5/3$ (magenta double dash-dot line).

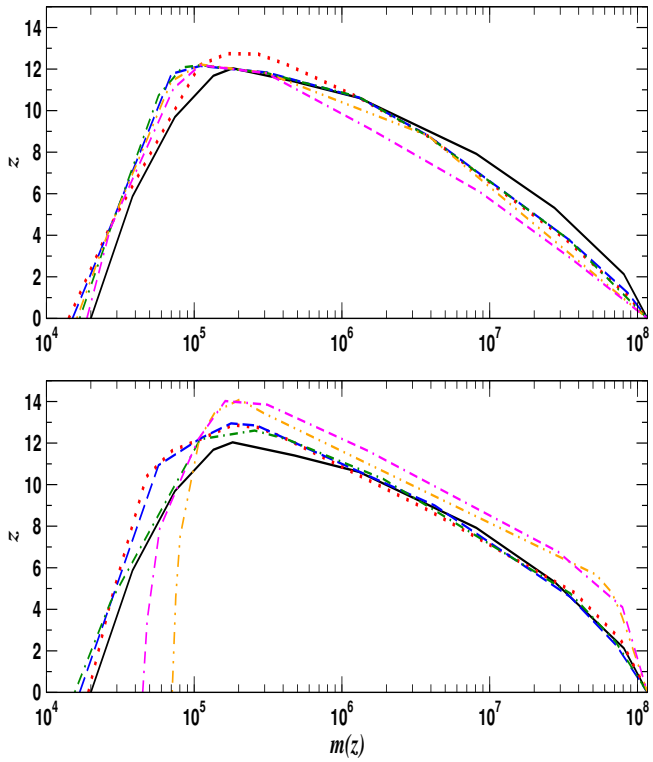

Figure 8.4: *Detection horizons as a function of redshifted total mass for positive (top figure) and negative (bottom figure) non-GR corrected waveforms. In each figure we compare the different theories: GR (solid black line), $b = -1/3$ (red dotted line), $b = -2/3$ (blue dashed line), $b = -1$ (green dot-dashed line), $b = -4/3$ (orange double dot-dashed line), $b = -5/3$ (magenta double dash-dot line).*

We first focus on the positive corrections. At the high mass range, the redshift horizons for the alternative theories are shifted to lower total masses. This is consistent with what we saw in Fig 8.3. The higher the values of β for different values of b, the more high mass waveforms are pushed towards lower frequencies and in some cases, the dominant harmonic exits the detector band. This results in these systems becoming undetectable as the remaining visible harmonics achieve a SNR less than the detection threshold. Conversely, we can see that at the low mass end, systems that would otherwise have been undetectable are now visible due again to the fact that they have been shifted to lower frequencies. This shift now moves the dominant harmonic further into the sweet-spot of the detector and out of the photon shot noise. This allows us gain a slight factor in the minimum total redshifted mass detectable with the eLISA detector as compared to when we are using GR signals. We should also note that there is a slight increase in the maximum achieved redshift when using non-GR waveforms.

Now focusing on the negative corrections, we can see that the situation is almost reversed, but still consistent with Fig 8.3. In this case, at the high mass end, systems that were undetectable due to the fact that the dominant harmonic was below the lower frequency cutoff of the detector, are now resolvable to higher redshift than in the GR case. This is due to the fact that with the negative corrections, the waveforms are moved to higher frequencies, thus making the dominant harmonic of the waveform visible. This allows us to make a visible gain in the redshift horizon particularly for the $b = -4/3$ and $b = -5/3$ theories. What is also impressive is that for these two theories the maximum achievable redshift increases from $z \sim 12$ in the GR case to $z \sim 14$. At the low mass end, we can see that for the $b = -1/3$, $b = -2/3$ and $b = -1$ we achieve a small increase in the minimum total mass we can detect. For the $b = -4/3$ and $b = -5/3$ theories, the sudden drop-off can be explained by the fact that the waveforms are moved to a low enough frequency due to the value of β that our waveform generation exceeds the constraint that the maximum

allowed array is 2^{23} elements long. Furthermore, we see that the detection horizon for the $b = -4/3$ is smaller than all other alternative theories in the negative correction case. This is due to the fact that the $b = -4/3$ theory introduces a correction at 0.5PN order in phase and frequency, which zero in GR. The effect of adding a negative quantity is that the detection horizon is very much reduced at low total redshifted masses.

8.5.2 Detectability of non-GR signals using GR templates and observed bias in the parameter estimation

In Fig. 8.5 we present the individual detection limits that our search code has found. The dashed black line represents the limits that we set on β, as depicted in Fig. 8.1. For the values of β and q that are below the yellow curve, our search code managed to detect the injected non-GR signal using only a GR template with a SNR threshold of $\rho \geq 10$. We find that all the considered non-GR signals can be detected, except for a small region in the case of a positive correction with $b = -5/3$. There, our search code fails to detect the non-GR signal for mass ratios $q \gtrsim 5$ slightly (less than a factor of two) before the upper limit on β. This is because lower order corrections have a larger impact on the GR waveform (as shown in Fig. 8.3), especially for a correction at 0PN order which is essentially a leading order correction of GR. For the negative $b = -5/3$ correction, this is no problem, as there the maximum allowed value for β is only around two thirds of the one for the positive correction (to prevent pathologies in the waveform, as introduced in Section 8.3.2).

For values of β and q that are in the red area of the plots in Fig. 8.5, the true source parameters are within the 2σ error prediction for the parameters recovered by the MCMC using the GR template. It is thus unclear whether the observed difference between the estimated parameters and the true source parameters should be put down to the presence of an alternative theory or can simply be attributed to noise. Consequently, GR templates can be used for detection in the red area. With increasing values of β, the estimated parameters are shifted away from the true source parameters, until the true source parameters are outside of the spread of the chain (yellow region). At this point, one can observe a significant fundamental bias in the estimated parameters and hence has to start to use non-GR waveforms for detection. Let us stress that our only concern here is to decide whether or not it makes sense to use a non-GR template for parameter estimation. In order to give statements about whether the detector data favours GR or an alternative theory, one has to employ model selection tools, such as an evaluation of the *Bayes factor* [67, 128]. We postpone such treatments to a future paper.

We observe that, with an increasing value of b, the red curves in Fig. 8.5 approach the detection limit more and more. Towards a 2PN correction ($b = -1/3$), the GR template is sufficient for parameter estimation for practically all considered mass ratios and the fundamental bias introduced to the parameters by the presence of an alternative theory is within the spread of the search algorithm. Going to lower values of b (from bottom to the top in Fig. 8.5), we notice that the yellow area takes more and more space, corresponding to an increasing number of cases where the GR waveform is still sufficient for detection, but insufficient for parameter estimation. In such cases, a corrected, non-GR waveform has to be used in order to recover unbiased binary parameters. For $b = -5/3$, this is the case for values of β that are around one order of magnitude below the detection limit, while for $b = -4/3$ it is a factor of a few. For the nearly equal-mass case with $q = 1.1$, the difference is around an order of magnitude for all corrections, decreasing towards higher mass ratios. We put this is down to the fact that the correction to the orbital phase (8.29) is not only proportional to β, but also to $\eta^{3b/5}$ and $q = 1.1$ corresponds to the largest considered value of η.

8.5.3 Conclusion

We have introduced perturbations to the 2PN time domain orbital phase evolution of non-spinning, quasi-circular supermassive black hole binary inspirals predicted by GR. To make sure that the considered modifications are perturbative, we limited them to be at maximum 50% of the fiducial PN coefficients. We found that for negative corrections the limits that have to be used are in reality up to a factor of ten lower than the ones for the positive corrections, because of pathologies in the evolution of the non-GR orbital frequency. In order to be able to compare our results with previous works that have been done in terms of the ppE framework in the stationary phase approximation, we have established an approximate relation between waveforms modified in the time and frequency domain. Using a Metropolis-Hastings search algorithm with an initial burn-in phase consisting of thermostated annealing followed by simulated annealing, we found that GR waveforms are sufficient for both detection and parameter estimation of non-GR theories that come with corrections beyond 1PN. On the other hand, for leading order and 0.5PN modifications, GR waveforms are not capable of covering the entire parameter space, making it necessary to use non-GR waveforms above a certain threshold in order to avoid a fundamental bias in the recovered parameters. This is due to the fact that low-order corrections can shift the power spectrum of the modified gravitational waveform by a significant fraction, while the effect of higher order corrections is relatively small. Moreover, we found that the detection horizon of the eLISA detector could be improved from maximum redshifts of 12 up to redshifts of 14 if GR suffers a 0 or 0.5PN correction.

In addition to the results presented here, in a future work we plan to assess which values of β allow a discrimination between GR and an alternative theory with sufficiently high betting odds. To this end, we intend to apply Bayesian model selection tools in the context of different LISA-like detector configurations. Possible future work could also be invested into the introduction of spin-precession and eccentricity to our waveform model. Thereby we could avoid the complicated computations that are required to reconcile such effects with the stationary phase approximation [25, 31].

8.6 Appendix

8.6.1 Antipodal sky solutions

Due to symmetries in the antenna pattern functions in the low-frequency approximation introduced in Section 5.2 and in the harmonic coefficients given in section 3.3.1, secondary maxima with alternative solutions for the angles θ, ϕ, ι and ψ exist on the likelihood surface, so-called *antipodal sky solutions*, that are almost indistinguishable from the true values at the global maximum. In particular, a secondary maximum is located at [143, 144]

$$\theta' = \pi - \theta, \qquad \phi' = \pi + \phi, \qquad \iota' = \pi - \iota, \qquad \psi' = \pi - \psi. \tag{8.41}$$

Two other local maxima can be found at (θ', ϕ', ι) and (θ, ϕ, ι'). At low frequencies, the solution is strictly antipodal and it is impossible to distinguish the true sky position from the alternative solutions. The degeneracy begins only to resolve with increasing frequency, reducing the height of the secondary maxima. As a consequence, the Markov Chain has a hard time to distinguish the true sky position from one of the alternative solutions. Since this is a similar problem for both GR and non-GR templates, we consider it to be a detection with correct parameters if the MCMC gets stuck on one of the antipodal sky solutions.

8.6.2 Pinpointing a detection

In order to clarify what we consider to be a successful recovery of the parameters of an injected non-GR signal through a GR template, we supply a few example chains here. Fig. 8.6 depicts a successful recovery

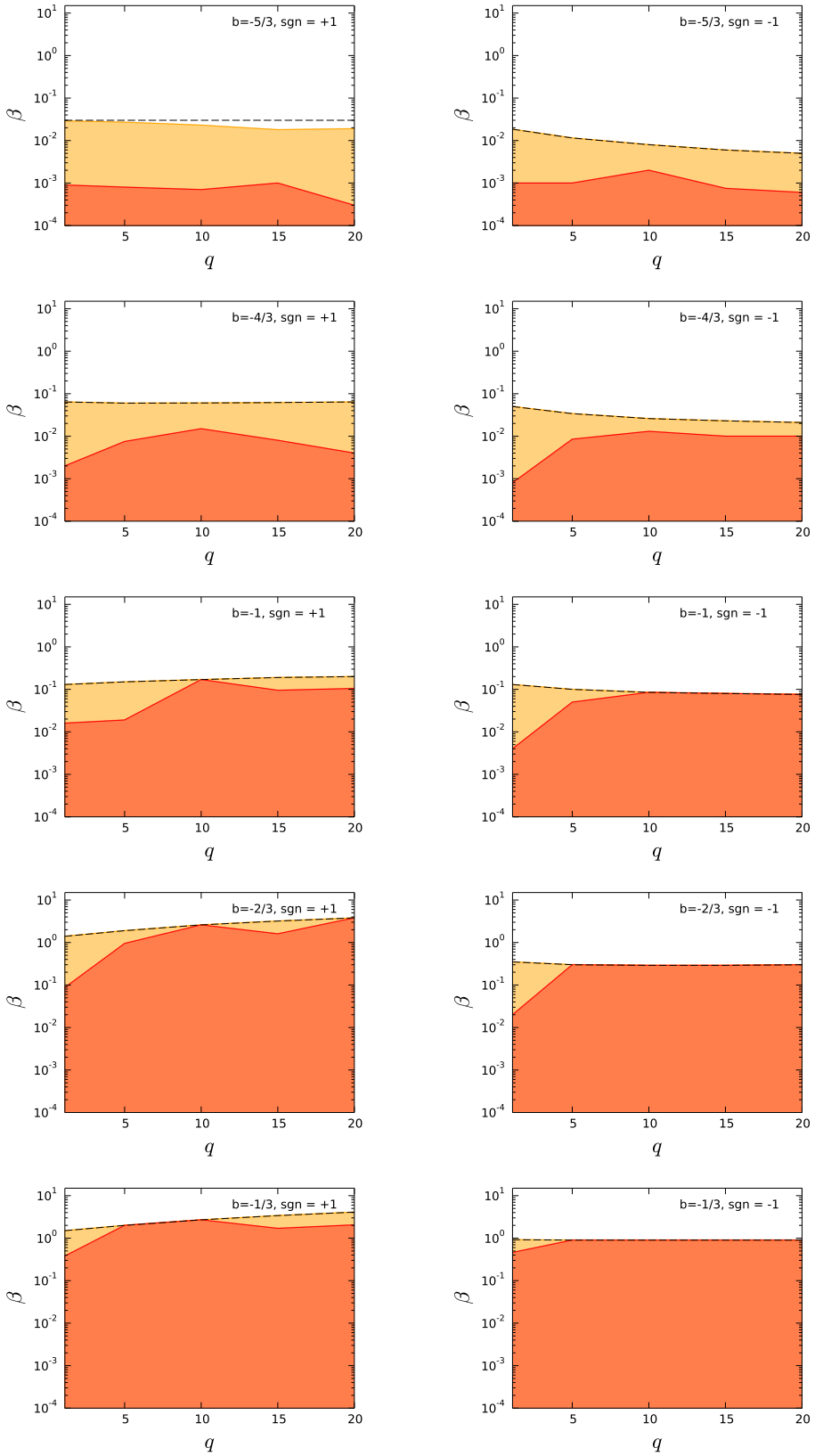

Figure 8.5: *Allowed upper limits for β (dashed black line), detection limits (yellow curve) and limits where unbiased parameter estimation is still possible with GR templates (red curve). We account for positive (left,* $\mathrm{sgn} = +1$*) and negative (right,* $\mathrm{sgn} = -1$*) corrections and increasing values of b (top to bottom). Except for the positive correction with* $b = -5/3$*, GR templates manage to detect all injected non-GR waveforms. With increasing values of b, the red curve below which GR templates are sufficient for parameter estimation approaches the detection limit.*

of the global maximum. The true parameters (black line) are within the 2σ spread of the chain (red), and hence one cannot distinguish whether the recovered parameter values differ from the true model because of the presence of an alternative theory of gravity or whether the observed deviation is just caused by noise. Consequently, the fundamental bias created by the alternative theory is not strong enough to overcome noise; using a non-GR template to recover the binary parameters is useless at this point. As discussed in the previous subsection, the chain can also end up on a secondary maximum representing an antipodal sky solution (green line), as shown in Fig. 8.7. As GR does not manage to distinguish antipodal sky solutions from the true solution either, we consider this case to be a detection where the bias introduced by the alternative theory is not strong enough to be possibly recovered. The mass parameters $\mathscr{M}$ and μ are slightly off in order to achieve the same likelihood as the true values have for the global maximum. In Fig. 8.8, a case is introduced where the recovered parameters show a significant difference from the true parameters: the true values are outside the spread of the chain. As a consequence, the parameters recovered with a GR template will be biased and the use of a non-GR template is mandatory in this case.

By starting a couple of MCMC chains for positive and negative corrections with $b \in \left\{-\frac{5}{3}, -\frac{4}{3}, -1, -\frac{2}{3}, -\frac{1}{3}\right\}$ and different values of β, one can hence infer the unbiased parameter estimation limits as they are illustrated in Fig. 8.5.

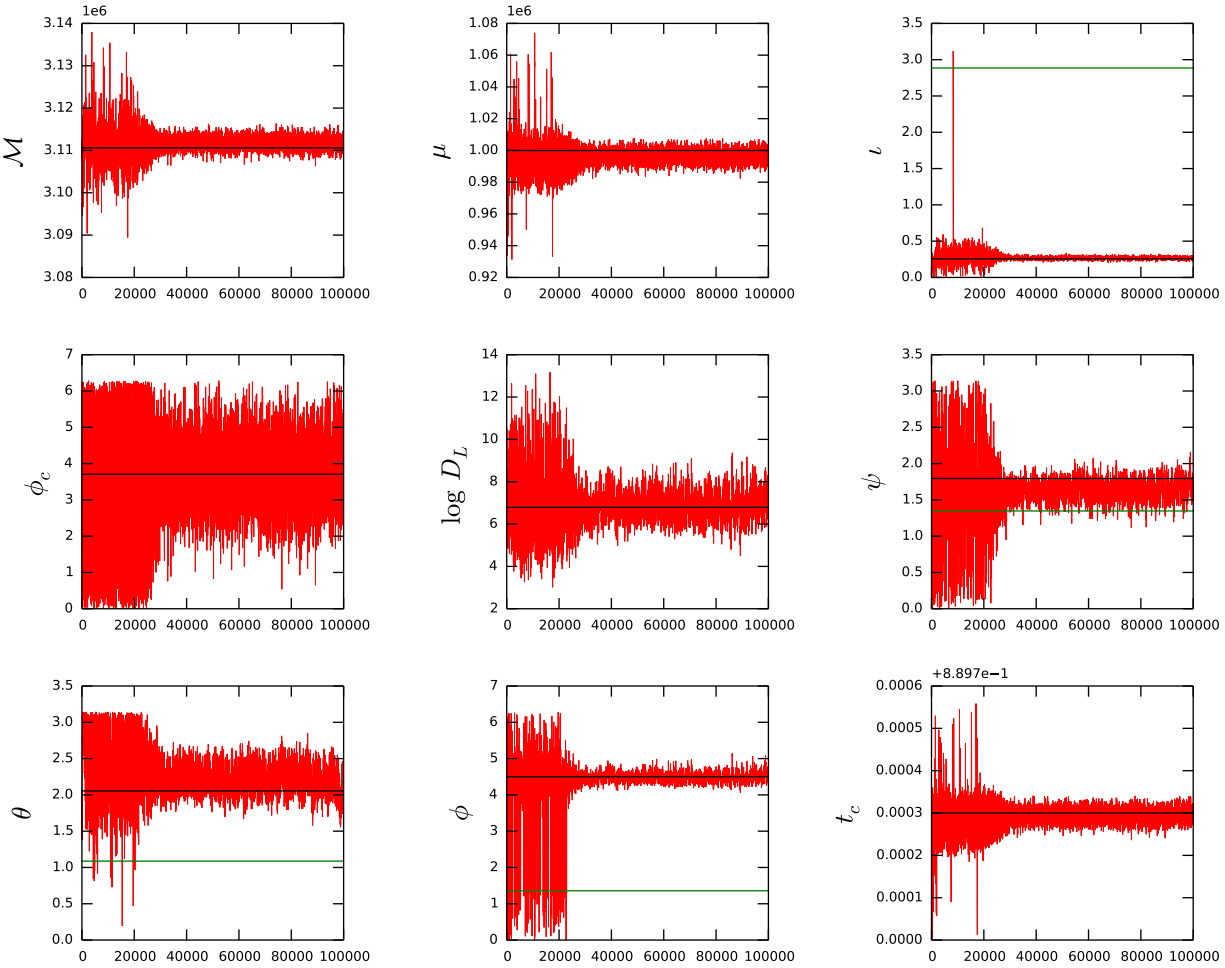

Figure 8.6: *Chain values for 500'000 iterations on a log-likelihood surface with an injected positively-corrected non-GR waveform with* $b = -2/3$ *and* $\beta = 0.025$*. The true values of the parameters (black line) are within the* 2σ *spread of the chain (red). Consequently, a GR-template and a non-GR template perform equally well in the recovery of the binary parameters, as the parameter biases introduced by the non-GR corrections fail to overcome noise.*

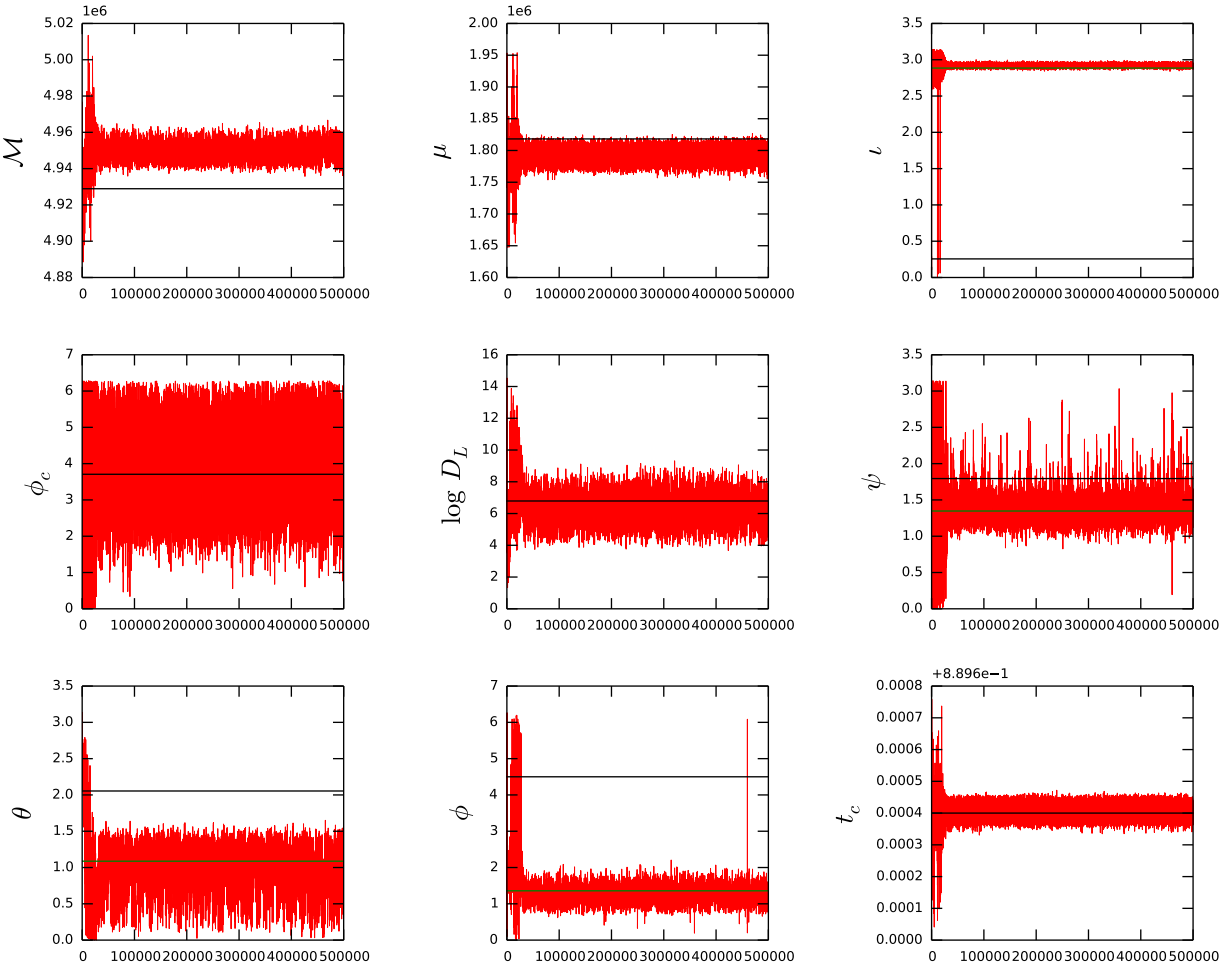

Figure 8.7: *Chain values for 500'000 iterations on a log-likelihood surface with an injected positively-corrected non-GR waveform with $b = -1$ and $\beta = 0.021$. The chain (red) prefers the secondary maximum provided by the antipodal sky solution (green line) to the true parameters (black line) and slightly shifts $\mathcal{M}$ and μ in order to achieve the same likelihood as is reached by the global maximum. Since GR cannot distinguish the two solutions either, we consider the true parameters to be within the spread of the chain and treat this case similar to the one shown in Fig. 8.6.*

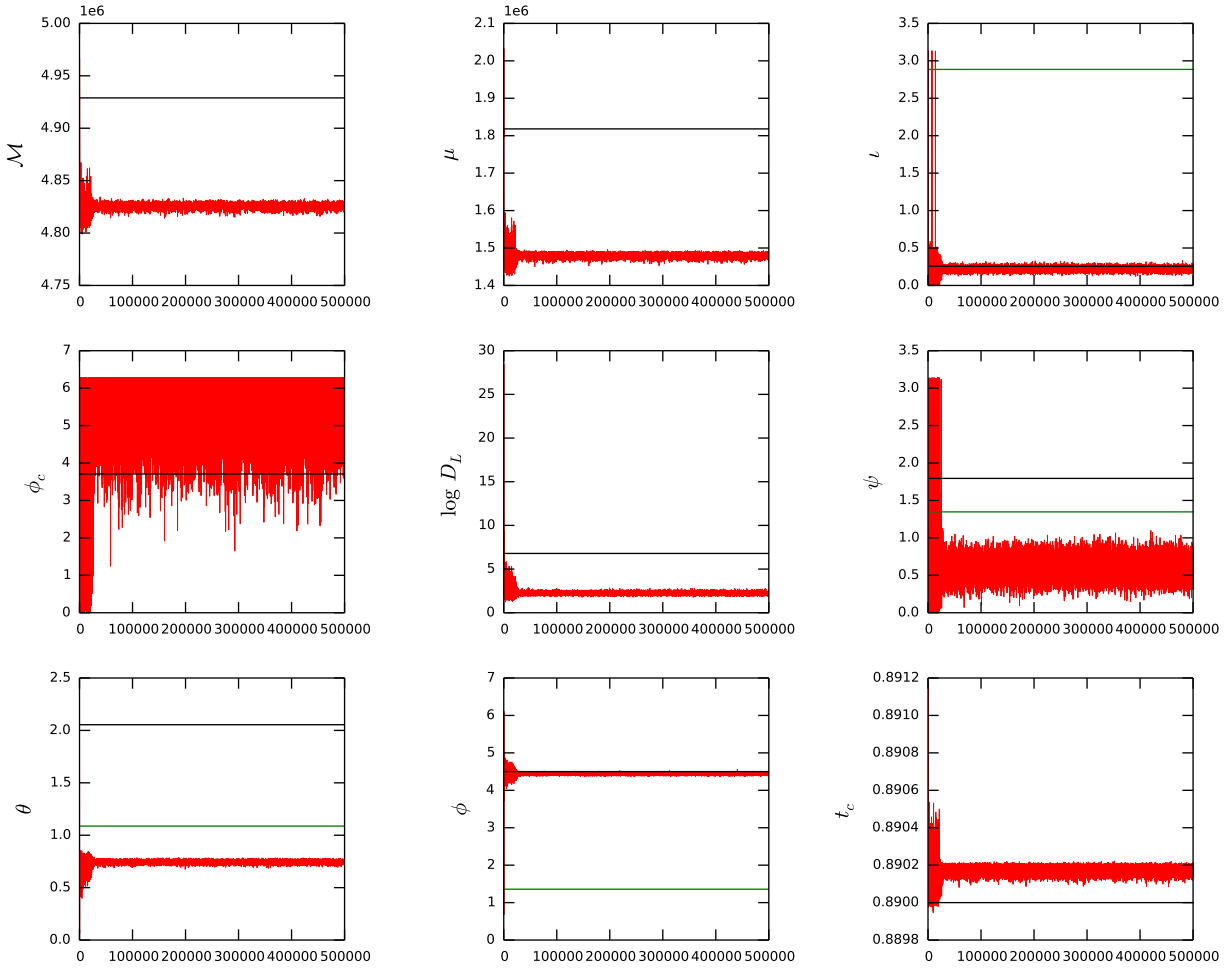

Figure 8.8: *Chain values for 500'000 iterations on a log-likelihood surface with an injected positively-corrected non-GR waveform with $b = -5/3$ and $\beta = 0.0029$. The true parameter values (black line) and also the antipodal sky solutions (green line) are outside the spread of the chain (red). Therefore, in this case the GR template is not fit for parameter estimation and the use of a non-GR template is necessary in order to recover unbiased parameters.*

Appendix A

Signal Processing Basics

In contrast to the analytical stationary phase approximation of the Fourier transform that is presented in Section 3.3.2, one can also compute the Fourier transform numerically. In order to avoid numerical artifacts, the sampling of the data needs to be treated carefully. In the following we give a brief overview on the basics of signal processing.

A.1 Sampling the time domain waveform

Sampling is the process of discretizing a waveform. To this end, let us take N samples at equally spaced time steps Δt_s. The *sample rate* $f_s = 1/\Delta t_s$ is defined as the number of samples that are taken per second. For a signal observed for a time span $T_{\rm obs}$, the required number of samples is $N = T_{\rm obs}/\Delta t_s$.

In order to capture a representative sample of a given signal, we need to consider the *Nyquist theorem*. This theorem states the requirement that $f_s \geq 2f_{\rm max}$, where $f_{\rm max}$ is the maximum frequency appearing in the signal. This fact can be illustrated when considering periodic signals, such as sine and cosine: there we need at least two data points per cycle such that the frequency content of the signal is analyzed properly. Taking less samples leads to undersampling effects that introduce spurious frequencies (Fig. A.1). In practice, taking four points per signal cycle provides sufficient accuracy, i.e. we work with a sample rate of $f_s = 4\,f_{\rm max}$. This means in terms of the number of samples that $N = 4\,T_{\rm obs}\,f_{\rm max}$.

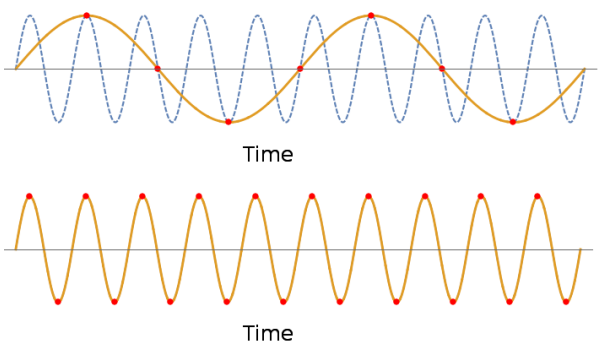

Figure A.1: *According to the Nyquist theorem, at least two samples per signal cycle have to be collected, as done for a harmonic signal in the bottom plot. If less samples are taken, the frequency content of the signal is wrong, as illustrated in the top plot (undersampling).*

Fast Fourier transforms require an array of samples of length $n = 2^k$, $k \in \mathbb{N}$. We incorporate this by taking the next higher sample number that is a power of two:

$$n = 2^{\lceil \log_2 N \rceil}. \tag{A.1}$$

The adjusted sample rate can then be computed as $f_s = n/T_{\text{obs}} = 2^{\lceil \log_2 4\, T_{\text{obs}} f_{\text{max}} \rceil}$ and lets us compute the waveform samples

$$h_k = h(k\,\Delta t_s), \qquad k \in \{0, \ldots, n-1\}. \tag{A.2}$$

A.2 Windowing

As in this work we are only considering the inspiral part of the gravitational waveform, we will stop at some predefined last stable orbit or even before if we encounter a breakdown of a certain approximation. This leads to a waveform that suddenly sets on when the detector starts to listen and is then immediately cut off at a certain point. If not accounted for, such cut offs lead to excessive ringing in the Fourier domain, in terms of frequencies that are higher than the maximum frequency present in the signal. This is because sinusoids with very short periods are required to model a sharp cut off. To prevent ringing, the cut off has to be smoothed out by a *windowing function*. We use the so-called *Hann Window*

$$H(t) = \cos^2\left(\frac{\pi t}{2T_H}\right), \tag{A.3}$$

with the full-width-half-maximum T_H. In order to window a gravitational-wave chirp such as e.g. the one in Fig. 3.2, we apply (A.3) to both ends of it:

$$h_{\text{Hann}}(t) = h(t) \times \begin{cases} \cos^2\left(\pi \frac{t - T_H}{2T_H}\right) & t < T_H, \\ \cos^2\left(\pi \frac{t - t_{\text{max}} + T_H}{2T_H}\right) & t > t_{\text{max}} - T_H, \end{cases} \tag{A.4}$$

where t_{max} is the time when the chirp is cut off. This has by design the property that the waveform is set to zero at $t = 0$, slowly increases to the normal amplitude until $t = T_H$, and then decreases again to zero between $t = t_{\text{max}} - T_H$ and $t = t_{\text{max}}$. In our work we use $T_H = 10^5$s, what is about 0.3% of a typical total observation time of one year.

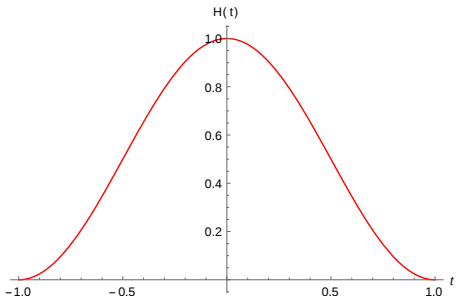

Figure A.2: *This is a plot of the typical shape of a Hann Window that is used to smooth out sharp cut-off edges in the time domain waveform which would introduce excessive ringing in the FFT.*

A.3 The Fast Fourier Transform algorithm (FFT)

In the following we summarise the idea behind the Fast Fourier transform (FFT) algorithm [145] that we use in our codes. Suppose we sample a time domain signal at times $t_k = k\,\Delta t$, $k = 0,\ldots,N$. We want to compute the discrete Fourier transform (DFT) sampled at frequencies $f_n = \frac{n}{N\,\Delta t}$, $n = -N/2,\ldots,N/2$, namely

$$H(f_n) = \int_{-\infty}^{\infty} dt\, h(t)\, e^{2\pi i f_n t} \approx \sum_{k=0}^{N-1} h_k\, e^{2\pi i f_n t}\,\Delta t = \Delta t \sum_{k=0}^{N-1} h_k\, e^{2\pi i n k/N}. \tag{A.5}$$

The DFT computes

$$H_n \equiv \sum_{k=0}^{N-1} h_k\, e^{2\pi i n k/N}, \qquad H(f_n) \approx \Delta t\, H_n, \tag{A.6}$$

with $\mathcal{O}(N^2)$ evaluations of the exponential. The FFT exploits the symmetries of H_n to reduce the amount of evaluations to $\mathcal{O}(N \log N)$. In particular, H_n can be written in terms of even and odd parts as

$$H_n = \sum_{k=0}^{N/2-1} h_{2k} e^{\frac{2\pi i n 2k}{N}} + \sum_{k=0}^{N/2-1} h_{2k+1} e^{\frac{2\pi i n (2k+1)}{N}} = \underbrace{\sum_{k=0}^{N/2-1} h_{2k} e^{\frac{2\pi i n k}{N/2}}}_{A_n} + e^{\frac{2\pi i n k}{N}} \underbrace{\sum_{k=0}^{N/2-1} h_{2k+1} e^{\frac{2\pi i n k}{N/2}}}_{B_n}. \tag{A.7}$$

One can immediately observe the following symmetries:

$$A_{n+\frac{N}{2}} = A_n, \qquad B_{n+\frac{N}{2}} = B_n, \qquad e^{\frac{2\pi i\left(n+\frac{N}{2}\right)}{N}} = -e^{\frac{2\pi i n}{N}}. \tag{A.8}$$

This enables us to compute the Fourier transform as

$$H_n = \begin{cases} A_n + e^{\frac{2\pi i n}{N}} B_n, & 0 \le n < \frac{N}{2}, \\ A_{n-\frac{N}{2}} - e^{\frac{2\pi i n}{N}} B_{n-\frac{N}{2}}, & \frac{N}{2} \le n < N. \end{cases} \tag{A.9}$$

It is now sufficient to compute $\{A_n, B_n\}$ for $0 \le n < \frac{N}{2}$, amounting to $\mathcal{O}\left(N^2/2\right)$ evaluations of the exponential. Following a similar procedure, A_n and B_n can subsequently be decomposed into odd and even parts, leading to the desired $\mathcal{O}(N \log N)$ behaviour. In order to achieve maximum efficiency, the FFT algorithm requires an array of evenly spaced time domain samples that has a length of 2^n with n being an integer number. This has to be taken into account when determining the correct sample frequency.

References

[1] C. Huwyler, A. Klein, and P. Jetzer, Phys. Rev. D **86**, 084028 (2012).

[2] C. Huwyler, E. Porter, and P. Jetzer (2014), in preparation.

[3] C. W. Misner, K. S. Thorne, and J. A. Wheeler, *Gravitation. Volume I.* (W. H. Freeman, San Francisco, USA, 1973).

[4] R. M. Wald, *General Relativity* (University of Chicago Press, Chicago, USA, 1984).

[5] N. Straumann, *General Relativity, With Applications to Astrophysics* (Springer Verlag, Berlin, Germany, 2004).

[6] M. Maggiore, *Gravitational Waves - Volume 1: Theory and Experiments* (Oxford University Press, Oxford, England, 2008).

[7] A. Buonanno, ArXiv e-prints (2007), `arXiv:0709.4682`.

[8] L. Blanchet and T. Damour, Royal Society of London Philosophical Transactions Series A **320**, 379 (1986).

[9] L. Blanchet, Royal Society of London Proceedings Series A **409**, 383 (1987).

[10] L. Blanchet, Classical and Quantum Gravity **15**, 1971 (1998).

[11] L. Blanchet, Living Reviews in Relativity **17**, 2 (2014).

[12] C. M. Will and A. G. Wiseman, Phys. Rev. D **54**, 4813 (1996).

[13] M. E. Pati and C. M. Will, Phys. Rev. D **62**, 124015 (2000).

[14] S. Gillessen, F. Eisenhauer, T. K. Fritz, H. Bartko, K. Dodds-Eden, O. Pfuhl, T. Ott, and R. Genzel, ApJ **707**, L114 (2009).

[15] A. Sesana, M. Volonteri, and F. Haardt, MNRAS **377**, 1711 (2007).

[16] E. Barausse, V. Cardoso, and P. Pani, Phys. Rev. D **89**, 104059 (2014).

[17] P. Ade et al. (Planck Collaboration), A&A **566**, A54 (2014).

[18] T. A. Apostolatos, C. Cutler, G. J. Sussman, and K. S. Thorne, Phys. Rev. D **49**, 6274 (1994).

[19] L. Blanchet, Living Reviews in Relativity **9** (2006).

[20] L. Blanchet, T. Damour, G. Esposito-Farèse, and B. R. Iyer, Phys. Rev. D **71**, 124004 (2005).

[21] L. Blanchet, T. Damour, and G. Esposito-Farèse, Phys. Rev. D **69**, 124007 (2004).

[22] L. Blanchet, B. R. Iyer, and B. Joguet, Phys. Rev. D **65**, 064005 (2002).

[23] L. Blanchet, G. Faye, B. R. Iyer, and B. Joguet, Phys. Rev. D **65**, 061501 (2002).

[24] A. Buonanno, B. R. Iyer, E. Ochsner, Y. Pan, and B. S. Sathyaprakash, Phys. Rev. D **80**, 084043 (2009).

[25] N. Yunes, K. G. Arun, E. Berti, and C. M. Will, Phys. Rev. D **80**, 084001 (2009).

[26] S. Droz, D. J. Knapp, E. Poisson, and B. J. Owen, Phys. Rev. D **59**, 124016 (1999).

[27] B. M. Barker and R. F. O'Connell, Phys. Rev. D **12** (1975).

[28] M. Dotti, M. Volonteri, A. Perego, M. Colpi, M. Ruszkowski, and F. Haardt, MNRAS **402**, 682 (2010).

[29] A. Vecchio, Phys. Rev. D **70**, 042001 (2004).

[30] L. Blanchet, A. Buonanno, and G. Faye, Phys. Rev. D **74**, 104034 (2006).

[31] A. Klein, N. Cornish, and N. Yunes, Phys. Rev. D **88**, 124015 (2013).

[32] C. M. Will, Living Reviews in Relativity **17**, 4 (2014).

[33] J. R. Gair, M. Vallisneri, S. L. Larson, and J. G. Baker, Living Reviews in Relativity **16**, 7 (2013).

[34] N. Yunes and X. Siemens, Living Reviews in Relativity **16**, 9 (2013).

[35] N. Yunes and F. Pretorius, Phys. Rev. D **80**, 122003 (2009).

[36] J. M. Weisberg, D. J. Nice, and J. H. Taylor, ApJ **722**, 1030 (2010).

[37] Y. Fujii and K.-I. Maeda, *The Scalar-Tensor Theory of Gravitation* (Cambridge University Press, Cambridge, England, 2003).

[38] S. Mirshekari and C. M. Will, Phys. Rev. D **87**, 084070 (2013).

[39] R. N. Lang, Phys. Rev. D **89**, 084014 (2014).

[40] B. Bertotti, L. Iess, and P. Tortora, Nature **425**, 374 (2003).

[41] C. M. Will and N. Yunes, Classical and Quantum Gravity **21**, 4367 (2004).

[42] H. W. Zaglauer, ApJ **393**, 685 (1992).

[43] B. Famaey and S. S. McGaugh, Living Reviews in Relativity **15**, 10 (2012).

[44] K. Yagi, L. C. Stein, N. Yunes, and T. Tanaka, Phys. Rev. D **85**, 064022 (2012).

[45] P. Pani and V. Cardoso, Phys. Rev. D **79**, 084031 (2009).

[46] S. Alexander and N. Yunes, Phys. Rep. **480**, 1 (2009).

[47] A. Ashtekar and J. Lewandowski, Classical and Quantum Gravity **21**, 53 (2004).

[48] A. de Felice and S. Tsujikawa, Living Reviews in Relativity **13**, 3 (2010).

[49] W. Pauli and M. Fierz, Helv. Phys. Acta **12**, 297 (1939).

[50] C. M. Will, Phys. Rev. D **57**, 2061 (1998).

[51] C. Talmadge, J.-P. Berthias, R. W. Hellings, and E. M. Standish, Physical Review Letters **61**, 1159 (1988).

[52] D. Baskaran, A. G. Polnarev, M. S. Pshirkov, and K. A. Postnov, Phys. Rev. D **78**, 044018 (2008).

[53] E. Berti, A. Buonanno, and C. M. Will, Phys. Rev. D **71**, 084025 (2005).

[54] A. Stavridis and C. M. Will, Phys. Rev. D **80**, 044002 (2009).

[55] K. G. Arun and C. M. Will, Classical and Quantum Gravity **26**, 155002 (2009).

[56] D. Keppel and P. Ajith, Phys. Rev. D **82**, 122001 (2010).

[57] K. Yagi and T. Tanaka, Phys. Rev. D **81**, 064008 (2010).

[58] E. Berti, J. Gair, and A. Sesana, Phys. Rev. D **84**, 101501 (2011).

[59] S. Mirshekari, N. Yunes, and C. M. Will, Phys. Rev. D **85**, 024041 (2012).

[60] A. S. Sefiedgar, K. Nozari, and H. R. Sepangi, Physics Letters B **696**, 119 (2011).

[61] P. Hořava, Phys. Rev. D **79**, 084008 (2009).

[62] R. Garattini, in *American Institute of Physics Conference Series*, edited by J. Kouneiher, C. Barbachoux, T. Masson, and D. Vey (2012), vol. 1446 of *American Institute of Physics Conference Series*, pp. 298–310.

[63] N. Yunes, F. Pretorius, and D. Spergel, Phys. Rev. D **81**, 064018 (2010).

[64] M. E. S. Alves, O. D. Miranda, and J. C. N. de Araujo, Classical and Quantum Gravity **27**, 145010 (2010).

[65] K. Chatziioannou, N. Yunes, and N. Cornish, Phys. Rev. D **86**, 022004 (2012).

[66] L. Sampson, N. Cornish, and N. Yunes, Phys. Rev. D **87**, 102001 (2013).

[67] N. Cornish, L. Sampson, N. Yunes, and F. Pretorius, Phys. Rev. D **84**, 062003 (2011).

[68] M. Vallisneri and N. Yunes, Phys. Rev. D **87**, 102002 (2013).

[69] L. Sampson, N. Yunes, and N. Cornish, Phys. Rev. D **88**, 064056 (2013).

[70] K. G. Arun, B. R. Iyer, M. S. S. Qusailah, and B. S. Sathyaprakash, Classical and Quantum Gravity **23**, L37 (2006).

[71] K. G. Arun, B. R. Iyer, M. S. S. Qusailah, and B. S. Sathyaprakash, Phys. Rev. D **74**, 024006 (2006).

[72] T. Accadia, F. Acernese, F. Antonucci, P. Astone, G. Ballardin, F. Barone, M. Barsuglia, A. Basti, T. S. Bauer, M. G. Beker, et al., Classical and Quantum Gravity **28**, 025005 (2011).

[73] T. Damour, B. R. Iyer, and B. S. Sathyaprakash, Phys. Rev. D **63**, 044023 (2001).

[74] T. Damour, B. R. Iyer, and B. S. Sathyaprakash, Phys. Rev. D **66**, 027502 (2002).

[75] V. Varma, P. Ajith, S. Husa, J. Calderon Bustillo, M. Hannam, and M. Puerrer, ArXiv e-prints (2014), `arXiv:1409.2349`.

[76] eLISA Consortium, P. A. Seoane, S. Aoudia, H. Audley, G. Auger, S. Babak, J. Baker, E. Barausse, S. Barke, M. Bassan, et al., ArXiv e-prints (2013), arXiv:1305.5720.

[77] P. Amaro-Seoane, S. Aoudia, S. Babak, P. Binétruy, E. Berti, A. Bohé, C. Caprini, M. Colpi, N. J. Cornish, K. Danzmann, et al., Classical and Quantum Gravity **29**, 124016 (2012).

[78] O. Jennrich, P. Binétruy, M. Colpi, K. Danzmann, P. Jetzer, A. Lobo, G. Nelemans, B. Schutz, R. Stebbins, T. Sumner, et al., *NGO assessment study report (Yellow Book), ESA/SRE(2011)19,* http://sci.esa.int/ngo/49839-ngo-assessment-study-report-yellow-book/ (2012).

[79] K. Danzmann, T. A. Prince, P. Binétruy, P. Bender, S. Buchman, J. Centrella, M. Cerdonio, N. Cornish, M. Cruise, C. J. Cutler, et al., *LISA assessment study report (Yellow Book), ESA/SRE(2011)3,* http://sci.esa.int/lisa/48364-lisa-assessment-study-report-yellow-book/ (2011).

[80] M. Tinto and S. V. Dhurandhar, Living Reviews in Relativity **17**, 6 (2014).

[81] T. A. Prince, M. Tinto, S. L. Larson, and J. W. Armstrong, Phys. Rev. D **66**, 122002 (2002).

[82] L. J. Rubbo, N. J. Cornish, and O. Poujade, Phys. Rev. D **69**, 082003 (2004).

[83] M. Vallisneri and C. R. Galley, Classical and Quantum Gravity **29**, 124015 (2012).

[84] C. Cutler, Phys. Rev. D **57**, 7089 (1998).

[85] N. Seto, Phys. Rev. D **66**, 122001 (2002).

[86] N. J. Cornish and L. J. Rubbo, Phys. Rev. D **67**, 022001 (2003).

[87] N. J. Cornish, Phys. Rev. D **65**, 022004 (2002).

[88] K. G. Arun, S. Babak, E. Berti, N. Cornish, C. Cutler, J. Gair, S. A. Hughes, B. R. Iyer, R. N. Lang, I. Mandel, et al., Classical and Quantum Gravity **26**, 094027 (2009).

[89] G. Nelemans, L. R. Yungelson, and S. F. Portegies Zwart, MNRAS **349**, 181 (2004).

[90] S. E. Timpano, L. J. Rubbo, and N. J. Cornish, Phys. Rev. D **73**, 122001 (2006).

[91] L. S. Finn, ArXiv e-prints (1999), arXiv:gr-qc/9903107.

[92] M. Vallisneri, Phys. Rev. D **77**, 042001 (2008).

[93] C. L. Rodriguez, B. Farr, W. M. Farr, and I. Mandel, Phys. Rev. D **88**, 084013 (2013).

[94] N. J. Cornish and E. K. Porter, Classical and Quantum Gravity **23**, 761 (2006).

[95] T. B. Littenberg and N. J. Cornish, Phys. Rev. D **82**, 103007 (2010).

[96] R. M. Neal, Tech. Rep. CRG-TR-93-1, Departement of Computer Science, University of Toronto (1993), URL http://www.cs.toronto.edu/~radford/ftp/review.pdf.

[97] D. J. C. MacKay, in *Learning in Graphical Models*, edited by M. I. Jordan (Kluwer Academic Press, 1998), NATO Science Series, pp. 175–204.

[98] N. J. Cornish and E. K. Porter, Classical and Quantum Gravity **24**, 5729 (2007).

[99] E. K. Porter and J. Carré, Classical and Quantum Gravity **31**, 145004 (2014).

[100] C. Brans and R. H. Dicke, Phys. Rev. **124**, 925 (1961).

[101] J. Bekenstein and M. Milgrom, ApJ **286**, 7 (1984).

[102] J. D. Bekenstein, Phys. Rev. D **70**, 083509 (2004).

[103] V. Faraoni, ArXiv e-prints (2008), `arXiv:0810.2602v1`.

[104] L. S. Finn, Phys. Rev. D **46**, 5236 (1992).

[105] E. Poisson and C. M. Will, Phys. Rev. D **52**, 848 (1995).

[106] C. M. Will, Phys. Rev. D **50**, 6058 (1994).

[107] P. D. Scharre and C. M. Will, Phys. Rev. D **65**, 042002 (2002).

[108] K. G. Arun, A. Buonanno, G. Faye, and E. Ochsner, Phys. Rev. D **79**, 104023 (2009).

[109] E. Komatsu, J. Dunkley, M. R. Nolta, C. L. Bennett, B. Gold, G. Hinshaw, N. Jarosik, D. Larson, M. Limon, L. Page, et al., Astrophysical Journal Supplement Series **180**, 330 (2009).

[110] C. M. Will, *Theory and Experiment in Gravitational Physics* (Cambridge University Press, Cambridge, England, 1993).

[111] K. S. Thorne, Reviews of Modern Physics **52**, 299 (1980).

[112] A. Klein, P. Jetzer, and M. Sereno, Phys. Rev. D **80**, 064027 (2009).

[113] N. Yunes and S. A. Hughes, Phys. Rev. D **82**, 082002 (2010).

[114] C. Cutler and É. E. Flanagan, Phys. Rev. D **49**, 2658 (1994).

[115] T. B. Littenberg and N. J. Cornish, Phys. Rev. D **80**, 063007 (2009).

[116] T. G. F. Li, W. Del Pozzo, S. Vitale, C. Van Den Broeck, M. Agathos, J. Veitch, K. Grover, T. Sidery, R. Sturani, and A. Vecchio, Phys. Rev. D **85**, 082003 (2012).

[117] R. N. Lang and S. A. Hughes, Phys. Rev. D **74**, 122001 (2006).

[118] A. Vecchio and E. D. Wickham, Phys. Rev. D **70**, 082002 (2004).

[119] R. N. Lang, S. A. Hughes, and N. J. Cornish, Phys. Rev. D **84**, 022002 (2011).

[120] A. Buonanno, Y. Chen, and M. Vallisneri, Phys. Rev. D **67**, 104025 (2003).

[121] L. E. Kidder, C. M. Will, and A. G. Wiseman, Phys. Rev. D **47**, 4183 (1993).

[122] L. E. Kidder, Phys. Rev. D **52**, 821 (1995).

[123] A. Buonanno, Y. Chen, and M. Vallisneri, Phys. Rev. D **67**, 024016 (2003).

[124] N. J. Cornish and J. S. Key, Phys. Rev. D **82**, 044028 (2010).

[125] O. Dreyer, B. Kelly, B. Krishnan, L. S. Finn, D. Garrison, and R. Lopez-Aleman, Classical and Quantum Gravity **21**, 787 (2004).

[126] E. Berti, V. Cardoso, and C. M. Will, Phys. Rev. D **73**, 064030 (2006).

[127] S. Gossan, J. Veitch, and B. S. Sathyaprakash, Phys. Rev. D **85**, 124056 (2012).